

NATIONAL AERONAUTICS AND SPACE ADMINISTRATION

*The Deep Space Network
Progress Report 42-37*

November and December 1976

(NASA-CR-149668) THE DEEP SPACE NETWORK
Progress Report, Nov. - Dec. 1976 (Jet
Propulsion Lab.) 277 p HC A13/MF A01

CSCI 14B

N77-19091

THRU

N77-19120

Unclass

G3/12 16334

REPRODUCED BY
NATIONAL TECHNICAL
INFORMATION SERVICE
U. S. DEPARTMENT OF COMMERCE
SPRINGFIELD, VA. 22161

JET PROPULSION LABORATORY
CALIFORNIA INSTITUTE OF TECHNOLOGY
PASADENA, CALIFORNIA

February 15, 1977

NATIONAL AERONAUTICS AND SPACE ADMINISTRATION

*The Deep Space Network
Progress Report 42-37*

November and December 1976

JET PROPULSION LABORATORY
CALIFORNIA INSTITUTE OF TECHNOLOGY
PASADENA, CALIFORNIA

February 15, 1977

Prepared Under Contract No NAS 7-100
National Aeronautics and Space Administration

Preface

Beginning with Volume XX, the Deep Space Network Progress Report changed from the Technical Report 32- series to the Progress Report 42- series. The volume number continues the sequence of the preceding issues. Thus, Progress Report 42-20 is the twentieth volume of the Deep Space Network series, and is an uninterrupted follow-on to Technical Report 32-1526, Volume XIX.

This report presents DSN progress in flight project support, tracking and data acquisition (TDA) research and technology, network engineering, hardware and software implementation, and operations. Each issue presents material in some, but not all, of the following categories in the order indicated.

Description of the DSN

Mission Support

- Ongoing Planetary/Interplanetary Flight Projects
- Advanced Flight Projects

Radio Science

Special Projects

Supporting Research and Technology

- Tracking and Ground-Based Navigation
- Communications—Spacecraft/Ground
- Station Control and Operations Technology
- Network Control and Data Processing

Network and Facility Engineering and Implementation

- Network
- Network Operations Control Center
- Ground Communications
- Deep Space Stations

Operations

- Network Operations
- Network Operations Control Center
- Ground Communications
- Deep Space Stations

Program Planning

- TDA Planning
- Quality Assurance

In each issue, the part entitled “Description of the DSN” describes the functions and facilities of the DSN and may report the current configuration of one of the five DSN systems (Tracking, Telemetry, Command, Monitor & Control, and Test & Training).

The work described in this report series is either performed or managed by the Tracking and Data Acquisition organization of JPL for NASA.

Contents

DESCRIPTION OF THE DSN

Network Functions and Facilities	1
N. A. Renzetti	
Mark III-77 DSN Command System.	4
W. G. Stinnett	
NASA Code 311-03-43-10	

MISSION SUPPORT

Ongoing Planetary/Interplanetary Flight Projects

Viking Mission Support.	12
D. W. Johnston, T. W. Howe, and G. M. Rockwell	
NASA Code 311-03-21-70	
Intermediate Data Record Support for the Viking Prime Mission	26
J. A. Swindlehurst	
NASA Code 311-03-21-70	
Pioneer Mission Support	35
T. P. Adamski	
NASA Code 311-03-21-90	
Helios Mission Support	39
P. S. Goodwin, E. S. Burke, and T. P. Adamski	
NASA Code 311-03-21-50	

SUPPORTING RESEARCH AND TECHNOLOGY

Tracking and Ground-Based Navigation

A Solar Plasma Stream Measured by DRVID and Dual-Frequency Range and Doppler Radio Metric Data	43
F. B. Winn, S. C. Wu, T. A. Komarek, V. W. Lam, H. N. Royden, and K. B. W. Yip	
NASA Code 310-10-60-46	
Feasibility Study of Far-Field Methods for Calibrating Ground Station Delays	55
T. Sato	
NASA Code 310-10-61-08	
Preliminary Demonstration of Precision DSN Clock Synchronization by Radio Interferometry	57
W. J. Hurd	
NASA Code 310-10-61-08	

Preceding page blank

Communications—Spacecraft/Ground

Radio Frequency Interference from Near-Earth Satellites	69
B. K. Levitt and J. R. Lesh	
NASA Code 310-20-66-07	
Low-Noise Receivers: Microwave Maser Development	78
R. Quinn and E. Wiebe	
NASA Code 310-20-66-08	
On the Inherent Intractability of Finding Good Codes	83
R. J. McEliece and H. C. A. van Tilborg	
NASA Code 310-20-67-11	

Station Control and Operations Technology

DSN Automation	88
R. B. Crow	
NASA Code 310-30-68-10	
Automated Fourth-Harmonic Analyzer	105
C. F. Foster	
NASA Code 310-30-68-11	

Network Control and Data Processing

Control and Computation Module Development	112
R. A. Winkelstein	
NASA Code 310-40-72-04	
Stochastic Models for Software Project Management	118
R. C. Tausworthe	
NASA Code 310-40-72-05	
Walsh Transforms and Signal Detection	127
L. R. Welch	
NASA Code 310-40-72-08	

NETWORK AND FACILITY ENGINEERING AND IMPLEMENTATION

Network

Evaluation of DSN Data Processing With 7200-b/s GCF High-Speed Data Interfaces	132
H. C. Thorman	
NASA Code 311-03-43-10	

Baseband Recording and Playback	136
S. S. Kent and J. I. Molinder	
NASA Code 311-03-43-10	

Simulation of Time Series by Distorted Gaussian Processes	146
C. A.-Greenhall	
NASA Code 311-03-43-10	

Deep Space Stations

Computer Modeling of a Regenerative Solar-Assisted Rankine Power Cycle	152
F. L. Lansing	
NASA Code 311-03-41-08	

Precision Insolation Measurement Under Field Conditions	169
M. S. Reid, R. A. Gardner, and C. M. Berdahl	
NASA Code 311-03-41-08	

Implementation of a Maximum Likelihood Convolutional Decoder in the DSN	176
M. E. Alberda	
NASA Code 311-03-42-49	

Implementation of New-Generation Recorders/Reproducers Into the DSN	184
G. B. Hamilton	
NASA Code 311-03-42-50	

Calibration of Block 4 Translator Path Delays at DSS-14 and CTA 21	188
T. Y. Otoshi, P. D. Batelaan, and K. B. Wallace	
NASA Code 311-03-42-54	

Phase and Group Delay of S-Band Megawatt Cassegrain Diplexer and S-Band Megawatt Transmit Filter	198
R. Lay	
NASA Code 311-03-42-59	

Solar Plasma: Viking 1975 Interplanetary Spacecraft Dual-Frequency Doppler Data	204
S. C. Wu, F. B. Winn, and K. B. W. Yip	
NASA Code 311-03-42-60	

OPERATIONS

Network Operations

A Comprehensive Two-Way Doppler Noise Model for Near-Real-Time Validation of Doppler Data	224
A. L. Berman	
NASA Code 311-03-13-20	

DSN System Performance Test Doppler Noise Models; Noncoherent Configuration	239
R. Bunce	
NASA Code 311-03-14-20	
Bibliography	251

D1
14
22D

N77-19092

Network Functions and Facilities

N. A. Renzetti

Office of Tracking and Data Acquisition

The objectives, functions, and organization of the Deep Space Network are summarized; deep space station, ground communication, and network operations control capabilities are described.

The Deep Space Network (DSN), established by the National Aeronautics and Space Administration (NASA) Office of Tracking and Data Acquisition under the system management and technical direction of the Jet Propulsion Laboratory (JPL), is designed for two-way communications with unmanned spacecraft traveling approximately 16,000 km (10,000 miles) from Earth to the farthest planets of our solar system. It has provided tracking and data acquisition support for the following NASA deep space exploration projects: Ranger, Surveyor, Mariner Venus 1962, Mariner Mars 1964, Mariner Venus 1967, Mariner Mars 1969, Mariner Mars 1971, and Mariner Venus Mercury 1973, for which JPL has been responsible for the project management, the development of the spacecraft, and the conduct of mission operations; Lunar Orbiter, for which the Langley Research Center carried out the project management, spacecraft development, and conduct of mission operations; Pioneer, for which Ames Research Center carried out the project management, spacecraft development, and conduct of mission operations; and Apollo, for which the Lyndon B. Johnson Space Center was the project center and

the Deep Space Network supplemented the Manned Space Flight Network (MSFN), which was managed by the Goddard Space Flight Center (GSFC). It is providing tracking and data acquisition support for Helios, a joint U.S./West German project; and Viking, for which Langley Research Center provides the project management, the Lander spacecraft, and conducts mission operations, and for which JPL also provides the Orbiter spacecraft.

The Deep Space Network is one of two NASA networks. The other, the Spaceflight Tracking and Data Network, is under the system management and technical direction of the Goddard Space Flight Center. Its function is to support manned and unmanned Earth-orbiting satellites. The Deep Space Network supports lunar, planetary, and interplanetary flight projects.

From its inception, NASA has had the objective of conducting scientific investigations throughout the solar sys-

tem. It was recognized that in order to meet this objective, significant supporting research and advanced technology development must be conducted in order to provide deep space telecommunications for science data return in a cost effective manner. Therefore, the Network is continually evolved to keep pace with the state of the art of telecommunications and data handling. It was also recognized early that close coordination would be needed between the requirements of the flight projects for data return and the capabilities needed in the Network. This close collaboration was effected by the appointment of a Tracking and Data Systems Manager as part of the flight project team from the initiation of the project to the end of the mission. By this process, requirements were identified early enough to provide funding and implementation in time for use by the flight project in its flight phase.

As of July 1972, NASA undertook a change in the interface between the Network and the flight projects. Prior to that time, since 1 January 1964, in addition to consisting of the Deep Space Stations and the Ground Communications Facility, the Network had also included the mission control and computing facilities and provided the equipment in the mission support areas for the conduct of mission operations. The latter facilities were housed in a building at JPL known as the Space Flight Operations Facility (SFOF). The interface change was to accommodate a hardware interface between the support of the network operations control functions and those of the mission control and computing functions. This resulted in the flight projects assuming the cognizance of the large general-purpose digital computers which were used for both network processing and mission data processing. They also assumed cognizance of all of the equipment in the flight operations facility for display and communications necessary for the conduct of mission operations. The Network then undertook the development of hardware and computer software necessary to do its network operations control and monitor functions in separate computers. This activity has been known as the Network Control System Implementation Project. A characteristic of the new interface is that the Network provides direct data flow to and from the stations; namely, metric data, science and engineering telemetry, and such network monitor data as are useful to the flight project. This is done via appropriate ground communication equipment to mission operations centers, wherever they may be.

The principal deliverables to the users of the Network are carried out by data system configurations as follows:

- The DSN Tracking System generates radio metric data; i.e., angles, one- and two-way doppler and range, and transmits raw data to Mission Control.

- The DSN Telemetry System receives, decodes, records, and retransmits engineering and scientific data generated in the spacecraft to Mission Control.
- The DSN Command System accepts coded signals from Mission Control via the Ground Communications Facility and transmits them to the spacecraft in order to initiate spacecraft functions in flight.

The data system configurations supporting testing, training, and network operations control functions are as follows:

- The DSN Monitor and Control System instruments, transmits, records, and displays those parameters of the DSN necessary to verify configuration and validate the Network. It provides operational direction and configuration control of the Network, and provides primary interface with flight project Mission Control personnel.
- The DSN Test and Training System generates and controls simulated data to support development, test, training and fault isolation within the DSN. It participates in mission simulation with flight projects.

The capabilities needed to carry out the above functions have evolved in three technical areas:

- (1) The Deep Space Stations, which are distributed around Earth and which, prior to 1964, formed part of the Deep Space Instrumentation Facility. The technology involved in equipping these stations is strongly related to the state of the art of telecommunications and flight-ground design considerations, and is almost completely multimission in character.
- (2) The Ground Communications Facility provides the capability required for the transmission, reception, and monitoring of Earth-based, point-to-point communications between the stations and the Network Operations Control Center at JPL, Pasadena, and to the mission operations centers, wherever they may be. Four communications disciplines are provided: teletype, voice, high-speed, and wideband. The Ground Communications Facility uses the capabilities provided by common carriers throughout the world, engineered into an integrated system by Goddard Space Flight Center, and controlled from the communications Center located in the Space Flight Operations Facility (Building 230) at JPL.

(3) The Network Operations Control Center is the functional entity for centralized operational control of the Network and interfaces with the users. It has two separable functional elements; namely, Network Operations Control and Network Data Processing. The functions of the Network Operations Control are:

- Control and coordination of Network support to meet commitments to Network users.
- Utilization of the Network data processing computing capability to generate all standards and limits required for Network operations.
- Utilization of Network data processing computing capability to analyze and validate the performance of all Network systems.

The personnel who carry out the above functions are located in the Space Flight Operations Facility, where mission operations functions are carried out by certain flight projects. Network personnel are directed

by an Operations Control Chief. The functions of the Network Data Processing are:

- Processing of data used by Network Operations Control for control and analysis of the Network.
- Display in the Network Operations Control Area of data processed in the Network Data Processing Area.
- Interface with communications circuits for input to and output from the Network Data Processing Area.
- Data logging and production of the intermediate data records.

The personnel who carry out these functions are located approximately 200 meters from the Space Flight Operations Facility. The equipment consists of minicomputers for real-time data system monitoring, two XDS Sigma 5s, display, magnetic tape recorders, and appropriate interface equipment with the ground data communications.

N 77 - 19 093

Mark III-77 DSN Command System

W. G. Stinnett
TDA Engineering

A description of the Mark III-77 DSN Command System configuration is discussed. A comparison is made with the Mark III-75 System Configuration to explain the implementation required to establish the Mark III-77 System Configuration.

I. Introduction

The DSN Command System, one of the six Network systems, will be undergoing implementation during the next 15 months that will lead to the Mark III-77 configuration. Of significance is the implementation that will occur at the Deep Space Stations (DSS) and in the Ground Communications Facility (GCF). On December 16, 1976, installation of the Mark III-77 configuration was completed on the first¹ DSS (DSS 12 at Goldstone). The station was brought back on line at that time for flight support. The first two months of operational use is planned for mission demonstration passes and station personnel training. (At the time of submittal of this article, the second station (DSS 62 in Spain) is off line and installation of the Mark III-77 configuration is in process.) Stations will be taken off line (nonoperational), implemented per the Mark III-77 configuration, and returned to flight support status. The last station to be implemented will be DSS 11 at Goldstone in March 1978. Implementation in the GCF is

occurring at two locations. At the stations the implementation is consistent with the station-by-station reconfiguration schedule. At JPL, implementation is planned for October 1977.

Figure 1 provides a block diagram of the Mark III-75 DSN Command System. Figure 2 provides a block diagram of the Mark III-77 DSN Command System. Comparison of the two figures shows that major configuration changes will occur in two subsystems of the DSN Command System: the DSS Command Subsystem and the GCF High-Speed Data Subsystem.

The Mark III-77 DSN Command System will support the ongoing Pioneers 6 through 11, Helios 1 and 2, and the Viking missions. The configuration will also support the yet to be launched Mariner-Jupiter-Saturn 1977 and Pioneer Venus 1978 missions. The configuration is multimission and will consist of no mission dependent hardware or software elements.

¹CTA 21 (Compatibility Test Area) at JPL and STDN (MIL 71) at Cape Canaveral were implemented prior to DSS 12.

II. Deep Space Station Implementation

Figure 3 contains a block diagram of the Mark III-77 Deep Space Station configuration and denotes items requiring implementation or modification from the Mark III-75 configuration. The major modifications are shown in the exploded view. Implementation plans include the following:

- (1) Replacement of the existing Telemetry and Command Processors (TCPs) with dedicated Command Processor Assemblies (CPAs) at all stations.
- (2) A change in interface between the DSS Command Subsystem and the GCF High-Speed Data Subsystem (i.e., the Star Switch Controller).
- (3) Implementation of a computer at the terminal end of the GCF High-Speed Data Subsystem (i.e., the Communications Monitor and Formatter Assembly (CMF)).
- (4) A change in interface between the DSS Command Subsystem and the DSS Monitor & Control Subsystem. This includes an interface via the Star Switch Controller between the CPA and the Monitor and Control Computer (the Digital Instrumentation Subsystem (DIS)). This interface change also includes implementation of a Data System Terminal (DST) that places the DSS Command Subsystem under the DSS centralized operations concept.
- (5) A change in interface between the Frequency & Timing Subsystem (FTS) and DSS Command Subsystem. Includes the implementation of a Time Format Assembly (TFA).
- (6) Minor modifications to the Command Modulator Assembly (CMA).
- (7) An upgrade of the DSS Transmitter Subsystem at DSS 12 and 62; upgrade from 10 kW to 20 kW.

The CPA is a Modcomp Computer, Model II-25. Its implementation is part of the DSN plans to replace the existing XDS-920 computers in the Network. The first phase of this replacement is being carried out via the DSN Mark III Data Subsystem (MDS) Implementation Project. (Telemetry Processor Assemblies (TPAs), Metric Data Assemblies (MDAs), and Communication Monitor and Formatter Assemblies are being implemented by this project simultaneously with the CPAs.) In the Mark III-75 configuration, the DSS command processing function shared the same computer with telemetry. In the Mark III-77 configuration, the command function

resides in a dedicated command computer. (Note backup available at each DSS.) This newer dedicated computer will provide higher reliability, greater processing speed, and more core available for the command function. The higher reliability will derive from isolation from the telemetry function. The increased processing speed will allow the DSN to support higher spacecraft command bit rates. In the Mark III-75 configuration, where the command and telemetry functions were shared in the XDS-920 TCP, the DSN had reached the limit of command bit rate support. The 8 b/s used to support the Helios mission very nearly matched the limit of the DSN capability. The 16-b/s command rate required by the Mariner-Jupiter-Saturn 1977 mission required the DSN to replace the TCP. The CPA processing speed will allow the DSN to support expected major increases in command bit rates for future missions.

As part of the implementation at the DSS, Star Switch Controllers (SSC) are to serve as the intercomputer communications hardware devices. Connected to the SSCs will be two CPAs, two TPAs, one MDA, one DIS, and two CMFs. All communication between the computers is via the SSCs.

The Mark III-77 configuration includes the implementation of two Modcomp II-25 computers (CMFs, prime and backup) at each DSS for the terminal end of the GCF. The prime functions of the CMF include interfacing with the communication equipment at the DSS to receive/transmit high-speed data blocks from/to JPL, to communicate with the station computers (CPAs, TPAs, MDA, and DIS) via the Star Switch Controllers, and to provide a centralized station digital original data record (ODR). It should be noted that the centralized ODR concept is different from what exists in the Mark III-75 configuration. In the Mark III-75 configuration the TCP and DIS provided digital tape recordings (ODRs) of all inbound and outbound high-speed data blocks. In the Mark III-77 configuration, this function has been centralized where the CMF logs all station inbound and outbound data.

As in the Mark III-75 configuration, DSS Command Subsystem status data is provided to the DSS Monitor and Control Subsystem in the Mark III-77 configuration. However, in the Mark III-77 configuration, the data are communicated via the Star Switch Controller. The major change that is occurring in the interface between these two subsystems is due to the implementation of the DSS centralized input/output device (the DST). The Data System Terminal Assembly (DST) consists of two cathode ray tubes (CRTs) and a prime and backup keyboard. After each computer has been loaded, all operator input/output functions can be accomplished from the DST. This will permit a more rapid operator response for controlling and monitoring the station computer-based subsystems.

With the implementation of the Modcomp Computers, a new interface with the Frequency & Timing Subsystem is required. The Time Format Assembly (TFA) provides the required interface. The TFA furnishes GMT and timing pulses of 1, 10, 100, and 1000 pulses per second to the CPA.

Minor modifications are to be accomplished in the Command Modulator Assembly (CMA) during the Mark III-77 upgrade. Due to implementation of CPA (CPA does not have an analog to digital converter whereas the TCP does), the method of checking the voltage output level of the CMA to the exciter will be changed. A voltage comparator will be installed in the CMA and a good or bad signal will be provided to the CPA software. In the Mark III-75 configuration, the TCP software does the comparison to nominal limits. Changes will also be made that will invert bit sync of Manchester encoded coherent phase-shift keying (PSK) data to make it compatible with the MJS 77 spacecraft (inverted from Viking). Additionally, an improvement will be made where symbol-by-symbol checking of Manchester encoded data will be accomplished. (In the Mark III-75 configuration, checking is done on a bit-by-bit level.)

As indicated in Fig. 3, implementation is required in the DSS Transmitter Subsystem. DSS 12 and 62 transmitters are to be upgraded from 10 kW to 20 kW. This will provide 20-kW transmitter capabilities at all DSN stations.

III. Ground Communications Facility Implementation

Due to the nature of support provided by the Ground Communications Facility (GCF) High-Speed Data Subsystem, the implementation of the Mark III-77 configuration will coexist with the Mark III-75 configuration for a significant period of time. Figure 4 provides a block diagram of the dual configurations that will exist from late CY 1976 through late CY 1978. The reasons that the dual configurations have to remain in existence for two years are

- (1) Both Mark III-75 configured stations and Mark III-77 configured stations will exist through March 1978.
- (2) The committed interface to the Viking and Helios missions will be maintained through end of missions.

The implementation of the Mark III-77 GCF High-Speed Data Subsystem will occur at the Deep Space Stations and at the Jet Propulsion Laboratory. At the DSS, the CMF computers are being implemented on a schedule consistent with the station-by-station upgrade to the Mark III-77 configuration. In the Central Communications Terminal (CCT) at JPL,

three types of functional computer assemblies are planned to be implemented for the Mark III-77 configuration. The three types of assemblies are: (1) Error Detection Correction (EDC), (2) High-Speed Switch (HSW), and (3) Central Communications Monitor (CCM). All computers will be Modcomp. Implementation in the CCT is planned to be completed in October 1977 for initial Pioneer Venus 1978 testing.

The EDC assembly, as previously stated, will be physically installed and in line with data flow in late 1977. The functions of this assembly will be to establish a protocol with the GCF computer (CMF) at a Deep Space Station such that short line outages and block errors are corrected by retransmission. With this correction scheme, the DSN should approach 100 percent in the delivery of real-time data. The primary driver for this implementation is to cut down on the station time and personnel effort for posttrack replay of missed telemetry data. The DSN can then more easily meet the completeness criteria for project data records with this real-time correction by retransmission scheme.

The HSW provides the data block routing function for the GCF High-Speed Data Subsystem at JPL. Data are received from a DSS and routed to the appropriate destination — Ames Research Center, Network Operations Control Center (NOCC), and/or Mission Control and Computing Center (MCCC). Likewise, data destined for a DSS are received from Ames, NOCC, or MCCC, and routed to the appropriate DSS.

Included in the Mark III-77 configuration is the Central Communications Monitor Assembly (CCM). This assembly will receive status data from GCF equipment at a DSS (the CMF) and at the CCT. These data will be processed and displayed for all data streams such that the GCF status can be monitored from one central location.

IV. Network Operations Control Center Implementation

As can be seen from Fig. 1 and Fig. 2, there are no changes from the Mark III-75 to Mark III-77 configuration in the NOCC affecting the DSN Command System. The physical assemblies do not change. There are some changes in the nature of software sustaining effort — improvements in operator displays, inputs, etc.

V. Future Plans

This article primarily discusses the physical configuration of the Mark III-77 DSN Command System rather than the

functional capabilities. Due to the nature of the DSS implementation occurring over an extended period of time, in which a given project is supported by both Mark III-75 and Mark III-77 configured stations, the software functions performed by the CPA closely match those of a TCP (see Progress Report 42-29 for description). When all TCPs in the DSN have been

replaced by CPAs, plans are to update the software. The prime change will be to greatly increase the command storage capability at a DSS such that outages upstream in the system have little, if any, affect on the function of commanding a spacecraft. The operation and capabilities resulting from that implementation will be discussed in a later article.

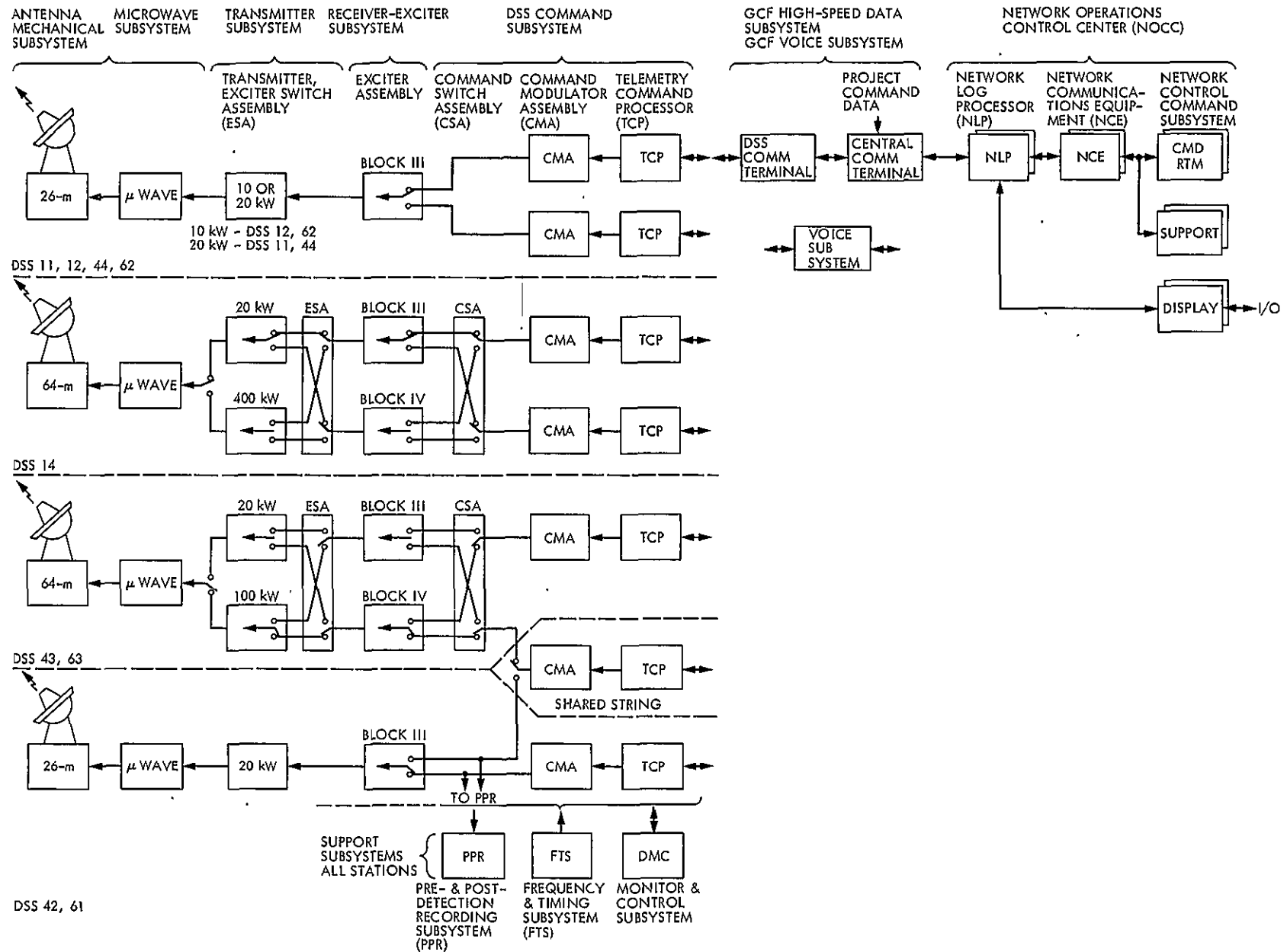


Fig. 1. DSN Mark III-75 Command System

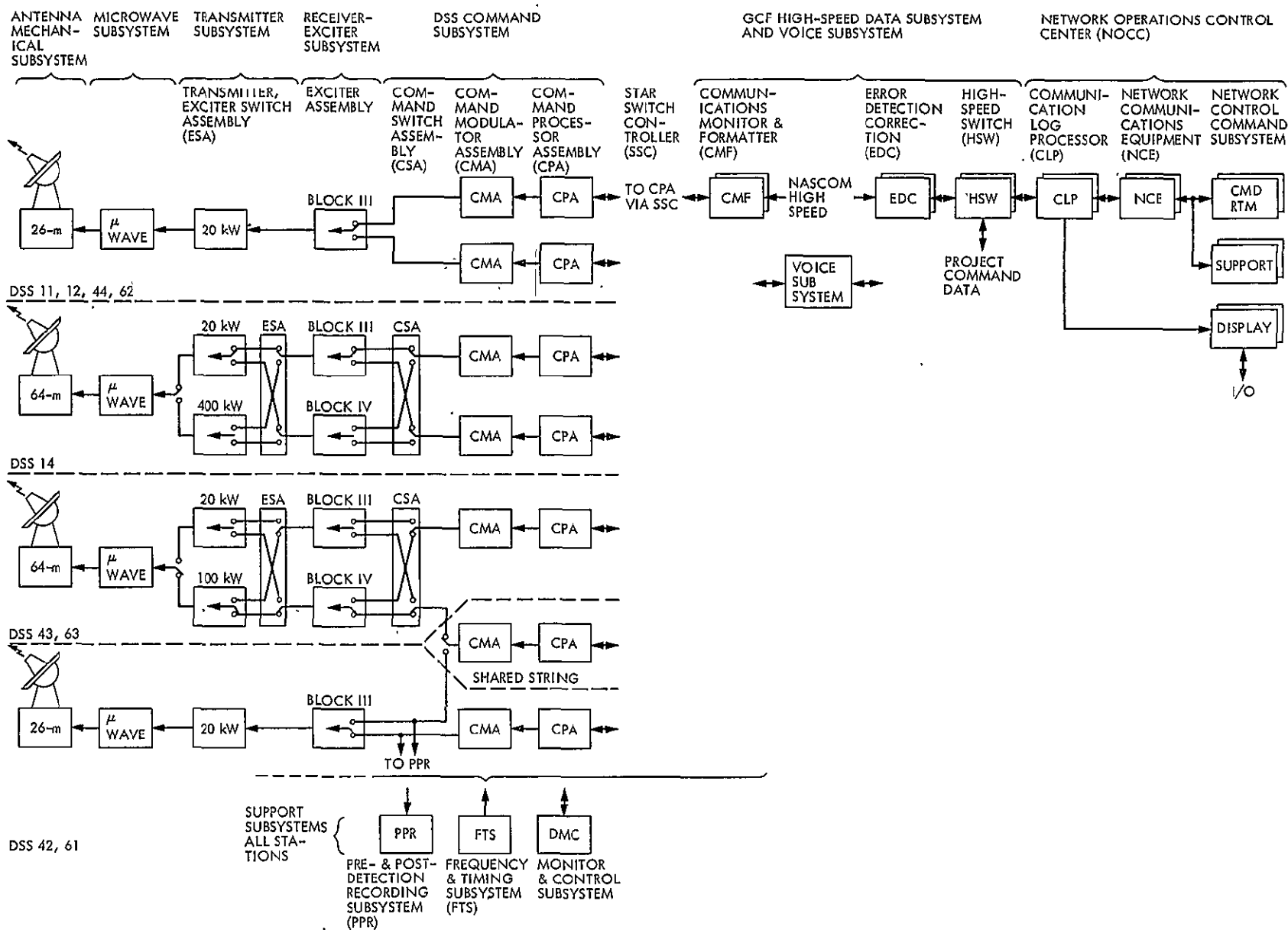


Fig. 2. DSN Mark III-77 Command System

Fig. 3. Deep Space Station implementation of DSN Mark III-77 Command System

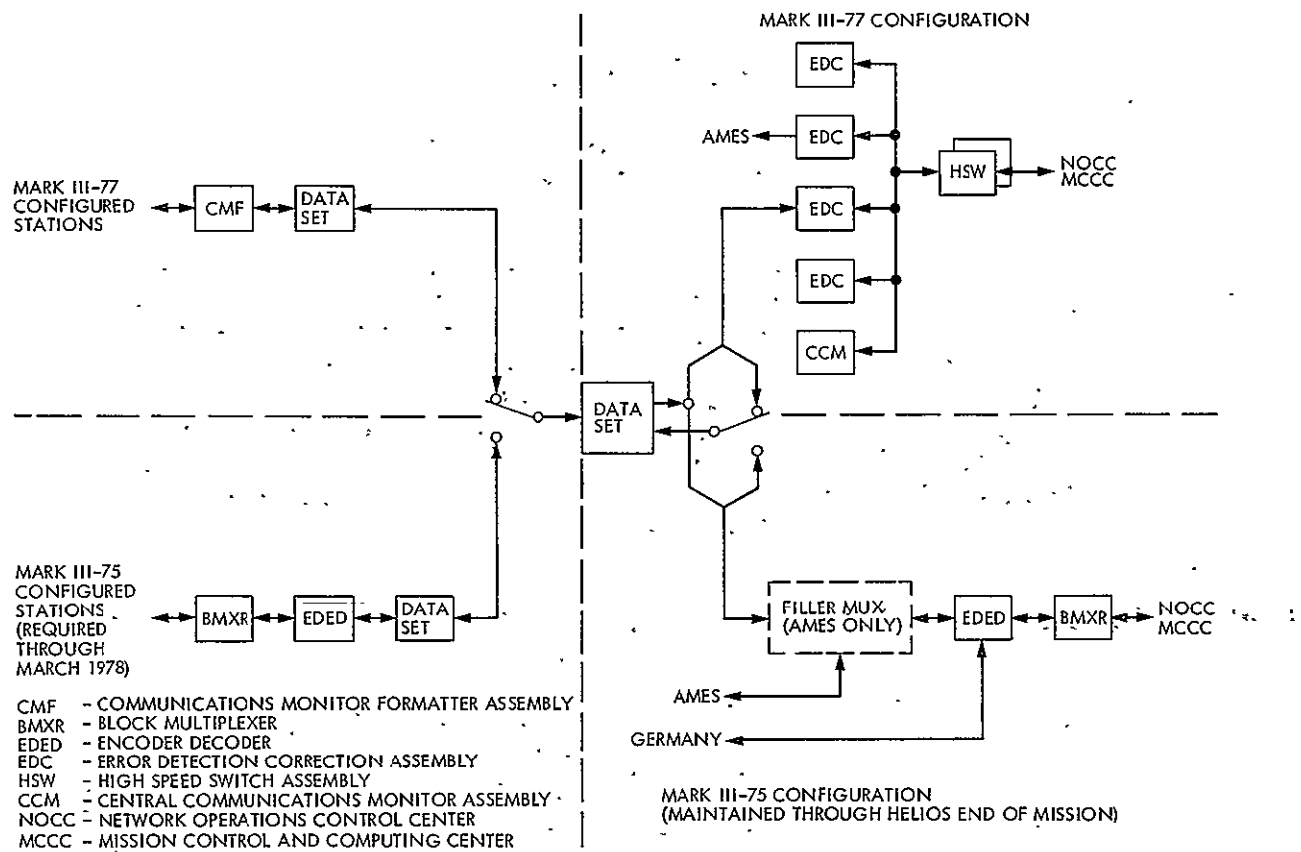


Fig. 4. GCF High-Speed Data Subsystem configuration (1976 through 1978)

N77-19094

Viking Mission Support

D. W. Johnston, T. W. Howe, and G. M. Rockwell
DSN Network Operations Section

This report summarizes Deep Space Network support for the four Viking spacecraft during October and November 1976. The period covers the last portion of the prime mission which officially terminated on 15 November 1976 and the start of the Viking Extended Mission on that date. November also covered the Mars-Sun-Earth superior conjunction period with the rapid degradation of RF link performance resulting in the tapering off and termination of telemetry data coincident with a rapid increase in Radio Science Experiment activity. The various Radio Science Experiments are described in detail and the Computer Aided Countdown Program utilized by the tracking stations during the Viking mission is also described.

I. Viking Operations Activities

Network Operations support of Viking planetary operations continued through the period with the official end of the prime and start of the extended mission occurring on 15 November. The actual support of radio science started on a regular basis with Solar Corona and Earth Occultation Experiments beginning on 3 and 6 October, respectively. High-power transmitter (usually at 100 kW) support for the Relativity Experiment began on 3 November. High-rate telemetry support was terminated on 7 November. These conditions were established primarily because of the link degradation during the superior conjunction period and remained in effect through the end of this reporting period. Due to the nature of the radio science organization and requirements and the degradation of all data types during superior conjunction, an extra effort was required in short range planning and control of the required support. This effort was expended mainly in the production and coordination of special procedures and in the generation of the sequence of events (SOE) to be used by the Network Operations Control Team (NOCT) and supporting Deep Space Stations (DSSs). Added tracking by DSS 43 in

Australia was also required, affecting support of other projects and station activities.

Other support during the period included additional Lander receiver tests utilizing DSS 63 in Spain. The special procedures required were implemented without problems during the tracks from 9 through 12 October. A special alternating ranging test was successfully supported by DSSs 61 and 63 on 17 October with Orbiter 2. The purpose of the test was to develop the procedures to be used for the Mariner Jupiter-Saturn (MJS) Project ranging support requirements.

The 64-m stations, Network Data Processing Area (NDPA), and the Ground Communications Facility (GCF) were released from Viking Modified Configuration Control (soft freeze) on 15 November. All Network facilities remained in standard configuration control throughout the period except for DSS 12 at Goldstone and DSS 63. DSS 12 was released on 3 October for Mark III Data System (MDS) reconfiguration. DSS 63 was released on 15 November for antenna bearing corrective maintenance.

A significant problem occurred during the period when DSS 14 was unable to process high-rate telemetry during the period 22 to 27 October due to Block Decoding Assembly (BDA) failures requiring special coordination of data recovery procedures. The data recovery involved shipping the analog recordings to Compatibility Test Area 21 (CTA 21) for digitization and subsequent Intermediate Data Record (IDR) production. Time was not available for this effort at DSS 14 due to tracking and station internal requirements. On 16 November a second problem occurred when DSS 14 tracking support was cancelled in order to extend the hydrostatic bearing maintenance work in progress. Viking support requirements were successfully negotiated in real time, using DSS 11.

II. Occultation and Solar Corona Support

On 1 October, Lander 1 was continuing to send data via daily direct S-band link. Lander 2 was continuing to send science data via both the relay link and direct link. Orbiter 1 was synchronized over Lander 2 and acting as a relay station. Orbiter 2 had just begun an orbital walk to begin observations of the Martian northern polar cap. Highlights of DSN support and Viking activities during this reporting period are as follows:

- 2 Oct The first "grazing" Earth occultation for VO-1 occurred with no degradation observed on the downlink.
- 3 Oct DSSs 14 and 43 began taking data for the Solar Corona Experiment.
- 4 Oct "Grazing" Earth occultations continued for VO-1 with no degradation observed on the downlink.
- 5 Oct The first "hard" Earth occultation occurred during DSS 43's pass on this date. No effects of superior conjunction on AGC or SNR had been observed.
- 7 Oct The third Earth occultation occurred. It was noted that the VO-1 X-band downlink AGC increased by 3 dB when the uplink transmitter was turned off.
- 11 Oct Following Earth occultation exit, VO-1 was found to be transmitting in the cruise mode at a data rate of 33.333 b/s. The Attitude Control Electronics had switched to the backup system. The CCS had erroneously responded to a loss of Sun signal during solar occultation and issued a "Sun Loss Routine."

VO-2's Infrared Thermal Mapper (IRTM) was commanded on. It had been turned off earlier due to the mirror stepping problem.

- 15 Oct VO-1 Earth occultations now occurring during the DSS 63 view period.
- 17 Oct An alternating range experiment during the DSS 61/63 view period for the MJS 77 Project.

A special Radio Science Coordination Voice Net for DSSs 14 and 43 was introduced for the purpose of technical information exchange between the radio science advisors and the stations. Superior conjunction effects have not yet been observed on the downlinks. Some noise has been observed on the uplink.

- 21 Oct A high-gain antenna calibration for VO-2 took place during the DSS 14 pass. The DSS 14 Digital Instrumentation Subsystem (DIS) program halted during this test, causing 2 data points to be lost. AGC levels were reported by voice during the DIS outage.
- 26 Oct Effects of solar conjunction are now being seen in uplink and downlink. Variations are seen in uplink AGC and downlink SNRs.
- 29 Oct Severe RFI at DSS 14 caused loss of 8-kb/s data for half an hour. A message was sent to all Network stations requesting system noise temperatures be included in the post-track reports for the purpose of determining solar conjunction effects on station parameters. The data are to be taken between 4 November and 17 December 1976.
- 4 Nov Message sent to all Network stations advising them of a requirement to use high-power transmitters during the time frame of 3 November to 15 December 1976. Power levels to be used are as follows:
 - 100 kW at DSS 14
 - 50 kW at DSSs 43 and 63
 - 20 kW at DSSs 11, 42, and 61
 Use of higher power levels decreases noise on two-way doppler and ranging.
- 6 Nov Solar conjunction effects continue to be seen. Effects are as follows: Up to 10-dB fluctuation on uplink AGC; up to 20-dB degradation on engineering SNRs. The 26- and 64-meter stations indicate the same SNR. Downlink degraded by 2 dB.

10 Nov 2-kb/s data being received on this date showed SNR of 6 dB but had extremely high bit error rate. The Sun-Earth-probe angle on this date was 4.5 degrees. This was the last attempt for VO high-rate data.

15 Nov This was the last day of the Viking prime mission. Engineering data were still being received at an SNR of 3 dB at 26-m DSSs and 5 dB at 64-m DSSs. Bit error rate for 26-m DSSs was estimated to be 23 in 4687 bits or 0.005.

Table 1 lists the Viking DSS support during the reporting period.

III. Viking Radio Science

A very important part of the Viking prime mission has been the radio science experimentation. This activity was increased considerably during the latter part of the Viking prime mission as mentioned earlier. The specific experiments that were performed, and in many cases will continue into the Viking Extended Mission (VEM), are:

- (1) Orbiter-quasar VLBI
- (2) Earth occultation
- (3) Solar corona
- (4) General relativity
- (5) Orbiter S- and X-band doppler and ranging
- (6) Lander ranging

Each of these experiments is designed to provide scientists with specific data to help answer pending questions concerning the solar system and our environment. Following is a brief description of what each experiment is and to what extent it has been carried out to date, including what results have been obtained.

A. Orbiter-Quasar VLBI

During a Very Long Baseline Interferometry (VLBI) Experiment, radio signals from a spacecraft and quasar will be alternately recorded, simultaneously, at two Deep Space Stations (DSSs). The VLBI will yield precise measurements of angular separation of the two sources. The results will show precise location of the spacecraft and in turn that of Mars and Earth as well. By performing such experiments over a period of years, exact orbits can be determined and also a test of the general theory of relativity.

There have been a total of six Orbiter-Quasar VLBI passes of data acquired between DSSs 14 and 42 since Viking arrived at Mars. These passes were:

Date	Orbiter	Quasar
14 July	VO-1	OL 064.5
15 July	VO-1	OL 064.5
19 August	VO-1	P1148-00
22-23 September	VO-2	3C 279
23-24 September	VO-2	3C 279

The data from the first two passes have been processed through the Caltech VLBI correlator and appear to be of good quality.

Continued acquisition of the Orbiter-Quasar VLBI data type during the Viking Extended Mission will depend upon the resources available to plan, acquire, process, and analyze this data type.

At DSSs 14 and 42 special equipment is required to perform these VLBI functions. This equipment is listed below, and its configuration is depicted in Fig. 1.

- (1) VLBI S-band receiver
- (2) Hydrogen maser
- (3) Viking frequency converters
- (4) Mark II recorder system
- (5) VLBI frequency synthesizer

B. Earth Occultations

Toward the end of the prime mission, the orbit of Orbiter 1 passed behind Mars as viewed from Earth. Thus, in early October, the Orbiter's signal was gradually cut off, or occulted by the atmosphere and later by the surface of Mars. The variations in the signal on entry and exit from occultation are used to determine Martian atmospheric and ionospheric properties. In addition, occultation measurements produce precise radii of Mars at the occultation points.

The Viking Orbiter 1 Earth occultations started on 6-October over DSS 43 (Canberra), "walked" into DSS 63 (Madrid), and ended over DSS 14 (Goldstone). This complicated sequence was the result of the Lander 2 landing site selection. Orbiter 1 was synchronized over Lander 2 during the occultation period, and since the Lander 2 site was changed, the first Earth occultations moved from the Goldstone to Canberra view period. This upset years of plans and tests of

the occultation ground data system and could have resulted in the majority of the occultations occurring over Madrid, where there are no occultation open-loop receivers or recorders. However, the Radio Science Team and Viking Project finally elected to eliminate the "radio science walk," and, consequently, the occultations occurred over all three 64-m DSN stations.

There were 27 pairs of occultations. Ten exit occultations occurred over DSS 63 for which there were no coverages scheduled due to conflicting requirements, or there were only closed-loop one-way data acquired as soon as the station S- and X-band receivers were able to lock up. These 10 exits are really of no value to the experiment. In addition there were three enter occultations over DSS 63 for which there were conflicting requirements, and no closed- or open-loop occultation data were acquired. Finally, DSS 14 lost its first exit occultation due to conflicting Project requirements. Consequently, only about 75 percent of the occultations provided data. This record is very good, considering all the conflicts. The DSN and Viking Flight Team (VFT) did an excellent job in acquiring the data due to the amount of preparation that went into the planning, procedures, and occultation demonstration tests.

The first closed-loop data from DSS 43 enter occultations showed no indication of any ionosphere with the entry and exits occurring on the dark side of the planet. The atmospheric pressure and temperature profiles and the planetary radii suffer from the data noise due to the solar corona effects. The Sun-Earth-probe angle at the start of occultations was about 15 degrees.

The configuration used for occultation observations at DSSs 14 and 43 consists of the standard closed-loop system and also the open-loop system, which is the most important. The open-loop system consists of two open-loop receivers and two dedicated open-loop FR-1400 analog recorders. The open-loop system is shown in Fig. 2, and the FR-1400's track assignments are listed in Table 2.

The pattern of occultations for the first phase is shown in Fig. 3. This phase ran from 1 October to 1 November. The next phase begins on 16 January 1977 over DSSs 63 and 14. The first phase involved Orbiter 1 only. The next segment will utilize only Orbiter 2 in a similar manner. A more detailed look at Orbiter 2's occultations will be discussed in future articles.

The analog data recorded during these occultation passes were forwarded to the Compatibility Test Area (CTA 21) via the DSN's Network Information Center (NIC). The configuration (refer to Fig. 4) of CTA 21 at the Jet Propulsion

Laboratory includes special equipment to support the analog-to-digital conversion of Viking occultation data recorded at the 64-meter stations. Analog occultation tapes received at CTA 21 contain recordings of both S- and X-band data from receivers operated in both the open-loop and closed-loop modes. The closed-loop receiver data can consist of up to 16 parameters which are digitized in pairs. A single occultation could result in analog tapes containing 22 minutes of entry and exit data from the open-loop receivers and 22 minutes of closed-loop receiver data. Digitization of all analog data by CTA 21 would require approximately 12 to 15 hours. However, typical requirements during the prime mission have been on the order of 4 hours digitization time for each occultation. In addition to the occultation data conversion support, CTA 21 provides a backup capability for analog-to-digital conversion of Viking telemetry data. During the prime mission a combined total of 38 occultation and telemetry analog tapes, resulting in 63 digital tapes, were processed by CTA 21.

C. Solar Corona

As Mars and Earth approached superior conjunction on 24 November, radio signals from the Viking spacecraft passed close to the Sun and were gradually affected by the influence of the solar corona. Signal variations, using dual-frequency downlinks, will provide new information on regions close to the Sun.

Eight days of intensive solar corona data were acquired from 3 through 10 October to check out the solar corona data acquisition process and also to get useful solar corona data at a Sun-Earth-probe angle of about 15 degrees. These data were acquired from DSSs 14 and 43 using Orbiter 1, Orbiter 2, and Lander 2. Data were acquired in two modes: a multiple spacecraft-single station mode, and a single spacecraft-dual station mode. Both closed-loop data (4 streams of 10 per second data for 2 hours) and open-loop data were acquired. The open-loop receivers at DSS 14 were operated in two modes: a mode to collect dual S-band data from two orbiters using Synthesizer Local Oscillator (SYNLO) predictions, and a mode to collect S- and X-band data from one orbiter using Programmed Local Oscillator (PLO) predictions. This week of successful operations provided the experience and data needed to design the solar corona passes during the solar conjunction period.

The configurations at DSSs 14 and 43 differ somewhat, in that DSS 14 uses a PLO at certain times, as described above. These differences in configurations are shown for comparison in Figs. 5 and 6. Table 3 also lists the different modes DSS 14 can operate in due to this addition. The track assignments are the same as for occultation (see Table 2) except that only tracks 1, 2, 4, and 6 are used.

Fortunately for the Solar Corona Experiment, there will be extensive periods of one-way tracking of the "second" orbiter during the General Relativity Experiment. Since one-way S- and X-band data are not corrupted by the uplink solar corona scintillations, the Solar Corona Experiment can get all the data they can use without the usual conflict between the Relativity and Solar Corona Experimenters. Solar corona observations started again on 2 November and have been scheduled through 11 January 1977. Both digital and analog tapes from DSS 14 and analog tapes of the open-loop receiver will be available. Closed-loop S- and X-band doppler data from the two-way orbiter used for the General Relativity Experiment will also be useful for the Solar Corona Experiment even though it suffers from uplink solar corona scintillations.

D. General Relativity

Because signals are affected by the Sun's gravitational field, a precise solar gravitational time-delay test of the general relativity theory will be performed. These tests can have a major impact on fundamental physical laws and on studies of the evolution of the universe.

In September the Viking Project reviewed and approved the proposed Radio Science Team General Relativity Time Delay Experiment. This experiment proposal is based upon the use of lander ranging with simultaneous orbiter ranging for solar corona charged-particle calibrations. The period of time covered by the simultaneous lander and orbiter ranging extends from 3 November through 9 December. In addition, near-simultaneous lander and orbiter ranging before and after this time period is used as an essential part of the General Relativity Experiment data base, to solve for planetary ephemerides errors and as part of the radio science lander location and Martian pole location and dynamics experiment.

Experience during the Viking prime mission has shown that the ranging system (the planning, sequencing, data acquisition, and processing) does not operate in a hands-off mode. Due to various reasons, including Lander 1 direct link receiver failure, Orbiter 2-Lander 2 separation anomaly, Lander 2 Traveling Wave Tube Amplifier (TWTA) 1 failure, and several operational procedural errors, only about 25 percent of the near-simultaneous lander and orbiter ranging passes that were scheduled actually acquired good near-simultaneous orbiter and lander ranging. As a consequence of this poor record, and the Helios experience during the solar conjunction period, a real-time radio science ranging team was organized and started into operation near the end of October. One of the first problems observed by the real-time ranging team was a degradation in the ranging signal-to-noise ratio from Lander 2. This foretold the ultimate failure of TWTA 1, which resulted in a reduction in the amount of ranging coverage available from Lander 2 (both in length of ranging period and number

of periods) which resulted in a revision of the whole General Relativity Experiment plan.

As of 10 November 1976, there have been four attempts to acquire simultaneous lander and orbiter ranging from DSSs 14 and 43. The first pass with Lander 1 on 3 November experienced a Mu 2 ranging machine failure that was corrected in time for the next day's pass, which was successful. The two passes with Lander 2 on 8 and 9 November were successful. The real-time ranging team has been able to monitor and correct many operational errors which, if they were not caught, would have resulted in lost ranging data. If this success rate continues, the General Relativity Experiment should be able to achieve its objectives. However, the solar corona effects will become much more severe as we approach solar conjunction on 25 November.

E. Orbiter S- and X-Band Doppler and Ranging

Since November 1975, when the X-band transponders on the orbiters were turned on, several hundred S- and X-band doppler and ranging passes of excellent data have been acquired during cruise and planetary operations. During planetary operations, tracking data taken near periapsis have enhanced the accuracy of determining the Martian gravity field and local gravity anomalies. This will be accomplished through elimination of error sources by use of dual-frequency S- and X-band tracking. The gravity field definition provides information on the mass, internal structure density and mass distribution, geological processes, and the evolution of Mars. These data have been extremely useful in evaluating the new X-band system performance, monitoring solar flares and solar corona noise, and for the charged-particle calibration of doppler and ranging data. Four data types, i.e., S- and X-band doppler and ranging, have been compared and yielded the same charged-particle results. Namely, S- and X-band differential doppler, S-band DRVID, X-band DRVID, and S-X band range yield the same change of total electron content during recent high solar activity passes. This demonstrates the performance of the DSN S- and X-band doppler and ranging system beyond any reasonable doubt.

F. Lander Ranging

By acquiring lander doppler and ranging data along with near-simultaneous ranging from the lander and orbiter, much knowledge will hopefully be gained concerning Martian polar properties and lander position. Specifically, these data will be used for Radio Science Lander location, and Martian pole location, and dynamics experiment. The near-simultaneous ranging (see Fig. 7) from the lander and orbiter from the same DSS have been requested to eliminate the effects for differential charged-particle differential station location errors for stations located on different continents.

The power of the lander doppler and ranging data has been demonstrated by the navigation and radio science use of the small amounts of data to solve for very accurate lander locations and pole directions. Efforts will continue during the extended mission to improve on the quality and quantity of lander and near-simultaneous orbiter ranging for the radio science lander position and Martian pole location and dynamics experiment. Hopefully, this experiment will yield knowledge about changes in the Martian spin rate and Martian pole precession and mutation. These would be important results for understanding Martian dynamics and internal structure.

In addition, lander and near-simultaneous orbiter ranging can be used for another test of general relativity: a dynamic test as contrasted to the time delay test discussed earlier. This dynamic test of general relativity will require lander and orbiter ranging over the lifetime of the landers and orbiters.

Therefore, the lander ranging and near-simultaneous orbiter ranging are the most unique and probably the most important radio science data to be collected on the Viking project.

IV. Viking Computer-Aided Countdown Program

The Computer-Aided Countdown (CAC) Program DXI-5140-TP was developed by personnel of the Madrid Deep Space Station (DSS 62) within its "DSN Engineering Program," with the assistance of the DSN System Support Group. Work on the program began in March 1975; however, due to heavy workload associated with preparations for Viking launch and tracking support, it was not completed until March 1976. During the month of March the program was evaluated and software acceptance testing was performed.

The program combines tasks previously performed by other test software programs, shortening the time required to

support station precalibrations, and thus making more effective use of station time.

The program provides for a centralized verification of station performance in four important areas:

- (1) Telemetry System performance
- (2) Command System performance
- (3) Doppler performance
- (4) Planetary Ranging Assembly countdown performance

The program was written for a typical 64-meter DSS with the ability of testing six telemetry channels, two command processors, and Block III S-band, and Block IV S- and X-band doppler. For 26-meter DSSs the program is capable of testing four telemetry channels, two command processors, and Block III S-band doppler.

The software was designed with the flexibility of accommodating all possible Viking telemetry rates, Orbiter and/or Lander commanding, and any combination of Block III, Block IV, S-band, X-band doppler processing.

The CAC Program was first used by the DSN in April 1976. The months of April and May were designated as a trial and training period. During this period the three levels of computer-aided countdowns were exercised, while DSS personnel became familiar with the program and developed procedures for its optimum use. Table 4 defines the CAC level by station and identifies the options of each. Beginning on 1 June 1976 the level 1 computer-aided countdowns were committed at all Network stations supporting Viking.

The level 1 CACs were continued throughout the Viking prime mission and into the Viking Extended Mission. The level 2 CAC will become the prime countdown level with the option of using level 1 for passes in which a critical event is scheduled. Table 5 identifies the results of the level 1 CACs during two months of continuous use.

Acknowledgment

The authors would like to thank J. P. Brenkle of the Viking Radio Science Team for his contributions to this article.

Table 1. Viking support

Period	DSS	Tracks	Track time	Commands
September	11	29	216:14	1430
	12	6	45:21	6
	14	72	487:59	1205
	42	35	315:42	1532
	43	68	578:06	2685
	44	11	91:29	4
	61	29	261:13	1078
	62	7	59:37	332
	63	83	557:52	438
		340	2613:33	8660
October	11	32	212:43	1515
	12	0	0:0	0
	14	77	413:57	1292
	42	32	351:08	2776
	43	85	787:16	2967
	44	1	4:51	0
	61	31	251:52	2676
	62	5	35:36	319
	63	79	590:02	1524
		342	2647:25	13069
November 1-15	11	18	103:36	339
	12	0	0	0
	14	30	167:18	403
	42	11	113:43	444
	43	36	327:16	1963
	44	0	0	0
	61	17	133:49	0
	62	2	15:40	0
	63	24	181:01	143
		138	1042:23	3292

Table 2. FR-1400 recorder configuration for DSSs 14 and 43 (dedicated recorders for occultation data)

Track	Data					Mix ratio ^a
	IRIG channel	Function	VCO center freq, kHz	Deviation percentage	Deviation voltage, volts	
1		Speedlock Voice	Direct 13.50	±40.0	±5	1:1
2		S-band OLR Digitizing tone	108/432 ^b	±40.0	±1	1:1
3	9	RCVR 3 AGC	3.90	± 7.5	±5	1:1
	10	RCVR 3 SPE	5.40	± 7.5	±5	1:1
	11	RCVR 4 AGC	7.35	± 7.5	±5	1:1
	12	RCVR 4 SPE	10.50	± 7.5	±5	1:1
	13	RCVR 3 DAGC	14.50	± 7.5	±1	1:1
	15	RCVR 3 DPE	30.00	± 7.5	±5	1:1
	17	RCVR 4 DAGC	52.50	± 7.5	±1	1:1
	20	RCVR 4 DPE	124.00	± 7.5	±5	1:1
4		NASA time Speedlock	13.50 Direct	±40.0	±5	1:1
5	9	RCVR 1 AGC	3.90	± 7.5	±5	1:1
	10	RCVR 1 SPE	4.50	± 7.5	±5	1:1
	11	RCVR 2 AGC	7.35	± 7.5	±5	1:1
	12	RCVR 2 SPE	10.50	± 7.5	±5	1:1
	13	RCVR 1 DAGC	14.50	± 7.5	±1	1:1
	15	RCVR 1 DPE	30.00	± 7.5	±5	1:1
	17	RCVR 2 DAGC	52.50	± 7.5	±1	1:1
	20	RCVR 2 DPE	124.00	± 7.5	±5	1:1
6		X-band OLR Digitizing tone	108/432 ^b	±40.0	±1	1:1
7		NASA time Speedlock	13.50 Direct	±40.0	±5	1:1

^aThe input to each recorder track will be adjusted to 2.8 volts p-p.

^bUse the 108.0-kHz VCO when recording solar corona data and the 432.0-kHz VCO when recording occultation data.

Table 3. DSS 14 solar corona local oscillator configuration model

Mode	OLR configuration to be selected	Local oscillator source	Setting, MHz	
			5100B synthesizer 1	5100B synthesizer 2
1 ^a	S/S	SYN	≈23	≈23
	S/X	SYN	≈46	NA
2	S/X	SYN	≈46	30.00135
3	S/S	PLO	NA	NA
4	S/S	PLO	NA	30.00135
5	S/X	PLO	NA	NA
6	S/X	PLO	NA	30.00135

^aFail safe mode. To be selected for unmodified OLR operation.

Table 4. CAC options

DSS	CAC level	Time, hours	Options
14 43 63	1	6	2 hours of full DSS testing followed by a built-in 2.5-hour hold (or rectification). Then 1.5 hours of retest and data transfer test.
	2	3	2 hours of full DSS testing followed by a 1-hour retest and data transfer test.
42 61	1	4.5	1.5 hours of full DSS testing followed by a 2-hour built-in hold. Then a 1-hour retest and data transfer test.
	2	2.5	1.5 hours of full DSS testing followed by a 1-hour retest and data transfer test.
11 12 44 62	1	3	1.5 hours of full DSS testing followed by a 0.5-hour built-in hold. Then a 1-hour retest and data transfer test.
	2	2.5	1.5 hours of full DSS testing followed by a 1-hour retest and data transfer test.
	3	1.5	1 hour of full DSS testing followed by 0.5 hour of data transfer test.

Table 5. CAC performance

Performance	Number of passes			
	DSS 14	DSS 43	DSS 63	Total
64-m CAC scheduled for 6-channel support	50	36	57	143
Station green after full DSS testing	38	30	50	118
Equipment anomalies corrected during built-in hold	8	3	6	17
Equipment anomalies corrected during testing and built-in hold	2	3	2	7
DSS unable to support 6 channels at the end of the CAC due to equipment anomalies	2	0	2	4

Conclusions: 1. DSSs were red for 6-channel support prior to the built-in hold 17.5 percent of the passes.
2. DSSs were red for 6-channel support prior to AOS 2.8 percent of the passes.

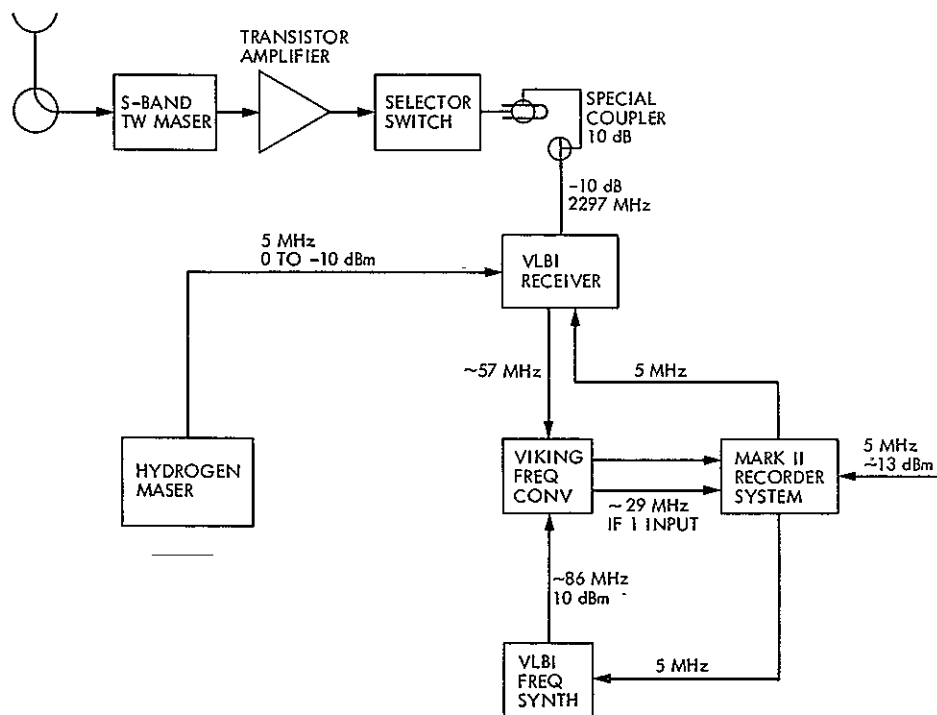


Fig. 1. VLBI configuration for DSSs 14, 42, and 43

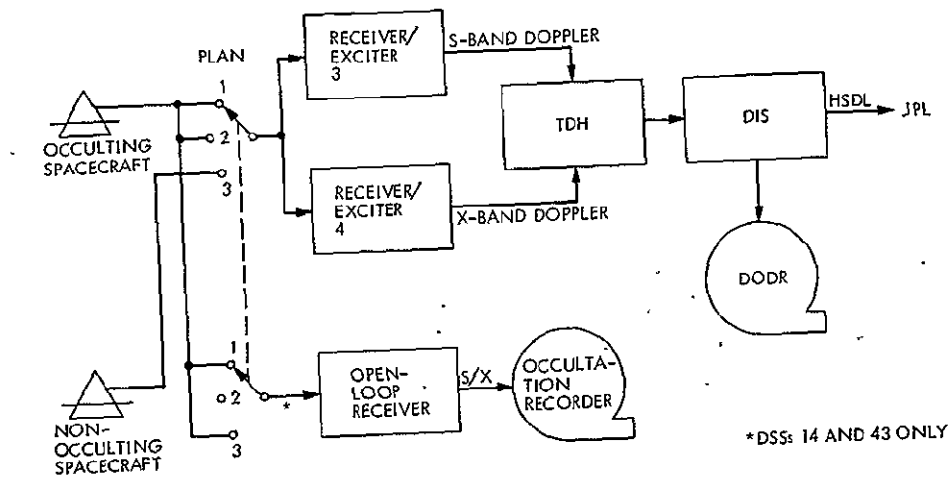


Fig. 2. Occultation configuration

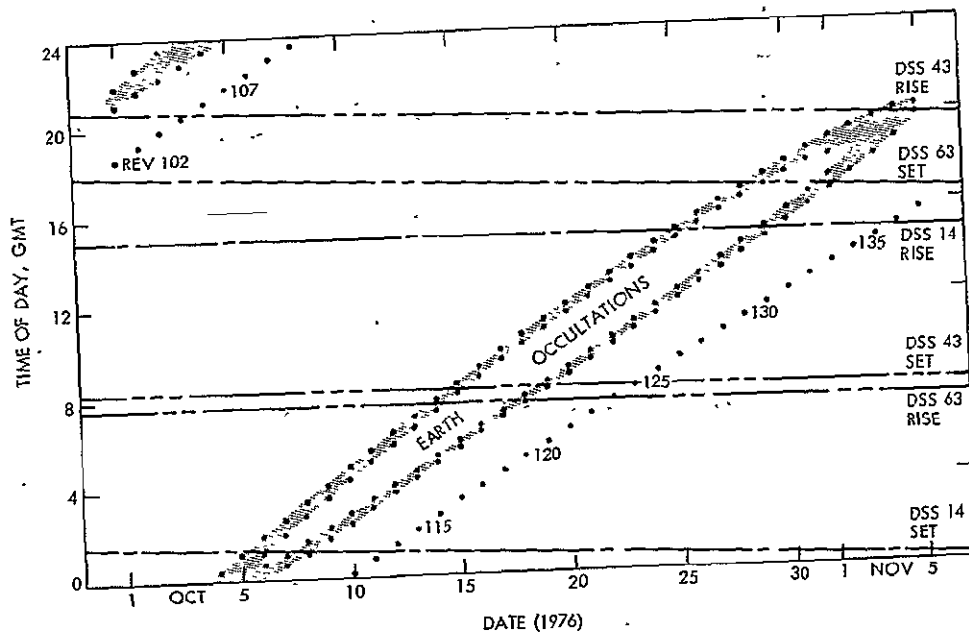


Fig. 3. VO-1 Earth occultations

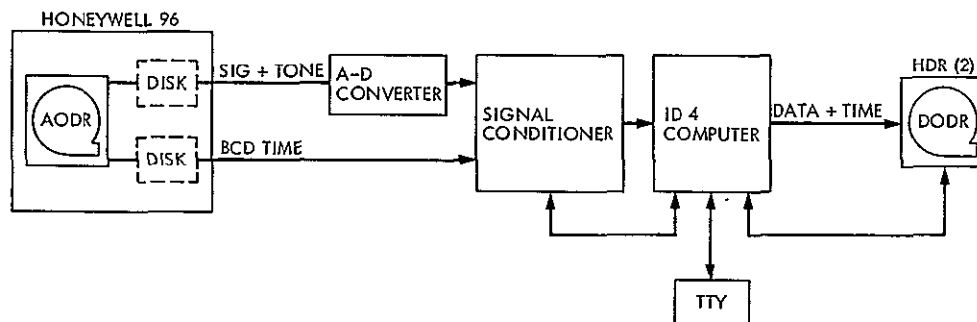


Fig. 4. Simplified block diagram of typical digitizing configuration

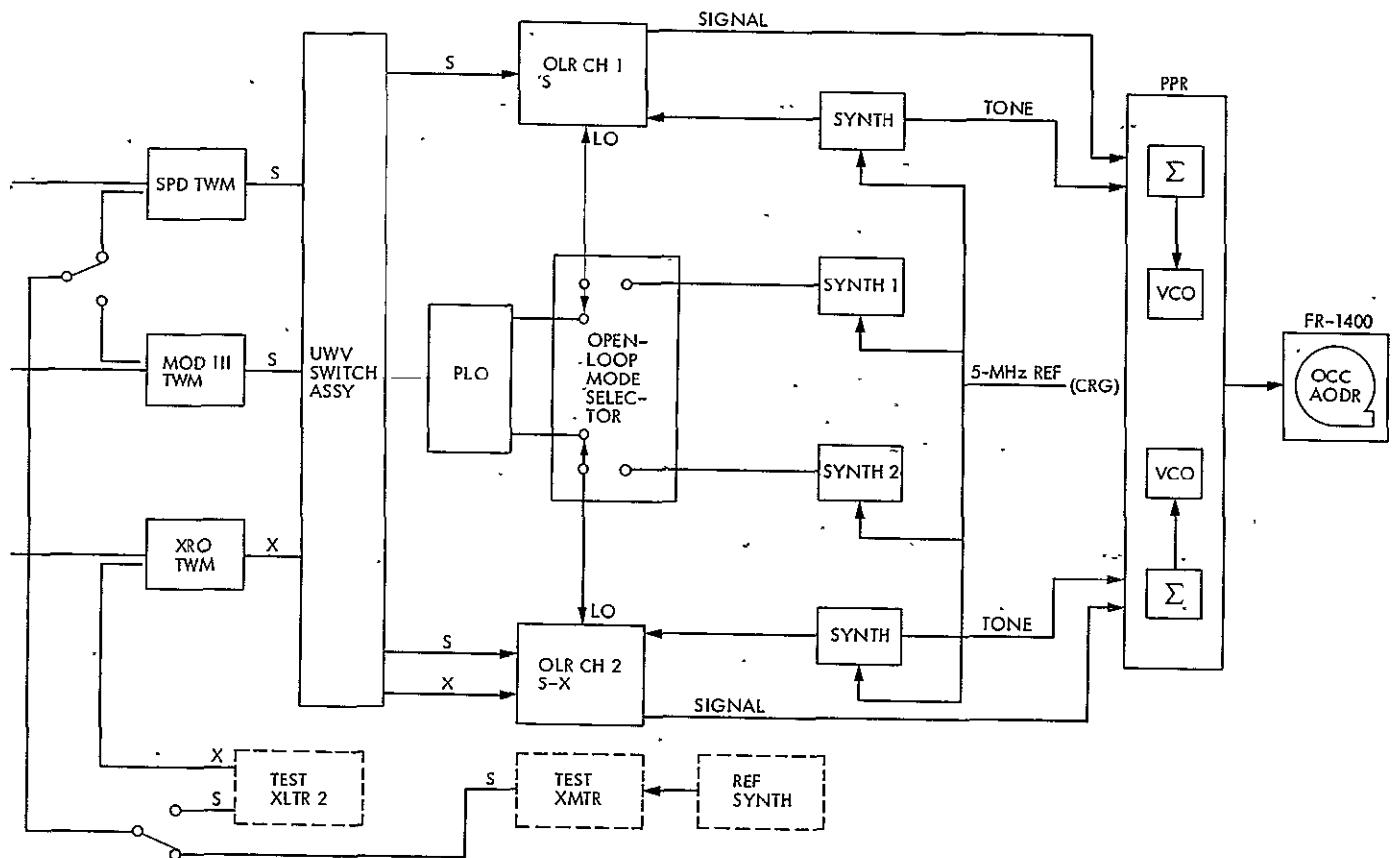


Fig. 5. Simplified open-loop system block diagram for DSS 14

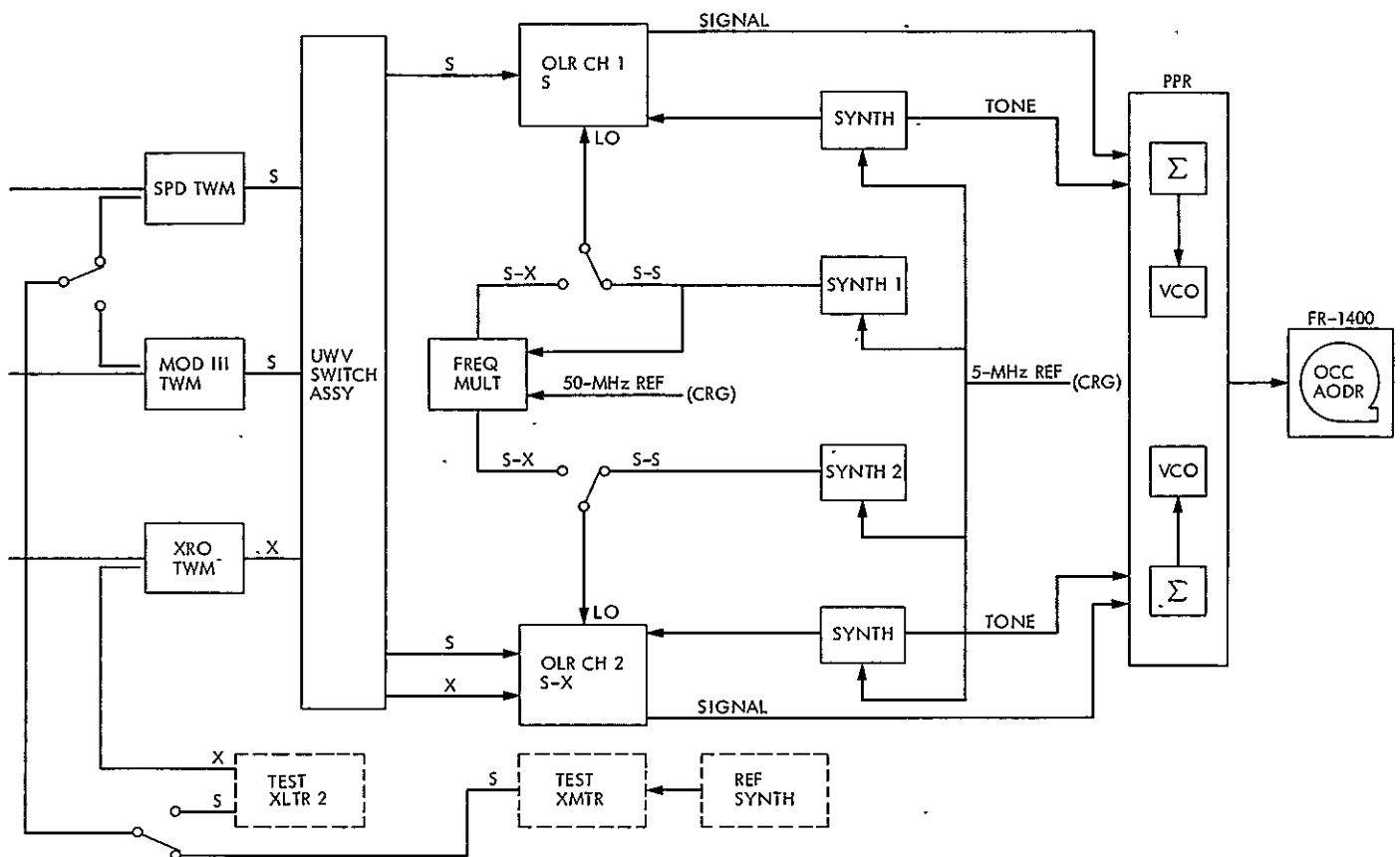


Fig. 6. Simplified open-loop system block diagram for DSS 43

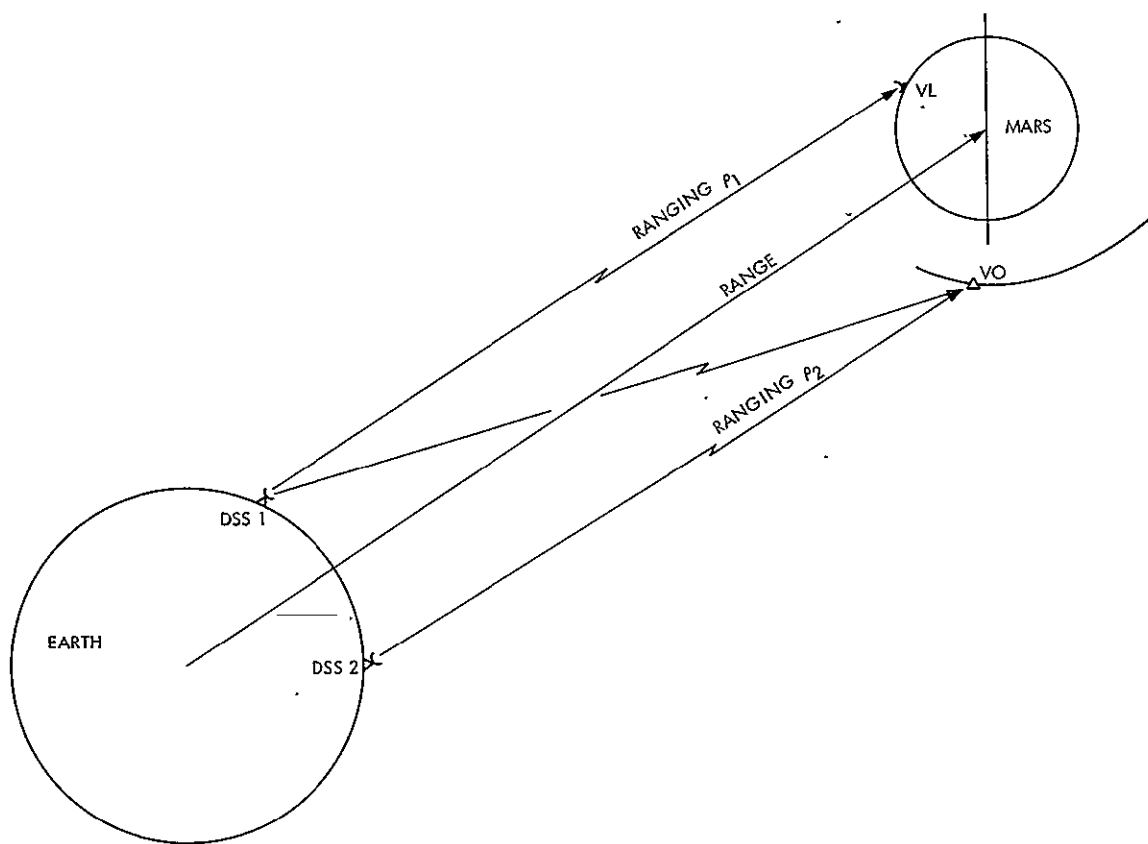


Fig. 7. Near-simultaneous lander/orbiter ranging

dy 17, 17B
N 77-19095

Intermediate Data Record Support for the Viking Prime Mission

J. A. Swindlehurst
DSN Facility Operations Section

In producing Intermediate Data Records (IDRs) to satisfy the demanding requirements of the Viking Prime Mission, the DSN was called upon to make many procedural, hardware, and software workarounds to compensate for the deficiencies that inevitably come to light when a complex new capability such as the Network Data Processing Area is exposed to a high-demand operational environment for the first time. In due course, most of the problems were identified and corrected, or modifications were made to the IDR system design. Despite these difficulties, IDR production for the Viking Prime Mission achieved an astonishing level of performance both in quantity of data delivered and timelines of delivery. This article discusses the more significant problems encountered in IDR production during the mission and gives a definitive statement of the production levels accomplished.

I. Introduction

The DSN has met the telemetry Intermediate Data Records (IDR) commitment to the Viking Project Prime Mission. As with any new system, there were numerous anomalies which had an adverse impact on accomplishment of that task. Experience with the Data Records Processor (DRP), coupled with improvements to the hardware and software and the development of more efficient operational strategies to cope with many of the problems, led to a maximization of data percentages delivered and minimized generation/delivery times.

Generation of IDRs is the prime task of the Network Data Processing Terminal (NDPT) located in Building 230 (Fig. 1). The DRP software is used for the recall and merge functions,

while the Network Log Processor (NLP) records all data on Network Data Log tapes

This report presents an analysis of the NDPT's performance in the accomplishment of that commitment from 19 April through 10 November 1976. Included are all orbital IDRs containing lander direct and relay data, as well as the remake and supplemental IDR requests received from Viking Project Data Records personnel. Each IDR includes tapes and summaries required for each unique station pass.

Following the performance analysis is a discussion of the constraints and problems that were encountered, and the corrective actions taken to cope with those problems. Additionally, the planned enhancements to the system are discussed.

II. Performance

The percentage of telemetry Intermediate Data Record data delivered to the Viking Project averaged 99.988 percent of the committed data from the stations' Digital Original Data Record magnetic tapes. The majority of the missing data were delivered at a later date. Delivery times ranged from less than 1 h to several days from the end of each station pass.¹

Figure 2 depicts the weekly data percentages delivered over the 28 weeks covered by this report. The first 14 weeks show an erratic pattern of accomplishment, while the last 14 weeks' output was basically stable. This improvement was due to the development of new operational techniques to handle magnetic tape "read" problems and two key milestone events. On 6 June, a new Data Records Processor software package, with a new magnetic tape handler, was incorporated into the system. Unfortunately, this new handler had been written for a slightly different hardware package. An investigation by NDPT personnel uncovered the needed changes and, on July 27, a modification to the DRP's tape controller was implemented. From that point on, the data percentage stabilized and the generation times decreased.

Prior to Orbital Operations, the merge/Intermediate Data Records work load was sporadic, as was the output. Starting with 21 June, through 3 November, around-the-clock coverage became mandatory. There were 782 Intermediate Data Records delivered, with an additional 102 Remake/Supplemental IDR Requests completed (Table 1). An average of 99.990 percent of the required data were delivered within 9.07 h of the scheduled station loss-of-signal at the 64-m stations. Of this total, 46 IDRs were delivered more than 24 h after Loss of Signal (LOS). Approximately 36 more were delivered partially completed.

Both the data percentage delivered and the delivery/generation times show a steady improvement over the period depicted in this table. Of special interest is the decrease in delivery time. The apparent increase in time after 20 September is due to a change in the IDR pickup (from the NDPT) procedure. At about that time, there was a decrease in the manning available to the Network Operations Control Area for around-the-clock coverage, and delays of 6 and 7 h between generation and pickup/delivery times became common. Actual generation times stabilized at approximately 4.8 h from station LOS. The delivered data percentages improved after 27 July due to those enhancements mentioned above.

¹Extracted from the Prime Mission IDR Statistics Report generated by the NDPT.

A profile of the quality of the IDRs delivered, excluding remakes, is depicted by Fig. 3. This shows the percentage of IDRs that were delivered with missing data blocks. To illustrate, approximately 83.4 percent were delivered with five or less missing blocks. The actual percentage of the total delivered data is shown in Table 1 and Fig. 1. A different view of IDR quality is provided by Fig. 4. In Fig. 3, only orbital operations original IDRs were included (remakes and supplemental excluded). The percentage figure listed in the abscissa reflects a given delivery percentage, while the ordinate shows the percentage of all IDRs that met that criterion. For example, 84.3 percent of all IDRs contained 99.990 percent (or more) of the required data.

Figure 4 indicates that 60.6 percent of all IDRs were delivered without any missing data. The remaining 39.4 percent of IDRs saw one or more malfunctions occurring during the merge/recall operation, and those IDRs represent 100 percent of the data that were recoverable at the time of delivery. In some cases, the decision was made to release a less than 100 percent IDR to Project, so that the data could be processed.

Early in the orbital period, the decision was made to deliver IDRs with 99.8 percent or more of all required data logged by the stations. Then, Viking Data Records personnel established the guideline of requesting only remakes of IDR gaps of more than six blocks. These two decisions relieved much of the pressure from operating personnel in the Network Data Record Terminal, and the workload backlog became reduced to a more workable level.

III. Constraints

One of the major factors impacting IDR generation was the limited amount of time available for data recall. With only two wideband lines available, and three stations (64-m) engaged in around-the-clock support, there was not much time available for extended recalls.

Under normal conditions, with the Data Records Processor and Automatic Total Recall System (ATRS) interface working, there was sufficient time to meet all requirements and insure a high-percentage IDR. However, 5.88 percent of all IDRs (46) were one or more days late due to recall and/or playback problems resulting from hardware malfunctions at either end, high numbers of recallable gaps, systems interface problems, or tape "read" problems encountered after the station had been released.

The problem worsened when a large number of gaps were waiting recall from both the current pass and any backlog. When this occurred, the operational priorities required recall

of the current pass first, followed by the backlog. The capability of recalling multiple streams of data did exist, but a backlog (and the attendant pressures on NDPT personnel), coupled with the current day's requirements, made it difficult to verify that all recall tapes were complete and readable. One day's backlog could impact several days of normal IDR production until all the backlog was worked off.

IV. System Anomalies

There were several areas in which problems could impact the production of IDRs within the Viking delivery time requirements. These were the Network Data Log function, recall and gap editing function, and merge function.

A. Logging Function

The Network Log Processor provides the interface between the NDPT and the rest of the Network. All incoming and outgoing traffic is routed through it, to include interfaces between Building 230 (NDPT) and Building 202 (NDPT) (Fig. 1). In addition to routing all data, the NLP logs all inbound high-speed and wideband data plus the outbound messages to the Network. As the data are received by the NLP, they are logged on one of four Network Data Log (NDL) tapes: one for all high-speed inbound, one for each of two wideband lines, and one for outbound messages. Unfortunately, the NLP does not have the capability to validate that it writes tapes correctly, and improperly written data blocks/records are not detected until the merge function is carried out.

B. Recall Function

The recall portion of the Data Records Processor interfaces with the ATRS program in the station TCP (Fig. 1). Edited gap lists received from the Sigma 5 in the Network Control System are stored on the DRP disk. Full capacity is twelve streams of up to 199 gaps each. Recall can start only when the DRP has one or more streams available and the station TCP is initialized for ATRS recalls. Typical problems encountered with this arrangement were.

- (1) TCP not responding. The DRP recall initialization blocks were observed to leave Building 230, but the TCP did not acknowledge receipt. A variation of this problem occurred when the TCP acknowledged and then remained inactive. Resolution normally consisted of one or more reloads/recoveries of the ATRS program. This problem occurred frequently throughout the period of this report.
- (2) Initialization acknowledged, tape positioned, no data received. Usually the station Digital Original Data

Record (DODR) tapes appeared to be searching for data, but none were recovered at the Data Records Processor. Either the DODR tape started after the recall request, or the program required another reload/recovery.

- (3) Data blocks rejected. Sometimes the data received were outside the time range of the active recall request. Either the data contained a timing anomaly, or the TCP's high-speed status block was received prior to the last block of recall data transmitted. The latter problem was found to be due to the routing of the data streams. Normally the status block is transmitted on land lines, and the wideband data are relayed through a satellite. When the gaps are sufficiently close, the status block is received prior to the data due to the greater distance (and longer time) the wideband data have to travel. At the station, the sequence is as follows: when the data buffer is empty (recall data sent), a status block is transmitted to the Data Records Processor within a few microseconds after the data blocks.

Example:

17,700-km (11,000-mi) high-speed line for status blocks
72,400-km (45,000-mi) wideband line (via satellite) for data

$$\text{Circuit delay} = \frac{17,700 \text{ km (11,000 mi.)}}{299,300 \text{ km/s (186,000 mi/s)}} = 0.059 \text{ s for status blocks}$$

and

$$\frac{72,400 \text{ km (45,000 mi)}}{299,300 \text{ km/s (186,000 mi/s)}} = 0.242 \text{ s for data}$$

The difference of 0.183 s is greater than the computer times at either end, and the status block arrives prior to the data. When DRP receives the status block, that message is closed and a new one opened. The data then arrives and are rejected as being out of range of the new message.

The only operational fix was to have both data streams assigned to the same type of communications circuit. Recently, a software fix has been designed to provide the capability of writing the data to tape rather than rejecting them as was done previously.

- (4) Availability of edited recall messages: Any systems failure in the telemetry processor (TLM, RTM), the support system (NCS/Sigma), or the DRP software can cause the need for a reload of the system. This can delete the required gap files. The options available are

to either recreate the gap list by reading the NDLs back through the Test and Training System into the Telemetry System, or to do an "NDL only" merge and build a manual recall stream. Both actions are time-consuming and normally cause an IDR to be late.

- (5) Bad data lines. An excessive number of gaps or late receipt of edited Gap Lists from NOCA can also cause problems. When there are less than 200 gaps, the system normally works well. However, instances of over 700 gaps in a pass have occurred and saturated the system. Gap editing time requirements have exceeded the man and machine hours available for the task and have caused delays of 24 h or more in delivery times. A further complication is the slow rate at which the DRP prints out recall status messages (approximately 70 characters per second when 300 characters per second are required to keep up with system messages). This means that the initial validation of the recall has to await the machine printout and may lag the data by several minutes.

C. Merge Function

The merge processor is the first place the validity of the NDL and Recall tapes are checked. Until the merge summary prints out, or the system alarms over a read error, there is no way of ensuring that the data are recoverable. Under the original DRP software and tape controller, there was no way of knowing if the IDR was even valid until processed by the Viking Project. The introduction of the new tape handler software on 9 June 1976 remedied that but introduced new problems. Until the hardware tape controller was modified on 26 July 1976, the new software was halting several times during each IDR run and severely impacting generation times.

However, several anomalies continued to hinder the merge process:

- (1) System would not accept tape. The system refused to read NDL or merge tape because an apparent parity error had been detected by the tape handler. The operational workaround was to then mount a second NDL on a separate drive, reassign the drive address, and open the new tape. If that was unsuccessful, a series of NDL tapes were tried until one was accepted. Once the tape had been opened, the drive addresses were reset and the merge proceeded.
- (2) "Terminal" read errors. When the Merge program encountered a "terminal" read error, it closed out the IDR, wrote a summary, and terminated the run prior to the end of data. Originally, the corrective action was to put a new load point on the tape at the point of the read error. Then the tape would be mounted on a drive

assigned to the NLP, and a new tape header written there. The merge job would then, if the process worked, be started after the new load point. Unfortunately, this procedure did not prove very successful and caused large outages.

Currently the operational "fix" is to halt the tape when the terminal read error is detected; then, a new job is started using the false NDL option with reassigned tape addresses as in the problem covered in Paragraph C-1.

- (3) "End of Recall Data" errors. This condition arose when trying to merge multiple recall files from a single recall tape. The system would sense a false "end of data" condition and refuse to process the remainder of the recall data. In this case, the only recourse was to recall the data again.
- (4) System halts. System "halts" occurred on a random basis and only a system recovery/reload could restore operations. This condition required a "reinitialization" of the merge program with a further loss of time.
- (5) Data block "time tag" errors. Occasionally a data block would be received where the day, hour, or minute was outside the "window" of the IDR request. When this occurred, the system believed it had recovered all the available data and terminated the job. The only way to merge any data past the data record containing that block was to stop the tape at that record and use the tape address procedure mentioned for other tape problems. The merge then would be restarted using a start time of a few seconds after the error.

To ensure that the above problems did not cause Intermediate Data Records to be late, the merge function was started on a backup Display Computer as soon as the first recall tape became available. By doing this, the content of the recall tape and Network Data Log tapes could be validated, and any data losses due to any of the above listed anomalies could be made good. This procedure produced a high percentage of complete IDRs during orbital operations, as shown in the accompanying data.

V. Improvements

There are several design improvements in progress that are expected to have significant impact on IDR production performance. In order of their potential for improving performance, they are:

- (1) Redesign of the magnetic tape controller (hardware) and handler software.
- (2) Revision of the merge program to allow reading NDLs past tape records with "terminal" error.

- (3) Change to the recall processor software to allow data to be logged to the Recall tape after the status block is received.

VI. Conclusions

The Intermediate Data Record generation system has proven to be a viable means of supporting the Viking Project Data Records requirements. While there are still problems that need resolution, the combination of known operational workarounds and pending systems enhancements should minimize their effect.

Central to the successful generation of any IDR is the recall function. All the other anomalies can be dealt with, given time

to recall any missing data. But recall problems have a limited time frame in which to be resolved. It is the one function that ties everything together. As illustrated in Fig. 1, all other computer systems that handle the data to be merged have to interface correctly and in a timely manner for the recall function to work.

Because of the anomalies in the system, a real-time tradeoff has to be continually made as to when an IDR should be released. The guideline followed throughout most of the orbital operations period was to release any IDR that had over 99.80 percent of the committed data rather than delay for the next available recall periods. Gaps of excessive size (over 6 data blocks) were then marked for a "remake" at a later date.

Table 1. IDR performance

Time Period	No. of Passes	No. of Remarks	Avg. Percentage	Avg. Delivery Time, h	No. Late	% Late
20 June-20 July	84 ^a	5	99.966	10.93	10	11.9
20 Aug.	160	42	99.983	10.45	17	10.56
20 Sept.	192	10	99.996	4.867	6	3.1
20 Oct.	221	27	99.994	6.33 ^b	13	5.9
10 Nov.	125	18	99.997	4.89 ^b	0	0.0
Totals	782	102	99.990	7.07	46	5.88

^aTwo passes waived due to excessive gaps and recall problems.

^bTimes reflect change in “pickup” policy. Generation times average approximately 1 h less.

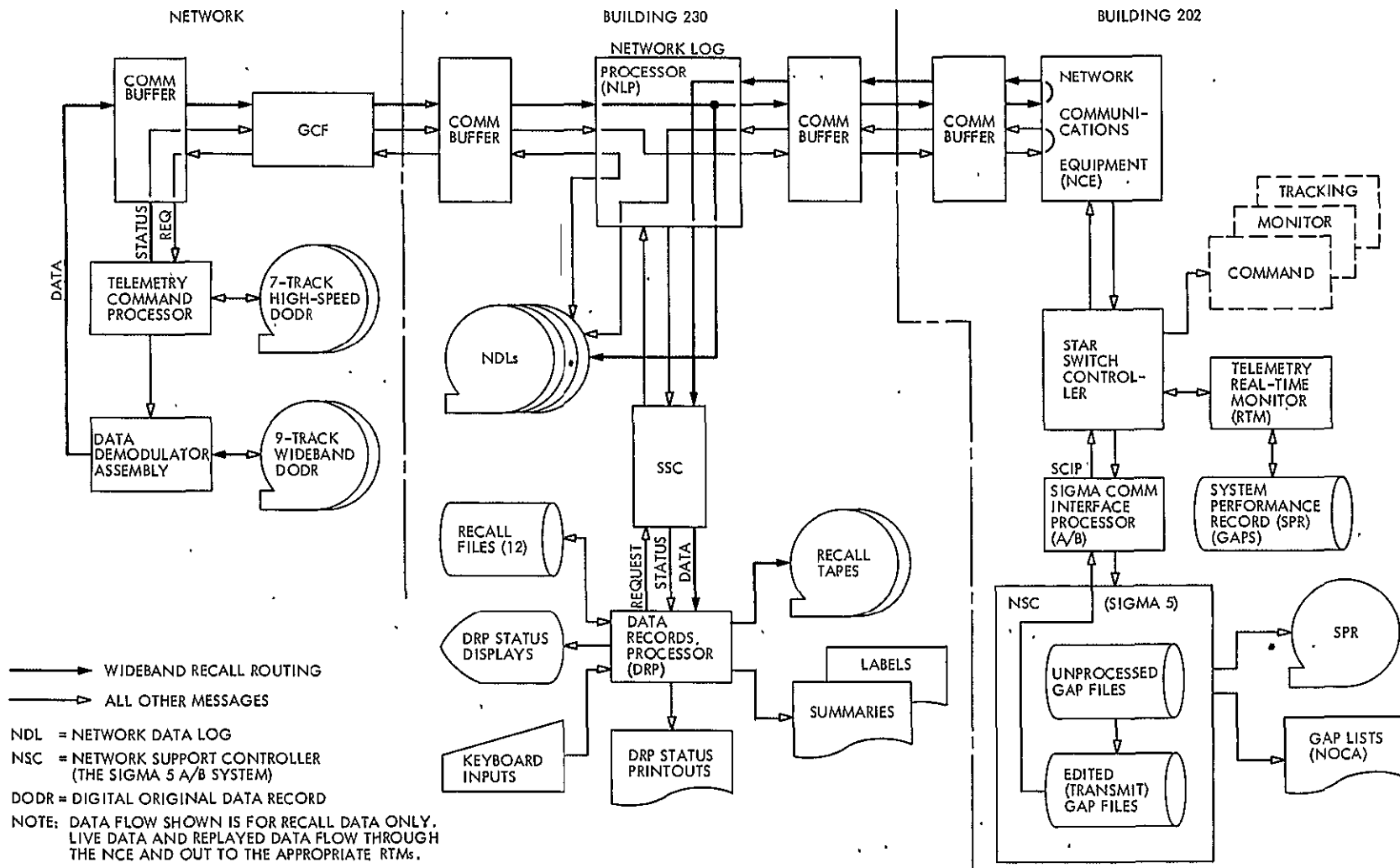


Fig. 1. Data flow paths for Intermediate Data Record production

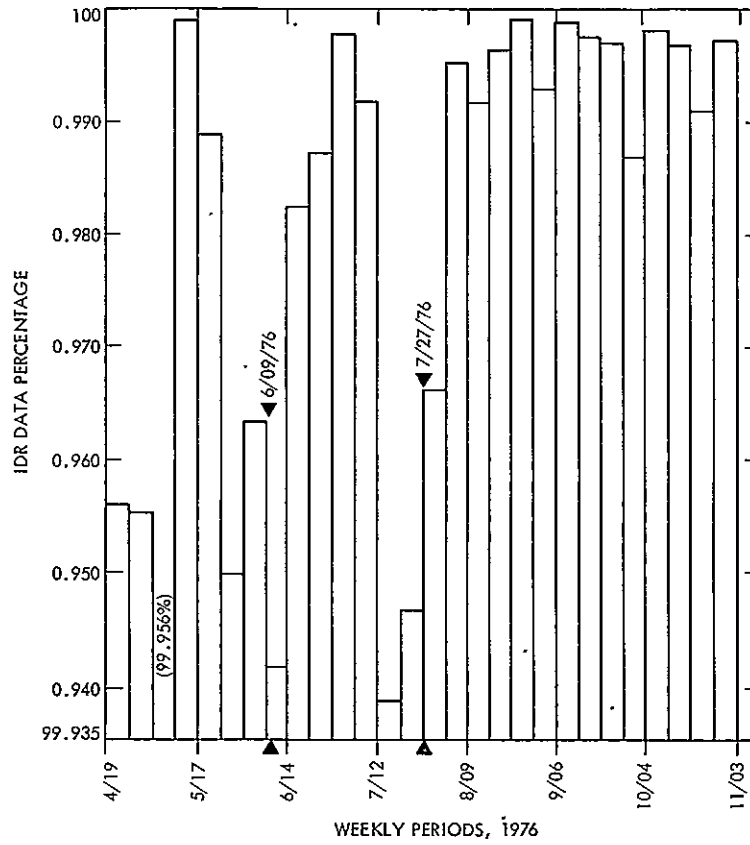


Fig. 2. Viking IDR weekly data percentage history

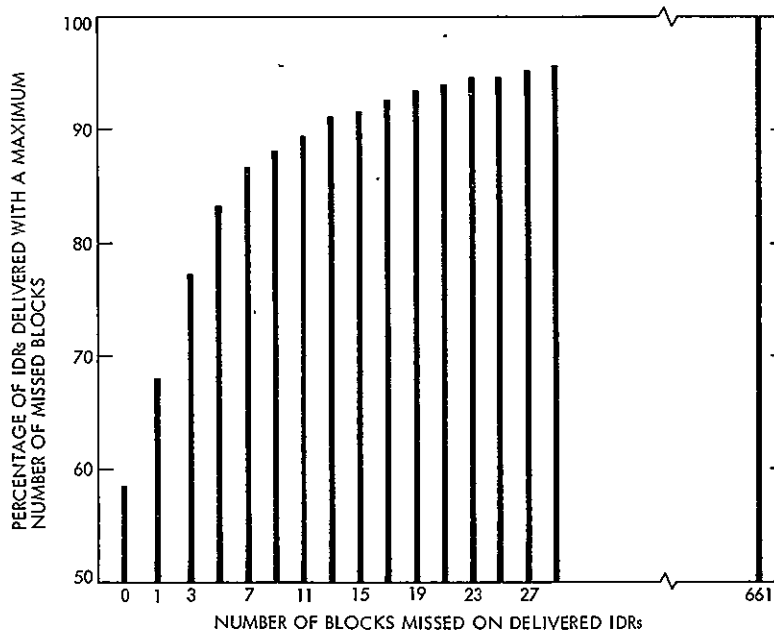


Fig. 3. IDR profile of actual missed blocks for all Viking Support

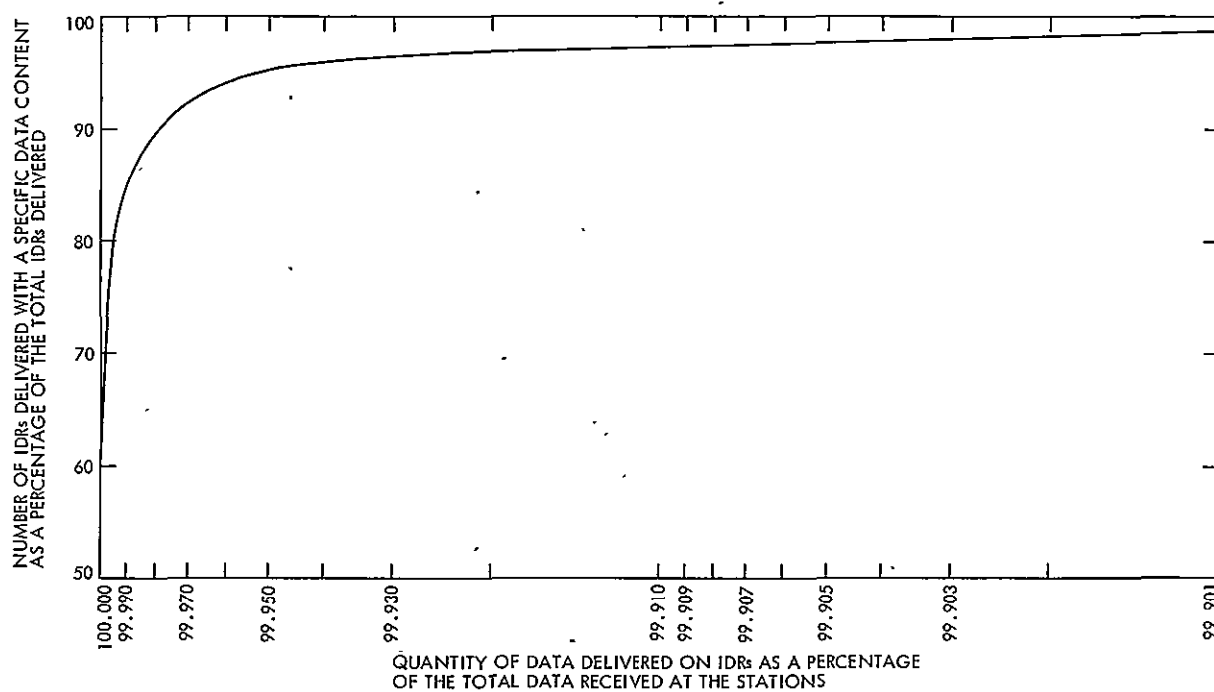


Fig. 4. IDR quantity profile for orbital operations

N77-19096

Pioneer Mission Support

T. P. Adamski

DSN Network Operations Section

This article reports on some recent activities within the Deep Space Network in support of the Pioneer Project's in-flight spacecraft. The amount of tracking coverage provided by the Network and the current status of operational testing of the Mark III Data Subsystems are presented.

I. Pioneers 6, 7, 8, and 9

Coverage of these spacecraft has continued to be at minimal levels. Pioneers 6 and 9 were tracked a total of seven times during the period from September through November, but Pioneers 7 and 8 were not tracked at all. The only anticipated coverage in the foreseeable future will be limited tracking of Pioneer 7 in February. This will be in support of the spacecraft's passage through the geomagnetic tail, at a range of approximately 20 million kilometers from Earth.

II. Pioneers 10 and 11

A. Mission Operations and Status

Both spacecraft continue to be in excellent health. Tracking coverage has increased recently due to the lessening of other commitments on the Network. Total tracking coverage times appear in Table 1.

On September 20, a failure was detected in the Pioneer 10 high-gain antenna feed movement mechanism. This unit moves the feed to provide a constant offset of one degree against which measurement is made of the actual angular separation between the spacecraft spin axis and the spacecraft-Earth line. The feed assembly is moved by means of a piston traveling within a bellows filled with Freon 21. The bellows burst, allowing the Freon to escape and the antenna feed to return to its normal position. This was not an unexpected failure, since the projected life of the bellows was approximately two years and the spacecraft is now in its fifth year of flight. The backup feed movement mechanism will be used for all future measurements. It should be noted that the Navigation Team was able to detect the failure from radio metric data. The escaping Freon imparted a velocity change to the spacecraft equivalent to a doppler shift of 0.02 Hertz. Such accuracy of detection and measurement is impressive, considering the fact that the spacecraft is more than one billion kilometers from Earth.

The Navigation Team also detected an unexplained velocity change of 0.057 meters/second during a Pioneer 11 precession maneuver on September 15. The reason for the change is unclear, but it may have been caused by one of the thruster jets sticking open, resulting in an excessive pulse length. Subsequent precession maneuvers have been conducted successfully with another pair of thrusters and this pair will continue to be used until the problem is understood.

B. Mark III Data Subsystems Support of Pioneer

Implementation of the Mark III Data Subsystems (MDS) hardware has been completed at the Goldstone Echo Station, DSS 12, and the first in a series of three Pioneer demonstration passes was conducted on December 18. The purpose of the pass was to exercise the station equipment and personnel while in a Pioneer 11 flight support configuration.

The pass was structured to closely resemble a typical Pioneer track. Activities included standard downlink and uplink acquisitions, the processing of telemetry at several bit rates and frame lengths, the transmission of commands to the spacecraft, and the generation and transmission of monitor and radio metric data to the Network Operations Control Center (NOCC). The initial station configuration used for the pass is shown in Fig. 1.

A successful data transfer test was completed prior to acquisition for command, radio metric, and telemetry data.

Monitor data could not be verified due to the absence of the appropriate NOCC software. The station acquired the downlink signal in a three-way mode with DSS 61 in Spain, accepted a transfer of the uplink, and commenced commanding. Three remote mode commands were generated by the Project and transmitted from the station. Although spacecraft response to these commands was verified by the Project, no such response was observed for a bit rate change command which the station had transmitted locally. It was later determined that this was due to an incorrect hexadecimal command value that had been provided by the Project.

Two telemetry frame size changes and two bit-rate changes were processed by the station without serious difficulty. However, some problems were discovered in the preliminary operational procedures for effecting these changes. Some minor procedural problems were also experienced with the operation of the Metric Data Assembly, but it is felt that such problems are to be expected in the early phases of training and should disappear as operator familiarity increases.

Operational software did not exist in the NOCC for handling monitor data from an MDS-equipped station and the station software did not include a recall capability. Both of these functions will be fully verified during later operational testing with DSS 12 as software development continues.

Table 1. Pioneer tracking coverage

	Spacecraft	Station type	Tracks	Tracking time, h:min
September	Pioneer 6	26-meter	1	5:22
	Pioneer 10	26-meter	30	127 51
		64-meter	1	8:53
	Pioneer 11	26-meter	39	290 37
October	Pioneer 6	26-meter	1	3:56
	Pioneer 9	26-meter	3	12:50
	Pioneer 10	26-meter	30	195 04
		64-meter	6	44 02
	Pioneer 11	26-meter	40	274:43
November	Pioneer 6	26-meter	2	8:18
	Pioneer 10	26-meter	39	298 23
		64-meter	22	145.18
	Pioneer 11	26-meter	50	407.35
		64-meter	6	41.59

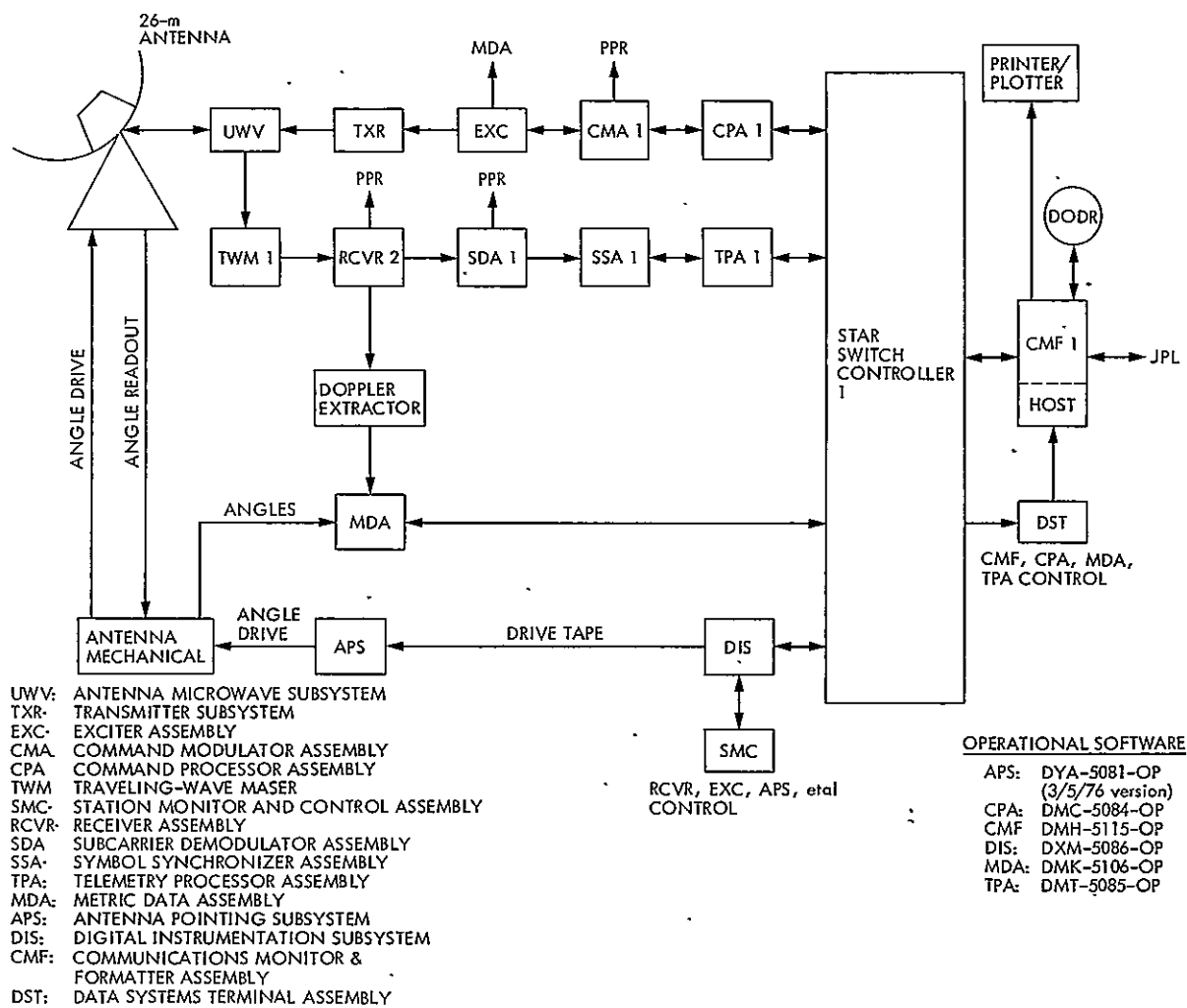


Fig. 1. Standard Pioneer configuration—DSS 12

N77-19097

Helios Mission Support

P. S. Goodwin
TDA Mission Support

E. S. Burke and T. P. Adamski
DSN Network Operations Section

This article reports on activities of the Network Operations organization in support of the Helios Project during October and November 1976.

I. Introduction

This article is the thirteenth in a continuing series of reports that discusses Deep Space Network support of Helios mission operations. Included in this article is information concerning Spacecraft Tracking and Data Network (STDN)-DSN telemetry and command cross-support, the Helios-2 ranging anomaly, the first operational demonstration of the Mark III Data System for Helios support, and other mission-oriented information.

II. Mission Operations and Status

Helios-1 continues to operate normally in its extended mission. Perigee occurred on November 30 when the spacecraft was approximately 52 million kilometers from Earth. The fourth aphelion will occur on January 9. Deep Space Network coverage during October and November is shown in Table 1.

The Helios-2 spacecraft is operating normally with the exception of the ranging anomaly reported in Ref. 1. After extensive troubleshooting, the Project has determined that traveling wave tube (TWT) number 2 cannot be turned on in either the high- or medium-power modes. They have further theorized that the attempt to turn on the spacecraft's ranging channel somehow damaged its transmitter logic circuit. As a result, ranging will not be attempted until the entire failure has been analyzed and is well understood.

Helios-2 passed through inferior conjunction on November 18. The data "greyout" due to solar interference lasted for approximately 26 hours, but was covered with an onboard memory read-in operation. Greyout entry was at a Sun-Earth-probe angle of 0.4 degrees; exit was at 0.7 degrees. The spacecraft will pass perigee (minimum distance of 4 million kilometers) on January 4 and aphelion on January 21. Table I shows the tracking coverage provided this spacecraft by the DSN during October and November.

III. Special Activities

A. STDN-DSN Cross-Support

The previous article in this series (Ref. 1) reported on the configuration used by the Goldstone STDN station to support the two Helios spacecraft and presented some preliminary comparative results of that support. The cross-support period ended on November 15 when the STDN station was taken down for extensive reconfiguration. Up to that point, the station had tracked Helios-1 eleven times and Helios-2 five times. It was found that the STDN station could support Helios at a signal-to-noise ratio approximately 4 dB below that of a 26-meter DSN station. This difference was due primarily to a higher system operating temperature and a lower receiver sensitivity at the STDN site.

Based on this 4-dB offset, it was possible to predict STDN performance relative to DSN stations. The signal-to-noise ratios of data received from Helios-1 during the period of cross-support were consistently within one-half dB of the predicted values, but the SNRs of Helios-2 data were an average of 2.5 dB lower than predicted. The reason for this difference is presently unclear, but it is anticipated that further study will be possible during future STDN support of the Helios spacecraft.

B. Mark III Data System Support of Helios

Implementation of the Mark III Data System equipment has been completed at the Goldstone Echo Station, DSS 12. The first in a series of demonstration tracks was conducted on December 21 to exercise the new equipment in a Helios support configuration and to provide an opportunity for operator training. The initial configuration used for the track is shown in Fig. 1.

Activities during the demonstration were designed to emulate a typical Helios track. The station acquired the downlink signal, performed an uplink acquisition, commanded the spacecraft, and attempted to output monitor, radio metric, and telemetry data. The individual subsystems appeared to function normally, but extreme difficulty was experienced in maintaining data flow from the Communications Monitor and Formatter Assembly (CMF). The most common failures involved cessation of high-speed output during failures of the digital recorder, or losses of the interface between the CMF and the high-speed communication buffers.

Although the track was less than successful as a demonstration of equipment reliability, the troubleshooting performed on-site provided valuable hands-on training for the station operators. Future Helios demonstration tracks should be more successful as minor hardware and software problems are resolved and as familiarity with the new equipment increases.

Reference

1. Goodwin, P. S., Burke, E. S., and Morris, R. E., "Helios Mission Support," in *The Deep Space Network Progress Report 42-36*, pp. 28-34, Jet Propulsion Laboratory, Pasadena, Calif., Oct. 15, 1976.

Table 1. Helios tracking coverage

Month	Spacecraft	Station type	Number of tracks	Tracking time, h, min
October	Helios-1	26-m	37	121:14
		64-m	3	9:48
	Helios-2	26-m	25	191:10
		64-m	22	63:17
November	Helios-1	26-m	41	381:30
		64-m	2	6 04
	Helios-2	26-m	35	297.34
		64-m	3	19.14

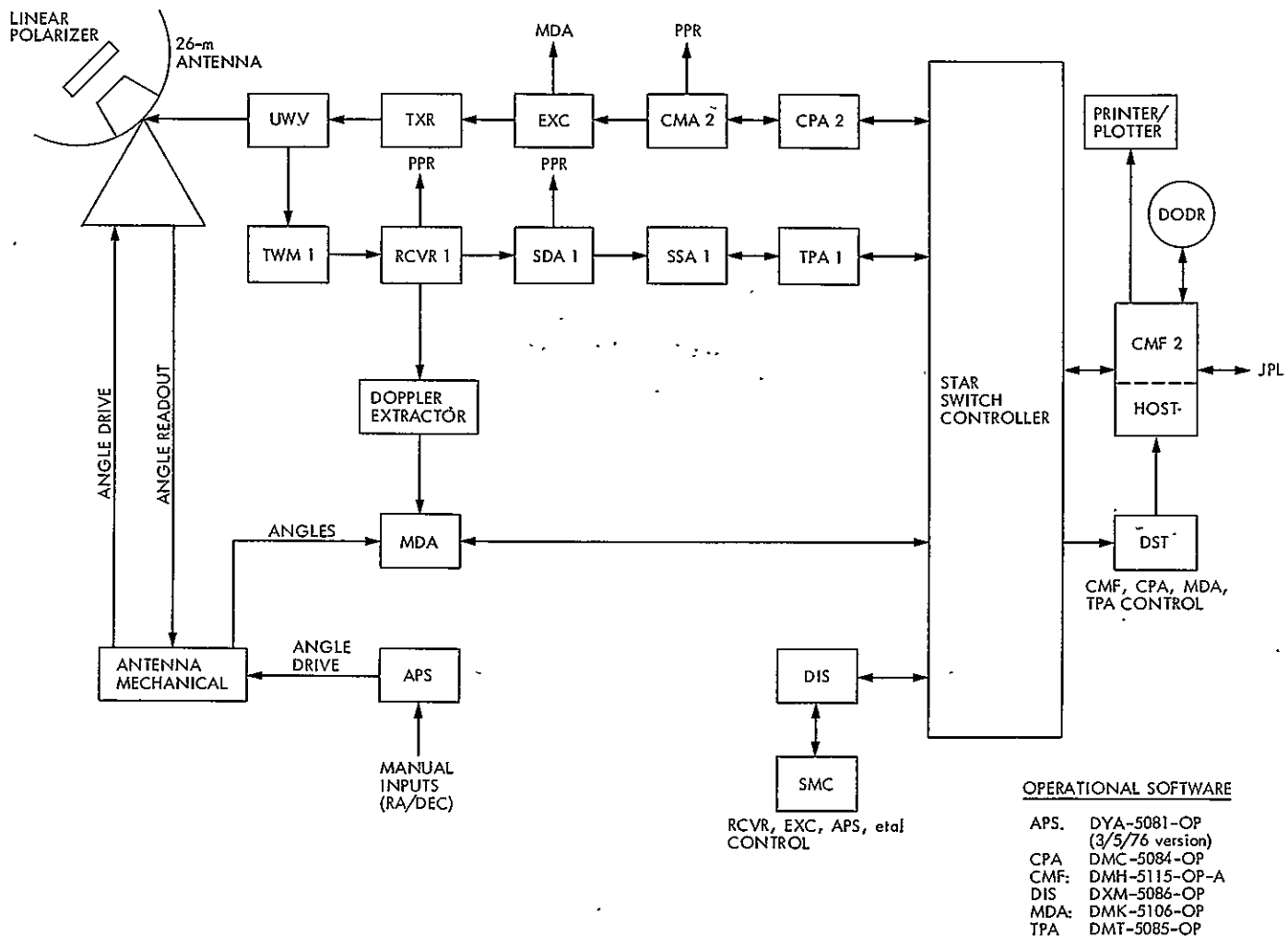


Fig. 1. DSS 12 support configuration

N77-19098

A Solar Plasma Stream Measured by DRVID and Dual-Frequency Range and Doppler Radio Metric Data

F. B. Winn and S. C. Wu

Tracking Systems and Applications Section

T. A. Komarek

Telecommunications Systems Section

V. W. Lam, H. N. Royden, and K. B. W. Yip

Navigation Systems Section

S- and X-band DRVID, S- and X-band dual-frequency range (SX (ρ)), and doppler (SX (ρ)) measured a 15-fold increase in the line-of-sight electron content of the solar plasma above the normal plasma background. A general increase in the plasma electron content continued for nearly 50 hours: it started about 12:00 (GMT) on 12 March 1976 and continued to grow until 17:00 (GMT) on 14 March. For the next 55 hours, between 17:00 (GMT) on 14 March to 00:54 (GMT) on 17 March, the plasma level diminished as the background level was again approached.

Not only were the temporal changes and absolute level of the plasma content measured but the measurements were also used to ascertain the mean-plasma-concentration location. it was estimated to be 4.1 light minutes from Earth.

It is demonstrated that if round-trip S-band range is to be calibrated for plasma influence to the meter level, then some knowledge of the plasma distribution must exist.

I. Introduction

Two Viking spacecraft were navigated to Mars by analyzing radio metric data acquired from the spacecraft while they were in heliocentric orbits. When the spacecraft were at a geocentric distance of ~ 1.2 AU and were angularly 96 deg from the Sun

as viewed from Earth, S- and X-band DRVID, S- and X-band dual-frequency range (SX (ρ)) and doppler (SX (ρ)) measured a 15-fold increase in the line-of-sight electron content of the solar plasma above the normal plasma background. A general increase in the plasma electron content continued for nearly 50 hours: it started about 12:00 (GMT) on 12 March 1976

and continued to grow until 17:00 (GMT) on 14 March. For the next 55 hours, between 17:00 (GMT) on 14 March to 00:54 (GMT) on 17 March, the plasma level diminished as the background level was again approached.

Not only were the temporal changes and absolute level of the plasma content measured but the measurements were also used to ascertain the mean-plasma-concentration location: it was estimated to be 4.1 light minutes from Earth.

An examination of the radio metric data in the presence of this plasma shows:

- (1) S-band group delays as large as 27 m occurred (3.33 ns/m).
- (2) S-band phase changed at rates up to 3.6 m/h.
- (3) S-band doppler rms noise was at 14 mHz at one time (~6 times greater than nominal for 60-second count time doppler).
- (4) S-band doppler rms noise does not necessarily correlate with plasma level.

II. Charged-Particle Calibrations

Electromagnetic group and phase velocities are slowed down and speeded up, respectively, by electron concentrations as shown by

$$V_g = c \left(1 - \frac{1}{2} \frac{Ne^2}{4\pi^2 \epsilon_0 m f^2} \right)$$

$$V_p = c \left(1 + \frac{1}{2} \frac{Ne^2}{4\pi^2 \epsilon_0 m f^2} \right)$$

where

V_g = group velocity (modulation)

V_p = phase velocity (carrier)

c = velocity of light (2.998×10^8 m/s)

e = electron charge (-1.602×10^{-19} coulombs)

ϵ_0 = free space permittivity (8.85×10^{-12} farad/m)

m = electron mass (9.109×10^{-31} kg)

f = carrier frequency (Hz)

N = density of electrons along propagation path (electrons/m³)

The transit time for modulation propagating at the group velocity between the spacecraft ($x = 0$) and station ($x = R$) is

$$T_g = \int_0^R \frac{dx}{V_g}$$

Similarly, the transit time for the carrier phase is

$$T_p = \int_0^R \frac{dx}{V_p}$$

Using the formula for V_g and V_p , and introducing the integrated electron content $I = \int N dx$, gives the group and phase transit times between the spacecraft and Earth-bound station

$$T_g = \frac{R}{c} + \frac{1}{2} \frac{e^2}{4\pi^2 \epsilon_0 m f^2} I$$

$$T_p = \frac{R}{c} - \frac{1}{2} \frac{e^2}{4\pi^2 \epsilon_0 m f^2} I$$

where

T_g = group transit time

T_p = phase transit time

R = distance between spacecraft and station (m)

$I = \int_0^R N dx$ = integrated electron content along signal path (electrons/m²)

The charged-particle calibration data types (Table 1) exploit the dispersive nature of the plasma or the opposite, but equal, influence of the plasma on group and phase velocities.

III. Plasma Event as Measured

Prior to March 1976, when the Sun-Earth-probe (SEP) angle was >96 deg, very little plasma activity was apparent (Fig. 1). Figure 1 shows the amount of phase shifts due to changes in columnar content experienced by S-band radio waves. Each plotted point shows the accumulated phase shifts over a view period. Since the view periods were of variable time duration, many of the lower points can be ignored. The connected line segments (which tie together tracking passes greater than 6 hours in duration) offer a coarse estimate of the relative plasma activity from November 1975 to March 1976. The peak-to-peak phase shifts over each view period were divided by the time interval in hours to give the average hourly rates (Fig. 2). These also reveal the two large plasma events in the month of March. These plasma events are detected when plasma concentrations cross the Earth-spacecraft propagation paths, which move almost perpendicular to the solar radial (Fig. 3).

The absolute plasma content, as measured by SX (ρ), shows the 15 March plasma event to have commenced to cross the Viking raypaths at about 15:00 (GMT) on 12 March (Fig. 4). The plasma concentration continued to move onto the raypaths until ~ 55 hours later on 17 March. Relative plasma levels, as indicated by S-band differenced range versus integrated doppler (DRVID) and SX (ρ), are consistent with SX (ρ) (Fig. 4).

SX (ρ) absolute content calibrations are negatively biased. SX (ρ) and Faraday rotation (Ref. 3) calibrations of the electron content of Earth's ionosphere appear to have a 6-m offset (Fig. 5). The SX (ρ) calibration is approximately 6 m less than the Faraday calibration independent of DSS (Table 2) or Viking spacecraft. This SX (ρ) was acquired from Viking 1975 (VK '75) spacecraft A when the probe was 146 deg from the Sun as seen from Earth and at a distance of ~ 0.3 AU. Thus, the probability is high that the plasma contribution to SX (ρ) is small ($\ll 1$ m). This negative 6-m bias has been corrected for in Fig. 4.

The total electron content (Fig. 4) at 12:00 (GMT) on 12 March results in an S-band range delay of 5.5 m. At 16:52 (GMT) on 12 March, the combined electron content equals $\sim 16 \times 10^{17}$ electrons/m², which produces an S-band range delay of ~ 20.5 m. At this time, the ionospheric content is $\sim 10^{17}$ electrons/m², and the plasma content is $\sim 15 \times 10^{17}$ electrons/m². The plasma level changes 11.5×10^{17} electrons/m² in 4 hours 52 minutes. Following this rise in content at a rate of 2.3×10^{17} electrons/m²/hour for ~ 5 hours, a less rapid, linear accumulation of $\sim 0.2 \times 10^{17}$ electrons/m²/hour was observed for about the next 45 hours. It reached a maximum level of $\sim 20 \times 10^{17}$ electrons/m² (27 m of S-band

range delay) at 16:32 (GMT) on 14 March. This maximum level persisted for at least 9 hours. At 01:00 (GMT) on 15 March, the data were interrupted for ~ 13 hours. When the SX (ρ) calibrations were once again acquired at $\sim 13:00$ (GMT) on 15 March, the electron content was at $\sim 14 \times 10^{17}$ electrons/m² (19 m of S-band range delay). SX (ρ), SX (ρ), and S-band DRVID are consistent and show another ~ 9 -m decrease in the S-band range delay between 13:00 (GMT) on 15 March and 02:00 (GMT) on 16 March. Subsequent data passes continued to reveal a general decrease in the plasma level. It was not until 19 March that SX (ρ) calibrations were again at the ionospheric content level.

IV. Plasma Stream Influence on S-Band Doppler

Root-mean-square S-band doppler noise increased 5- to 6-fold as the plasma stream swept through the line-of-sight (Fig. 6). This increase in noise stems from the high frequency fluctuations of the plasma (plasma turbulence, Ref. 4), which scintillates radio carriers. S-band doppler is acquired from the Viking probes nearly continuously. A running 2-hour average of the doppler noise (Fig. 7) compares the noise levels of the Viking 1 and 2 spacecraft doppler. The angular separation of the 2 probes is 1.1 deg. The maximum linear separation of the probe line-of-sight is ~ 0.02 AU. Since large-scale plasma structures usually extend over distances of tenths of AU or more, it is expected that the rms noise levels of the radio carriers will correlate highly as shown in Fig. 7. If the total doppler scintillation is directly proportional to the total electron content of the plasma at large SEP angles (i.e., 96 deg) as indicated by researchers (Refs. 4 and 5) for small SEP angles (i.e., <5 deg), then the rms noise pattern suggests two peaks in the line-of-sight electron content. One peak occurs between 06:00 and 14:00 (GMT) on 14 March and the second between 02:00 and 16:00 (GMT) on 15 March. On 14 March when SX (ρ) is indicating a maximum plasma electron content of 20×10^{17} electrons/m², S-band doppler rms noise is at its lowest level. This suggests that at large SEP angles the net scintillation of a radio carrier is not necessarily directly proportional to the line-of-sight electron content. Additional investigation is needed.

V. Plasma Mean Distance Estimate

Transmissions to the spacecraft are at S-band frequencies; transmissions from the spacecraft are at S- and X-band frequencies. S-band DRVID is a round-trip measurement, SX (ρ) is downleg only in character.

If the space plasma concentration is (1) singular, (2) localized, and (3) fixed in space, then a DRVID-SX (ρ)

cross-correlation yields the mean distance of the plasma concentration from the spacecraft. The procedure is to find that Δt for which the minimum rms difference between DRVID and 2-way SX ($\dot{\rho}$) exists:

$$\text{minimum} \sum_t \{ \text{DRVID}_t - [\text{SX}(\dot{\rho})_t + \text{SX}(\dot{\rho})_{t-\Delta t}] \}^2$$

for $\Delta t = 1, 2, 3, \dots$, round-trip light minutes from plasma to probe to plasma.

If the plasma concentration is at the spacecraft, then the light-time separation between upleg and downleg encounters with the plasma is zero ($\Delta t = 0$).

The rms difference for $\Delta t = 0$ is then

$$\sum_t [\text{DRVID}_t - 2 \text{SX}(\dot{\rho})_t]^2$$

Fig. 8 shows 2 SX ($\dot{\rho}$) and DRVID for the 15 March view period. The rms difference equals 0.4 m, which is 2 times the DRVID rms noise.

If the plasma were located at Earth, then the separation in time between plasma encounters would equal the total round-trip time from Earth to spacecraft to Earth. For the plasma concentration assumed at Earth (Fig. 9), the rms discrepancy between DRVID and $[\text{SX}(\dot{\rho})_t + \text{SX}(\dot{\rho})_{t-18.2}]$ is 0.7 m.

For an 11-minute light-time separation between upleg and downleg encounters, a minimum rms difference of 0.2 m is obtained (Fig. 10). Thus, $[\text{SX}(\dot{\rho})_t + \text{SX}(\dot{\rho})_{t-11}]$ and DRVID calibrations are in closest agreement when the concentration is assumed 4.1 light minutes from Earth (5.5 minutes from the spacecraft) and are shown in Fig. 11.

Once the light-time separation between plasma encounters, Δt , is known, SX (ρ) and SX ($\dot{\rho}$) yield round-trip range calibrations for plasma dynamics. First, SX ($\dot{\rho}$) is fit to SX (ρ) such that a minimum rms difference results (Fig. 12). For the 15 March data, a minimum rms difference of 0.3 m is obtained for the two SX measurement types. Now SX ($\dot{\rho}$), as plotted, possesses absolute plasma level information. The round-trip range calibration is then:

$$\text{SX}(\dot{\rho})_t + \text{SX}(\dot{\rho})_{t-\Delta t}$$

If a comparison is made between 2 SX ($\dot{\rho}$)_t and SX ($\dot{\rho}$)_t + SX ($\dot{\rho}$)_{t-Δt} at each point within the pass, the maximum difference is ~0.3 m. This is comparable to the rms uncertainty of the SX (ρ) - SX ($\dot{\rho}$) fit. Thus, in this case, computing the "true" upleg calibration did not make much difference; however, as the SEP angle diminishes (plasma levels increase) and as the spacecraft-to-Earth light-time increases (more time separation between upleg and downleg plasma encounters), it is expected that plasma influences on upleg and downleg doppler and range will become increasingly different. For example, for the 15 March plasma (Fig. 12), if the spacecraft to plasma light-time distance was ½ hour, then the doubled downleg SX (ρ)_t minus $[\text{SX}(\dot{\rho})_t + \text{SX}(\dot{\rho})_{t-\Delta t}]$ difference is >3 m at the point where SX ($\dot{\rho}$) has its greatest slope.

The Mariner Jupiter-Saturn mission will place the spacecraft ~10 AU from Earth (round-trip light-time ~160 minutes). Round-trip S-band range acquired by multiple DSS, when differenced, is required to a $4.5\sqrt{2}$ -m accuracy (1σ). That is the total error due to all error sources. To realize this accuracy, differenced range calibrations for plasma effects must be achieved to at least the meter level.

If the time interval between range measurements is small (10-20 minutes), then it appears that much of the plasma effects in the two range measurements will cancel in the difference. To what extent cancellation occurs is currently under study.

VI. Summary

S- and X-band DRVID, S- and X-band dual-frequency range, and doppler have been used to determine the absolute and relative electron content of a plasma concentration. The plasma appears to have taken more than 100 hours to cross the radio propagation paths between Earth and the Viking space probes. At times the electron content was $\sim 20 \times 10^{17}$ electrons/m².

The mean location of the plasma concentration was determined from 15 March 1976 data to be 4.1 minutes away from Earth.

The Sun-Earth-probe angle was ~96 deg.

It is demonstrated that if round-trip S-band range is to be calibrated for plasma influence to the meter level, then some knowledge of the plasma distribution must exist.

References

1. MacDoran, P. F., "A First-Principles Derivation of the Differenced Range Versus Integrated Doppler (DRVID) Charged-Particle Calibration Method," in *The Deep Space Network*, Space Programs Summary 37-62, Vol. II, pp. 28-34, Jet Propulsion Laboratory, Pasadena, Calif., Mar. 31, 1970.
2. Madrid, G. A., "The Measurement of Dispersive Effects Using the Mariner 10 S- and X-Band Spacecraft to Station Link," in *The Deep Space Network Progress Report 42-22*, pp. 22-27, Jet Propulsion Laboratory, Pasadena, Calif., Aug. 15, 1974.
3. Yip, K. W., et al., "Decimeter Modeling of Ionospheric Columnar Electron Content at S-Band Frequencies," edited by J. M. Goodman, *Symposium on Effect of the Ionosphere on Space Systems and Communications*, Naval Research Laboratory, Washington, D. C., Jan 20-22, 1975, p. 345.
4. Anderson, J. D., et al., "A Measurement of the General Relativistic Time Delay with Data from Mariner 6 and 7," edited by R. W. Davies, *Proceedings of the Conference on Experimental Tests of Gravitation Theories*, California Institute of Technology, Pasadena, Calif., Nov 11-13, 1976, p. 111.
5. Berman, A. L., and Wackley, J. A., "Doppler Noise Considered as a Function of the Signal Path Integration of Electron Density," in *The Deep Space Network Progress Report 42-33*, pp. 159-193, Jet Propulsion Laboratory, Pasadena, Calif., June 15, 1976.

Table 1. Charged-particle calibration data types^a

Type/principle	Formulation	
DRVID (differenced range versus integrated doppler) exploits the opposite, but equal, effect of the electron content on group and phase velocities (Ref. 1).	$\text{DRVID} = \frac{c}{2} \{ \rho_s(t_i) - \rho_s(t_0) - K [\Phi_s(t_i) - \Phi_s(t_0) - f_b(t_i - t_0)] \}$	
	DRVID = S-band phase shift, m	t_0 = reference time
	c = velocity of light, m/s	f_b = frequency bias, Hz
	ρ_s = S-band round-trip travel time, s	K = constant, s/cycle
	Φ_s = S-band phase, cycles	t_i = observation time
SX ($\dot{\rho}$) (dual-frequency dispersive doppler) exploits the inverse squared relationship between phase change and carrier frequency in an electron medium (Ref. 2).	$\text{SX}(\dot{\rho}) = \Phi_s - \frac{3}{11} \Phi_x$	
	Φ_x = X-band phase, cycles	
SX (ρ) (dual-frequency dispersive range) also exploits the inverse frequency squared dependence of group velocity in an electron medium (Ref. 2).	$\text{SX}(\rho) = \rho_s(t_i) - \rho_x(t_i) \text{ (group delay)}$	
	$\rho_x(t_i)$ = X-band group travel time, s	

^aIn a companion article, "Solar Plasma: Viking 1975 Interplanetary Spacecraft Dual-Frequency Doppler Data," a summary of the plasma history throughout the heliocentric, ballistic "cruise" phase of the Viking mission is provided. Additionally, some comparisons of the calibrations derived from DRVID, dispersive doppler are offered

Table 2. Deep Space Station coordinates

DSS	Location	λ , deg	Distance from Earth spin-axis, km
14	Goldstone, California	243.11047	5203.999
43	Canberra, Australia	148.98127	5205.252
63	Robledo, Spain	355.75198	4860.819

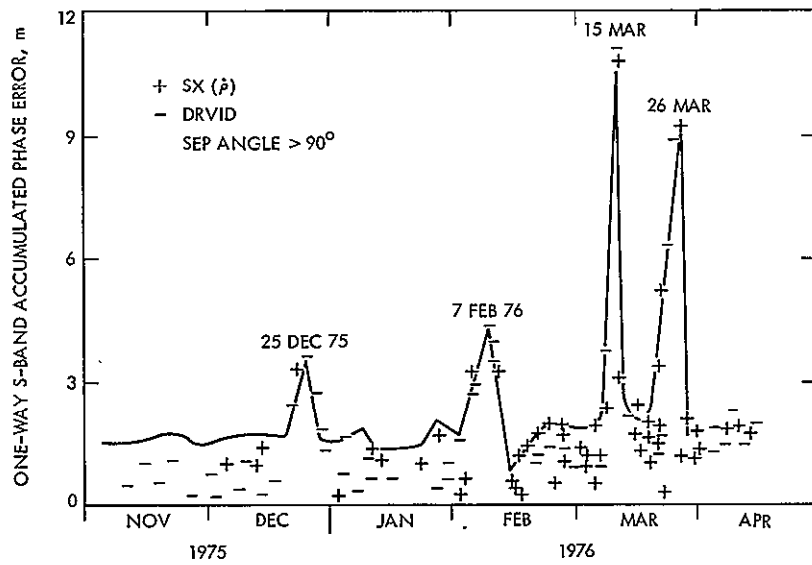


Fig. 1. Viking A observed plasma dynamics

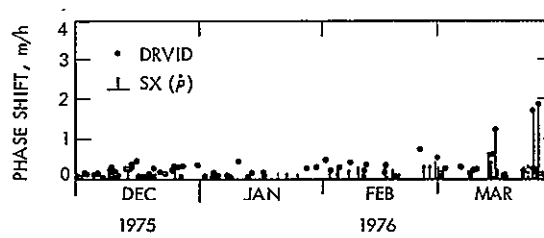


Fig. 2. Viking A average phase shift per hour

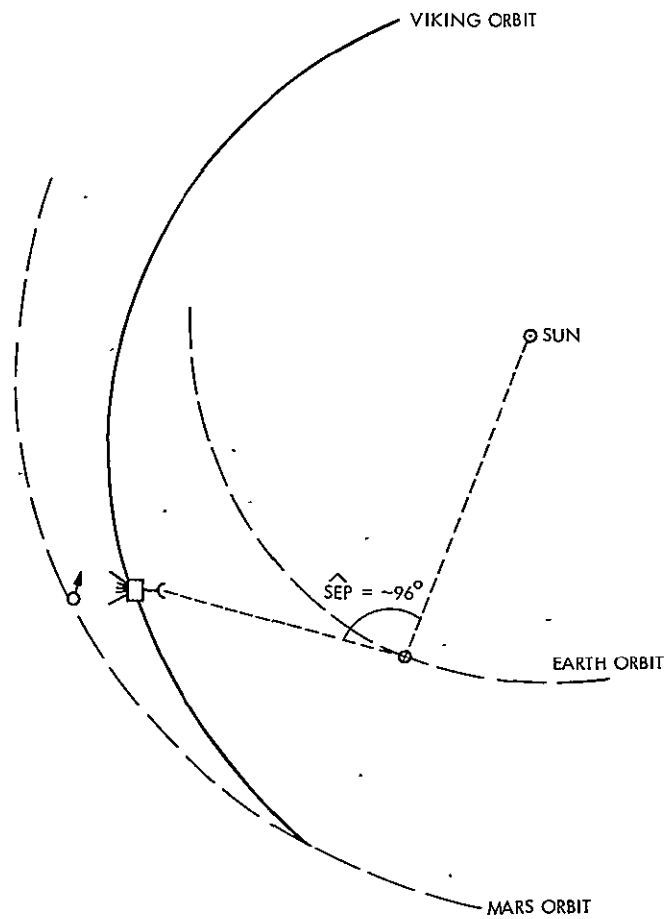


Fig. 3. Angular separation of Viking spacecraft from Sun as viewed from Earth

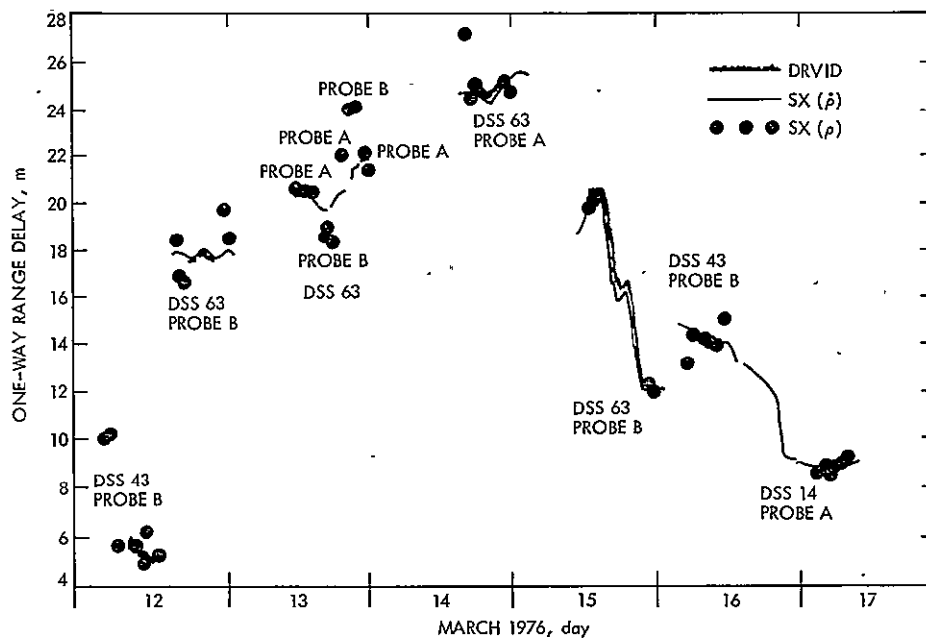


Fig. 4. SX (ρ), SX ($\dot{\rho}$), S-band DRVID measurements of solar plasma plus Earth's ionosphere

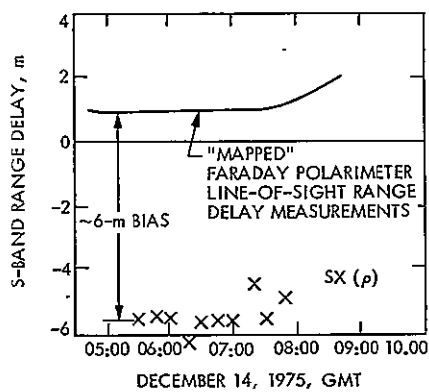


Fig. 5. Comparison of ionospheric measurements with SX (ρ)

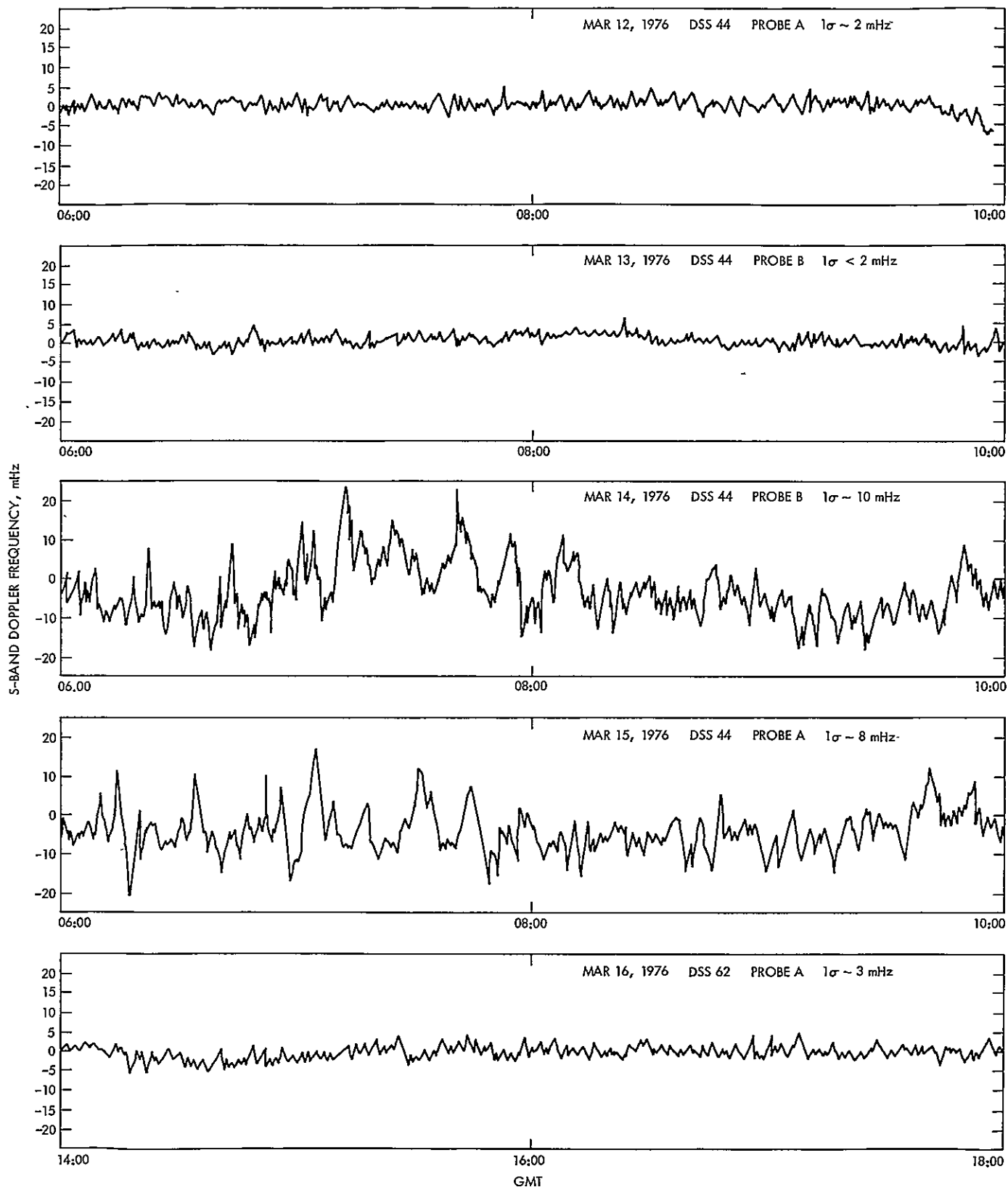


Fig. 6. Doppler noise characteristics as a function of plasma activity⁵

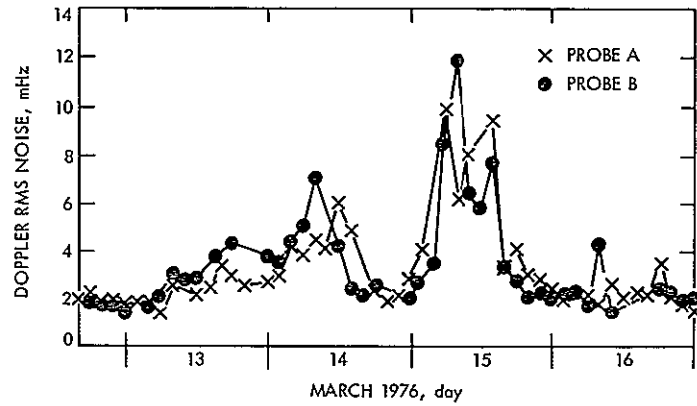


Fig. 7. Rms doppler noise during plasma disturbance

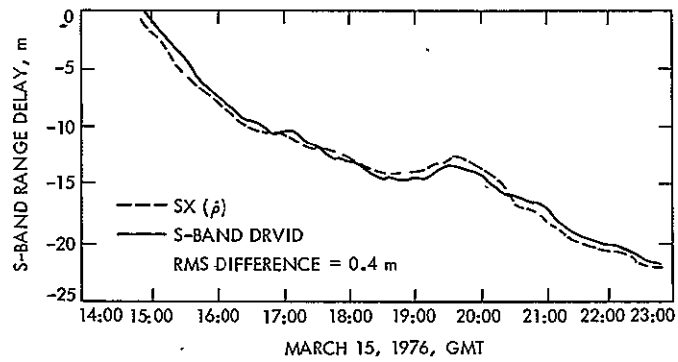


Fig. 8. Round-trip 2-way effects with plasma concentration assumed at spacecraft

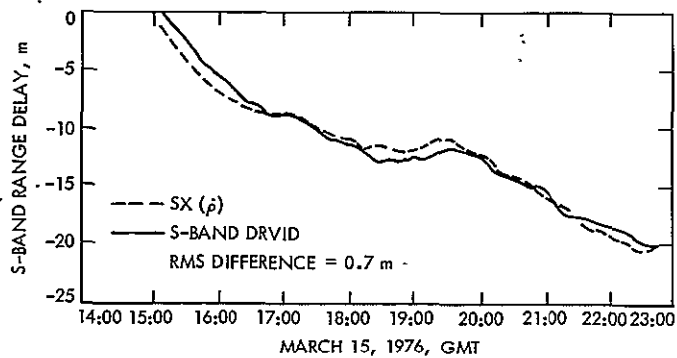


Fig. 9. Round-trip 2-way effects with plasma concentration assumed at Earth

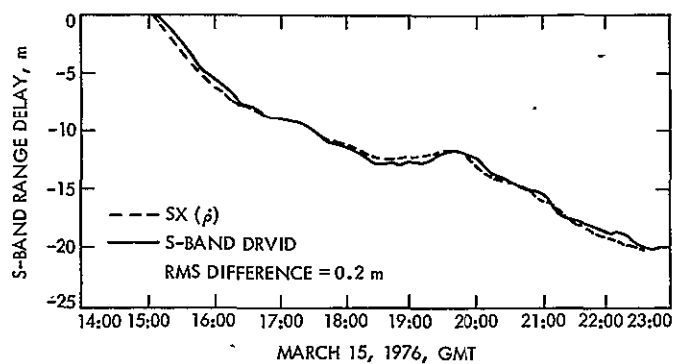


Fig. 11. Round-trip 2-way effects with plasma concentration assumed at 4.1 light minutes from Earth

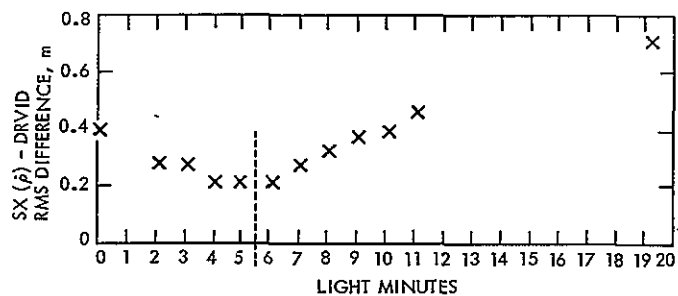


Fig. 10. Estimated light-time separation between upleg and downleg plasma encounters

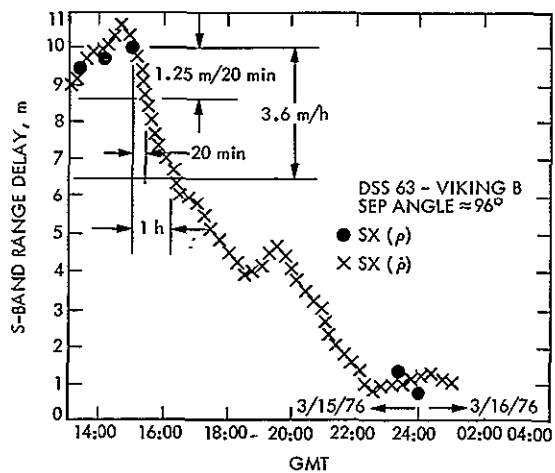


Fig. 12. Upleg/downleg range delay differences for 20-minute and 1-hour light-time separations between upleg/downleg plasma encounters

N77-19099

Feasibility Study of Far-Field Methods for Calibrating Ground Station Delays

T. Sato

Radio Frequency and Microwave Subsystems Section

The first phase of a study to survey various methods of directly implementing a far-field means of calibrating ranging systems is described. Consideration is given to means of determining test range distances independent of microwave techniques.

I. Introduction

This is the first phase of a study to survey various methods of directly implementing a far-field means of calibrating ranging systems. For 13-cm wavelength, the far field begins at a distance of 65-km for a 64-m-diameter antenna. Because this distance is sufficiently large to preclude the normal collimation tower approach, various free-moving platforms were surveyed to determine their suitability to this task.

An important associated problem, that of determining the absolute range to an accuracy <0.5 m over the range test distances, was addressed. It appears that it would be desirable to determine the transponder range by means independent of microwave techniques. A laser system has been suggested, since the wavelength employed is sufficiently different from the microwave to be affected differently by the transmission media.

II. Balloons

The Weather Bureau routinely probes the atmosphere with Rawinsonde balloon systems. These balloons are small (~ 2 m

diameter), and the instrument package is very light (~ 2 kg). An altitude of about 30 km is achieved during flight.

A balloon large enough to carry a transponder package, which can weigh as much as 20 kg with power supply, would be much larger (~ 5 m diameter) than those utilized for Rawinsondes. The larger the balloon, the more difficult it is to launch, especially under windy conditions, and this considerably complicates the logistics and procedures.

Balloons, by their very nature, can trace rather capricious paths due to winds of varying speed and direction at different altitudes. These motions could make accurate tracking of the transponder package difficult, particularly for a laser ranging system.

Not negligible is the potential loss risk of an expensive transponder package.

III. Aircraft

A high-performance aircraft can be used as a transponder platform. Perhaps the outstanding advantage of the aircraft is the positive control of the transponder at all times, both in its location and operation. The aircraft can be flown on a prescribed flight path and the actual range to the aircraft determined by a laser ranger. A malfunctioning transponder can be brought back for repair. The possibility of losing the transponder package is essentially nil.

The main disadvantage of an aircraft platform is the altitude achievable by aircraft. Excluding special high-performance military aircraft, usable altitudes are limited to about 13.5 km. This altitude translates into an elevation angle of about 12 deg at a slant range of 65 km. Because of the greater far-field distance, aircraft are not usable for X-band. Achievable elevation angles (~ 3 deg) are below limits.

IV. Satellites

A geostationary satellite would make a good transponder platform. Such a platform is easily in the far field of a 64-m-diameter antenna at any foreseeable frequency. Other advantages are the availability of the transponder at any time and good elevation angles. Elevation angles up to about 50 deg are possible, depending on the location of the receiving station and the satellite.

Placing a transponder on the moon is a special case. The geometry is somewhat more complex and is time-dependent. Operation of this transponder will require use of a ranging system similar to that used in the Lunar Laser Ranging Experiment. Accuracies in the region of 40 cm have been achieved at lunar distances.

Cost is an important factor in the utilization of satellites for a transponder platform. Space-qualified components are enormously expensive, in addition to the launching costs. The Space Shuttle may offer a considerable reduction in launch costs.

V. Independent Ranging Systems

The use of a ranging system not employing microwaves appears attractive. The outstanding candidate is the laser ranging system. A system developed for the LAGEOS Program is capable of determining distances to about 200 km with an accuracy of a few centimeters. Such systems are very expensive and complex. They must have an autotracking capability for use with rapidly moving targets such as balloons, aircraft, and nonsynchronous satellites including lunar packages.

A nontracking laser system, the Geodimeter, can determine distances up to 50 km with an accuracy better than 10 cm.

Exotic high-performance pulse radars were not considered for independent ranging systems. Though techniques are available to resolve return echoes to an accuracy of about 30 cm, transmission media effects may preclude the use of pulse radars for the range problem because of frequency commonality.

VI. Summary

Several methods of far-field ranging calibration have been surveyed. All of these approaches have been direct; the placement of the transponder is in the far-field region. All of the transponder platforms are free-moving, requiring a means of accurately determining the range to an accuracy of <0.5 m.

The leading approach at this time seems to be the aircraft but would be usable only at S-band. Satellites, whether geosynchronous or lunar-based, seem to be prohibitively expensive.

Future directions of this study should be towards refining some of the cost performance numbers and investigating alternative approaches such as near-field methods.

N77-19100

Preliminary Demonstration of Precision DSN Clock Synchronization by Radio Interferometry

W. J. Hurd

Communications Systems Research Section

Radio interferometry can be used to measure the offsets between the clocks at the various stations of the DSN, and to monitor the rates of the station frequency standards. A wideband digital data acquisition system has been developed to measure the clock offsets to the 10-ns accuracy required to facilitate three-way spacecraft ranging, to monitor the hydrogen maser frequency standard rates to 1 part in 10^{14} , and to potentially reduce operational costs by replacing the current DSN Operational Time Sync System. Three experiments have been conducted with this system; two short-baseline experiments at Goldstone and one long-baseline experiment between Goldstone and Australia. All achieved subnanosecond resolutions. These accuracies were independently confirmed to within about 3- μ s, as limited by the accuracy of available independent measurements.

I. Introduction

Radio interferometry can be used to monitor the offsets between the clocks and the frequency standards of the DSN stations, as first demonstrated in the DSN by Goldstein (Ref. 1). A wideband digital data acquisition system (WBDAS) which has been developed for this purpose is described here, and the results of three experiments are presented. All three experiments achieved subnanosecond resolutions, with accuracies confirmed to within 3 μ s by independent measurements. The goal of the development effort is to demonstrate the ability to routinely measure the clock offsets to the 10-ns accuracy required for three-way spacecraft ranging, and to

monitor the hydrogen maser frequency standard rates to 1 part in 10^{13} with a few minutes of observing time and to 1 part in 10^{14} over approximately 1 week.

The fundamental process of radio interferometry is the observation of radio emissions from a quasar or other radio energy source simultaneously at two (or more) antenna stations. The difference in the time of arrival of the signal at the stations and the rate of change of the time difference are measured by cross-correlating the noise-corrupted signals at the receiver outputs. The time difference and its rate of change are also calculated from the source observing geometry, and

the differences in the measured and calculated values are attributed to the station clock and clock-rate offsets, plus errors in geometry, etc. Multiple observations of several radio sources can be used to solve for the source positions, the station locations, and Earth's orientation (UT1 and polar motion) (Refs. 2, 3). When these parameters are adequately known a priori, the clock synchronization accuracy which can be achieved in a single measurement is limited primarily by uncertainties in the propagation delays through the transmission media, and is thus comparable to the transmission medium calibration accuracies achieved for spacecraft tracking (see, e.g., Ref. 4).

The data acquisition system also can limit the achievable accuracies. Wide bandwidths are required for accurate time delay estimates, and long time durations are required for accurate frequency offset or "fringe rate" measurements, which are used to estimate the rate of change of time delay. It is desirable to utilize the full available bandwidth of the receiving systems — tens of Megahertz — and to have a time duration of tens to hundreds of seconds per observation. Since the data must be recorded at both stations and then brought together for processing, continuous recording of the full bandwidth would require extremely high recording rates and densities. Fortunately, however, it is not necessary to record the full time-bandwidth space, and various schemes exist for selecting portions of the time-frequency space to be sampled and recorded.

One method for sampling the time-frequency space is called bandwidth synthesis (Refs. 5-8). Two or more narrow bands of the spectrum are sampled and recorded, either sequentially or in parallel, and time delay estimates are constructed from the fringe phase measurements at the various frequency bands. This utilizes the fact that group delay is the derivative of phase delay with respect to frequency. Efficient utilization of the recording medium is achieved. For clock synchronization, however, the method appears to require elaborate phase calibrations of the entire receiving system.

The wideband digital data acquisition system spans the time-frequency domain using the technique of full band sampling with burst recording. The full instantaneous bandwidth of the receivers is sampled, up to a bandwidth of 55 MHz, but not all the data samples are recorded. Short bursts of data samples are stored in a high-speed buffer. Then, when the buffer is full, sampling is inhibited and the buffer is emptied through a small computer onto digital magnetic tape. The full bandwidth and time duration are utilized, but the average data rate is matched to the recording rate by deleting segments of the time domain. Per bit of data, the same time delay resolution is achieved as if the full bandwidth were sampled continuously. This method has been known for some

time (Ref. 5), and has been demonstrated in the DSN with fairly narrow bandwidths, with supporting analysis (Refs. 9-11). The WBDAS implementation has become practical with the improved technology in high-speed analog-to-digital (A-D) conversion, digital filtering, and data storage.

A major advantage to full-bandwidth sampling over bandwidth synthesis is that receiving system phase calibrations are not required, although the actual clock offsets can be separated from the station group delays only if the group delays are calibrated, similarly to the ranging system zero delay system (Ref. 12). Clock rate offsets can be measured without delay calibration, provided only that the delays are stable. Furthermore, three-way ranging, the major navigational method requiring high-resolution clock synchronization, does not require station delays to be separated from the clock offsets, provided that sampling of the ranging and very-long-baseline interferometry (VLBI) data is accomplished at the same point in the system.

Of course, the time-bandwidth space required for an experiment can also be spanned by methods combining bandwidth synthesis and burst storage. This could result in bandwidth synthesis processing, but with frequency bands wider than could be accommodated continuously on the recording medium. The WBDAS is well suited to such applications.

II. WBDAS System Description

A block diagram of the wideband digital data acquisition system is shown in Fig. 1. The signal input to the system, from the radio source, is at IF, either from a Block III receiver 50-MHz IF amplifier, a Block IV receiver 55-MHz IF amplifier, or another receiver with a comparable IF frequency. The signal is digitally demodulated, filtered, sampled and buffered in a digital memory, and then written onto digital magnetic tape through a station computer. The data are later transmitted to JPL over the GCF or by airmail. Using the GCF, clock synchronization could be achieved in near-real time, since less than 10^6 bits are usually required (Refs. 9, 10, 11, 13).

The input signal from the receiver IF amplifier is sampled at the 50- or 55-Ms/s rate by each of two three-bit A-D converters. The A-D conversion times are controlled directly from 50- or 55-MHz reference signals, derived from the station frequency standards, or by dividing the 100-MHz output of a hydrogen maser by 2. The two converters effectively sample 90 deg out of phase, at the sampling frequency. This demodulates the signal to baseband, extracting the quadrature phase components of the "narrowband" process, in a manner similar to the Mu-II ranging system (Ref. 14). The 90-deg phase shift

is actually accomplished by delaying the signal to one converter in a cable of the correct length, which is more stable than delaying a clock signal digitally. The total sampling rate of 100 or 110 Ms/s is sufficient for receiving bandwidths of up to 55 MHz.

The overall phase stability of the input signal paths, the sampling clocks, and the A-D converters have been tested as better than 0.3 deg/°C at 50 MHz, or 20 ps/°C.

Whenever desired, the sampling rate at the input to the digital buffers can be reduced to below the A-D converter sampling rate by digital low-pass filtering of the raw samples with the filter bandwidth controlled by the computer. Specifically, these filters sum N consecutive samples, $1 \leq N \leq 2^{16}$, similar to the operation of an analog integrate-and-dump filter. The bandwidth is reduced to $f_o/(2N)$ and the final sampling rate to f_o/N in each channel, where f_o is the A-D converter sampling rate. Only the sign bits of the filter outputs are used in the final samples, which are stored in the 4096-bit buffer. This is typical of radio interferometers because there is more information per bit in the sign of the number than in the less significant bits.

The data samples are precisely time tagged by a high-resolution clock contained within the data acquisition system. The clock is derived from the same 50- or 55-MHz reference input used by the A-D converters, and is included because no clock of adequate resolution and stability is available from the Frequency and Timing Subsystem (FTS). The clock is initially synchronized to the 1-p/s signal from the FTS, and then allowed to free-run from the IF reference. When the FTS 1 p/s and the IF reference are derived from the same frequency standard, the 1-p/s output of the high-resolution clock should remain in phase with the FTS 1 p/s within the resolution of the FTS pulse. This provides a monitoring capability for both systems. Sometimes the WBDAS frequency reference may not be derived from the station standard, for example, when a hydrogen maser is available but is not operational as the prime station standard. In this case, the WBDAS 1-p/s output and the FTS 1 p/s can be used to monitor the phase and frequency offsets of the two standards.

Not only must the data samples be precisely time tagged, but the exact times at which data sampling is initiated at the two stations must be carefully coordinated, since the buffer can be filled in about 40 μ s at the highest sampling rates. To assure that the same data are sampled at the two stations, the relative time of arrival of the signal at the stations must be predicted to within a few microseconds and sampling initiated at times offset by this amount. This is accomplished by having

each computer predict the geometric time delay from the station to the geocenter, using the station location and the source position of date, and offsetting the sampling time by this amount from the nominal times. The station clock offsets must also be accounted for, and the widest bandwidth should not be used when the uncertainty in the a priori knowledge of clock offset exceeds the normal uncertainty of 2-10 μ s. Precise timing is accomplished by reading the station binary-coded decimal (BCD) clock in the computer and the microsecond clock in the hardware, with sampling initiated at the first tick of the A-D converter clock after the microsecond clock reaches the computer selected count.

Besides the data samples, the hardware transmits some performance monitoring data to the computer, including the microsecond at which the buffer was completely full. This provides a check on the timing and filter bandwidth, and is written onto the digital tape along with other header information.

The experiments to date have utilized the station Telemetry and Command Processor Assembly (TCP) computers, although the hardware and software are also compatible with the Digital Instrumentation Subsystem (DIS) computers. Since some of these computers have tape units which operate at only 79 b/cm (200 b/i), the data recording rate has been limited to about 56 kb/s. The hardware is also completely compatible with the standard DSN minicomputer, since all communication is over the DSN standard interface. It will thus be practical to upgrade the data rate to about 640 kb/s when minicomputers with 630-b/cm (1600-b/i) tape units become operational.

III. Experiment Results

Three experiments have been conducted with the wideband system, two short-baseline experiments at Goldstone and one long-baseline experiment between Goldstone and Australia. The objectives of these experiments were to develop and demonstrate the capability of the combined data acquisition hardware and software, and the processing software. All experiments were successful, and achieved subnanosecond time delay resolutions. This resolution is not to be confused with accuracy, because the station and propagation medium delays were not calibrated, and the source position uncertainties were significant on the long baseline. In all cases, the estimated clock offsets agreed with the standard DSN measurements to within 3 μ s, which is within the accuracies of these measurements and the expected variations in station delays.

All of the experiments were at S-band, using rubidium frequency standards.

A. First Experiment

The first experiment was performed on the short baseline between DSS 11 and DSS 14 at Goldstone on December 14, 1975, in conjunction with an Astronomical Radio Interferometric Earth Surveying (ARIES) experiment. The primary purpose of this experiment was to obtain sufficient data to develop and test the processing program, and to demonstrate that the hardware/software system was operating properly. The RF signal bandwidths were restricted to about 8 MHz by using the telemetry C-channel outputs of the Block III receivers at both stations. The local oscillator references were derived from the rubidium frequency standards by replacing the voltage-controlled oscillator (VCO) output signal with 23.33333333 MHz from Hewlett Packard 5100 frequency synthesizers. No attempts were made to do any station calibrations, except to obtain a priori clock offsets with respect to the DSN master clock, as is routinely done by microwave links.

Successful results were obtained for a total of eight observations, using six different radio sources and digital filter bandwidths of 0.495, 3.34, 5.56, and 10.0 MHz. The estimated offsets between the station clocks are shown for these eight runs in Fig. 2, for the 3 min of data using a digital filter bandwidth of 5.56 MHz. The ordinate scale, $T_{14} - T_{11}$, is the estimated clock reading at DSS 14 minus the reading at DSS 11 made at the same time. The measured clock offsets of about $8.6 \mu\text{s}$ for $T_{14} - T_{11}$ agree to within $1.6 \mu\text{s}$ of the a priori value of $7 \mu\text{s}$ determined from the microwave link measurements, relative to the DSN master clock ($T_{14} - T_{\text{DSN}} = -1 \mu\text{s}$ and $T_{11} - T_{\text{DSN}} = -8 \mu\text{s}$). The error bars indicate the $1-\sigma$ sample deviations, as determined by dividing the 180 s of data into several shorter intervals. The slope of the line fitted to the data was determined from the fringe rate data. This indicates the consistency between the two data types: frequency and time delay.

One result of the first processing of the data from this experiment was to emphasize the need to model the receiving system passbands to get an estimate of the signal cross-correlation function. Although optimum processing requires knowledge of the cross-correlation function, the data were first processed with only the digital filter effects modeled. Failure to model the receiver passbands when the filter bandwidths were comparable to the receiver bandwidths resulted in a detector function which was sometimes bimodal, causing extraneous results and a higher than expected sample deviation. Fitting a single tuned filter model to the data at each station alleviated this problem. A major impact on future experiments was the realization that some data should always be taken at the maximum sampling rate (without digital filtering) in order to facilitate the modeling.

B. Second Experiment

The second short-baseline experiment was performed on June 2, 1976, between DSS 11 and DSS 12, both at Goldstone. The objective of this experiment was to gain experience in using the wideband data acquisition system with several different receiving systems of different bandwidths. A simultaneous experiment was conducted by J. Faselow and J. B. Thomas of the JPL Tracking and Orbit Determination Section, using the 48-kb/s computer-based recording system developed by D. S. Robertson and A. H. Legg of the Weapons Research Establishment, Australia (Ref. 15), and using the technique of bandwidth synthesis (Refs. 5, 6, 7, 8) to achieve wide effective bandwidths.

Three different receiver configurations were used in the June 2 experiments:

- (1) Block III Receiver. This configuration was essentially the same as in the Dec. 14, 1975, experiment, except that the non-AGC'd 50-MHz amplifier outputs were used, whereas the AGC'd TLM-C channel outputs had been used previously. Hewlett-Packard 5100 frequency synthesizers were used in the local oscillator generation as before.
- (2) Wideband. This configuration utilized a pair of wideband open-loop receivers developed for VLBI by the JPL Tracking and Orbit Determination Section. The S-band local oscillator in these receivers is generated by direct multiplication of the 5-MHz frequency standard output.
- (3) 10-MHz Bandwidth. This configuration utilized the wideband receivers, as in (2), but filtered the IF outputs to 50 ± 5 MHz using multiple-pole tuned filters, achieving nearly rectangular passbands.

The passband shapes for the wideband receivers are shown in Fig. 3 and for the Block III receiver in Fig. 4. The curves shown are not measured power spectral densities but are the shapes of multi-pole tuned filter approximations to the passbands. These tuned filter approximations were determined by fitting filter models to the observed autocorrelation functions. The models were used to obtain an approximation to the cross-correlation function of the two receiving systems, which was in turn used by the processing program. The configurations using the 10-MHz filter were modeled as ideal rectangular filters with passbands of 49.826 ± 5.383 MHz at DSS 11, and 49.740 ± 5.474 MHz at DSS 12.

The measured clock offsets for 27 observations of three radio sources were typically $-1.5 \mu\text{s}$ for $T_{12} - T_{11}$, compared to the a priori value of $-4 \mu\text{s}$ determined by the microwave

links. Figure 5 shows the residual clock estimates for all cases, relative to a straight line fit between all cases having the wideband configuration. The system configurations are indicated for each observation, and the error bars are sample standard deviations using all of the data for each observation. The differences in sample standard deviations are primarily due to different source strengths, receiver bandwidths, and digital filter bandwidths. Also, the fourth observation was for only 3 min, due to low source elevation, whereas the others were all for 9 min.

The results are surprisingly consistent from one receiver configuration to another, considering that the different station delays were not calibrated. For the wideband receiver, the results for different filter bandwidths differ by as much as 7 ns. This could be due to differences in average group delays in different portions of the overall system passbands and/or to errors in modeling the cross-correlation function. For the narrower-bandwidth receiver configurations, the variations in time delay estimates with digital filter bandwidth are obscured by the larger sample deviations and by drifts due to the oscillators or temperature changes.

Specific results for the wideband receiver configuration are shown in Fig. 6. The observed time delay resolution ($1-\sigma$ sample deviation) is shown as a function of inverse digital filter bandwidth for three observations of source 3C273. The sample deviations are per 0.75 Mb of data. Assuming the bandwidth to be determined entirely by the digital filter, the theoretical standard deviations of time delay estimate are directly proportional to inverse system bandwidth, so that the points would fall close to the straight line, within experimental error. The results indicate that the receiving system bandwidths have some effect when the 25-MHz digital filters are used, and when there is no filtering. With this strong source, a resolution of 0.8 ns was achieved with only 0.75 Mb of data.

The Block III receiver and the 10-MHz filter configuration realized the time delay resolutions shown in Fig. 7 for various digital filter bandwidths. The resolutions are approximately proportional to inverse digital filter bandwidth, even when the nominal filter bandwidth was 12.5 MHz, which is wider than the receiver bandwidths. This indicates that, for these receiver passbands, best results are obtained when the digital filter bandwidth is somewhat wider than the receiver bandwidths. The sample deviations are better for the 10-MHz filter than for the Block III receiver. For both receiver configurations, resolutions of better than 5 ns were achieved for the normalized data size of 0.75 Mb, which corresponds to subnanosecond resolution for the entire 30 Mb per observation.

C. Long-Baseline Experiment

The first long-baseline experiment was performed on October 14, 1976, using DSS 14 at Goldstone and DSS 43 in Australia. The primary objectives were to demonstrate that the data acquisition system could be installed and operated properly by station personnel, that the system operates properly with Block IV receivers, and that the data acquisition hardware and software and the processing software perform properly for long baselines. These objectives were all achieved with an experiment scheduled for less than 3 h, including the time required to install and remove the data acquisition systems.

Figure 8 shows the modeled signal passbands as observed at the 55-MHz IF amplifier outputs on the Block IV receivers. With proper wideband tuning of the RF maser amplifiers, the passbands at this point in the system should be dominated by the receiver three-pole Chebychev filters with 3-dB bandwidths of ± 18 MHz. This was clearly not the case for this experiment. The passband was especially bad at DSS 14, where it was necessary to use a traveling wave maser having a narrower bandwidth than is usually available.

Five successful 9-min observations were made, each using three different digital filter bandwidths: 5 MHz, 27.5 MHz, and unfiltered. The clock offset estimates for the five observations, one of CTA 26 and four of NRAO190, are shown in Fig. 9 for the 27.5-MHz and the unfiltered configurations. The clock offset estimates are in the range of $T_{43} - T_{14} = 0.64$ to $0.71 \mu\text{s}$, which is within $3 \mu\text{s}$ of the a priori offset determined from the microwave link estimate of $T_{14} - T_{\text{DSN}} = -4 \mu\text{s}$, and the estimate of $T_{43} - T_{\text{DSN}} = -2 \mu\text{s}$ from the DSN operational time sync system, using the moon bounce technique. The discrepancy of less than $3 \mu\text{s}$ is within the approximate $5\text{-}\mu\text{s}$ accuracy of the moon bounce system (Refs. 16, 17).

The slopes of the clock offset estimates versus time in Fig. 9 were determined from the fringe frequency estimates. For the four observations of NRAO190, the slopes are in good agreement with the changes in clock offset estimates with time. Changes both in the slopes and in the clock offset estimates, and the differences between the two sources, can be attributed to various effects, including oscillator offsets and instabilities, source position errors, propagation medium delays, and uncertainty in UT1. The assumed source positions of date were RA = 70.021958 deg, dec = -0.388889 deg for NRAO190, and RA = 54.245708 deg, dec = -1.937944 deg for CTA 26. These could be in error either due to the catalog position used or to inaccuracies in the precession program. The assumed value for UT1-UTC was -92.2 ms.

Sample standard deviations of clock offset estimate were determined for all cases by dividing the data into 18 independent 10-s intervals. Normalized to 10^6 bits, the 10-MHz, 27.5-MHz, and unfiltered cases achieved sample deviations of 5.37, 1.41, and 1.33 ns for CTA 26, and 12.68, 2.67, and 2.24 ns for NRAO190. The deviations improved almost as inverse bandwidth as the digital filter was widened from 5 to 27.5 MHz, but there was little improvement from 27.5 MHz to the unfiltered cases. This seems to be in line with the passband shape at DSS 14, which is about 22 MHz wide at

the 6-dB points. It would not have been surprising if the deviations had been higher for the unfiltered cases than for the 27.5-MHz filter. When the full 36-MHz bandwidth of the Block IV 55-MHz output is realized, the unfiltered case will certainly be best.

The overall resolution for each observation was better than 1 ns for both the 27.5-MHz and the unfiltered cases, with a total of about 10^7 bits of data.

Acknowledgements

The author acknowledges the contributions of many persons to the success of this project, including J. L. Fanelow, L. Skjerve, D. J. Spitzmesser, J. B. Thomas, and J. G. Williams for assistance with general and specific information on VLBI and in conducting experiments, B. Bronwein, W. P. Hubbard, and J. W. Layland for assistance in hardware design and construction; W. A. Lushbaugh for development of the DSN Standard Interface Adaptor for the XDS 900 series computers; and the Cognizant Operations Engineers, Cognizant Sustaining Engineers, and station personnel without whose cooperation successful experiments would have been impossible.

References

1. Goldstein, R., "Clock Calibration via Quasar," in the *Space Programs Summary 34-48*, Vol. II, pp. 79-82, Jet Propulsion Laboratory, Pasadena, Calif., November 30, 1967.
2. Williams, J. G., "Very Long Baseline Interferometry and Its Sensitivity to Geophysical and Astronomical Effects," in the *Space Programs Summary 37-62*, Vol. II, pp. 49-55, Jet Propulsion Laboratory, Pasadena, Calif., March 31, 1970.
3. Melbourne, W. G., et al., *Constants and Information for Astrodynamical Calculations*, Technical Report 32-1306, Jet Propulsion Laboratory, Pasadena, Calif., November 5, 1968.
4. Madrid, G. A., et al., *Tracking System Analytic Calibration Activities for the Mariner Mars 1971 Mission*, Technical Report 32-1587, Jet Propulsion Laboratory, Pasadena, Calif., March 1, 1974.
5. Rogers, A. E. E., "Very Long Baseline Interferometry with Large Effective Bandwidth for Phase-Delay Measurements," *Radio Science*, Vol. 5, No. 10, pp. 1239-1247, October 1970.

6. Thomas, J. B., "An Analysis of Long Baseline Radio Interferometry," in *The Deep Space Network Progress Report*, Technical Report 32-1526, Vol. VII, p. 37, Jet Propulsion Laboratory, Pasadena, Calif., February 1972.
7. Thomas, J. B., "An Analysis of Long Baseline Radio Interferometry, Part II," in *The Deep Space Network Progress Report*, Technical Report 32-1526, Vol. VIII, p. 29, Jet Propulsion Laboratory, Pasadena, Calif., May 1972.
8. Thomas, J. B., "An Analysis of Long Baseline Radio Interferometry, Part III," in *The Deep Space Network Progress Report*, Technical Report 32-1526, Vol. XVI, p. 47, Jet Propulsion Laboratory, Pasadena, Calif., August 15, 1973.
9. Hurd, W. J., "DSN Station Clock Synchronization by Maximum Likelihood VLBI," in *The Deep Space Network Progress Report*, Technical Report 32-1526, Vol. X, pp. 82-95, Jet Propulsion Laboratory, Pasadena, Calif., August 15, 1972.
10. Hurd, W. J., "A Demonstration of DSN Clock Synchronization by VLBI," in *The Deep Space Network Progress Report*, Technical Report 32-1526, Vol. XII, pp. 149-160, Jet Propulsion Laboratory, Pasadena, Calif., December 15, 1972.
11. Hurd, W. J., "An Analysis and Demonstration of Clock Synchronization by VLBI," *IEEE Transactions on Instrumentation and Measurement*, Vol. IM-23, No. 1, pp. 80-89, March 1974.
12. Otoshi, T. Y., ed., *A Collection of Articles on S/X-Band Experiment Zero Delay Ranging Tests*, Technical Memorandum 33-747, Vol. I, Jet Propulsion Laboratory, Pasadena, Calif., November 1, 1975.
13. Layland, J. W., "Threshold Analysis for VLBI Delay and Doppler," in *The Deep Space Network Progress Report*, Technical Report 42-31, pp. 67-74, Jet Propulsion Laboratory, Pasadena, Calif., February 15, 1976.
14. Martin, W. L., Zygielbaum, A. I., *Mu-II Ranging*, Technical Memorandum 33-768, Jet Propulsion Laboratory, Pasadena, Calif. (in press).
15. Thomas, J. B., et al., "Radio Interferometry Measurements of a 16 km Baseline with 4 cm Precision," in *The Deep Space Network Progress Report*, Technical Report 32-1526, Vol. XIX, pp. 36-54, Jet Propulsion Laboratory, Pasadena, Calif., February 15, 1974.
16. Smith, J. R., and W. S. Baumgartner, "Precision Time Synchronization Equipment," in the *Space Programs Summary 37-47*, Vol. II, pp. 90-92, Jet Propulsion Laboratory, Pasadena, Calif., September 30, 1967.
17. Ward, S. C., "Moon Bounce Time Synchronization," in *Time and Frequency Theory and Fundamentals*, ed. by B. E. Blair, NBS Monograph 140, May 1974, pp. 286-287.

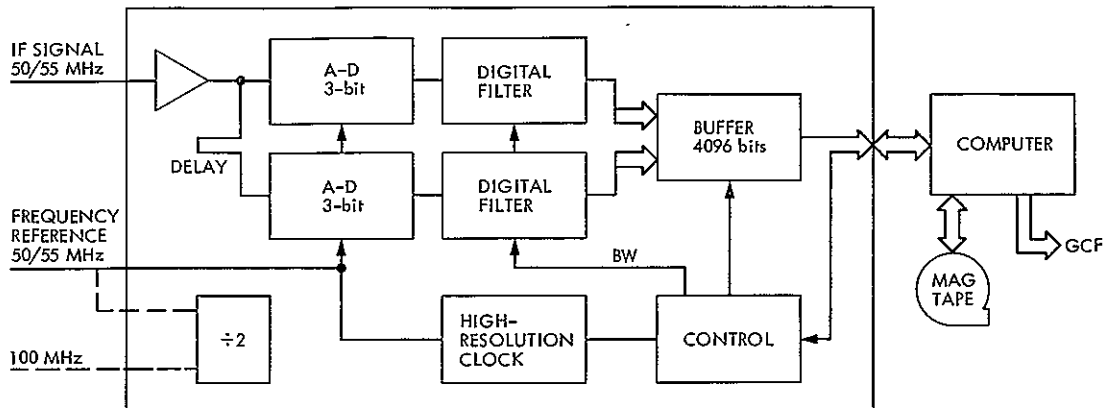


Fig. 1. Wideband digital data acquisition system block diagram

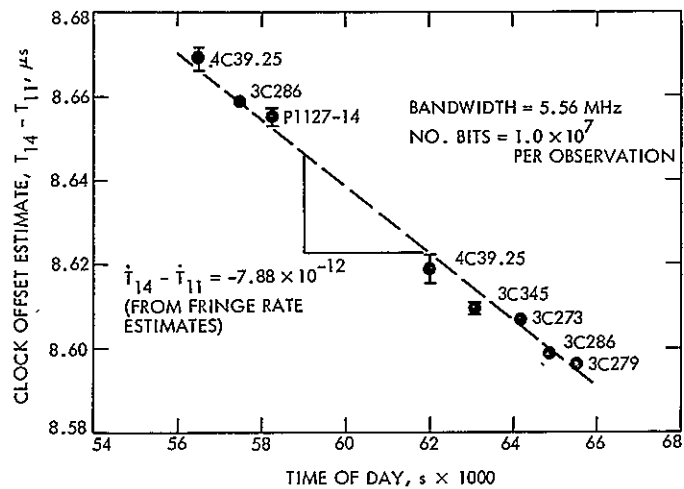


Fig. 2. Clock offset estimates for Dec. 14, 1975, with 1- σ sample deviations

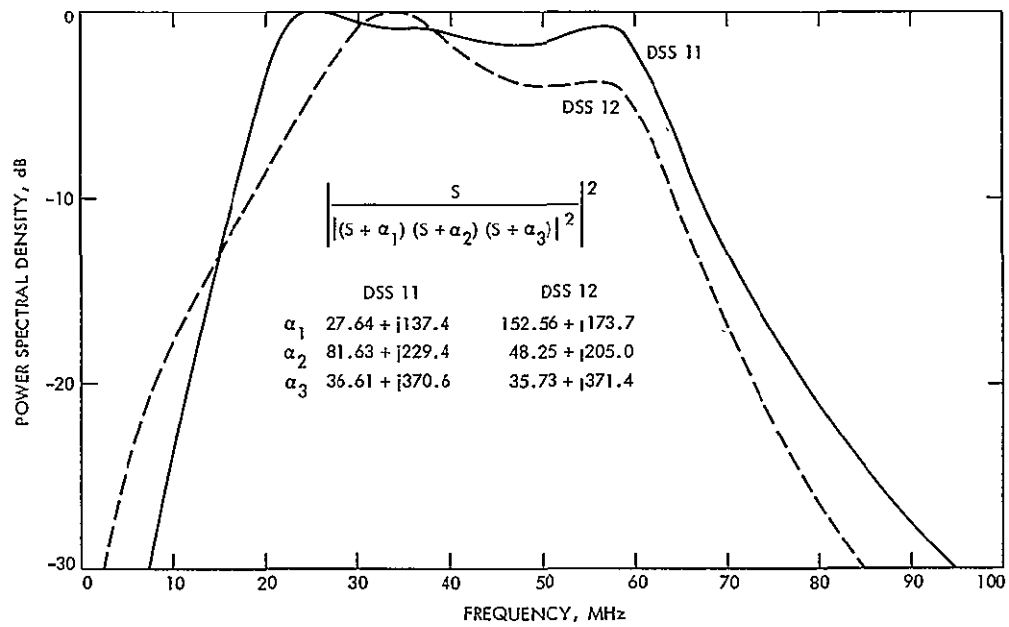


Fig. 3. Modeled receiver passbands, wideband receiver (June 2, 1976)

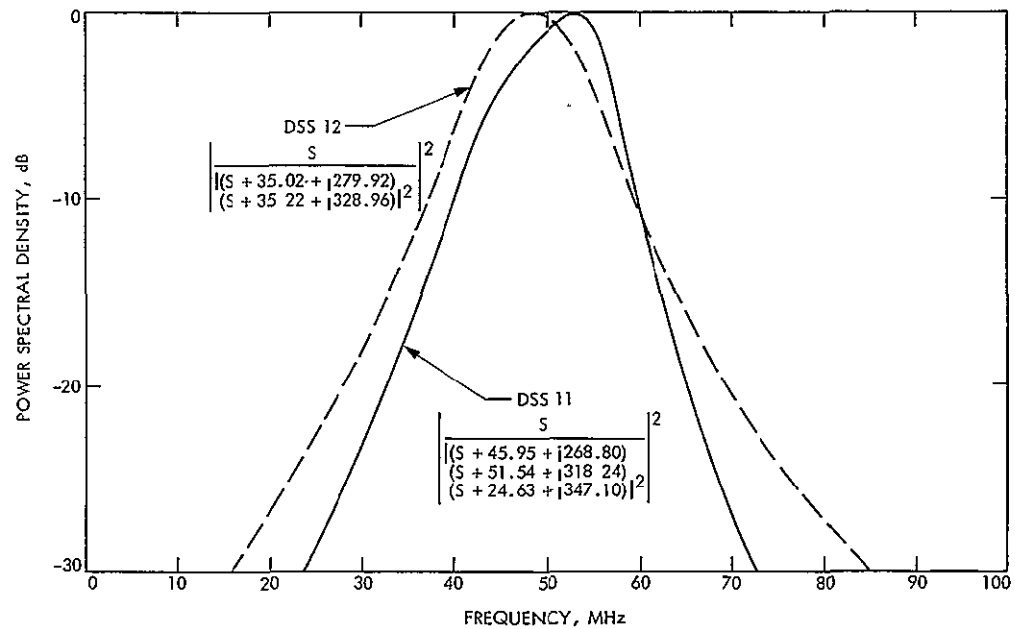


Fig. 4. Modeled receiver passbands, Block III receivers (June 2, 1976)

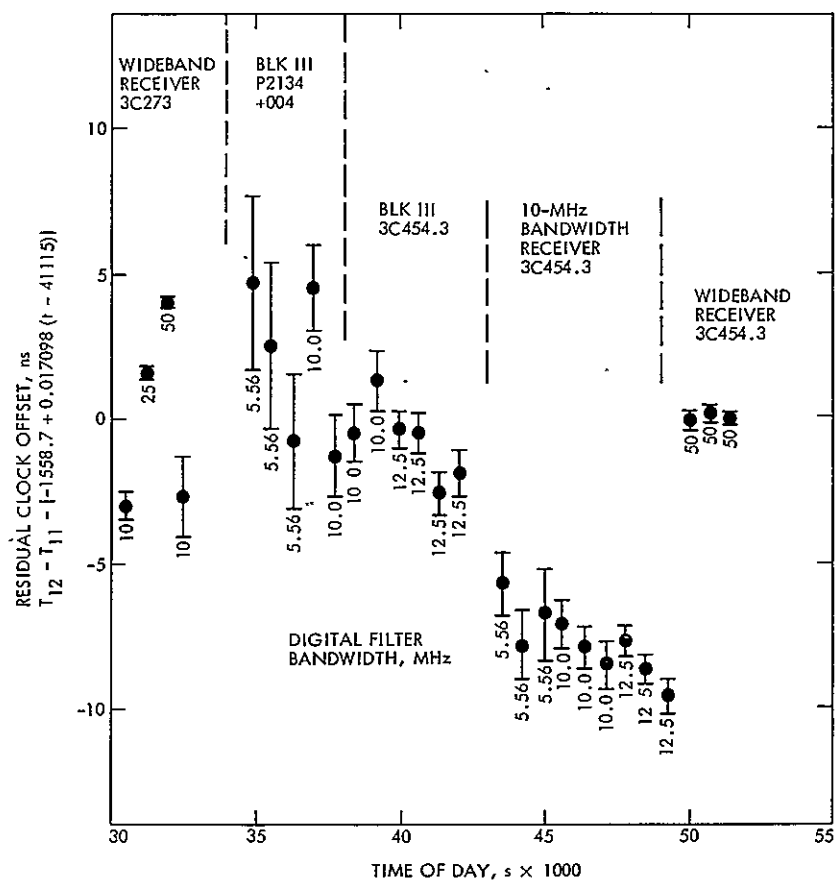


Fig. 5. Residual clock offset estimates for June 2, 1976

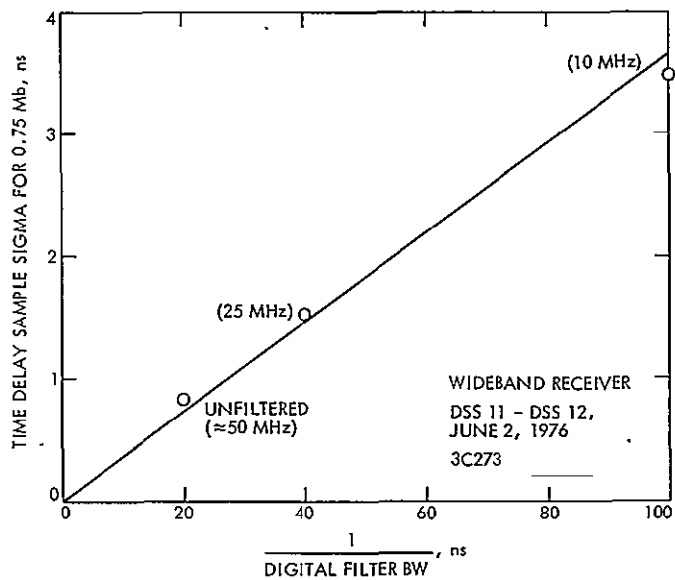


Fig. 6. Time delay resolution vs. bandwidth, wideband receiver

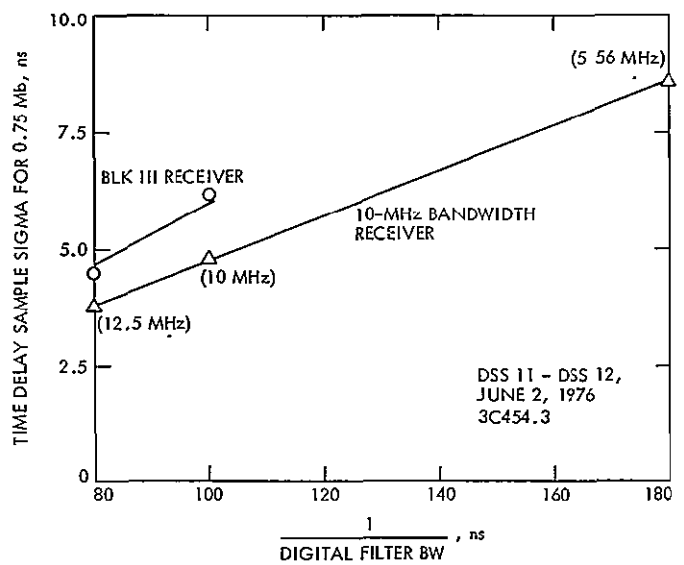


Fig. 7. Time delay resolution vs. bandwidth, Block III receivers

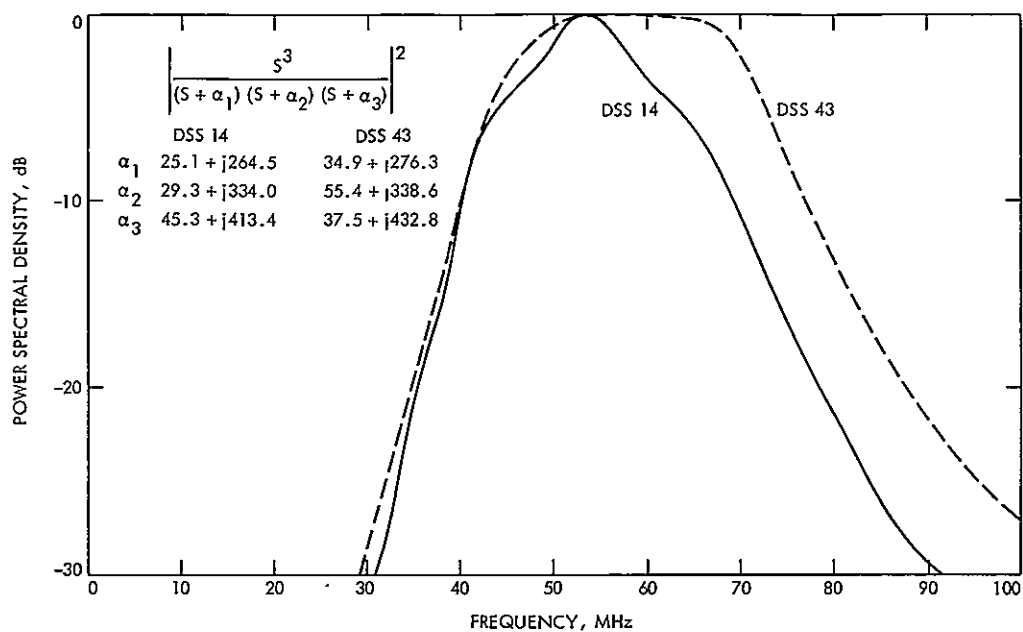


Fig. 8. Modeled receiver passbands, Block IV receivers (Oct. 14, 1976)

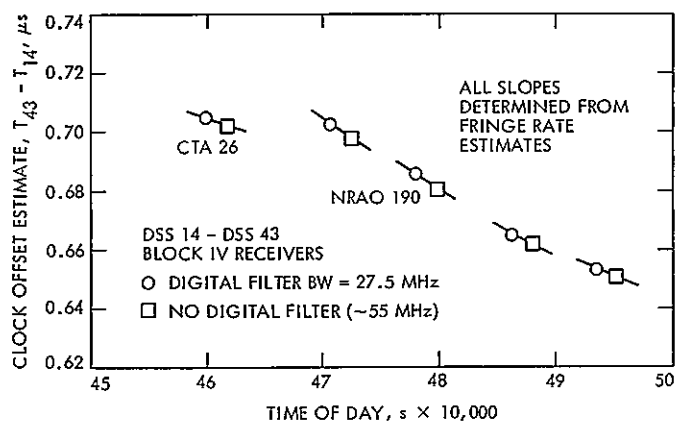


Fig. 9. Clock offset estimates for Oct. 14, 1976

N77-19101

Radio Frequency Interference from Near-Earth Satellites

B. K. Levitt and J. R. Lesh

Communications Systems Research Section

In the near future, radio frequency interference (RFI) from a growing number of Earth-orbiting satellites may seriously degrade deep space telemetry reception. This article develops a pessimistic statistical model for predicting the extent of this interference. Based on the assumptions underlying the model, DSN S-band operations can expect one RFI interruption every 4.1 days, with the average incident lasting 24 s. This implies that 52 or more such satellites, with uncorrelated orbital trajectories, will cause in excess of 5 min of RFI per day at a DSN station (the maximum level recommended by the Consultative Committee for International Radio).

I. Introduction

Over the past 2 years, DSN operators at Goldstone, California, have logged a combined average of nearly 10 min of radio frequency interference (RFI) per day, 25 percent of which resulted in complete outages (see Fig. 1). Much of this RFI was in fact traced to ground-based and airborne sources; however, over the next decade, we can anticipate a significant RFI problem due to the ever-increasing number of Earth-orbiting satellites, whose transmissions are crowded into a limited frequency band. The RFI problem is being carefully assessed since a telemetry outage during a critical phase of a deep space mission could be disastrous (e.g., during the 2-hour lifetimes of the 1978 Pioneer Venus atmospheric probes).

From the DSN viewpoint, part of the problem is that the International Telecommunications Union (ITU) has decreed

that the frequency bands used for deep space telemetry must be shared with the much higher-powered transmissions of near-Earth satellites. For example, the Tracking and Data Relay Satellite System (TDRSS, 1979 launch date) will have multiple-access, spread-spectrum operations centered at 2287.5 MHz (DSN S-band downlink telemetry uses the 2290- to 2300-MHz band); and the Geodetic Earth-Orbiting Satellite (GEOS, 1977 launch date) downlink carrier frequency is 2299.5 MHz. In addition, because of significant sidelobe gains, a DSN antenna need not be pointing directly at an Earth-orbiting satellite to experience RFI from it.

This article represents an initial attempt to project the extent of the RFI problem due to near-Earth satellites. In particular, several simplifying assumptions are made leading to the development of a pessimistic statistical model, which may

be used to compute the average cumulative RFI experienced by a DSN station, the average duration of an RFI incident, and the average time between incidents, per interfering satellite. To complete the projection of the RFI problem over the near future, this model should be combined with trend data on the number of Earth-orbiting satellites within and near each of the DSN receive bands expected over this period. (The Electromagnetic Capability Analysis Center is currently gathering this information under a contract with JPL.) Furthermore, with the acquisition of more detailed data, such as distributions of satellite altitudes and transmitted power flux density levels, some of the simplifying assumptions underlying the model could be refined, resulting in a more accurate assessment of the RFI problem.

II. Analysis at S-Band

As shown in Fig. 2, consider the situation in which a DSN receiver is experiencing white noise-like (spectrally flat) in-band RFI from an Earth-orbiting satellite at an angle ϕ (deg) off the antenna boresight. Then

$$PSD = PFD + G + 10 \log_{10} \left(\frac{\lambda^2}{4\pi} \right) \quad (1)$$

where PSD (dBW/Hz) is the received power spectral density, PFD (dBW/m²/Hz) is the received power flux density, G (dBi) is the receive antenna gain, and λ (m) is the wavelength to which the receiver is tuned. For DSN downlink operations at S-band (2295 MHz),

$$10 \log_{10} \left(\frac{\lambda^2}{4\pi} \right) = -28.67 \quad (2)$$

The 64- and 26-m DSN antenna sidelobe power gain envelopes are well approximated by

$$G = 32 - 25 \log_{10} \phi; 1 \leq \phi \leq 48 \quad (3)$$

Finally, the Consultative Committee for International Radio (CCIR) Recommendation 365-2 states that the interference PSD from a single RFI source, measured at the input to a DSN receiver, shall not exceed -220 dBW/Hz¹ for more

¹The conversion formula from PSD to noise temperature T (K) is $T = (1/k)10^{PSD/10}$ where $k = 1.38 \times 10^{-23}$ W/Hz/K is Boltzmann's constant. So -220 dBW/Hz is equivalent to 7.25 K; as an example, this results in a 1.7-dB degradation in signal-to-noise ratio for a 15 K receiver.

than 5 min/day. From Eqs. (1-3), we conclude that PSD exceeds the CCIR recommended level whenever ϕ satisfies the constraint

$$25 \log_{10} \phi \leq PFD + 223.33 \quad (4)$$

We shall say that a DSN receiver is experiencing RFI from an S-band satellite transmission whenever Eq. (4) is satisfied.

We need to make some assumptions about PFD . Under Article 7 of the ITU Radio Regulations, the radio emissions from an Earth-orbiting satellite, incident on Earth's surface at an angle α (deg) above the horizon, must satisfy the restriction

$$PFD \leq \begin{cases} -190, 0 \leq \alpha \leq 5 \\ -190 + \frac{1}{2}(\alpha - 5); 5 \leq \alpha \leq 25 \\ -180; 25 \leq \alpha \leq 90 \end{cases} \quad (5)$$

We will assume that the center frequency of the interfering satellite telemetry is adjacent to the 2290- to 2300-MHz band, such that the RFI experienced by the DSN receiver is due to sidebands suppressed at least 20 dB below the maximum permissible levels of Eq. (5). Adopting a pessimistic approach, we therefore assume that the received S-band RFI from a given satellite has a PFD of -200 dBW/m²/Hz, independent of the satellite location and transmitting antenna direction. Then Eq. (4) implies that a DSN receiver experiences RFI from an S-band satellite transmission whenever $\phi \leq \phi_0 \equiv 8.57$ deg.

A. Average Cumulative RFI

In the absence of any specific satellite trajectory data, we will simplify the model by assuming that an interfering satellite is in a circular Earth orbit of radius r_s , and that its instantaneous location is uniformly distributed over the sphere of that radius. As a further simplification, we assume that the DSN receiving antenna is pointing vertically; therefore, the receiver experiences RFI whenever the satellite falls within the spherical cap shown in Fig. 3. (Note that a nonvertical antenna boresight direction would yield an RFI cap of greater area and proportionally larger average cumulative RFI.)

The angle ϕ_0 subtended by the RFI cap at the DSN station translates to an angle θ at the center of the Earth:

$$\theta = \sin^{-1} \left[\left(\sqrt{1 - \gamma^2 \sin^2 \phi_0} - \gamma \cos \phi_0 \right) \sin \phi_0 \right] \quad (6)$$

where $\gamma \equiv r_E/r_S$ and r_E is the radius of the Earth. The area of the cap is then $2\pi r_S^2(1 - \cos \theta)$, and the instantaneous probability of RFI occurring is the ratio of this area to that of the entire satellite orbital sphere, $\frac{1}{2}(1 - \cos \theta)$. Equating ensemble and time averages, the long-term average cumulative RFI from a single satellite at altitude $(r_S - r_E)$ is 43200 $(1 - \cos \theta)$ s/day. This expression is plotted in Fig. 4 for $\phi_0 = 8.57$ deg and $r_E = 6357$ km (polar radius of the Earth).

Based on a 1971 listing (Ref. 1) of 17 then-current and proposed nonsynchronous Earth-orbiting satellites, a histogram of their altitudes was extracted (see Fig. 5).² For our model, we approximate this distribution by a uniform one between 300 and 1200 km. Integrating over this simplified altitude distribution, we find that average cumulative RFI

$$= \frac{43200}{900} \int_{r_E+300}^{r_E+1200} dr_S [1 - \cos \theta(r_S)] \quad (7)$$

$$= 5.86 \text{ s/day/satellite}$$

Using a Union bound argument, N such satellites with independent orbital trajectories would produce an average of $5.86N$ s/day of RFI at a DSN station. Consequently, if $N \geq 52$, the combined average RFI at S-band exceeds the CCIR recommended level of 5 min/day.

B. Average Duration of an RFI Incident

Using simple physical arguments, a satellite in a circular Earth orbit of radius r_S (km) has a tangential velocity v (km/s) given by

$$v = 631.3/\sqrt{r_S} \quad (8)$$

From Fig. 3, if the satellite crosses the center of the RFI cap, the DSN receiver will experience t_{\max} seconds of continuous RFI (plotted in Fig. 6), given by

$$t_{\max} = \frac{2\theta}{v/r_S} = \frac{\theta r_S^{3/2}}{315.7} \quad (9)$$

where θ is in rad. However, in general, an RFI incident occurs when the satellite crosses the RFI cap off-center; so Eq. (9) is an upper bound for the duration of the incident.

²For satellites with noncircular orbits, the altitude was assumed to be uniformly distributed between the apogee and perigee.

To analyze the general case, fit Fig. 3 to a Cartesian coordinate system centered at Earth's center, such that the antenna boresight is along the z -axis. As shown in Fig. 7, the boundary of the RFI cap is specified by

$$x^2 + y^2 = r_S^2 \sin^2 \theta$$

$$z = r_S \cos \theta \quad (10)$$

Now construct a new Cartesian coordinate system by rotating the x - and z -axes an angle β about the y -axis. Without loss of generality, assume the satellite trajectory is in the $y'z'$ -plane, and is given by

$$x' = 0$$

$$(y')^2 + (z')^2 = r_S^2 \quad (11)$$

But

$$x = x' \cos \beta + z' \sin \beta$$

$$z = -x' \sin \beta + z' \cos \beta \quad (12)$$

Using Eq. (12) to specify the equation of the RFI cap boundary of Eq. (10) in the $x'y'z'$ coordinate system, we have, in part

$$x' \sin \beta = z' \cos \beta - r_S \cos \theta. \quad (13)$$

The intersection points of the RFI cap boundary and the satellite trajectory lie in the $y'z'$ -plane: setting $x' = 0$ in Eq. (13) yields

$$z' = \frac{r_S \cos \theta}{\cos \beta} = r_S \cos \xi$$

$$\Downarrow$$

$$\xi \equiv \cos^{-1} \left(\frac{\cos \theta}{\cos \beta} \right) \leq \theta \quad (14)$$

For fixed β , the transit time $t(\beta)$ (s) of the satellite through the RFI cap is

$$t(\beta) = \frac{2\xi}{v/r_s} = \frac{r_s^{3/2} \cos^{-1} \left(\frac{\cos \theta}{\cos \beta} \right)}{315.7} \quad (15)$$

per crossing.

In general, we assume that β is uniformly distributed over $(0, \pi/2)$. So for fixed r_s , the average duration t_{avg} (s) of a single RFI incident, conditioned on its occurrence, is given by

$$t_{\text{avg}} = \frac{1}{\theta} \int_0^\theta d\beta t(\beta) = \frac{r_s^{3/2} f(\theta)}{315.7} \quad (16)$$

where

$$f(\theta) \equiv \int_0^1 dx \cos^{-1} \left(\frac{\cos \theta}{\cos x\theta} \right) \leq \theta \quad (17)$$

It has been determined that for $0 \leq \theta \leq \pi/2$, $f(\theta)$ is accurately approximated by

$$f(\theta) \cong 0.789 \theta + 0.0423 \theta^4 \quad (18)$$

where θ is in rad. Combining Eqs. (6), (16), and (18), t_{avg} was computed as a function of satellite altitude (see Fig. 6). If we further average over the uniform satellite altitude distribution of Fig. 5, we find that the altitude-independent average S-band RFI duration is 23.95 s. Combined with the result of the previous section for N interfering satellites, this implies that the average time between RFI incidents is $23.95/5.86/N = 4.09/N$ days at S-band.

III. Comparison of RFI at S- and X-Bands

DSN X-band downlink operations use the 8400- to 8500-MHz band. Extending the RFI model derived above to a DSN receiver tuned to 8450 MHz yields the following N satellite comparison between the two deep space bands.

RFI parameter	S-band	X-band
ϕ_0 , deg	8.57	3.02
cumulative average, s/day	5.86 N	0.720 N
5 min/day	$N \geq 52$	$N \geq 417$
average incident duration, s	23.95	8.40
average time between incidents, days	4.09/ N	11.67/ N

IV. Review of RFI Model Assumptions

- (1) Telemetry from an Earth-orbiting satellite has a center frequency adjacent to the DSN receive band of interest, and in-band RFI is caused by spectrally flat sidebands of the satellite telemetry, suppressed 20 dB below the maximum PFD permitted under ITU regulations ($PFD = -200$ dBW/m²/Hz).
- (2) The satellite signals cause RFI in the DSN receiver whenever $PSD > -220$ dBW/Hz.
- (3) The 64- and 26-m DSN receive antenna sidelobe gains are specified by $G = 32 - 25 \log_{10} \phi$, for satellite-to-ground antenna boresight angle ϕ (deg).
- (4) The interfering satellites are in uncorrelated circular orbits, and their instantaneous locations are uniformly distributed above the Earth's surface.
- (5) The satellite altitudes are uniformly distributed between 300 and 1200 km.
- (6) The DSN antenna is pointing vertically.

V. Conclusions

Considering how rapidly the number of Earth-orbiting satellites is increasing, and the sharing of crowded frequency bands by deep space and near-Earth satellite telemetry, the model demonstrates that the DSN could experience a significant amount of RFI outages over the next decade, particularly at S-band. The model involves several simplifying assumptions, however, which should be replaced by statistical

distributions based on available trend data to make it more meaningful (this applies in particular to Assumptions 1, 4, 5, and 6 in the previous section). To control the RFI problem, and to minimize the possibility of an outage during a critical mission phase, some countermeasures are needed, such as:

(1) Frequency coordination procedures

(2) RFI monitoring equipment

(3) Frequency diversity techniques

(4) Sophisticated coding and modulation schemes to prevent mutual RFI between cooperating satellites.

Reference

1. Sudhoff, R. I., *Deep Space Research Band Occupancy — A Data Base and Analysis*, Rpt. #IITRI-E6203-F, IIT Research Institute, Aug. 3, 1971.

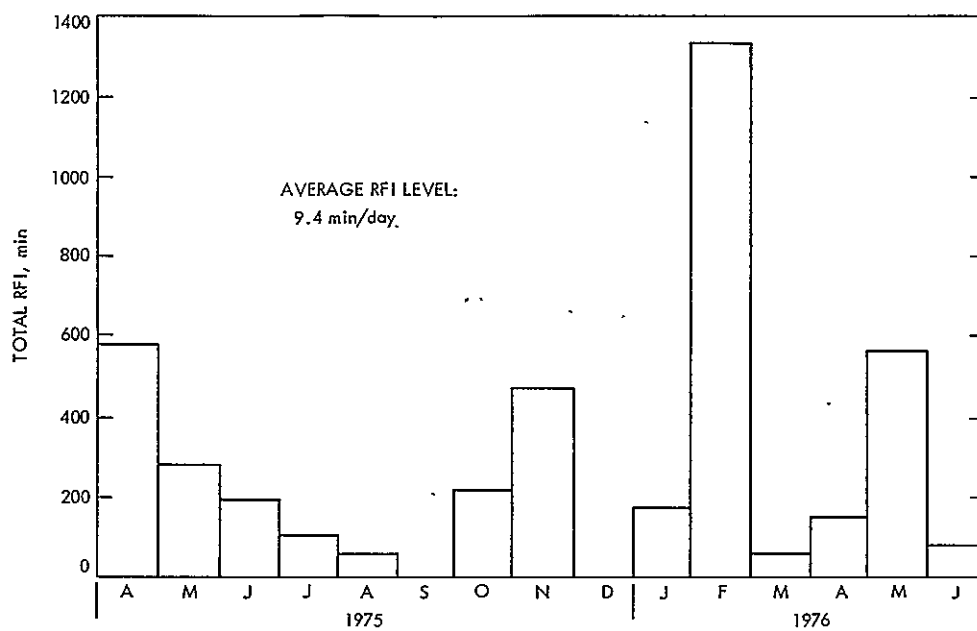


Fig. 1. History of recorded S-band RFI incidents at Goldstone DSN station

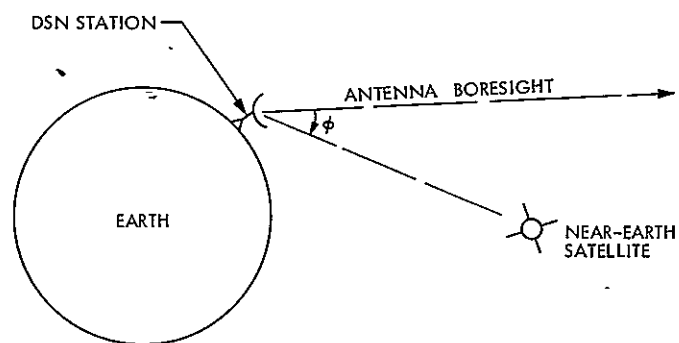


Fig. 2. Gross RFI geometry

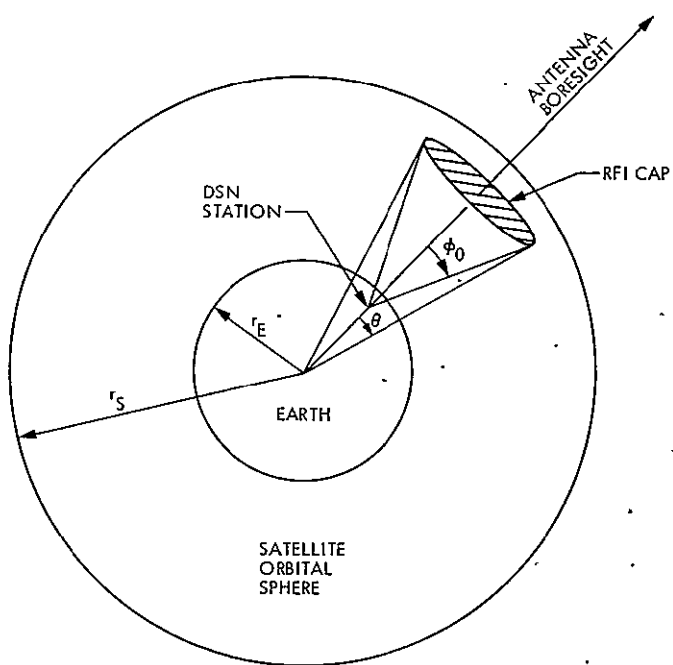


Fig. 3. Detailed RFI geometry for calculation of average cumulative RFI

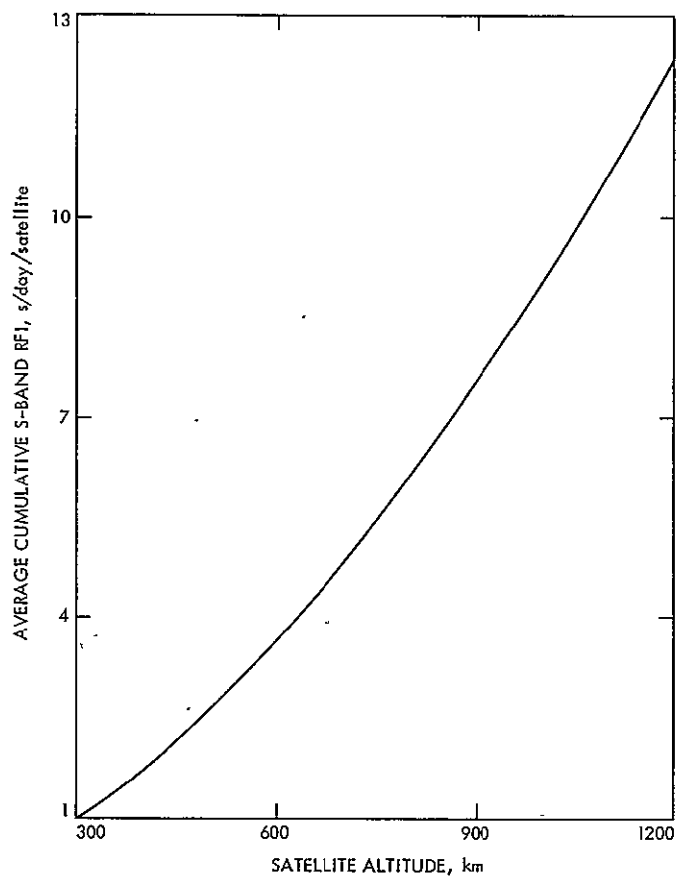


Fig. 4. Variation of amount of S-band radio frequency interference with altitude of interfering satellite

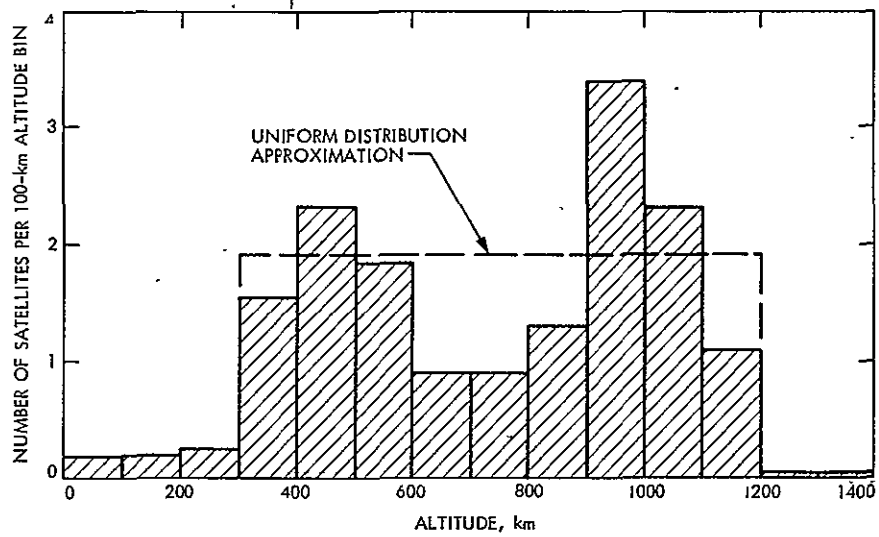


Fig. 5. Histogram of nonsynchronous, Earth-orbiting satellite altitudes (17 satellites)

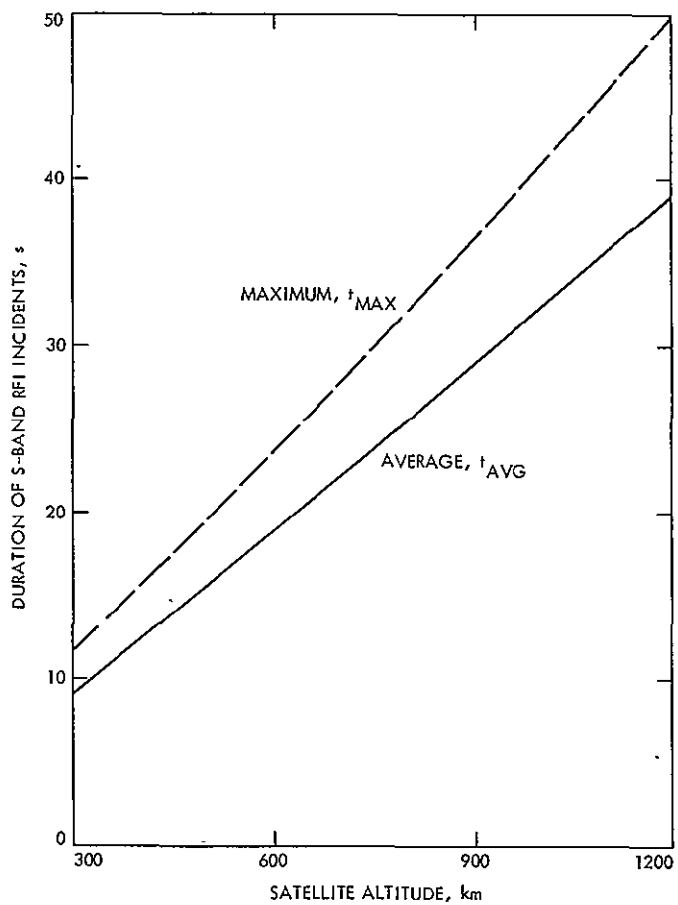


Fig. 6. Variation of average and maximum duration of S-band radio frequency interference incidents with altitude of interfering satellite

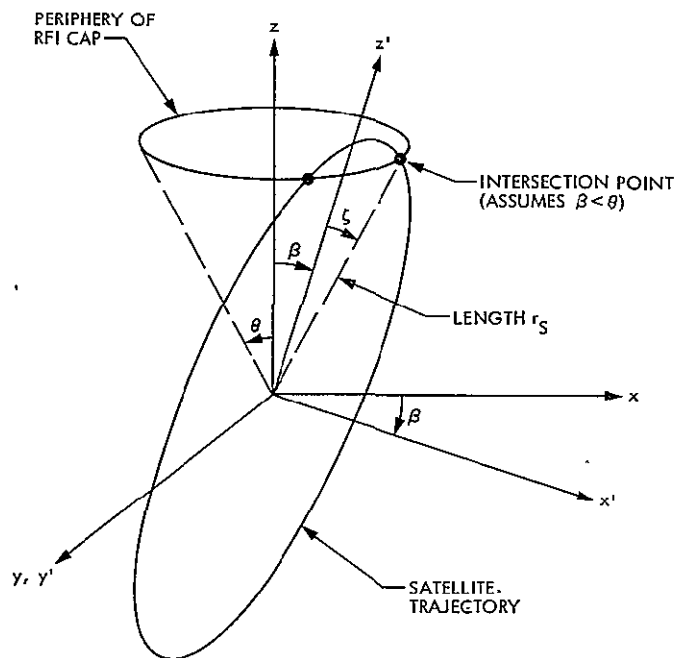


Fig. 7. Detailed RFI geometry for calculation of average RFI duration

N77-19102

Low-Noise Receivers: Microwave Maser Development

R. Quinn and E. Wiebe

Radio Frequency and Microwave Subsystems Section

An S-Band traveling-wave maser with a 2260- to 2400-MHz tuning capability has been built and installed on the 26-m antenna at the Venus Station of the Goldstone Deep Space Communications Complex. The Traveling-Wave Maser/Closed Cycle Refrigerator package was assembled within a limited time schedule and at low cost to meet the requirements of the Very Long Baseline Interferometry Validation Task. The maser uses a superconducting magnet with a field staggering coil for gain/bandwidth adjustment. The maser pump source is a Gunn effect oscillator with the capability of continuous tuning throughout the entire maser tuning range. The package was assembled from surplus components that have been used previously in the Deep Space Network in a variety of applications since 1967.

I. Introduction

The Traveling-Wave Maser (TWM) requirements for the Very Long Baseline Interferometry (VLBI) Validation Task include operation at a bandwidth of 40 MHz centered at 2290 MHz, with phase and group delay stability such that the VLBI measurement precision will not be degraded. Operation at 2388 MHz is required for planetary radar. Because the Venus Station (DSS 13) TWM did not meet the bandwidth requirement, a new package was assembled with previously used components and delivered at a procurement cost of \$5300 and a 4-man-month labor effort.

II. Closed Cycle Refrigerator History

The Closed Cycle Refrigerator (CCR) is one of the early Block III prototype refrigerators which are now in use throughout the DSN. This particular CCR was built in January 1967 and installed at DSS 13 in March 1967. During 1973 the TWM/CCR was returned to JPL for modifications which

included the installation of a cooled and shortened input transmission line and a superconducting magnet (Ref. 1). The system was then delivered to DSS 43 (Australia) to meet the special sensitivity and stability requirements of the Mariner Venus-Mercury missions (MVM'73). The refrigerator was used for MVM'73, in spite of its age, due to budgetary and schedule constraints.

Following the MVM'73 missions, the maser was returned to JPL to determine the cause of a refrigerator failure that occurred during the third Mariner Mercury encounter. By this time, the CCR had accumulated 60,000 h of run time. Cylinder wear in the region of the cryogenic seal on the #2 displacer had reached 0.38 mm. This wear results in ring leakage, which is aggravated by restriction in the regenerator pack. Replacement of the worn cylinder assembly and installation of new seals restored sufficient cooling capability to achieve maser operation. The reserve refrigeration capacity, however, was low and erratic. The use of a reserve capacity monitor was indispensable in this determination (Ref. 2).

Failure to achieve stable refrigeration capability has occurred on several occasions, both in the laboratory and in the field, as a direct result of drive unit replacement. It is believed that operation of a displacer assembly with a cryogenic seal in a badly worn cylinder can result in leakage when the edges of the seal contact the ridges at the ends of the cylinder wear. The leakage reduces regenerator efficiency. In some cases, excessive regenerator restriction has been noted. Such restriction increases the pressure differential across the seal and results in additional leakage and inefficiency.

To restore the refrigerator to "like new" condition, the following major repairs were effected: (1) The weld holding the cylinder was cut, the heat stations were unsoldered, and the worn cylinder was replaced. (2) The displacer and drive unit assembly were overhauled (all seals and worn parts were replaced). (3) The lead sphere regenerator pack in the second stage displacer was replaced, and the bronze screen pack in the first stage displacer was flushed with freon 11 to remove accumulated lead dust. (4) Both charcoal traps in the J-T circuit were cut out and replaced.

Following reassembly, a complete checkout of the CCR was made, and normal refrigeration capacity was achieved.

The cylinder and charcoal trap replacement is not currently within the scope of normal field maintenance. It is expected that the above-described rebuilding procedure can be used at the DSN Maintenance Depot to extend the life of worn CCRs at a small fraction of the CCR replacement cost.

III. Maser and Superconducting Magnet Assembly Modifications

The TWM used for this system (a tunable R&D type) was originally built in 1967 and used in the ultracone at DSS 14 (Ref. 3). It was returned to JPL in 1974. During inspection of the maser, several of the single crystal YIG disks on the isolator strips were found to be loose. Improved cutting and gluing techniques were used to fabricate new isolator strips. The TWM input coaxial line was modified to permit its use with the cooled and shortened input transmission line.

The comb structure body was machined to provide a mounting location for a magnetic field staggering coil. The field staggering coil covers half the maser's amplifying length and is used to increase maser bandwidth. The best gain/bandwidth tradeoff was achieved by using a current in opposition to that of the superconducting magnet, subjecting half the maser to an adjustable bucking field. This serves to magnetically separate the maser into two halves in much the same manner as the figure-eight field shaping coil that was

developed previously for an X-band maser (Ref. 4). The field staggering capability is used primarily at the 2290-MHz center frequency, where the 40-MHz bandwidth is required and the maximum gain/bandwidth product is available.

IV. Pump Source

The maser pump source is a Varian model VSU-9012Y varactor-tuned, Gunn-effect oscillator which is electronically tunable across the entire tuning range of the maser (Ref. 5). A 100-kHz oscillator is a part of the pump control/protective circuitry, it amplitude-modulates the varactor tuning bias voltage, thereby frequency-modulating the pump. The circuitry provides remote control for narrowband pumping of the maser at any single frequency within the maser tuning range and also across the wider bandwidth, as required by the VLBI Validation Task.

V. Performance

This maser uses a comb design intended for operation over a wide frequency range, it does not have the same gain/bandwidth capability that is achieved by the newer Block III maser used in the Deep Space Network. The magnetic field staggering necessary to achieve the 2270- to 2310-MHz bandwidth reduces the maser gain to 25 dB. A low-noise Avante model AM2402N transistor amplifier is used in series with the maser to achieve an overall package gain of 40 dB. The transistor amplifier's operating voltage is supplied by the Gunn-effect diode bias power supply. A bandpass filter is used behind the transistor amplifier to prevent wideband noise from entering the image response of the receiver following the maser package. The transistor amplifier contributes 2 K to the maser input noise temperature in the wide bandwidth mode of operation.

Operating characteristics of the tunable maser (with relatively narrow bandwidth) have been described previously (Ref. 3). The maser performance between 2270 and 2310 MHz is described here. The equivalent input noise temperature across the 40-MHz instantaneous bandwidth is between 4 and 5 K (including the transistor amplifier contribution). The amplitude response (flat within 1 dB) and the phase shift, as a function of frequency, are shown in Fig. 1. The outputs of a Hewlett-Packard network analyzer were recorded with the maser bypassed to produce reference lines. The difference in the slope of the phase reference recording and the phase response of the maser is used to determine the group delay time through the entire maser package.

Figure 1 shows that the delay time through the maser is 114×10^{-9} s at 2270 MHz, 106×10^{-9} s at 2290 MHz, and



111×10^{-9} s at 2310 MHz. The dispersive characteristics of the maser can be observed more easily, with improved resolution, by using a delay line in the reference path of the network analyzer measurement system. Figure 2 is a recording of the phase and amplitude as a function frequency with improved phase resolution. Recordings were made at refrigera-

tor temperatures of 4.41 and 4.55 K. Increasing the CCR temperature by 0.14 K reduced the phase slope between 2270 and 2310 MHz by 14 deg. The corresponding 0.97×10^{-9} s delay time change and the 2.8-dB gain change are 10 times larger than would be experienced during tracking operations on a moving antenna.

References

1. Clauss, R., and Wiebe, E., "Low Noise Receivers: Microwave Maser Development" in *The Deep Space Network Progress Report*, Technical Report 32-1526, Vol. XIX, pp. 93-99, Jet Propulsion Laboratory, Pasadena, Calif., Feb. 15, 1974.
2. Wiebe, E., "Microwave Maser Development: Automatic Monitoring of Closed Cycle Refrigerators for Mariner," in *The Deep Space Network Progress Report 42-20*, pp. 49-52, Jet Propulsion Laboratory, Pasadena, Calif., April 15, 1974.
3. Clauss, R. C., "Low Noise Receivers: Ultracone Maser Development," in *Space Programs Summary 37-46*, Vol. III, pp. 67-72, Jet Propulsion Laboratory, Pasadena, Calif., July 31, 1967.
4. Clauss, R., Wiebe, E., and Quinn, R., "Low Noise Receivers. Microwave Maser Development," in *The Deep Space Network Progress Report*, Technical Report 32-1526, Vol. XI, pp. 71-80, Jet Propulsion Laboratory, Pasadena, Calif., Oct. 15, 1972.
5. Quinn, R., "Low Noise Receivers: Solid State Pump Source for S-band Traveling-Wave Masers," in *The Deep Space Network Progress Report*, Technical Report 32-1526, Vol. XIV, pp. 46-49, Jet Propulsion Laboratory, Pasadena, Calif., April 15, 1973.

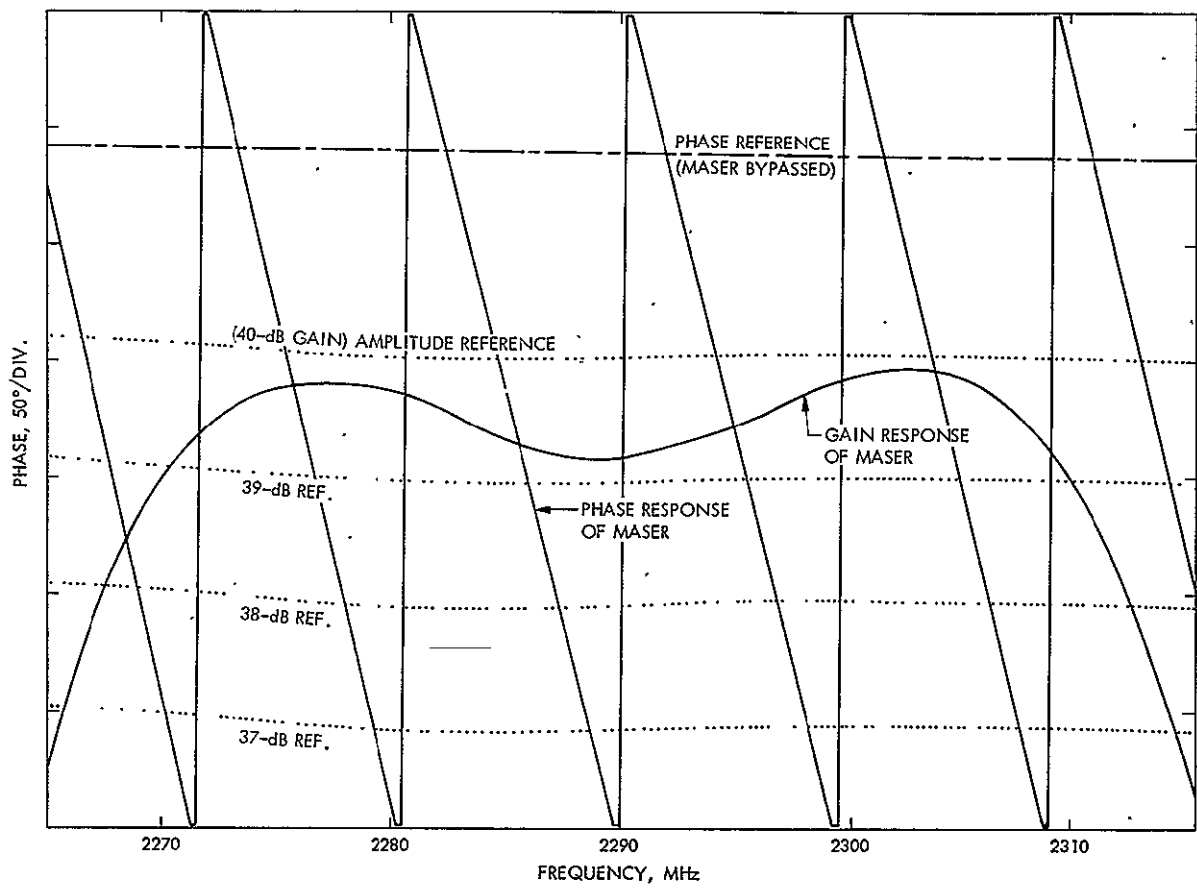


Fig. 1. Gain and phase response of maser .

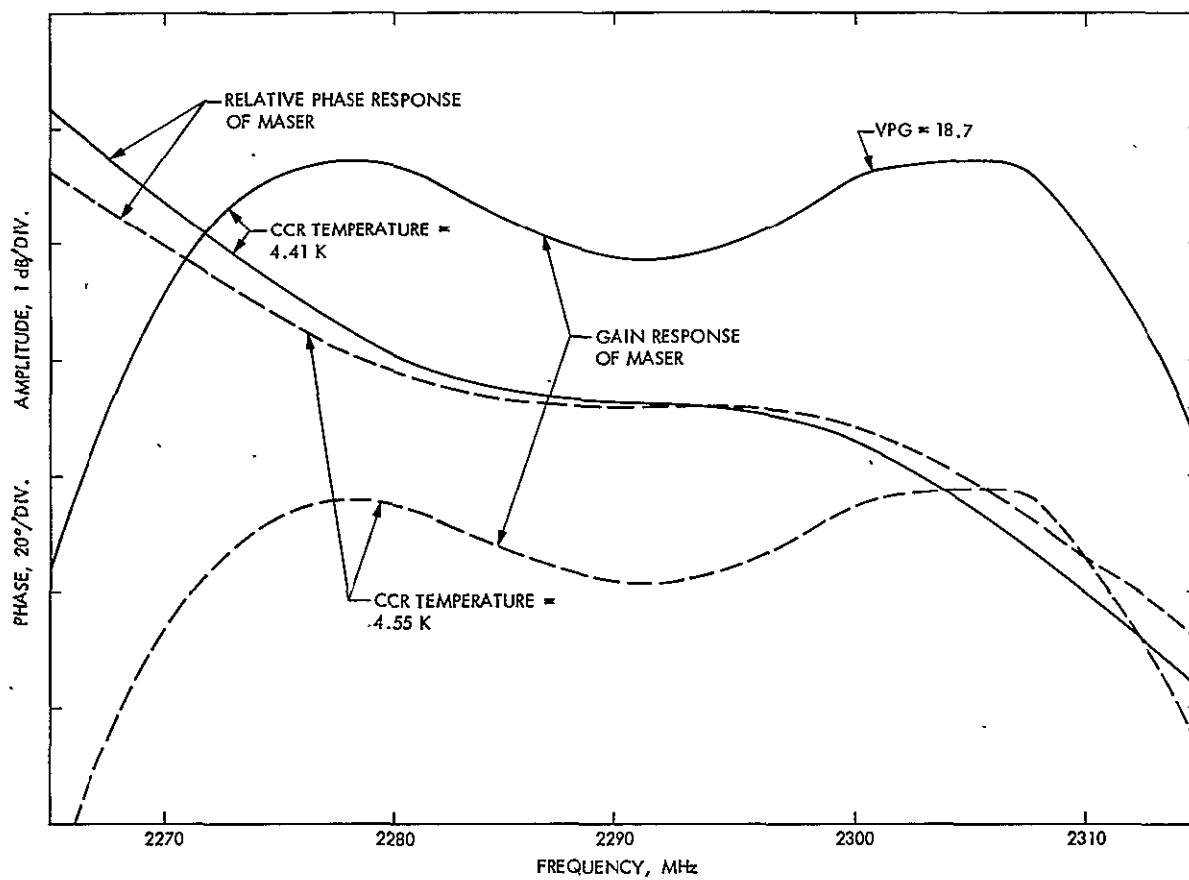


Fig. 2. Gain and relative phase response of maser at two different CCR temperatures

N77-19103

On the Inherent Intractability of Finding Good Codes

R. J. McEliece and H. C. A. van Tilborg¹
Communications Systems Research Section

In this article we will show that the problem of computing the minimum distance of an arbitrary binary linear code is NP complete. This strongly suggests, but does not imply, that it is impossible to design a computer algorithm for computing the minimum distance of an arbitrary code whose running time is bounded by a polynomial in the number of inputs.

I. Introduction

One of the recurring problems in the design of coded communication systems for the DSN or other applications is the search for the best code for the job. For reasons of economy and simplicity, the search is usually restricted to the class of binary linear codes, a linear code being one that is defined as the row-space of a certain binary matrix G called the code's *generator matrix*. If the matrix G has size $k \times n$ and row-rank k , the code is called an (n, k) *linear code*; its transmission rate is k/n bits per symbol. Among all linear codes C with a fixed n and k there is a wide range of performance possible; the best such code (on a memoryless channel) is, however, the one with the largest *minimum distance* d_{min} . Here

$$d_{min} = \min \{d_H(x, y) : x, y \in C, x \neq y\}$$

where $d_H(x, y)$ is the Hamming distance between the distinct code vectors x and y , i.e. the number of components in which

x and y differ. Since the code is linear, d_{min} is equal to the *minimum nonzero weight* of the code w_{min} :

$$w_{min} = \min \{w_H(x) : x \in C, x \neq 0\}$$

where $w_H(x)$ is the Hamming weight of x , i.e. the number of nonzero components of x .

Now given an arbitrary binary $k \times n$ matrix G , to find w_{min} for the corresponding code it is apparently necessary to compute each of the $2^k - 1$ nonzero linear combinations of the rows. This procedure is not feasible even by computer unless k is relatively small; we would like to find a more efficient procedure, if possible. However, in the remaining sections of this paper we will show that it is quite unlikely that such a procedure exists.

In the next section we shall describe a recently-developed technique that can sometimes be used to show the inherent intractability of a specific problem. In Section III we shall apply this technique to the w_{min} problem.

¹Caltech visiting Assistant Professor of Mathematics.

II. NP-Complete Problems

The following discussion will describe in heuristic language a set of results that can be made quite precise. The interested reader should consult Ref. 1, Chapter 10, or Ref. 2 for details.

The class P is defined to be the set of computational problems that can be solved by an algorithm that is guaranteed to terminate in a number of steps bounded by a polynomial in the length of the input. (P is sometimes called the class of *polynomial-time* algorithms.) Problems in the class P are generally regarded to be tractable; conversely those not in P are considered intractable. The class P includes such problems as solving linear equations, finding the minimum cut in a flowgraph, certain scheduling problems, etc.

The class NP is defined to be the set of computational problems that can be solved by a backtrack-search-type algorithm, where the depth of search is bounded by a polynomial in the length of the input. Alternatively, NP is the set of problems solvable by a nondeterministic algorithm whose running time is bounded by a polynomial in the length of the input. A nondeterministic algorithm is one that when confronted with a choice between two alternatives, can create two copies of itself and simultaneously follow up the consequences of both courses. This repeated splitting may lead to an exponentially growing number of copies; the algorithm is said to solve the given problem if any of these copies produces the correct answer. For this reason the class NP is often called the class of *nondeterministic polynomial-time* algorithms.

The class NP is quite extensive, it contains such problems as the traveling salesman's problem, the 0-1 integer programming problem, the graph characteristic number problem, and many decoding problems.

The class NP clearly contains the class P as a subclass. $NP \supseteq P$. It is conversely intuitively evident that NP is "much larger" than P , however, no one has yet succeeded in proving this and the query $NP \neq P$? is currently one of the central problems of computer science. However, recently a circle of results has been developed that strongly suggests, but does not rigorously imply, that $NP \neq P$. We now describe these results.

In 1971 Cook (see Ref. 1, Theorem 10.3) proved that a certain problem in NP (called the *satisfiability* problem) has the following curious property. Any problem (p) in NP can be reduced to the satisfiability problem, in the sense that if a polynomial-time algorithm could be found for the satisfiability problem, then that algorithm could be modified to yield a polynomial-time algorithm for problem (p). Thus while it is possible that satisfiability *might* possess a polynomial-time algorithm, if it does, so would the traveling salesman's

problem, integer programming, etc., indeed any problem in NP . But researchers have worked on these NP problems for many years without ever finding a polynomial-time algorithm for *any* of them. This is strong evidence that satisfiability does not possess a polynomial-time algorithm and that $NP \neq P$.

In a later paper Karp (Ref. 2) reversed things and showed that the satisfiability problem can itself be reduced in the sense described above to many other (21, to be exact) NP problems. Thus if any of these NP problems possesses a polynomial time algorithm, then so does every problem, and hence $NP = P$. NP problems with this property are now called *NP-complete* problems. At this writing there are dozens of problems known to be NP complete; and if the "obvious" assertion $NP \neq P$ is true, then no NP-complete problem can have a polynomial-time algorithm.

In the next section we shall show that certain problems related to assessing the performance of a binary linear code are NP complete. We shall do this by reducing a known NP-complete problem to the problems that interest us.

III. The NP completeness of Finding w_{min}

In this section we will show that the problem of finding w_{min} for a linear code from its generator matrix is NP complete. However, we must first state our problem in a suitable form. Here is our formally stated problem:

$$(G_k, w)$$

INPUT: A binary $k \times n$ matrix G_k of rank k , and a positive integer w .

PROPERTY: There is a linear combination of rows of G with Hamming weight w .

(In this subject, the problems are always stated in this way, since the theory can deal only directly with problems possessing a "yes" or "no" answer. The input must be encoded into a binary string of length N , say, and fed into a computing device, which outputs either 0 (yes) or 1 (no) after a certain length of time. If there is such a device for which the time is bounded by a polynomial function of N , the problem is in P , otherwise not.)

Although we have so far been describing codes by their generator matrices, it is also possible to use the *parity-check* matrices. If the code C has G_k as a generator matrix, then it will possess a $(n - k) \times n$ parity-check matrix H_{n-k} , where $c \in C$ iff $Hc^T = 0$. Since one can compute H_{n-k} from G_k (and

vice versa) in polynomial time via elementary row operations, it follows that the problem (G_k, w) is *NP* complete iff the following problem is:

$$(H_{n-k}, w)$$

INPUT: A binary $(n - k) \times n$ matrix of rank k and a positive integer w .

PROPERTY: There is a vector c of weight w such that $H_{n-k}c^T = 0$.

We show now that (G_k, w) (and hence also (H_{n-k}, w)) is *NP* complete by successively showing that the following problems are *NP* complete.

PARTITION INTO TRIANGLES

INPUT: The incidence matrix of an undirected graph Γ .

PROPERTY: The vertices of Γ can be covered by disjoint triangles.

$$(G, \ell, w)$$

INPUT: A binary matrix G and integers ℓ, w .

PROPERTY: There exists a linear combination of ℓ rows of G having weight w .

$$(G, w)$$

INPUT: A binary matrix G and an integer w .

PROPERTY: There exists a linear combination of rows of G having weight w .

$$(G_k, \ell, w)$$

INPUT: A binary $k \times n$ matrix G of rank k and integers ℓ, w .

PROPERTY: There exists a linear combination of ℓ rows of G_k having weight w

It is easily verified that each of the 6 problems listed above is in *NP*. Furthermore, the problem PARTITION INTO TRIANGLES is known to be *NP* complete (Ref. 3).

We shall now produce a sequence of reductions (see Fig. 1) that will show that each of the other five is also *NP* complete.

A reduction from problem A to problem B will be denoted by the symbol $A \propto B$. Such a reduction will always be of the following general form: we show that problem A can be "encoded" in polynomial time into problem B in such a way that a solution to the B problem immediately yields a solution to the corresponding A problem. In the cases that the input variables of problems A and B are denoted by the same letters, we shall add a prime to the input symbols for problem B.

$$\text{PARTITION INTO TRIANGLES} \propto (G, \ell, w)$$

Let the columns of G correspond to the n points of Γ ; the rows to the triangles of Γ . (Thus each row of G has exactly three nonzero entries.) Let $\ell = n/3$ and $w = n$. Then (G, ℓ, w) has an affirmative answer iff TRIANGLE does.

$$(G, \ell, w) \propto (G', w')$$

If G has n columns, let G' be the matrix formed by adjoining $n + 1$ copies of the identity matrix I to G , i.e. $G' = (G|I| \dots |I|)$. Let $w' = \ell(n + 1) + w$. Since ℓ and w can be recovered from w' (they are the quotient and remainder when w' is divided by $n + 1$), it follows that (G', w') has an affirmative answer iff (G, ℓ, w) does.

$$(G, \ell, w) \propto (G_k, \ell', w')$$

Let $G_k = (G|I|)$ and set $w' = w + \ell$, $\ell' = \ell$. Note that G_k has rank k even though G may have rank less than k .

$$(G_k, \ell, w) \propto (G'_k, \bar{w}')$$

If G_k has n columns, let G'_k be the matrix formed by adjoining to G_k $n + 1$ copies of the identity matrix I_k , i.e. $G'_k = (G_k|I_k| \dots |I_k|)$. Let $w' = \ell(n + 1) + w$ as before.

References

1. Aho, Alfred; Hopcraft, John, and Ullman, Jeffrey, *The Analysis and Design of Computer Algorithms*. Addison-Wesley Publishing Co., Reading, Mass., 1974.
2. Karp, Richard; "Reducibility Among Combinatorial Problems," in *Complexity of Computer Computations*, edited by R. Miller and J. Thatcher, pp. 85-103, Plenum Press, New York, 1972.
3. Karp, Richard, "On the Computational Complexity of Combinatorial Problems," *Networks*, Vol. 5, pp. 45-68, 1975.

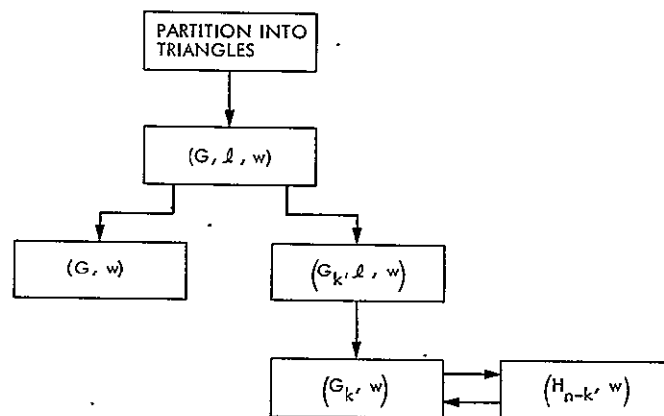


Fig. 1. The reductions showing the *NP* completeness of our problems

N77-19104

DSN Automation

R. B. Crow

Radio Frequency and Microwave Subsystems Section

Automation of the DSN has been under consideration for the past several years and has been justified on anticipated reduction in life cycle cost, resulting from increased productivity and reduced operations cost.

This article summarizes an overall hierarchical automation philosophy along with the results of the RF automation effort undertaken 2 years ago. A brief description of each subassembly controller's salient features, the software development process, and the common software used by these controllers will be presented. Comments will be made with respect to the relative advantages of PL/M high-level language and assembly language, the operational effectiveness of operator "Macro commands," and the program development, and a list of suggested future effort will be given.

This article provides for technology transfer and offers new ideas for consideration in future automation efforts.

I. Introduction

A philosophy of an hierarchical automation plan has been developed that emphasizes distributed control and the utilization of DSN hardware development engineers to develop the automation software.

Recent efforts in developing an automation capability for the RF subsystem are reported on. Comments are made on the facilities available to develop software for microcomputers and the common software developed for the RF automation demonstration.

II. Automation Philosophy

Several years ago, the DSN began investigating automation as a means of reducing DSN cost while furnishing the projects with more and better service.

A demonstration was held at the Goldstone Mars Station, DSS 14, in May of 1975, and more recently a second-generation demonstration was held at JPL in order to gain a data base. These experiences have contributed to the following automation philosophy.

A convenient approach in automating the DSN is to divide the task into four major areas: RF subsystems control, digital subsystems control, antenna subsystems control, and station control (see Fig. 1). This division of responsibility provides good development management posture since the technology base and administration control for each of the proposed major areas are contained in a single technical section.

A. RF Subsystems Control

The RF subsystems automation (see Fig. 2) has been accomplished by employing distributed control. Each major class of equipment (microwave, receiver-exciter, subcarrier demodulators, transmitters, RF subsystem) has its own controller. In this way, one or two engineers can be held responsible for assuring that the software they provide is capable of configuring, calibrating, and operating their equipment.

This is a slightly different approach from that implemented by the station manager control (SMC 2A) project, where the operator controls each of the RF subassemblies directly. The extra level of control (i.e., the subsystem controller) offers better monitoring, control and failure backup, and diagnostic capability than that offered by the SMC 2A approach, since the particular RF subsystem controller can devote most of its resources to monitoring and controlling the subsystem, and the required software to complement failure backup and diagnostics can be developed by the cognizant development engineer (CDE) of the equipment.

The RF subsystems controller serves the same function as the SMC in that it is responsible for subsystems coordination and is a focal point for all operator/machine interfaces. However, it differs from the SMC design in that it is intended that all RF subsystems at a DSS can be controlled from one control channel, instead of requiring three as the SMC has been implemented.

An important observation is that the further the controller is from the hardware, the more the level of detail is reduced (i.e., a CALIBRATE command to a receiver controller involves a large number of highly complicated communications, while a CALIBRATE command to a RF subsystem controller has little detail but more concern with subsystem coordination. A CALIBRATE command to the station controller would be a very high-level command with only simple intrasubsystem coordination required).

B. Digital Subsystems Control

The metric data subsystem (MDS) currently contains the same control structure used by the RF subsystems. A host task via the data system terminal is capable of controlling the other

subsystems controllers (i.e., metric data assembly, command processor assembly, telemetry processor assembly, and communication monitor formatter). Further, each of the previously mentioned assemblies is also capable of configuration control and monitoring the digital hardware assemblies under its control (i.e., the telemetry processor controls the symbol synchronizer and the decoders).

C. Antenna Subsystems Control

The automation of the antenna mechanical-subsystem will consist of antenna pointing as well as increased monitoring and control of the antenna servo and drive subsystems, so that unattended station operation is possible.

D. Station Controller

The station controller should be the focal point of the station and communicate with the operator in a high-level language. It should be adaptable and offer innovative solutions to new operational problems (i.e., each subsystem should have the ability to "read and write" all the functions in its area, but the station controller should be responsible for the "composition" of new operational scenarios). In this way, the antenna, RF subsystems, and digital subsystems areas can remain relatively unaffected, thereby localizing the changes to the station controller to meet the unexpected new problems. This division of control allows a viable fallback position for semiautomatic operation of the station should the station controller fail.

Some attention should be given to allowing the generation in near-real time of new operational scenarios. The new tools that will emerge from the integration of an automated station, such as improved acquisition procedures, real-time evaluation of downlink performance, rapid reconfiguration, etc., offer a considerable reward in increased productivity and should be pursued vigorously.

III. RF Automation Summary

The RF automation demonstration conducted in May 1975 (ref. DSN Progress Report 42-29, p. 66) identified two major goals for future activity:

- (1) Improve hardware/software reliability and maintainability.
- (2) Improve the operational effectiveness of the automation programs by providing *all* existing operator controls and offer new, more effective high-level operational techniques.

In answer to the problem of reliability and maintainability, an automation microcontroller was developed (ref. DSN Progress Report 42-30, p. 144) which appears to have satisfied the first goal.

Heavy Viking schedule pressure on DSS 14 caused the second RF demonstration, scheduled for November 1976, to be canceled. The demonstration was then rescheduled for the Compatibility Test Area at JPL (CTA 21); however, this has been subsequently delayed. A sequence of demonstrations is planned to be run at the Goldstone Venus Station, DSS-13, in FY'77 and '78 to demonstrate unattended station operation.

A JPL "lab" test has been run, in which the system capabilities have been exercised by simulating the proposed CTA 21 RF subsystem (the microwave subsystem, the Block IV receiver-exciter and the Block III subcarrier demodulator assemblies), that appears to have the capability of measurably expanding the operational tracking time in the DSN.

A brief description is presented for each subassembly controller in an attempt to illustrate any special features it may have and to note any change in its functional capability that was not present in the first RF automation demonstration.

A. RF Subsystems Controller

The RF subsystems controller links the operator (see Fig. 2) to the RF subsystems (i.e., microwave, Block IV receiver-exciter, and subcarrier demodulator assembly [SDA]) by accepting the operator's high-level input commands and distributing these commands to the appropriate subsystem controller. The RF subsystems controller also controls all subsystem coordination required to calibrate and acquire, maintains system status, and forms and stores mission configurations.

The RF subsystem controller has four phases (initiate, configure, calibrate, and operate). An improvement in operational effectiveness was achieved by allowing the operator to select any operational phase, instead of having a set sequence. The calibrate phase was modified to allow zero-delay range calibration and bit error test for the telemetry channel.

An important fundamental change was made to make the RF subsystem controllers essentially "station-independent." A subroutine was designed that allows the implementation of any set of logic tables which will direct its question to a particular input source. If the source message satisfies two test conditions (as programmed in the logic tables), the routine will set those status vectors identified in the logic table (for internal program control), send out control messages to other controllers, and output operator messages as defined in the

logic table (i.e., if receiver-exciter subsystem [RCV] 3 sends a calibration complete message and if SDA 1 is connected to RCV 3, then set F23 = 1, send SDA 1 a calibrate command, and notify the operator via the cathode-ray tube [CRT] and teletype [TTY] that "RCV 3 has calibrated").

Because of the station independence resulting from this subroutine, the conversion from a DSS 14 design to a CTA 21 design was completed in less than a week. In fact, such versatility was designed into the program that it could readily be applied as an RF subsystem controller, or a station controller, at any DSS.

Table 1 documents the details of the software development.

B. Subcarrier Demodulator Assembly Controller

The SDA controller can control and monitor up to six SDAs. These SDAs can be either automated Block III SDAs or a standard Block IV SDA. The SDA controller determines how many and what type of SDAs are connected to it (by analyzing the monitor words returned by the SDA). Knowledge of the type of SDA (Block III or Block IV) is required to properly configure and diagnose failure in the SDAs. A continuous monitor is kept to assure that all required references are present, that all relays are operating correctly, and that all control switches that are not under computer control have been set correctly.

Diagnostics are restricted to those that can be deduced directly from the SDA monitor words, which in general will not isolate the problem to a particular replaceable module. Future expansion of these diagnostics is planned for later development (see Table 1 for details of software development).

C. Receiver-Exciter Controller

The receiver-exciter (R-E) controller can control one Block IV receiver-exciter subsystem (consisting of two S-X receivers, one S-X exciter, three programmed oscillators, an instrumentation control assembly, and a time code distribution assembly). The subsystem elements can be operated independently or in any combination to allow one-way, two-way, or three-way operations.

The R-E controller is controlled by the RF subsystem controller; however, in a backup mode it can be controlled by a local TTY. A second "standard" mode allows the station monitor and control assembly (SMC) 2A to control the R-E controller either from the SMC console or the SMC keyboard.

A continuous monitor is maintained on all necessary conditions for operation (references are present, all relays confirmed, the actual configuration agrees with the last

operator configuration input, etc.). All programmed oscillator performance is measured against a locally generated model to confirm its operation.

The R-E controller is capable of effecting automatic carrier acquisition and automatic gain control (AGC) calibration (selectable from single point to 50 points in integer steps).

The R-E controller has a preliminary set of diagnostics built in and is capable of outputting current status of VCO frequencies, exciter frequency, configuration, dynamic and status phase error, AGC, etc. (see Table 1 for details of software development).

D. Microwave Controller

The antenna microwave subsystem (UWV) controller can control up to 5 bays of microwave equipment (approximately 65 microwave switches).

The program has been structured to be station-independent by incorporating a "station configuration overlay."

Since it is possible to attempt impossible (or catastrophic) configurations, an internal editor resident in the UWV controller reviews all input configuration messages to determine if they are acceptable. The UWV controller will configure all those switches that are allowable and issue a diagnostic warning to the operator for those switches that could not be configured.

A continuous monitor is kept on all relays, and an operator diagnostic message is sent in case of failure (see Table 1 for details of software development).

IV. Software Development

Stand-alone microcomputer high-level compilers did not exist at the time the RF automation project was started, since industry had adopted the use of larger, general-purpose computers to serve as the program development facility.

Presently there are two development computers at JPL equipped with functioning assemblers and PL/M compilers. (PL/M is an offshoot of IBM's PL/1. PL/M is a block structured language, well suited to structured programming, and has been adopted by both Intel [8080] and Motorola [6800], which are the current industry leaders.)

The Univac 1108 system (see Fig. 3) allows program development via a time-shared terminal through a high-speed modem. Once the program has been compiled, a paper tape is made through the 8080 microcontroller/high-speed punch.

This paper tape contains the object code that is read into the target microcontroller.

The Sigma 5 computer (see Fig. 4) has the same assembler and PL/M compiler installed in it. The operation of this equipment is similar to that of the Univac 1108 except that program development is via the batch mode and the object code is punched on cards. It is currently necessary to use a MAC 16 minicomputer to convert from the Sigma 5 cards to a paper tape suitable for input to the 8080 microcomputer.

A third development system (see Fig. 5) appears to be available in the near future. Intel has offered a "stand-alone" PL/M compiler that requires a 8080 microcomputer system with 64K bytes of memory and a floppy disk. The software for this compiler has been ordered and is due in the near future.

V. Common Software

A set of common software was developed to improve software maintainability and to reduce the overall RF subsystem software development activity. The common software consists of a variety of utility routines to make program development easier and to assist in debugging applications. The common software can be categorized as follows:

- (1) Operator control via the console keyboard
- (2) Input/output (I/O) interface procedure.
- (3) String procedures.
- (4) Arithmetic procedures.

A. Operator Control Via the Console Keyboard

It is assumed that all controllers have an executive routine that monitors the console input. This software routine is used to handle all operator console keyboard inputs. The KEY routine has an editing capability so that the configuration data under consideration can be loaded, displayed, and changed, a tape of the desired configuration can be punched, and it can catalog or delete the entry and set the required global control variable used by the main program. (See Appendix I for examples of the operator display for the RF subsystems.)

B. I/O Procedures

I/O procedures are high-level PL/M routines to control the standard 15-line interface, the star switch controller, the console device, the TTY, paper punch, and reader. (See Appendix II for a description of the I/O procedures.)

C. String Procedures for PL/M.

Various string procedures have been written to aid PL/M programmers in formatting, analyzing, and performing other string manipulations. The string procedures perform the following manipulations:

- (1) Concatenation
- (2) Segmentation
- (3) Comparison
- (4) Nulling
- (5) Binary to ASCII decimal conversion
- (6) Binary to ASCII hexadecimal conversion

(See Appendix III for a description of the string procedures.)

D. Arithmetic Procedures

Fixed-length, variable point arithmetic has been implemented because of the receiver-exciter control assembly's need for high precision. (See Appendix IV for a description of the arithmetic procedure.)

E. General Comments

The software development for the second RF demonstration was started in August 1975. The original estimate called for in an "in lab" demonstration by April 1976. This demonstration actually took place 5 months later than planned. Analyzing the reasons for the delay leads to the following observations.

The programs were more complex and detailed than first conceived in August 1975. The primary cause of the unforeseen complexity was a desire to be "station-independent" and produce "better operational effectiveness."

Several weeks' delay was caused by the installation of the PL/M compiler in the Univac 1108 computer with sufficient working core to handle programs up to 36K bytes. An interesting side note is the considerable unseen expense of Univac 1108 computer time. A 30K byte PL/M program costs approximately \$50 to compile!

It is interesting to note that the PL/M programs require approximately 11 bytes/record, while the assembly program (microwave controller) required approximately 4.5 bytes/record (i.e., PL/M takes two and a half times more storage than the assembly language). However, since PL/M is a higher-level language, it is not surprising that each PL/M record would take the place of several assembly records. What small premium is paid for in memory efficiency is more than offset by improved program readability and maintainability.

The communication between computers was through the standard star switch and was found to work well (the interface software was written in assembly language and was under interrupt control) when the RF subsystem was in a "stand-alone" configuration; however, if later plans call for an integration of the RF subsystem into a station complex, a high-speed interface must be designed in order for the RF subsystem to communicate at the required 250K SPS (instead of the current 1K SPS).

VI. Summary

The RF automation effort has developed a capability to use the new microcomputer technology to make automation practical from a cost and reliability viewpoint.

An interesting and valuable side benefit is the capability that now exists of the software engineer being the same person as the hardware engineer. This capability greatly enhanced the "operational effectiveness" of the finished software.

Table 1. Second RF demonstration software development data

Program Name	No. of Records	Storage Requirement, bytes	Software Development Time, man-weeks			Computer Language
			Design	Code	Debug	
Common software						
Star	1125	2K	2	2	2	Assembly
15-line interface	600	1K	2	2	2	Assembly
Arithmetic string procedures	675	5.4K	3	3	2	PL/M
Key	3000	11K	3	3	6	Assembly
RF Demo	1750	18K	26	8	10	PL/M
SDA	600	6.5K	8	4	4	PL/M
R-E	3000	34K	24	12	10	PL/M
UWV	4000	18K	26	6	8	Assembly

Note: 1. Time to install and check out PL/M compiler in Univac 1108 and the Sigma 5 was not counted against this development.
2. Most programmers were learning the language (except for the SDA programmer)
3. Main problem during development has been access to PL/M compiler and assembler.

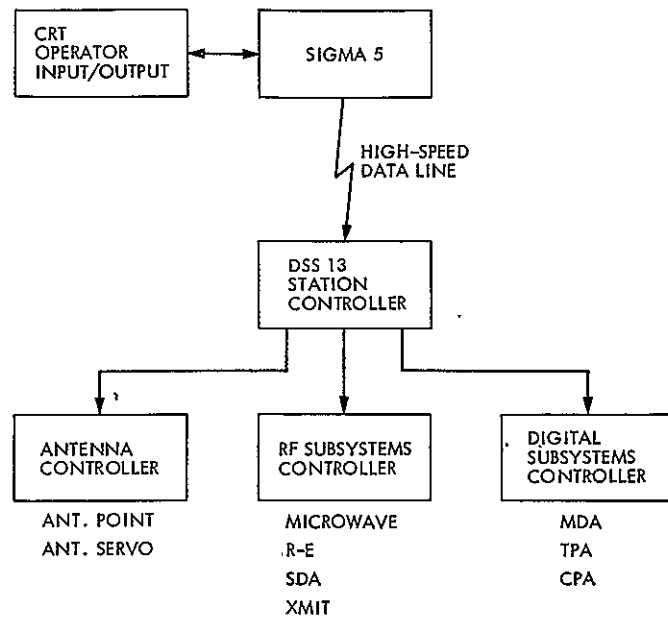


Fig. 1. Block diagram of DSS 13 unattended station control configuration

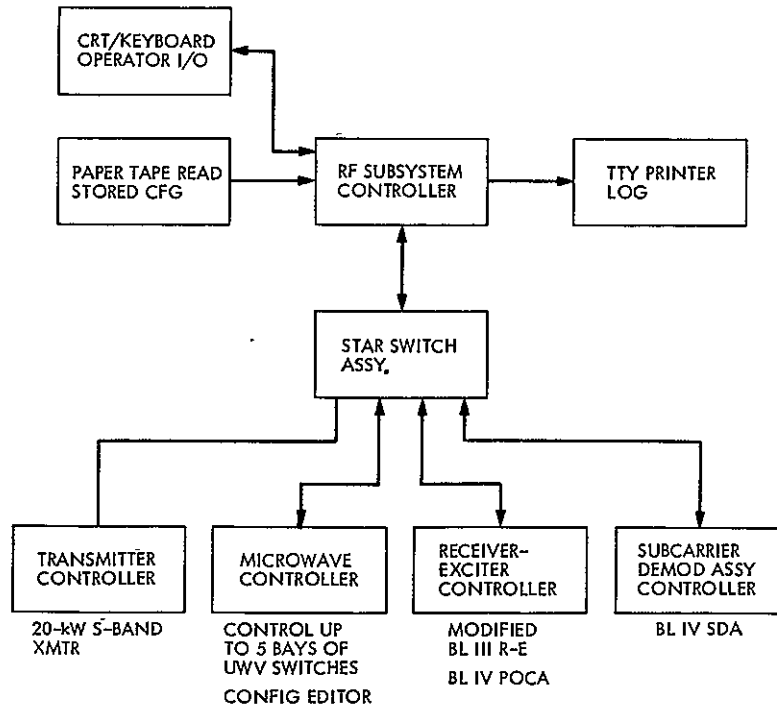


Fig. 2. Block diagram of DSS 13 RF subsystem automation configuration

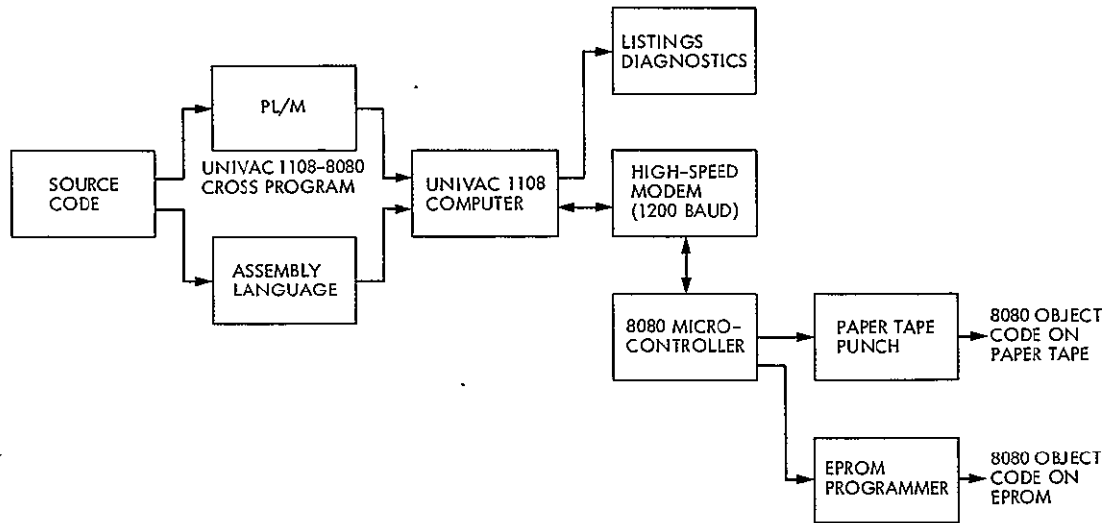


Fig. 3. 8080 software development using the UNIVAC 1108/8080 development system

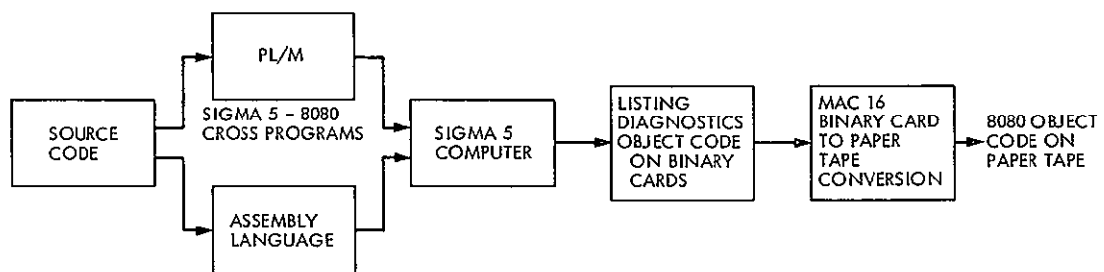


Fig. 4. 8080 software development using the Sigma 5/MAC 16 system

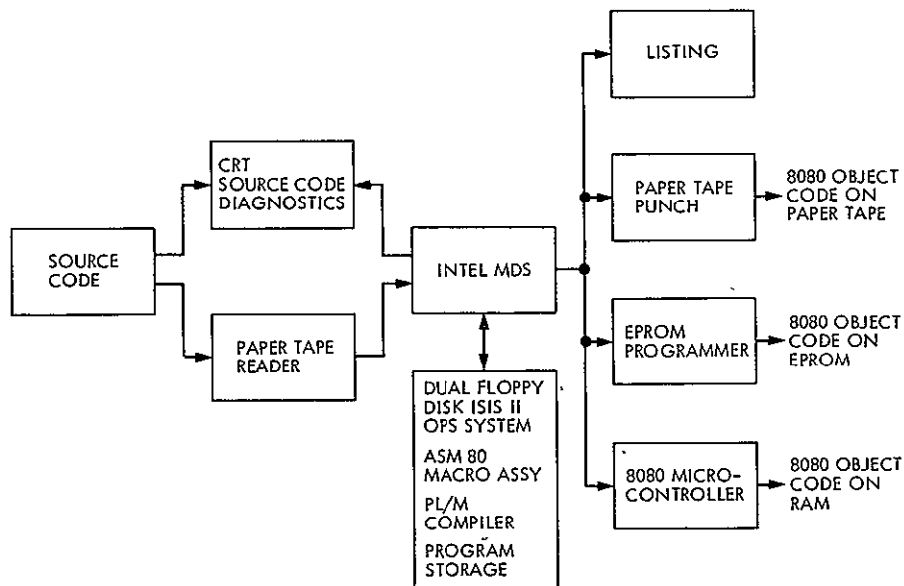


Fig. 5. Stand-alone 8080 software development system

Appendix A

“Key” Operator Display

I. Receiver 3 Configuration

A	BACKUP	= R3 (R3, R4, NONE)
B	LOOP MODE	= WIDE (WIDE, NARROW)
C	LOOP BW	= 4 (4, 3, 2, 1)
D	BAND SELECT	= X (X, S)
E	AGC BW	= WIDE (WIDE, MED, NARROW)
F	TELEMETRY BW	= 3 (4, 3, 2, 1)
G	ATZ ENABLE	= ON (ON, OFF)
H	LOOP FILTER	= OPERATE (SHORT, OPERATE)
I	LO AGC INPUT	= NORM (EXT, NORM)
J	TRANSFER FCN	= 2ND (3RD, 2ND)
K	RECEIVER LOOP	= OPEN (OPEN, CLOSED)
L	LO REF	= ON (ON, OFF)
M	LO REF TO	= EX4 (EX4, EX3, EX2, EX1)
N	LO OUTPUT	= ON (ON, OFF)
O	PREDIX SET	= 11 (III, II, I)

SAMPLE, CFG/R3/F=2/D=SS

Note: This is a typical Block IV receiver frame. All configuration switches are listed so that no oversight is possible. The KEY program allows these frames to be updated to reflect any mission configuration. Once all subassembly configurations are updated to the desired state, a paper tape can be punched so that this operational configuration can be recalled at will. This feature allows “offline” generation of operational configurations and fast retrieval so that quick turnaround is possible.

II. Exciter 1 Configuration

A	RANG MODS ON	= 1 2 3 (MISS G ARE OFF)
B	CMD MODS ON	= 1 2 3 4 (MISS G ARE OFF)
C	BAND SELECT	= X (X, S)
D	PH CTL LOOP	= OPERATE (SHORT, OPERATE)
E	MOD DLY LOOP	= SHORT (SHORT, OPERATE)
F	DOPPLER	= NORM (SIMULATE, NORM)

G	EXC FREQ	= NORM (SIMULATE, NORM)
H	CMD PH MOD	= NORM (BYPASS, NORM)
I	DOPPLER BIAS	= + (+, -)
J	EXC BAND	= X (X, S)
K	EXC DRIVE	= ON (ON, OFF)
L	EXC TEST SIG	= ON (ON, OFF)
M	PH CTL LOOP	= EXC (EXC, KLYSTRON)
N	STEP ATTN	= X (X, S)
O	PULS ATTN	= X (X, S)
P	XB STEP ATTN	= ZRO DLY (ZRO DLY, TEST)

SAMPLE, CFG/EI/A=13/C-S\$

III. Exciter 2 Configuration

A	X-BAND EXC	= DSN (RADAR, DSN)
B	TRAVSL (S/S)	= ON (ON, OFF)
C	TRAVSL (S/X)	= ON (ON, OFF)
D	TRAVSL (X/X)	= ON (ON, OFF)
E	ZRO DLY (S/S)	= ON (ON, OFF)
F	ZRO DLY (S/X)	= ON (ON, OFF)
G	ZRO DLY (X/X)	= ON (ON, OFF)
H	SB REFS ON	= 1 2 3 4 (MISS G ARE OFF)
I	XB REFS ON	= 1 2 3 4 (MISS G ARE OFF)
J	SB PULS ATTN	= NORM (BYPASS, NORM)
K	XB PULS ATTN	= NORM (BYPASS, NORM)
L	SB PULS ATTN	= NORM (BYPASS, NORM)
M	XB PULS ATTN	= NORM (BYPASS, NORM)
N	STEP ATTN	= 19 (2-DIGIT INTGR)
O	PULS ATTEN	= 199 (3-DIGIT INTGR)
P	PREDIX SET	= II (III, II, I)

SAMPLE, CFG/EII/N=99/B=OFF \$

IV. SDA 1 Configuration (Block III)

A	BACKUP	= S1 (S1, S2, NONE)
B	INPUT	= R1 (TEST, TAPE, R2, R1)

C VCO SHORT = OFF (ON, OFF)
 D LOOP BW = WIDE (WIDE, MED, NARROW)
 E MOD INDEX = 30 (0-30 DB)
 F SUBCARRIER = 24000.00 (HZ)
 G SYMBOL RATE = 99.00 (5.6 - 270000.0)
 H OUTPUT = DEMOD (TEST, TAPE, DEMOD)

SAMPLE, CFG/SDA1/A=S2/D-MED/E=6\$

H CONE = SPD (SPD, WTRLD)
 I POLARIZATION = LINEAR (LINEAR, RCP, LCP)
 J ANGLE = 180 (DEGREES)
 K CONE MODE = 1 (SEE MODE PROMPT)

SAMPLE, CFG/UL/A = II/G = 39°/H = WTRLD\$

MODES: 1. XMIT, 2. R&D, 3. LN RCV, 4. LN BYPASS, 5. DUAL RCV, 6. DUAL BYPASS, 7. DIPLX, 8. CAL SPD TWM, 9. CAL MOD TWM, 10. SAFE.

V. SDA 5 Configuration (Block IV)

A BACKUP = NONE (S5, S6, NONE)
 B LOCAL INPUT = TEST (TEST, TAPE)
 C REMOTE INPUT = R2 (R2, R1)
 D INPUT = REMOTE (LOCAL, REMOTE)
 E VCO SHORT = OFF (ON, OFF)
 F LOOP BW = WIDE (WIDE, NARROW)
 G LOOP GAIN = HIGH (HIGH, LOW)
 H AUTO ACQ = ON (ON, OFF)
 I MODE SELECT = INTRPLX (INTRPLX, NORM)
 J MOD INDEX = 30 (0-31DB)
 K SUBCARRIER = 32012.10 (HZ)
 L SYMBOL RATE = 199.00 (5.6 - 500000.0)
 M DEMOD OUTPUT = ON (ON, OFF)
 N LOCAL OUTPUT = TEST (TEST, TAPE)

SAMPLE, CFG/S5/B = TAPE/M = ON \$

Note: This frame also serves as an uplink status since power (item F) will be the "actual" uplink power.

VII. Downlink 1 Configuration and Status Data

A PREDIX = II (III, II, I)
 B CODE = SPD (SPD, XKRA, XK, RB, XRO)
 C POLARIZATION = RCP (LINEAR, RCP, LCP)
 D ANGLE = 0 (DEGREES)
 E CONE MODE = 4 (SEE MODE PROMPT)
 F
 G ALT CONE MODE = 5 (SEE MODE PROMPT)
 H RECEIVE = R3 (R1, R2, R3, R4)
 I ALT RECEIVER = R4 (R1, R2, R3, R4)
 J BL 3 SDA = 1 2 (MISSING ARE OFF)
 K BL 4 SDA = 5 6 (MISSING ARE OFF)
 L ALT 3 SDA = 2 1 (MISSING ARE OFF)
 M ALT 4 SDA = 6 5 (MISSING ARE OFF)
 N RECEIVER LOCK = ON
 O BLK 3 LOCK = 1, 2
 P BLK 4 LOCK = NONE

SAMPLE, CFG/PL1/A = III/B = XRO/K = 56\$

MODES. 1. XMIT, 2. R & D, 3. LN RCV, 4. LN BYPASS, 5. DUAL RCV, 6. DUAL BYPASS, 7. DIPLEX, 8. CAL SPD TWM, 9. CAL MOD TWM, 10. SAFE.

Note: This frame also serves as a downlink 1 status, since items N, O, P reflect the in-lock status of the receiver and associated SDAs.

VI. Uplink Configuration and Status Data

A PREDIX = I (III, II, I)
 B EXCITER = EXCI (EXC1 & 2, EXC2, EXC1)
 C ALT EXCITER = EXC2 (EXC1 & 2, EXC2, EXC1)
 D XMITTER = 400 R&D (400 R&D, 400 KW, 20 KW)
 E ALT. XMITTER = 20 KW (400 R&D, 400 KW, 20 KW)
 F POWER = 390 (KWS)
 G ALT POWER = 20 (KWS)

VIII. Predix 1 Configuration

A S/C CHANNEL = 0.000000000000 (MHz)
B ACQ BW = 0.000000 (Hz)
C ACQ DOPPLER = 0.000000 (Hz)
D ACQ RATE = 0.000000 (Hz/SEC)
E DOPPLER RATE = 0.000000 (Hz/SEC)
F RATE 2 = 0.000000 (Hz/SEC)
G RATE 3 = 0.000000 (Hz/SEC)
H TIME Ø = 000\$000000 (DDD\$HHMMSS)

I TIME 1 = 000\$000000 (DDD\$HHMMSS)
J TIME 2 = 000\$000000 (DDD\$HHMMSS)
K TIME 3 = 000\$000000 (DDD\$HHMMSS)
L EXC DRIVE ON = 000\$000000 (DDD\$HHMMSS)
M RANG MODS ON = 000\$000000 (DDD\$HHMMSS)
N CMD MODS ON = 000\$000000 (DDD\$HHMMSS)

SAMPLE, CFG/P1/K=100/65959/G-45\$

Note There are three Predix displays.

Appendix B

I/O Routines

I. Standard Interface Input and Output

The standard 15-line interface I/O routines are called L15IN and L15OUT for the input and output routines, respectively. The call for input is

```
CALL 15 IN(PORT,TIME$OUT,DATA$ARRAY,MAX$LENGTH),
```

where $1 \leq \text{PORT} \leq 12$ defines which of the standard interfaces is to be assessed. TIME\$OUT is a positive integer indicating the time-out period, DATA\$ARRAY provides the address of the data array to receive the input data, and MAX\$LENGTH is an integer defining the maximum number of bytes of input to accept. Note that the data array is a byte array. The calibration of one count in a time-out period will be established empirically and published later.

The routine L15IN sets the following items prior to exiting:

- FAIL to indicate successful receipt of data or failure
- FUNCTION to the received function code if data were received
- IO\$LENGTH to the number of bytes received
- DATA\$ARRAY receives the actual data bytes

The routine L15IN also utilizes the following global data items to determine its functional behavior:

- LOCKOUT to decide whether the routine should manipulate the enable/disable status of the interrupt system

Note that if the function code changes during input, the input is terminated. The user can pick up the data using the new function code by calling L15IN again.

The call to output via a standard 15-line interface is as follows:

```
CALL 15OUT(PORT,FCN,TIME$OUT,DATA$ARRAY,LNGTH),
```

where $1 \leq \text{PORT} \leq 12$ indicates the 15-line interface to use, $0 \leq \text{FCN} \leq 3$ indicates the function code to pass with the data, TIME\$OUT is a positive integer indicating the time-out period, DATA\$ARRAY contains the byte(s) to output over the interface, and the positive integer LNGTH indicates the

number of bytes to output with the given function code over the interface.

The routine L15OUT modifies the following items prior to exiting:

- FAIL to indicate success or failure of the transfer
- IO\$LENGTH to the actual number of bytes transferred (= LNGTH if a successful transfer)
- FUNCTION to the received function code if the computer was outprioritized by the device during or prior to the transfer

The routine L15OUT utilizes the following global data items to determine its proper functional behavior:

- LOCK\$OUT to decide whether the routine should modify the interrupt system enable/disable status
- STCOP to decide on the disposition of $\overline{\text{STC}}$ at the end of the transfer

II. Star Switch Input and Output

The star switch input and output routines, STARIN and STAROUT, respectively, are described separately from the 15-line interface routines because of routing parameters and other differences in the calling sequences.

For the RF automation demonstration, the following STAR\$ID will be used for routing:

STAR\$ID	Subassembly
0	RF Auto. Demo Controller
1	R-E Controller
2	SDA Controller
3	UWV Controller
4	XMT Controller
5	CCA
6	NOCC
7	SMC
	future

Note that when a message is received from STARIN, the global variable SOURCE\$ID contains the process code (STAR\$ID) of the source of the message.

The call for star switch input is

```
CALL STARIN (DATA$ARRAY,MAX$LENGTH);
```

where DATA\$ARRAY is a byte array of length MAX\$LENGTH, which will receive the first waiting message received over the star switch. Note that since star switch input is triggered by interrupts, the star switch input logic may have 0, 1, or multiple messages already within the computer memory.

The routine STARIN sets the following items prior to returning to the caller:

- FAIL to indicate successful/unsuccessful receipt of the data message (successful, always, for the user)
- STAR to indicate whether data were passed back to the caller
- 10\$LENGTH to indicate the number of bytes in the message
- SOURCE\$ID to furnish the process code of the system sending the message to this assembly

The call to output via the star switch controller is as follows:

```
CALL STAROUT (DESTINATION,DATA$ARRAY,LENGTH);
```

where 0 DESTINATION 15 is the process code to which to send the message, which is of length, LENGTH, in bytes, and is stored in the byte array, DATA\$ARRAY. The user must have previously set the global variable, STAR\$ID, to the process code of this computer.

The routine STAROUT sets the following global data items:

- FAIL to indicate the success or failure of the operation
- 10\$LENGTH to the actual number of bytes output

The routine STAROUT utilizes the following global data items for control:

- STAR\$ID, the process code being sent from

The function code used over the star is $\overline{FO}-\overline{FT} = 0$. The common software automatically transmits and verifies a checksum byte and also sends an acknowledge block for a successfully received message. These functions are performed automatically by the common software, so they are of no concern to the user.

III. Console Input and Output

The standard routines for console input and output are called CONIN and CONOUT, respectively. The call for console input is

```
CALL CONIN(DATA$ARRAY,MAX$LENGTH);
```

where the byte array DATA\$ARRAY is to receive the input bytes and MAX\$LENGTH is the maximum number of bytes to accept into the array.

The routine CONIN sets the following global items prior to returning to the caller:

- FAIL to indicate the success or failure of the operation
- 10\$LENGTH to indicate the actual number of bytes received

The routine CONIN looks for a carriage return to mark the end of an input operation.

The call for console output is

```
CALL CONOUT(DATA$ARRAY,LENGTH);
```

where the data to output are in the byte array DATA\$ARRAY and precisely LENGTH bytes are to be output.

The routine CONOUT sets the following global data items prior to returning to the caller:

- FAIL to indicate the success or failure of the I/O operation
- 10\$LENGTH to indicate the number of bytes actually output

IV. Paper Tape Input

The routine PTR is used to get paper tape input. The calling sequence is

```
CALL PTR(DATA$ARRAY,MAX$LENGTH);
```

where the byte array DATA\$ARRAY is to receive the input bytes and MAX\$LENGTH is the maximum number of bytes to accept into the array. The routine PTR sets the following global data items prior to returning to the caller

- FAIL to indicate the success or failure of the operation

- 10\$LENGTH to indicate the actual number of bytes received

V. List Output and Protocol

The routine to output to the TTY printer is called by the statement

```
CALL LISTOUT (DATA$ARRAY, LNGTH);
```

where the data to output are in the byte array DATA\$ARRAY and precisely LNGTH bytes are to be output

The routine LISTOUT sets the following global data items prior to returning to the caller:

- FAIL to indicate the success or failure of the operation
- 10\$LENGTH to indicate the number of bytes actually output

The subassembly controller will use the TTY printer of the RF demo controller using the following protocol:

- (1) The subassembly controller will send a message over the star switch with a TASK = list device request.
- (2) When a message is received from the RF demo with a TASK = list device available, the subassembly controller will send a message with TASK=list MSG. and the parameter string equal to or less than 72 ASCII characters.

- (3) This process is repeated, at a rate determined by the RF demo controller until the message has been sent. After the last line has been sent, the subassembly controller sends a message with TASK = list device released, which terminates this list process.

- (4) Should a subassembly controller request the list device when it is being used, the RF demo controller will place the request on a FIFO que and send a message to the subassembly controller with a TASK = list device busy. When the list device is available, the RF demo controller will send a message with TASK = list device available.

VI. Punch Output

The call for high-speed punch output is

```
CALL HISPEED (DATA$ARRAY, LNGTH);
```

where the data to output are in the byte array DATA\$ARRAY and precisely LNGTH bytes are to be output.

The routine TTYP sets the following global data items prior to returning to the caller.

- FAIL to indicate the success or failure of the I/O operation
- 10\$LENGTH to indicate the number of bytes actually output

Appendix C

String Procedures for PL/M

I. Editing Procedures

The editing procedures are

ADDSEG for appending a segment of one string to another

APPEND for appending an entire string onto the end of another

EQUATE for setting one string equal to another

SEGMENT for setting one string equal to a segment of another

REPLACE for copying one string into a fixed portion of another

A. The ADDSEG Procedure

This procedure, called by the statement

```
CALL ADDSEG (M1,M2, FIRST, LAST);
```

adds the segment from M2 (FIRST) to M2 (LAST) onto the end of M1, thereby increasing the length of M1. Here M1 and M2 are two strings and FIRST and LAST are variables, constants, or expressions indicating the segment of M2 to add onto M1.

Special cases:

- (1) If FIRST = 0, a value of 1 is used for FIRST.
- (2) If the $(LAST - FIRST + 1 = \text{LENGTH TO ADD TO } M1) > (255 - M1(0) = \text{SPACE IN } M1)$, the segment to add is reduced via $LAST = 255 - M1(0) + FIRST - 1$.
- (3) If $LAST > M2(0)$, $M2(0)$ is used for LAST.
- (4) If $FIRST > LAST$, no action is performed.

Normal case:

- (1) $M1(0)$ is increased by $LAST - FIRST + 1$.
- (2) $M1(I) = M2(J)$ for $J = FIRST, \dots, LAST$, where $I = M1(0) + 1 + J - FIRST$.

B. The APPEND Procedure

This procedure, called by the statement

```
CALL APPEND(M1,M2);
```

adds the entire string M2 to the end of the string M1.

Special cases:

- (1) M2 is void, no action is performed.
- (2) M1 is full, no action is performed.
- (3) Other special cases — see ADDSEG, as this procedure is equivalent to ADDSEG (M1,M2,1,255).

Normal case:

M1 is increased in length by the largest segment of M2 that will add onto M1.

C. The SEGMENT Procedure

This procedure, called by the statement

```
CALL SEGMENT (M1,M2,FIRST, LAST);
```

sets the string M1 equal to the selected substring from the string M2.

Special and normal cases:

The string M1 is first nulled, then the procedure ADDSEG is called via ADDSEG (M1,M2, FIRST, LAST).

D. The EQUATE Procedure

This procedure, called by the statement

```
CALL EQUATE (M1,M2);
```

sets the string M1 equal to the string M2.

Special and normal cases:

(1) This procedure is equivalent to `CALL NULL (.M1);`
then `CALL APPEND (.M1,.M2);`

(2) See those procedures for special and normal cases.

E. The REPLACE Procedure

This procedure, called by the statement

`CALL REPLACE (.M1,.M2, FIRST, LAST);`

sets the substring of M1 defined by the values of FIRST and LAST to be equal to the characters M2(1) to M2(LAST - FIRST + 1). The string M1 ought to be of length at least LAST.

II. Length Manipulations

The length manipulation procedures are

`NULL` for making a string empty

`TRUNCATE` for truncating a string

A. The NULL Procedure

The procedure, called by the statement

`CALL NULL (.M1);`

sets the length of the string M1 to zero.

B. The TRUNCATE Procedure

-This procedure, called by the statement

`CALL TRUNCATE (.M1, LAST)`

truncates the string M1 to length LAST, provided M1 is of length greater than LAST prior to the call.

III. Comparison

The procedure, `COMPARE`, is used to compare two strings. The procedure returns a value according to

0, string 1 less than string 2

1, string 1 = string 2

2, string 1 greater than string 2

The returned value can therefore be tested as a logical expression having value TRUE if the strings are equal and FALSE otherwise, or the value can be used in a relational expression or a DO-case construction. The expression to obtain the comparison value is

`.COMPARE (.M1,.M2)`

where M1 and M2 are the strings to be compared. If one string is shorter than the other, the shorter is considered to be rounded out with blanks for comparison purposes.

IV. Conversions

The procedures

`BINTOHEX`

`BINTODEC`

`HEXTOBIN`

`DECTOBIN`

convert binary values to their ASCII representations in either hexadecimal or decimal to binary.

The calling sequences are similar:

`CALL BINTOHEX (BIN$NO,.M);`

`CALL BINTODEC (BINSNO,.M);`

`Y = HEXTOBIN(.M);`

`Z = DECTOBIN(.M);`

For the latter two cases, the procedure actually produces an address value as its result. Note that the global variable, `SYNTAX`, is set according to

`SYNTAX = 0` if no syntax errors

`SYNTAX = 1` if a syntax error was discovered

The conversions that produce strings generate left-justified strings containing one space on the right-hand side.

Appendix D

Arithmetic Procedures

Because of the receiver/exciter control assembly's need for high precision, the software for fixed-length, variable-point operations has been implemented.

I. Fixed-Point Operations

These operations require definition of a global data item called `FXPT$LENGTH`, which describes the length of all the fixed point numbers in *bytes*. The internal structure of a fixed point number is a packed decimal digit string with two digits per data byte. The sign of a fixed point number is determined by the leftmost byte of the number. A zero here indicates a positive number, while any nonzero value indicates a negative number. Hence, the precision used by a program is $2 * \text{FXPT\$LENGTH} - 2$ digits, because of the presence of the sign.

The calling sequence

```
CALL FXPTADD (.A.,B.,C);
```

calculates $A = B + C$,

```
CALL FXPTSUB (.A.,B.,C);
```

calculates $A = B - C$,

```
CALL FXPTMPY (.A.,B.,C);
```

calculates $A = B * C$. In all these circumstances, the array *A* must be distinguished from the arrays *B* and *C*. That is,

```
CALL FXPTADD (.A.,B.,A);
```

is illegal.

ORIGINAL PAGE IS
OF POOR QUALITY

N77-19105

Automated Fourth-Harmonic Analyzer

C. F. Foster

Radio Frequency and Microwave Subsystems Section

This article describes the final design of a field portable microprocessor-based, microwave measuring and analysis instrument to be used for S-band transmitter fourth-harmonic power analysis and its impact on X-band reception in a dual S-X-band system.

I. Introduction

The requirement for a fourth-harmonic power analyzer has been previously discussed in *The Deep Space Network Progress Report 42-34*, pp. 39-42. The primary reason for the design of an instrument to automate the measurement is the speed gained by substituting a computer for the human operator. Through automation, the final results can be automatically calculated from raw measurement data in real time. Calibration data are measured and stored, and then used during the actual test to reduce systematic errors. Because all calculations are performed instantly, a hard copy of the corrected data is available immediately upon completion of the measurement.

This application also provides a test bed for generalized applications of microprocessors to the DSN to increase the capabilities of test equipment.

Hardware

A simplified system block diagram (Fig. 1) and the photographs (Figs. 2, 3) detail the major hardware elements of the

instrument. The instrument was designed around the Intel 8080 central processor unit (CPU). All components of the design are modular to the extent that they can be used as stand-alone building blocks in systems with similar design requirements. The control interface between the microprocessor and the measurement instruments is via the bus standard adopted by IEE (No. 488) and ANSI (MC 1.1). This is a standard which defines the electrical, mechanical, and functional aspects of an instrument interface. The hardware is designed so that on turn-on the program immediately controls the CPU.

The instrument includes an internal switch that allows the operator to select a diagnostic program which will provide help in case of hardware failure. The present program with diagnostic is contained in 7K of programmable read-only memory (PROM). The hardware allows for 3K expansion simply by plugging in the additional PROM as well as space for up to 8K additional PROM provided in the layout. There is also 9K of random access memory built in, and because of the modular design, any combination of random access memory (RAM)/PROM up to 27K can be utilized. A serial input/output port

with a 20-mA current loop has also been provided so that the collected data can be output for further analysis by a larger system and/or the instrument can be controlled remotely.

III. Software

The software was developed using a combination of PL/M (a high-level language) linked to assembly language to implement a program that was transportable, maintainable, and fast enough to meet the functional requirements. The program is stored in electrically erasable and programmable read-only memory.

IV. Operations

The operator is prompted how to operate the analyzer (how to start a measurement sequence, when the analyzer is ready for a new sample measurement, what port the measurement probe is in, etc.) by a built-in alphanumeric display. The program operates on each measurement [by converting the measured power to actual power using the known voltage standing wave ratio (VSWR) for the particular port] and then stores all 240 measurements. The operator can then request either the total fourth-harmonic power, or a listing (provided by a built-in printer for a hard-copy record) of each of the 240 ports and the total power.

The following is a typical operation sequence. The power meter is switched to the remote operation mode, and the

power meter is internally zeroed under computer control. After the zeroing process, the operator is prompted to select starting port number and probe gain. The operator then sees the prompt photo (Fig. 4) "ready for port 'N'," at which time the probe is inserted into the appropriate port and the operator commands the instrument to make another measurement by pressing the ready switch. The instrument makes the measurement and stores the data in memory, and then prompts the operator to proceed to the next port. This operation is repeated until interrupted by the operator, or all 240 ports have been measured. The operator is then prompted to select either the full report (consisting of a listing of corrected power at every port, plus a total corrected power) or a printout of total collector power only (Fig. 5).

V. Conclusion

The microprocessor-controlled portable instrument has been evaluated in the lab (Fig. 4) with the result that, after the harmonic probe has been installed, a complete measurement can be made every 30 min by one unskilled operator when previously it took two skilled operators 1 day. The instrument's operation can be taught in less than 10 min. The dynamic measurement range is 105 dB (-70 dBm to $+35$ dBm) and will be extended to 185 dB (down to -150 dBm) with the completion of an RF probe design. The instrument is presently being used in the lab to evaluate the design of high-power harmonic filters, and will soon be shipped to Goldstone for measurements on the high-power transmitter.

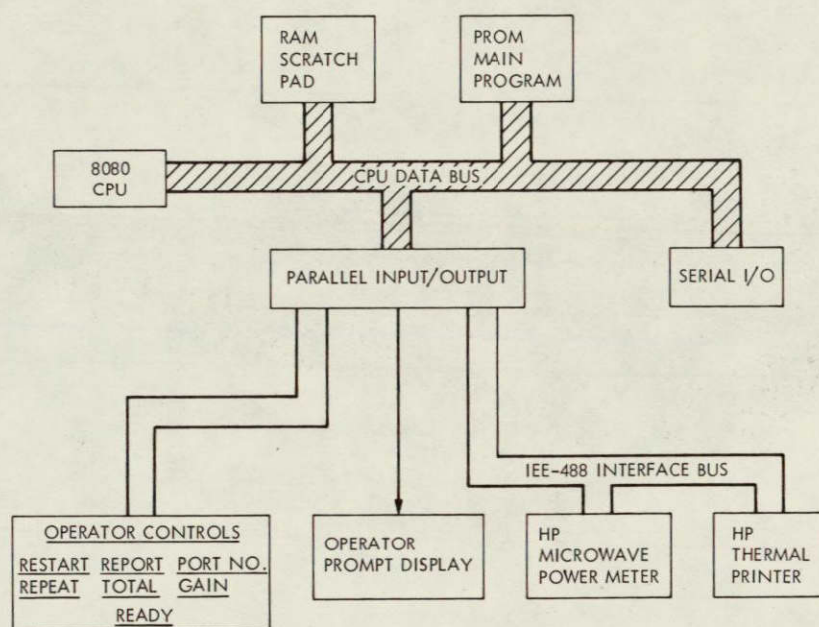


Fig. 1. Simplified block diagram (HPAS) harmonic power analyzer

ORIGINAL PAGE IS
OF POOR QUALITY

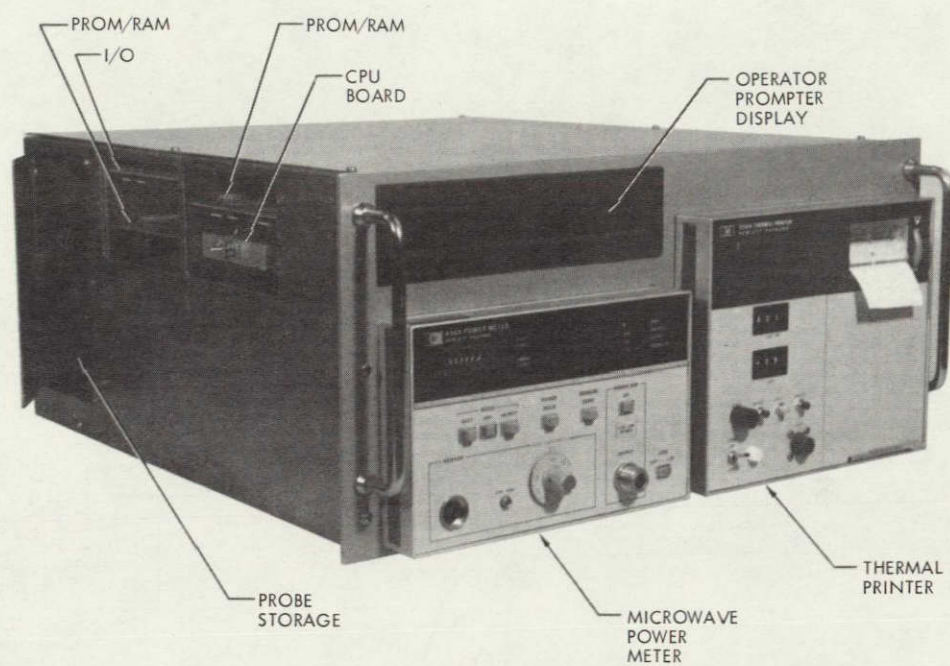


Fig. 2. Fourth-harmonic analyzer

REPRODUCIBILITY OF THE
ORIGINAL PAGE IS POOR

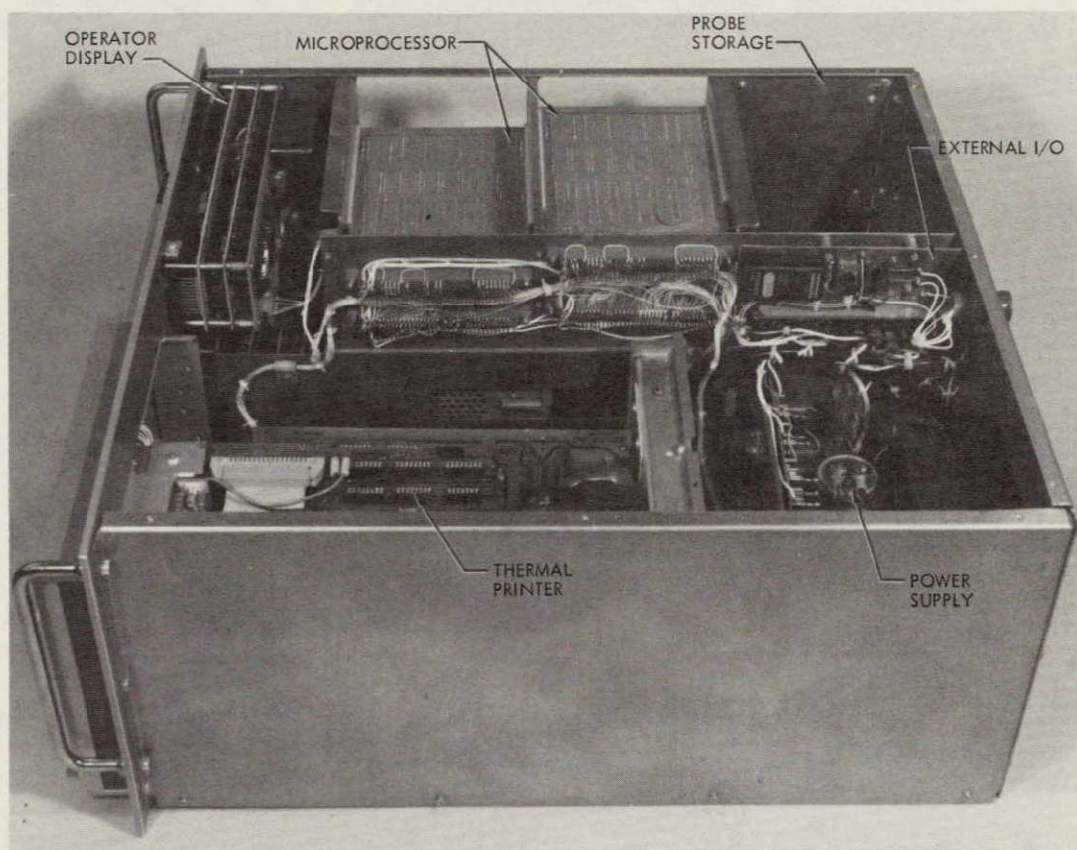


Fig. 3. Fourth-harmonic analyzer, internal view

ORIGINAL PAGE IS
OF POOR QUALITY

REPRODUCIBILITY OF THE
ORIGINAL PAGE IS POOR

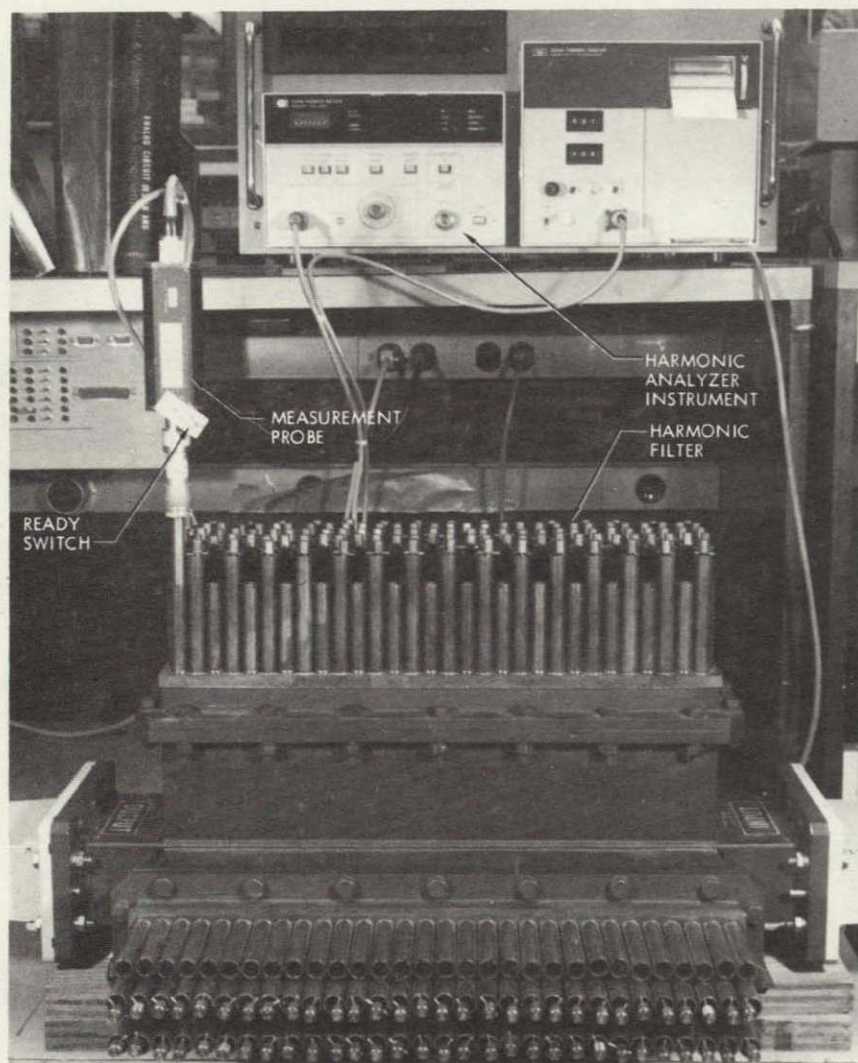


Fig. 4. Measurement setup, fourth-harmonic analyzer

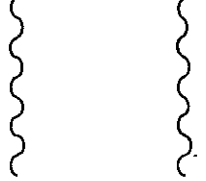
TOTAL CORRECTED POWER		
.25750 MILLIWATT		
I30	1.0583	MICROWATT
I29	1.0471	MICROWATT
I28	1.0666	MICROWATT
I27	1.0529	MICROWATT
I26	1.0789	MICROWATT
I25	1.0718	MICROWATT
		
A11	1.0641	MICROWATT
A10	1.0736	MICROWATT
A09	1.0637	MICROWATT
A08	1.0524	MICROWATT
A07	1.0853	MICROWATT
A06	1.0838	MICROWATT
A05	1.0949	MICROWATT
A04	1.1403	MICROWATT
A03	1.1444	MICROWATT
A02	1.1551	MICROWATT
A01	1.1558	MICROWATT

Fig. 5. Typical data printout

DIS 60, 09B

N77-19106

Control and Computation Module Development

R. A. Winkelstein

Communications Systems Research Section

The control and computation module (CCM) project has selected on the basis of developed criteria the 8080A microprocessor as its first candidate CCM. Software development methods have been investigated and two test bed projects have been chosen to evaluate application techniques of the 8080A and support microcircuits which will satisfy DSN requirements. Final recommendations will reflect successful JPL applications experience.

I. Introduction

It has been recognized that digital technology in the areas of control and computation is having an ever widening impact on the development of Deep Space Network (DSN) ground support equipment. A result of this recognition is the formation of the control and computation module (CCM) development project, whose objective is the assessment and development of a standardized set of digital control and computation modules, useful as building blocks for DSN equipment and meeting the criteria of functionalism, high reliability, and constrained life cycle costs.

Consideration of DSN functional applications, taken together with the advent of large-scale integration (LSI) of digital circuitry into small packages, led to the decision that the initial set of CCMs would consist of individual commercial LSI microcircuits as opposed to special modules housing some aggregate of digital circuitry. Thus the construction of

equipment using these CCMs could utilize packaging already developed for small-scale integration (SSI) microcircuits. Moreover, a relatively restricted set of CCMs could implement a large set of DSN applications such as listed in Table 1. Procurement of LSI devices selected as CCMs would be similar to current procurement of high-reliability SSI and medium-scale integration (MSI) devices for the DSN (Refs. 1 and 2).

Logistics considerations involving maintenance and sparing would also be similar to that of SSI and MSI devices. In the DSN station, maintenance would consist of the replacement of a circuit board containing many microcircuits, or on a higher level by replacement of a drawer or cage containing many circuit boards. These boards would then be repaired at the central maintenance depot serving the station complex. At the depot, the unit of replacement would be the individual microcircuit.

The first device type selected for use as a CCM was the microprocessor. This was industry's most visible effort in LSI, and was naturally suited for simple control and computation tasks. In addition, the high interest in these devices by engineers developing the DSN subsystems listed in Table 2, together with the profusion of devices offered by industry, lent some urgency to recommendation of a candidate device meeting suitable selection criteria. The device recommended is the 8080A microprocessor, first introduced by the Intel Corporation but now also available from several alternate sources.

II. Selection Criteria

The criteria developed for the CCM selection process falls into two categories, namely usefulness criteria and life cycle cost criteria. Usefulness criteria include device speed and functional capability, software requirements and support, and the availability of support microcircuits. Microprogrammable bipolar bit slice devices were initially studied because of their speed advantage over metal oxide semiconductor (MOS) preprogrammed microprocessors. Consideration of these bipolar devices was terminated however when a close examination of DSN requirements revealed that the narrow range of applications insufficient for MOS speed but not requiring the ultimate speed of SSI devices did not warrant the increased complexity and cost of microprogramming.

Life cycle cost criteria include initial procurement costs, device reliability, software design and maintenance costs, and logistics costs. Primary emphasis was placed on device reliability. Unique to LSI is the fact that testing and screening for reliable devices is far more complicated than for SSI and MSI devices. Experience has shown that reliability is coincident with product maturity, involving continuous production of thousands of items monthly, after a startup period of several years during which time incremental changes in the production process have been iteratively made to increase yield. Two devices which meet this maturity process are the 8080A and the 6800. Selection of the 8080A over the 6800 was based on higher commercial usage of the 8080A, estimated to be 2 or 3 times the usage of the 6800.

The rapidly advancing state of LSI technology and the proliferation of microprocessor devices currently available have raised concern that future procurement of spares may be jeopardized due to obsolescence and subsequent lack of sources. In the past, large commercial usage of a component has resulted in a type of usage inertia wherein demand has made the component available long after its recognized obsolescence. It is believed that this same principle applies to the 8080A and is an additional reason for its selection.

Support microcircuits for the 8080A are listed in Table 3. A typical DSN controller would consist of the three devices of the CPU group, selected devices from the memory and input/output (I/O) groups, and required discrete logic. Such a controller is shown in Fig. 1. The I/O block to the standard interface contains discrete logic for a standard interface adapter (SIA) driven by an 8255 programmable I/O unit. Subsystem hardware is also driven by the 8255 and required drivers. A major portion of the subsystem development effort involves the design of the program residing in the read-only memory (ROM).

III. Software Development

Development of software for a microprocessor controller requires a combination of special software development hardware and a software language system such as an assembly or higher level language. Complete development systems for the 8080A are available for less than \$20,000. During software development, the software development hardware is tied directly to the subsystem as shown in Fig. 2. The program resides in random access memory (RAM), where it may be easily modified as required. After the program has been successfully tested, it is programmed into programmable read-only memory (PROM) for use by the DSN subsystem.

If an external software facility is available, then the minimal 8080A development system shown in Fig. 3 may be purchased for less than \$500. Cross languages were developed under the CCM project for a software facility consisting of a Sigma 5 computer and a MAC 16 minicomputer. Software preparation on this facility is shown in Fig. 4. Here, the source code on punched cards is either assembled by the cross assembly language or compiled by the higher level PL/M cross compiler residing in the Sigma 5. Listings and diagnostics are output on the Sigma 5 line printer, and 8080A object code is output on binary punched cards. Information on the cards is punched on paper tape by the MAC 16 minicomputer. Software on the paper tape is then loaded into the development system via the paper tape reader shown in Fig. 3.

Objectives of the CCM project also include preparation of specifications useful in the procurement of the selected CCM and demonstration of the CCM utility in selected test bed projects. Specifications for the 8080A are currently being developed, and two test bed projects have been selected.

IV. Test Bed Projects

First of the two test bed projects to demonstrate 8080A application is a control unit for a 16000-point spectrum analyzer for radio frequency interference (RFI) indication.

This analyzer is being developed under another work unit and consists of discrete high-speed logic operating at a 10-MHz clock rate. The 8080A control unit will serve as an interface between the high-speed logic and the external environment to perform such functions as I/O, mode control, self testing, and automatic recovery procedures.

The second test bed project will demonstrate the use of more than one 8080A in a distributed control application. This application involves control of an ephemeris tuned receiver local oscillator. Several different control functions have been identified for this application including closed loop system control, ephemeris polynomial calculation, and system monitoring and I/O control.

Both projects meet the general criteria for test bed projects. Such criteria include the demonstration of CCM devices used

to solve DSN requirements, the furtherance of specific DSN objectives, the development of equipment not easily available from industry, and the ability to complete the project in a one-year time span.

V. Conclusion

The concept of the CCM as being an LSI microcircuit is a natural extension of the current DSN high-reliability program for small- and medium-scale integrated microcircuits. Although initial emphasis is on high usage commercial devices, this emphasis does not preclude future consideration of in-house developed circuits for DSN-unique application. Selection of the 8080A as a candidate CCM also implies selection of the required support circuits. Final approval of the 8080A as a CCM will be based on successful JPL applications experience.

References

1. Zundel, E. F., "High-Reliability Microcircuit Procurement in the DSN," in *The Deep Space Network*, Technical Report 32-1526, Vol. XI, pp. 121-123, Jet Propulsion Laboratory, Pasadena, Calif., Oct. 15, 1972.
2. Zundel, E. F., "High-Reliability Microcircuit Procurement Program in the DSN," in *The Deep Space Network Progress Report 42-27*, pp. 124-125, Jet Propulsion Laboratory, Pasadena, Calif., June 15, 1975.

Table 1. DSN applications

Line sensing and activation for monitoring and configuration control
Data manipulation and formatting
Limit comparison
Message generation: Human-machine interface
Simple low-speed calculations
Analog/digital and digital/analog conversion
Fast Fourier transformation
Digital filtering
Phase detection
Frequency counting and synthesizing
Digital interfacing

Table 2. DSN subsystems and assemblies

Utility control system
Antenna control assembly
RF subsystem controller
Receiver-exciter controller
SDA controller
Transmitter controller
VLBI recorder controller
Microwave controller
Fourth harmonic analyzer
Frequency standard controller
Noise adding radiometer
Tuned oscillator controller
Station manager's console
Automatic test equipment

Table 3. 8080A and support microcircuits

CPU Group	
8080A	microprocessor
8224	clock generator
8228	system controller
Memory Group	
8111	4 x 256 static RAM
8708	8 x 1024 EPROM
I/O Group	
8212	8-bit buffer
8214	interrupt controller
8251	universal synchronous/asynchronous receiver/transmitter
8255	programmable I/O port

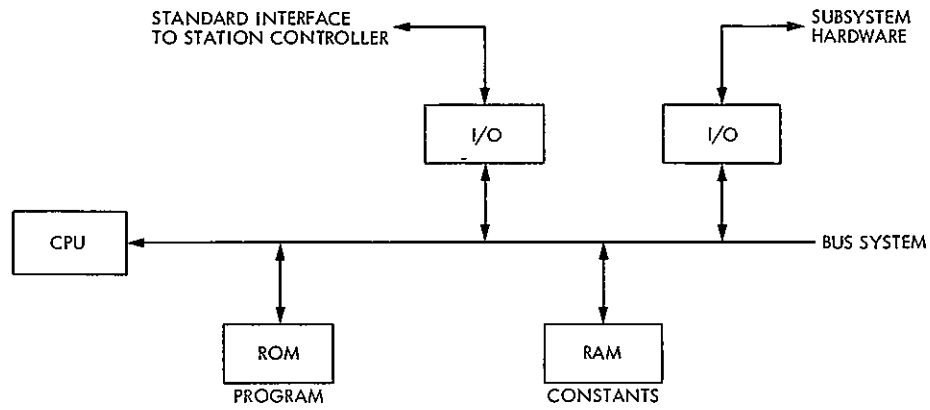


Fig. 1. Typical DSN controller

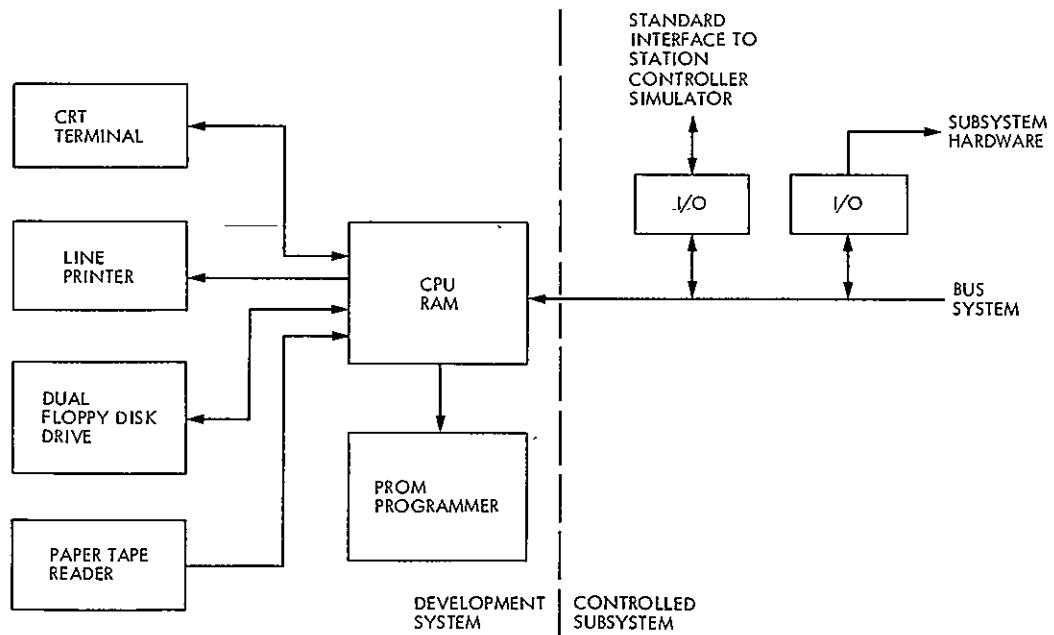


Fig. 2. Complete software development system

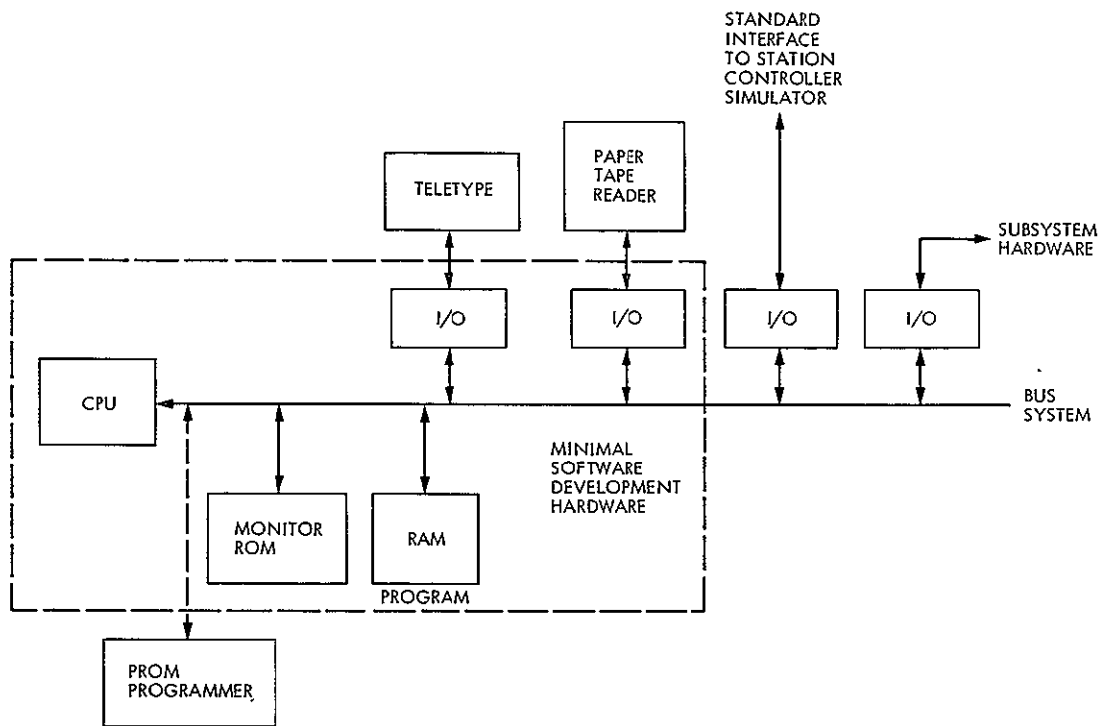


Fig. 3. Minimal software development system

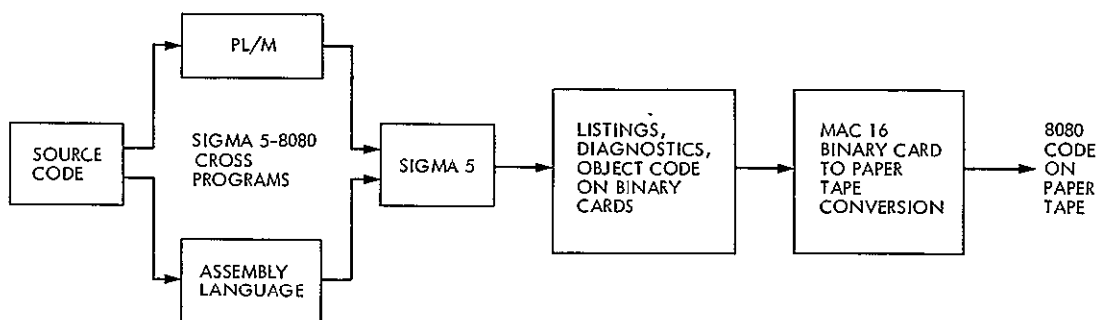


Fig. 4. Software preparation on external facility

4/5 81, 0314

N77-19107

Stochastic Models for Software Project Management

R. C. Tausworthe
DSN Data Systems Section

This article presents a method for determining the number and characteristics of milestones to be achieved during a development project in order that effective monitors of progress can be provided. Projections of progress data lead to estimates of the completion with determinable accuracy, but accuracy imposes a requirement that the number of milestones be inversely proportional to the estimate-error variance, and that the milestones themselves be defined in such a way that each represents approximately the same level of effort to complete.

I. Introduction

The progress in development of a piece of computer software (a program and its documentation) is, in many ways, like the classical random-walk problems associated with birth and death processes (Ref. 1). If a project has identified a number of milestones M to be achieved during the course of development, then the number of milestones achieved by a certain date can be modeled by a birth process in which the population never exceeds M . During acceptance testing of a "completed" program, anomalies are discovered in a similar birth process, whose population never exceeds some number A , the total number of anomalies in the program. As anomalies are repaired, the joint process describing anomalies found versus anomalies repaired is a birth-death process whose limiting condition is (hopefully) zero unrepaired anomalies.

During the course of development, project management requires effective monitors on which the health of the project can be assessed and corrective action initiated, should that assessment so indicate. Such monitors as cumulative mile-

stones and anomaly status have been used with success in the past, not only in software developments, but probably in almost all endeavors involving development activity.

This article explores the behavior of milestone-completion processes, and a later article will discuss anomaly discovery/repair processes. Both will be simplified for the sake of analysis, in that they will assume that uniform Markovian statistics apply. That is, the factors which influence the processes are not time-origin-dependent, and future statistics depend only on the current completion status of the process; i.e., at a given status, the remaining behavior of the process does not depend on any of the past history up to that status point. Should statistics change (by management decisions, for example), the remaining process to completion can be analyzed using only the new statistical parameters.

Uniformity of statistics depends on inertia over a project lifetime; it discounts such things as improvement of progress by learning and degradation of progress by attrition, as factors

that average out. The assumption of uniformity is one that permits statements to be made with predefined precision in the form, "If the team keeps progressing as it has so far, then . . .".

These monitors allow projections of completion dates to be made rather handily and accurately with only a minimum number of assumptions necessary on the underlying causal relationships within the development process. This is due, in a large development, to the multitude of factors which combine to make the progress appear stochastic in the first place. By the central limit theorem (Ref. 1, pp. 228–233), each such process appears normally distributed.

These are not necessarily optimistic assumptions to be making about processes involving expenditures of large amounts of money and other resources. Reviewing the progress via such monitors on a regular basis will reveal departures from theory rather dramatically, and thereby permit the management function to act appropriately. In fact, it is this feedback and corrective action on the part of management that tends to align the model with reality.

For example, should the series appear to exhibit some early adverse nonuniform statistics, management can take corrective action to bring the progress back into uniformity, so as to fall within the negotiated limits for the projected completion. Should the series appear to be favorably nonuniform, then management can again restore the uniformity by removal of resources, if appropriate to do so.

The point is that monitors based on theoretical models are quantitative tools that can be applied effectively in addition to the qualitative judgements normally necessary for management.

Models permit management in planning to make certain assumptions concerning the productivity of a team, thereby arriving at a preliminary schedule. During early development, the assumptions can be calibrated by actual measurements, and more realistic schedules drawn up. Management can thus preplan activities with known precision and can either utilize leverage as needed to maintain the plan, or renegotiate plans and capabilities.

As a final point in this introductory material, the theoretical model aids in defining the types of milestones to be monitored, and their number. Since events to be monitored are presumed by the theory to have certain statistical properties, then the accuracy of the results will be influenced

by the accuracy with which the actual events conform to these assumed statistics. The assumptions concerning the statistics are simple: normally distributed events, with uniform, history-independent time behavior. The law of large numbers helps keep the normality assumption approximately true, and project inertia and feedback tend to keep the process uniform. The proper definition of events for history-independence then remains as the principal challenge to the event definition process.

II. Schedule Prediction Model

For schedule prediction, let us assume that it is known *a priori* that the project will be completed after M milestones have been achieved. These milestones correspond to all the various tasks which have to be accomplished, and once accomplished, are finished forever (that is, some later activity does not reopen an already completed task; if such is the case, however, it can be accommodated by making M larger, to include all such milestones as separate events). The number M , of course, may not be known precisely *a priori*, but may be estimated via a preliminary design phase. Any uncertainty in the value of M will translate to an uncertainty in the estimated completion date, and we will treat this possibility a little later.

Let us now further suppose that at regular ΔT intervals (e.g., weekly, biweekly, or monthly) the numbers of milestones k reported as being achieved follows a time-independent statistical distribution function of the binomial form (Ref. 1, pp. 136–142);

$$P(k) = b(k; n, p) \triangleq \binom{n}{k} p^k (1-p)^{n-k} \quad (1)$$

The reported number k of milestones achieved each ΔT period is then a random variable whose mean value m and variance σ^2 are given by well-known formulas (Ref. 1, pp. 209, 214):

$$\begin{aligned} m &= pn \\ \sigma^2 &= np(1-p) = mq \end{aligned} \quad (2)$$

where we use $q \triangleq 1-p$ hereafter.

We use the binomial distribution function (1) above for two reasons: First, for very nominal values of m and σ^2 , the binomial distribution well approximates the normal distribution function (Ref. 1, pp. 168–173):

$$P(k) \approx \frac{1}{\sigma(2\pi)^{1/2}} \exp\left\{-\frac{(k-m)^2}{2\sigma^2}\right\} \quad (3)$$

thus fulfilling the intuitive requirement previously mentioned. The second reason is that the distribution (1) describes the probability of achieving exactly k out of n equally likely goals in which the figure p is associated with the success of each event.

Thus, if a set of M milestones can be defined for a project, a maximum of n to be achieved each ΔT reporting period, if each milestone represents the accomplishment of a task with approximately the same degree of difficulty, and if milestones scheduled in one ΔT period, but missed, can be rescheduled for future ΔT periods without altering the statistics, then the $P(k)$ form supposed above is a faithful description of the progress achievement process in the project.

The binomial distribution lends itself easily to solution and to interpretations. It is exactly the same formula which governs the statistics of obtaining k heads out of n coin tosses, using a coin that turns up heads with probability p each toss (the average number of heads being thus $m = np$). All the theoretical results known for coin tossings thus apply to our scheduling model, suitably interpreted. The "fine structure" of a productivity model for achieving milestones is thus simulated by corresponding a "toss" with a "trial for achieving a milestone," each with probability p which can in turn be related back to the m and σ^2 of the normal distribution. Each trial or step will require an average time

$$\Delta t = \frac{\Delta T}{n} = \frac{\Delta T (m - \sigma^2)}{m^2} \quad (4)$$

III. Progress Averages

The correspondence to coin tosses permits us to state a number of known results immediately. First, the time T_k to reach the k th milestone has average value

$$\begin{aligned} \bar{T}_k &= k/p \text{ steps} \\ &= k\Delta t/p = k\Delta T/pn \text{ units of time} \end{aligned} \quad (5)$$

and a variance about this value of

$$\text{var}(T_k) = \bar{T}_k^2 q/k \quad (6)$$

We may also compute the average cumulative progress $\bar{\pi}_s$ in milestones achieved after any particular number of steps s as the expression

$$\bar{\pi}_s = \sum_{k=0}^{M-1} kb(k; s, p) + Mp \sum_{t=0}^{s-M} b(M-1; M-1+t, p) \quad (7)$$

The first terms above represent the progress value k weighted by the probability that progress is at the k th milestone after s steps; the final terms represent the progress value M (completion) weighted by the probability that the M milestones were accomplished on or before step s (being the sum of the probabilities that M milestones were first reached on the $(M+t)$ th step, for $t = 0, \dots, s-M$ and $s \geq M$).

A closed-form formula for $\bar{\pi}_s$ is not known in the case $s > M$, but the sum may be readily approximated using the normal approximation (3) and integrating, rather than summing, to yield

$$\begin{aligned} \bar{\pi}_s &= sp \text{ for } s \leq M \\ &\approx \frac{sp}{2} \text{erfc}\left[\frac{sp - (M-1)}{(2pqs)^{1/2}}\right] - \left(\frac{pqs}{2\pi}\right)^{1/2} \exp[-(M-sp)^2/2pqs] \\ &\quad + M \left\{ 1 - (1/2) \text{erfc}\left[\frac{sp - (M-1)}{(2q(M-1))^{1/2}}\right] \right\} \text{ for } s > M > 10 \end{aligned} \quad (8)$$

At $s = M/p$ (the average time to project completion) the average progress is approximately

$$\bar{\pi}_{M/p} \approx M - \left(\frac{Mq}{2\pi}\right)^{1/2} = M \left[1 - \left(\frac{q}{2\pi M}\right)^{1/2} \right] \quad (9)$$

From (9) we may note that for $M \geq 16$, the average progress (taken over many projects) will show only at least 90% completion, even though the average project will have completed by this time!

The variance on π_s is

$$\text{var}(\pi_s) = q\bar{\pi}_s \text{ for } s \leq M \quad (10)$$

The expression for this variance when $s > M$ is too complicated to be enlightening.

IV. Scheduling With Accuracy When p Is Known

The ability to project schedules with accuracy based on the foregoing milestone-achievement model requires only two constants, m and p , and the definition of M milestones, which may be achieved in increments having the same likelihood distributions proposed in (1) or (3). No assumptions have been made relative to the precedence of milestones, or how individual milestones are placed on the schedule. It is only the cumulative number which enters the picture so far. Figure 1 shows what the typical achievement chart should look like.

If we suppose that p and m are known exactly, *a priori*, then from Eqs. (5) and (6), the relative accuracy with which this model predicts project completion time (as a one-sigma event) is $\epsilon = (q/M)^{1/2}$. Thus, to predict a completion time T_M within a factor ϵ requires

$$M > q/\epsilon^2 = \sigma^2/m\epsilon^2 \quad (11)$$

Recall that it was earlier mentioned that the assumed milestone achievement distribution is the same as if a maximum of n milestones were scheduled to be completed during each ΔT period, but only some lesser number k with average value $m = np$ will actually be achieved as scheduled. Milestones scheduled but unachieved in one ΔT period are then "slipped," the schedule reorganized with n milestones again scheduled for accomplishment in the next ΔT period, and so on, until completion. This type of schedule will be referred to as "maximum performance" schedule. The parameter p is the probability that a given milestone will be achieved in ΔT , and q is the probability that it will slip, to be rescheduled in some future period.

The original (unslipped) maximum-performance schedule shows the completion date after only M steps of length $\Delta t = \Delta T/n$. However, slippages lengthen this to \bar{T}_M on the average and to $\hat{T}_M [1 + (q/M)^{1/2}]$ as a "1 standard deviation" event. In order that an original schedule based on maximum performance be correct within a relative precision factor ϵ , it is necessary that

$$\begin{aligned} M &\geq \frac{1-p}{[(1+\epsilon)p-1]^2} = \frac{q}{[\epsilon-(1+\epsilon)]q^2} \\ p &> \frac{1}{1+\epsilon} \\ q &< \frac{\epsilon}{1+\epsilon} < \epsilon \end{aligned} \quad (12)$$

That is, the slip probability q must be no larger than about ϵ , and there must be enough milestones so as to make predictions fall within the desired precision. These relationships are shown in Fig. 2.

V. Estimation of the pn Parameter

It is seldom the case that m and σ^2 (or n and p) are known before a project begins, although the process of generating an initial schedule makes an implicit estimation of these parameters as a matter of course. More accurate values may be estimated once the project has begun by tabulating the progress in cumulative milestones achieved, as depicted in Fig. 3. If we let k_i for $i = 1, \dots, r$ be the individual accomplishments for each of the ΔT reporting periods up to the r th, then the best-fit line (least-square-error) to the cumulative progress up to that time is

$$\hat{\pi}_r \triangleq \hat{p}nr + b \quad (13)$$

in which the parameters \hat{p} and r are to be computed from observed data by

$$\begin{aligned} \hat{p} &= \frac{6}{nr(r+1)(r+2)} \sum_{j=1}^r (r+1-j)jk_j \\ b &= \frac{1}{(r+1)(r+2)} \sum_{j=1}^r (r+1-j)(r+2-3j)k_j \end{aligned} \quad (14)$$

These parameters have mean values given by

$$\begin{aligned} E(\hat{p}) &= p \\ E(b) &= 0 \end{aligned} \quad (15)$$

so that $\hat{\pi}_r$ is an unbiased estimator of the mean time to achieve a given milestone progress. The mean and estimated-mean time to completion, \bar{T}_M and \hat{T}_M then satisfy

$$M = p\bar{T}_M = \hat{p}\hat{T}_M + b \quad (16)$$

which provides the approximate estimation-error value

$$\hat{\epsilon} \triangleq \frac{\bar{T}_M - \hat{T}_M}{\bar{T}_M} = \left(\frac{\hat{p} - p}{p} \right) \frac{\hat{T}_M}{\bar{T}_M} + \frac{b}{M} \approx \left(\frac{\hat{p} - p}{p} \right) + b/M \quad (17)$$

within first-order effects. The average estimation error is zero (within first-order effects). The variance computation for $\hat{\epsilon}$ is straightforward, though somewhat lengthy, leading to bounds that are independent of M :

$$\frac{q}{pnr} F_{\min}(r) < \text{var}(\hat{\epsilon}) < \frac{q}{pnr} F_{\max}(r) \quad (18)$$

Both F_{\min} and F_{\max} are only slightly more than unity; these bounds and the ratio F_{\min}/F_{\max} are shown in Fig. 4.

The estimated completion date cannot be estimated with very high accuracy early in the project (when r is small) unless $pn = m$, the average number of milestones achieved per ΔT period, is large, or unless q is very small. The denominator value, pnr , is the expected number of accomplished milestones up to and including the r th reporting period. The accuracy in estimating the time to accomplish the k th milestone, given by (6), is thus about the same as the accuracy for drawing the best-fit line through the observed data (within the factor F).

VI. Scheduling With Accuracy Using Estimates of p

The uncertainty with which the completion date can be predicted at the r th report springs from two sources: variance in the value of \hat{p} to be used to estimate p and variance in the completion date due to p being other than unity:

$$\begin{aligned} \text{var}(T_M) &= \bar{T}_m^2 (q/M) (R/r) [F(r) + r/R] \\ &< 2.2 (\bar{T}_M^2 q/M) (R/r) \end{aligned} \quad (19)$$

where $R \triangleq M/m$, the average number of reporting periods to completion. When $r \ll R$, the prediction accuracy is, of course, dominated by the first term of the two; at any report r , the completion date variance is bounded according to the relation given above.

If it is therefore required, as before, to estimate the completion date to within an error factor ϵ , by a given report period r_0 , then the total number of milestones M must satisfy

$$M > (q/\epsilon^2) (R/r_0) [F(r_0) + r_0/R] \quad (20)$$

For good measure, we should probably have used the upper bound in (19), or $M > 2.2(q/\epsilon^2) (R/r_0)$ to set the number of milestones. The value of q to be used in (19) and (20) is a guess, and therefore should be more pessimistic (larger) than actual. In case no knowledge of q is to be had, we can always require $M \geq (2.2/\epsilon^2) (R/r_0)$ total milestones.

The refinement to the considerations given previously concerning estimating the deviation from an original maximum-performance schedule to within a factor of ϵ takes the same form as (12), except that M must be increased by a factor $[F(r_0) + r_0/R] (R/r_0)$:

$$\begin{aligned} M &> \frac{q (R/r_0) [F(r_0) + r_0/R]}{[\epsilon - (1 + \epsilon) q]^2} \\ q &< \frac{1}{1 + \epsilon} \end{aligned} \quad (21)$$

Figure 3 thus illustrates the constraints on M and ϵ when M is properly scaled.

Note that q is really needed only to judge how many milestones will be needed at the outset. A best-fit line to cumulative slip-statistics, using a proper reinterpretation of (14) will yield a $\hat{q}n$, if desired; together with $\hat{p}n$, all three parameters, \hat{p} , \hat{q} , and n (actually \hat{n}) can be found.

VII. Effect of Uncertainties in M

Up to this point, we have assumed M was known and fixed, in actuality, only an estimate of the total number of milestones may be known, perhaps by way of a preliminary, or architectural, design phase. The translation of a ΔM to a ΔT_M along the $p\bar{T}_k$ mean-time-to-completion-of- k -milestones line, coupled with estimation uncertainty in \hat{p} and random fluctuations in the progress, leads to a first-order-effect approximate value for the total relative error in the time to completion, estimated at the r th report:

$$\text{var}(T_M/\bar{T}_M) \approx (\Delta M/\bar{M})^2 + (q/\bar{M}) (R/r) [F(r) + r/R] \quad (22)$$

In (22), ΔM is the standard deviation of M , and \bar{M} is the mean value of M . Because $(\Delta M/\bar{M})$ appears squared in this expression its effect may not be felt so directly as the other terms contributing to schedule variance.

VIII. Conclusion

The progress of a development team is characterized by milestones achieved; whenever milestones can be defined in such a way that the expected number and variance of accomplishments is the same each for each status report, then the model explored in this article applies.

The main conclusion of this article is that schedule prediction accuracy is attainable only when a sufficient number of milestones to be achieved have been defined. The number of milestones needed is at least inversely proportional

to the desired estimation error variance, and even more drastic than this if conformance to a maximum-performance schedule is attempted. It is therefore both necessary and important to refine tasks and to generate a detailed work-breakdown structure (WBS) rather carefully, if monitoring accuracy is the aim.

The generation of a schedule from the WBS should then proceed to allocate a constant number m of milestones for each reporting interval, m being the believed mean achievability during such intervals.

Reference

1. Feller, W., *An Introduction to Probability Theory and Its Applications*, John Wiley & Sons, Inc., New York, 1950.

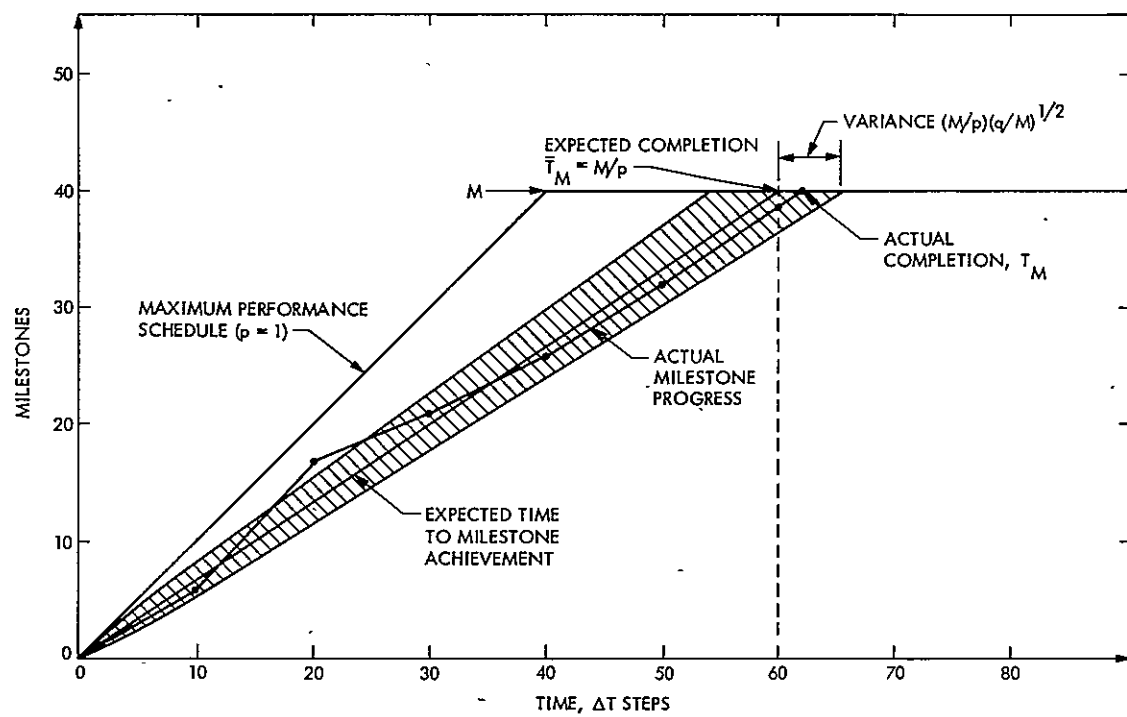


Fig. 1. Cumulative milestones achieved as a function of time. Case illustrated has parameters
 $n = 10, p = 2/3, M = 40$

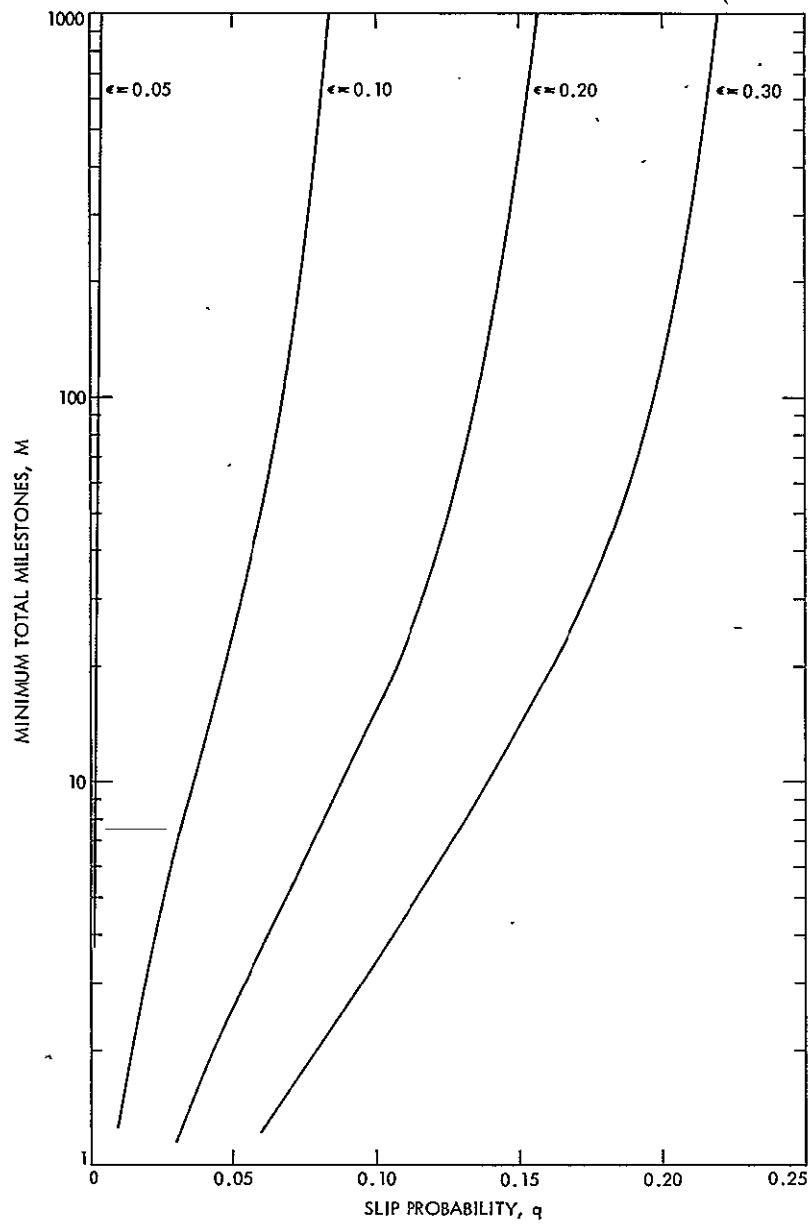


Fig. 2. Minimum number of schedule milestones required to achieve $1 = \epsilon$ estimation accuracy a given slip probability q from original maximum performance schedule

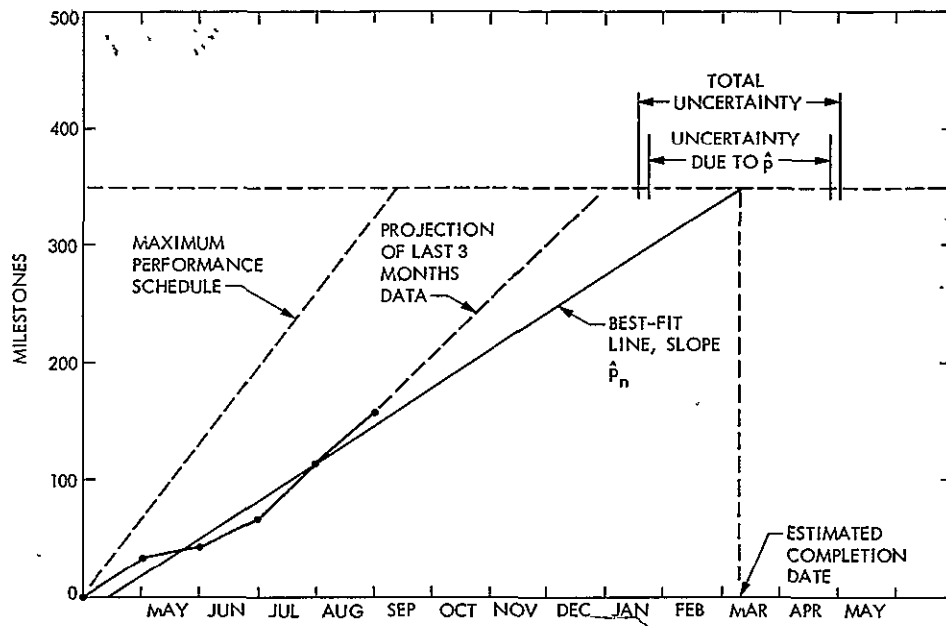


Fig. 3. Schedule prediction and uncertainty intervals based on 5 months' data

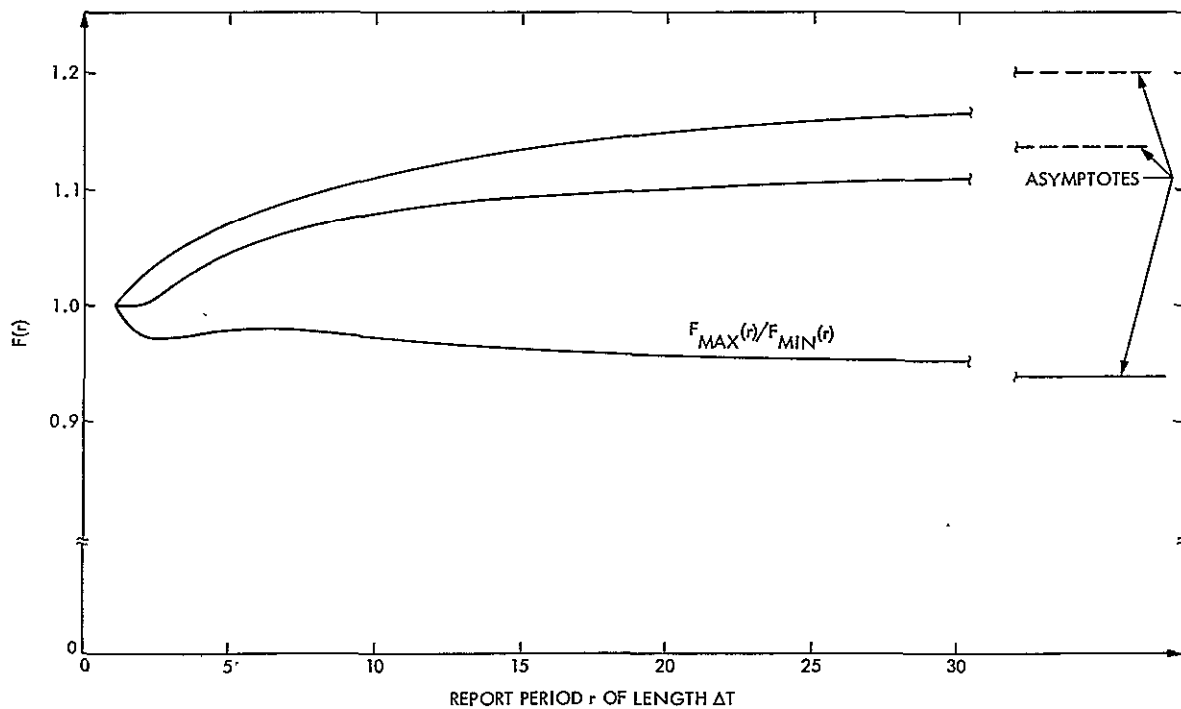


Fig. 4. Variance coefficient of completion date estimation from reported milestone data

N77-19108

Walsh Transforms and Signal Detection

L. R. Welch*

Communications Systems Research Section

This paper analyzes the detection of signals using Walsh power spectral estimates. In addition, a generalization of this method of estimation is analyzed. The conclusion is that Walsh transforms are not suitable tools for the detection of weak signals in noise.

I. Introduction

The economy of Walsh transform calculations has led to speculation on the feasibility of using Walsh power spectral estimates instead of Fourier spectral estimates in various estimation and detection problems such as in a signal presence indicator, precision signal power measurement and radio frequency spectrum monitoring for the DSN. At least one paper (Ref. 1) has appeared showing that there is a linear relation between the Walsh power spectrum and Fourier power spectrum when the signal is stationary.

However, in a practical problem, only a finite sample of a signal is available and only *estimates* of the spectra can be obtained. Simple examples can be constructed which show that there is not a one to one correspondence between Walsh and Fourier power spectral estimates obtained from finite signals. Hence, the Walsh power spectrum cannot be used to precisely reconstruct the Fourier power spectrum.

The idea of using the Walsh spectrum can be salvaged by posing a power estimation problem in the context of stochastic noise theory. When random noise is present in a received signal, Walsh power estimates are random variables which have some statistical structure. By examining this structure, "optimal" estimates of the power of a signal in noise can be obtained using the Walsh power estimates. If the signal is $\exp(j\omega t)$, this constitutes estimating a Fourier power component.

Another problem is the detection of weak signals in noise when there is some phase instability in the local oscillator. If the signal is sufficiently weak, its detection requires the gathering of data for a time period much greater than the period of stability of the oscillator. In this case a quadratic estimate can be constructed and accumulated over long time periods to provide a reliable estimate of signal power.

It will be seen that Walsh power estimates are not useful for these problems.

*Consultant from the University of Southern California.

II. An Estimation Problem

The following assumptions are made:

- (1) The received signal is a complex signal, $X(t)$, consisting of a signal, $\alpha \cdot S(t)$, plus broadband noise, $N(t)$.
- (2) The signal is sampled at time intervals, $k \cdot t_0$, to obtain samples

$$\left. \begin{aligned} x(k) &= X(t_0 \cdot k) = \alpha \cdot S(k \cdot t_0) + N(k \cdot t_0) \\ x(k) &= \alpha s(k) + n(k) \end{aligned} \right\} \quad (1)$$

- (3) The sequence, $[n(k)]$, is stationary, complex, Gaussian with mean zero,

$$\left. \begin{aligned} E[n(k)n(m)] &= 0 \\ E[\overline{n(k)}n(k+m)] &= 0, \text{ for } m \neq 0 \\ &= 1, \text{ for } m = 0 \end{aligned} \right\} \quad (2)$$

- (4) The signal amplitude, α , is less than 1 and the signal function, $s(k)$, has more or less constant energy of 1 over segments of length N ; that is,

$$\sum_{k=1}^N |s(k+m)|^2 \sim 1$$

The last normalization is the appropriate one for the Fourier power estimation problem. Also, with this normalization it is easy to characterize the detection problem in terms of α . For α near 1, a matched filter detector on N points is marginal for detection of the signal; for α much less than 1, the accumulation of data over many segments of length N is necessary. It is assumed that phase stability is such that longer matched filters are not possible, and this leads to the need for quadratic estimates. The relation between signal-to-noise ratio (SNR) and α is $\text{SNR} = \alpha^2/N$.

The relevant class of estimation processes is the following: A received signal sequence of length $N \cdot M$ is segmented into M segments of length N . On each segment a unitary transformation (such as Fourier or Walsh) is applied and the absolute value squared of each component is averaged over the M segments. These N numbers are to be used to estimate α^2 . The signal detection decision is obtained by comparing this estimate to a threshold.

III. Derivation of an Estimator

Let the unitary transformation have matrix $U = (u_{km})$ and define

$$\begin{aligned} x_U(m) &= \sum_{k=1}^N u_{mk} x(k) = \sum_{k=1}^N u_{mk} [\alpha s(k) + n(k)] \\ &= \alpha \cdot s_U(m) + n_U(m) \end{aligned}$$

and

$$\begin{aligned} |x_U(m)|^2 &= |n_U(m)|^2 + \alpha^2 \cdot |s_U(m)|^2 \\ &\quad + \alpha [n_U(m)\overline{s_U(m)} + \overline{n_U(m)}s_U(m)] \end{aligned} \quad (3)$$

Unitary transformations preserve all of the statistical properties of the Gaussian noise sequence. It can therefore be shown that the random variables

$$z(m) = |x_U(m)|^2 - \alpha^2 |s_U(m)|^2 - 1 \quad (4)$$

are mean zero, and pairwise orthogonal. Their variances are

$$\sigma^2(z(m)) = 1 + 2\alpha^2 |s_U(m)|^2$$

Next, make the calculations of Eq. (4) for the k th interval for k from 1 to M and average over the set of intervals

$$\begin{aligned} Y(m) &= \frac{1}{M} \sum_{k=1}^M z^{(k)}(m) = \frac{1}{M} \sum_{k=1}^M [|x_U^k(m)|^2 \\ &\quad - 1 - \alpha^2 |s_U^k(m)|^2] \\ &= \langle |x_U(m)|^2 \rangle - 1 \\ &\quad - \alpha^2 \langle |s_U(m)|^2 \rangle \end{aligned} \quad (5)$$

The $Y(k)$ are mean zero, orthogonal and have variance

$$\sigma^2(Y(m)) = \frac{1}{M} \left[1 + 2\alpha^2 \langle |s_U(m)|^2 \rangle \right]$$

The case where powerful methods of signal detection are needed is the case in which α is very small and indeed so small that all of the $\alpha^2 |s_U(m)|^2$ are much smaller than 1. In this case

$$\sigma^2(Y(m)) \sim \frac{1}{M}$$

For large M , the $Y(k)$ are approximately normally distributed, and the maximum likelihood estimate of α^2 is that value of α^2 in Eq. (5) which minimizes

$$E = \frac{1}{2} \sum_{m=1}^N \left[\frac{Y^2(m)}{\sigma^2(Y(m))} + \ln [\sigma^2(Y(m))] \right] \quad (6)$$

With the above approximation of the variance, this is equivalent to minimizing

$$E' = \sum_m \left[\langle |x_U(m)|^2 \rangle - 1 - \alpha^2 \langle |s_U(m)|^2 \rangle \right]^2 \quad (7)$$

Let $S_U(m) = \langle |s_U(m)|^2 \rangle$ and $W(m) = \langle |x_U(m)|^2 \rangle$. Then the value of α^2 which minimizes E' is

$$\hat{\alpha}^2 = \frac{\sum_{m=1}^N S_U(m) [W(m) - 1]}{\sum_{m=1}^N S_U^2(m)} \quad (8)$$

The numbers $W(m)$ are the accumulated spectral power estimates, and $S(m)$ are signal structure numbers relative to the particular transform.

IV. Properties of the Estimator

Again, assuming M is large so that the $W(\ell)$ can be assumed to be normally distributed, we have expectation and variance of $\hat{\alpha}^2$

$$\begin{aligned} E(\hat{\alpha}^2) &= \alpha^2 \\ \sigma^2(\hat{\alpha}^2) &= \frac{\sum_{m=1}^N S_U^2(m) \frac{1}{M}}{\left[\sum_{m=1}^N S_U^2(m) \right]^2} \\ &= \frac{1}{M \sum_{m=1}^N S_U^2(m)} \end{aligned} \quad (9)$$

If there is no signal present ($\alpha = 0$), the estimator has expected value 0 but has the same variance as Eq. (9).

It can therefore be seen that the ratio α^2 to the standard deviation,

$$R = \alpha^2 \sqrt{M \sum_{m=1}^N S_U^2(m)} \quad (10)$$

is a measure of the effectiveness of the estimator. If R is much less than 1, the estimator is ineffective in signal detection, and if R is much larger than 1, the estimator is a reliable indicator of the presence or absence of the signal. In terms of signal-to-noise ratio, SNR, this can be restated as: If

$$\text{SNR} \ll \left[N \cdot \sqrt{M \cdot \sum S_U^2(m)} \right]^{-1}$$

the estimator is ineffective, while if

$$\text{SNR} \gg \left[N \cdot \sqrt{M \cdot \sum S_U^2(m)} \right]^{-1} \quad (10a)$$

the estimator is effective.

Since

$$\sum_{m=1}^N S_U^2(m)$$

plays a key role in the effectiveness of the detection process, it will be called the efficiency factor and designated $E(U, s)$. For a given signal-to-noise ratio, SNR, and given efficiency, $E(U, s)$, the number of segments, M , of data that must be accumulated for reliable detection of the signal, s , satisfies

$$M > 1/(\text{SNR} \cdot N)^2 \cdot E(U, s) \quad (10b)$$

V. Efficiency of Unitary Transformations

When the unitary transformation, U , is the discrete Fourier transform, the numbers $S_U(m)$ are the averaged power spectrum of the desired signal. In the case where U is the Walsh transform, the $S_U(m)$ will be called the Walsh spectral power, and more generally $S_U(m)$ will be called the spectral power relative to U . Recalling that the signal, s , was normalized to unit energy over N samples, we have

$$\sum_{m=1}^N S_U(m) \sim 1$$

From this it can be seen that the maximum of $E(U, s)$ is 1.

This occurs when $S_U(m_0) = 1$ for some m_0 and $S_U(m) = 0$ for $m \neq m_0$. In this case, Eq. (10b) gives

$$M > 1/(\text{SNR} \cdot N)^2$$

for reliable detection.

The opposite extreme occurs when $S_U(m) = 1/N$ for all m . Then $E(U, s) = 1/N$ and

$$M > N/(\text{SNR} \cdot N)^2 = 1/N (\text{SNR})^2$$

for reliable detection.

An intermediate case is when $S_U(m) = 1/L$ for L choices of m and is 0 for all other m . In this case $E(U, s) = 1/L$ and

$$M > L/(\text{SNR} \cdot N)^2 = \frac{L}{N} \frac{1}{N (\text{SNR})^2}$$

This example shows that there is a relation between efficiency and bandwidth, since if the L choices of m are contiguous and U is the discrete Fourier transform, then the signal has bandwidth $L/N t_0$.

VI. Walsh Transforms Applied to Sinewaves

Let $N = 2^n$ and let (k_{n-1}, \dots, k_0) be the binary representation for k , $0 \leq k < N$; that is,

$$k = \sum_{i=0}^{n-1} 2^i k_i$$

Then the Walsh transform matrix is

$$W_{k, \ell} = \frac{1}{\sqrt{N}} (-1)^{\sum k_i \ell_i} \quad (11a)$$

If the signal to be detected is a complex sinewave of frequency f/t_0 , then

$$s(k) = \exp_f(k) = \frac{1}{\sqrt{N}} e^{j(2\pi f k + \phi)} \quad (12)$$

When the Walsh transform of the signal is taken, the result is

$$s_W(\ell) = \frac{1}{N} \sum_{k=0}^{N-1} e^{j(2\pi f k + \phi)} (-1)^{\sum k_i \ell_i}$$

$$= \frac{1}{N} e^{j\phi} \sum_{k=0}^{N-1} e^{\pi j \sum k_i (2f 2^i + \ell_i)}$$

$$s_W(\ell) = e^{j\phi} \prod_{i=0}^{n-1} \left[\frac{1 + e^{\pi j (2f 2^i + \ell_i)}}{2} \right] \quad (13a)$$

The power spectrum is

$$S_W(\ell) = |s_W(\ell)|^2 = \prod_{i=0}^{n-1} \cos^2 \left(\pi \left(2^i f + \frac{\ell_i}{2} \right) \right) \quad (14a)$$

and the sum of squares of the power spectrum terms is

$$\begin{aligned} \sum_{\ell=0}^{N-1} S_W^2(\ell) &= \sum_{\ell=0}^{N-1} \prod_{i=0}^{n-1} \cos^4 \left(\pi \left(2^i f + \frac{\ell_i}{2} \right) \right) \quad (15a) \\ &= \prod_{i=0}^{n-1} [\cos^4(\pi 2^i f) + \sin^4(\pi 2^i f)] \end{aligned}$$

$$E(W, \exp_f) = \prod_{i=0}^{n-1} \left[\frac{3}{4} + \frac{1}{4} \cos(4\pi 2^i f) \right]$$

For any particular choice of f , the efficiency $E(W, \exp_f)$ can be computed from Eq. (15a). In particular, if $f = 1/3$, the expression can be evaluated and is

$$E(W, \exp_{1/3}) = \left(\frac{5}{8} \right)^n = N^{-\log_2(8/5)} \sim N^{-2/3} \quad (16)$$

For $N = 1024$, the efficiency is only about 0.01, and becomes worse for larger N . Thus, the Walsh transform is very poor for detecting a sinewave with frequency $(1/3)t_0$.

For a sampled data system, the frequency, f lies in the range $[-1/2, 1/2]$. If Eq. (15a) is integrated over this range, the average efficiency is obtained.

$$\text{Ave}_f \{E(W, \exp_f)\} = \left(\frac{3}{4} \right)^n = N^{-\log_2(4/3)} \sim N^{-0.4} \quad (17)$$

Since the efficiency is never negative, this implies that the efficiency is less than $2 \times N^{-\log_2(4/3)}$ for at least half of the values of f in $[-1/2, 1/2]$. Therefore, for reliable detection, M grows like $\frac{1}{2} N^{0.4}$ for at least half of the values of f . For $n = 1024$, the efficiency is less than 0.06 for more than half the frequencies. Thus, Walsh transforms are poor for detecting most sinewaves.

The same calculations for the Fourier transform are

$$F_{k,\ell} = \frac{1}{\sqrt{N}} e^{-2\pi j k \ell / N} \quad (11b)$$

$$s_F(\ell) = \frac{1}{N} e^{j\varphi} \sum_{k=0}^{N-1} e^{2\pi j k (f - (\ell/N))} \quad (13b)$$

$$\sum_{\ell=0}^{N-1} S_F^2(\ell) =$$

$$\frac{1}{N^4} \sum_{\ell, k_1, k_2, k_3, k_4=0}^{N-1} \exp 2\pi j \left(f - \frac{\ell}{N} \right) (k_1 + k_2 - k_3 - k_4) \quad (15b)$$

With a little algebraic manipulation, this last expression is

$$E(F, \exp_f) = \frac{1}{3} \left(\frac{2N^2 + 1}{N^2} \right) + \frac{1}{3} \left(\frac{N^2 - 1}{N^2} \right) \cos(2\pi f N) \quad (15b')$$

The smallest value of this efficiency is

$$\min_f E(F, \exp_f) = \frac{1}{3} \left(1 + \frac{2}{N^2} \right) \sim \frac{1}{3}$$

VII. Conclusions

We have seen from the previous analysis that Walsh transforms are very inefficient in the detection of sinewaves. This analysis can be extended to show that they are inefficient whenever the signal to be detected is narrowband (when the energy is confined to a bandwidth which is a small multiple of $1/N$). Therefore, Walsh transforms are not useful in systems which must detect such signals.

Reference

1. Robinson, G. S., "Logical Convolution and Discrete Walsh and Fourier Power Spectra," *IEEE Transactions on Audio and Electroacoustics*, Vol AU-20, No. 4, October 1972.

N77-19109

Evaluation of DSN Data Processing With 7200-b/s GCF High-Speed Data Interfaces

H. C. Thorman
TDA Engineering

Test results confirm that the Deep Space Station (DSS) and Network Operations Control Center (NOCC) processing of telemetry, command, radio metric, and monitor data with the existing DSN Mark III-75 configuration will be unaffected by the recent change of the Ground Communications Facility (GCF) High-Speed Data Subsystem to a clock rate of 7200 bits per second.

I. General

A. HSD Conversion

Conversion of the GCF High-Speed Data Subsystem (GHS) (Ref. 1) to operate at a line rate of 7200 bits per second (b/s), instead of the previous 4800 b/s, was completed in early December 1976. The 7200-b/s clock rate has been used for transmissions of DSS telemetry, command, radio metric, and monitor data since that date.

Equipment of the type planned for the Network was implemented in May 1976 at the JPL-DSN Compatibility Test Area (CTA 21) and at the GCF Central Communications Terminal (CCT) to support engineering tests.

B. Analysis

Analyses of the DSN Mark III-75 Telemetry & Command Processor Assembly (TCP) and the Digital Instrumentation Subsystem (DIS) (Radio Metric and Monitor & Control) software programs indicated that the high-speed data (HSD)

interface change will not adversely affect performance of those XDS-920 processors.

The only apparent effect of increasing the GHS clock rate from 4800 to 7200 b/s is that the time available for servicing serial-to-parallel input and parallel-to-serial output transfers is reduced from 5 to 3.3 milliseconds per 24-bit word.

Servicing of each such transfer requires no more than about 50 microseconds (including exit from and return to computational routines). Since the maximum number of transfer interrupts that might coincide is typically only eight, the new clock rate poses no serious timing problem. Furthermore, the servicing of HSD input and output interrupts is given priority over all other processing functions except keyboard inputs and outputs. The programs are designed to minimize keyboard input and output during normal operations.

To verify the conclusions of these analyses, a series of tests was conducted at CTA 21, and between CTA 21 and the NOCC. Those tests are described herein.

II. Test Report

A. CTA 21 On-Site System Performance Tests

The TCP and DIS were tested at CTA 21 on 2, 3, and 7 June 1976, using on-site Systems Performance Test (SPT) procedures in which the DSS high-speed data equipment is operated in a loop-back configuration. The test results showed that the DSS performance with the 7200-b/s interface compared favorably to the performance with the 4800-b/s interface.

B. CTA 21 and NOCC Interactive Test

Additional testing was conducted at CTA 21 on 10 June 1976, in which real-time data were transmitted to and from the NOCC via the GHS subsystem at a line rate of 7200 b/s.

1. Telemetry & Command Subsystem (TCD)

a. Configuration and data types

TCD software: Viking Telemetry and Command

GHS configuration: 7200 b/s

NOCC configuration: Block III Telemetry Subsystem

Simulated Viking Data were input to the DSS Telemetry Subsystem from the Simulation Conversion Assembly as follows: Viking Orbiter low rate (VO-E224) at 33-1/3 b/s, uncoded; Viking Orbiter medium rate (VO-M560) at 2 kb/s, block coded.

b. *Test description.* Telemetry and Command Processor (TCP) output of 2-kb/s decoded M560 and 33-1/3-b/s E224 uncoded data to the NOCC via 7200-b/s HSD line was sustained for several hours. Frame synchronization of both data types was confirmed by observation of the NOCC Block III telemetry display at the Network Operations Control Area (NOCA).

While outputting the two telemetry streams, the TCD was configured for Viking Orbiter command and placed into remote-control mode. A standard command data transfer test was conducted, and then a set of six modules of commands was transmitted from the NOCC.

High-speed data block dumps and visual display observations at the NOCC indicated that the quality of the telemetry output was not affected by the additional load of command inputs.

c. *Discussion.* The telemetry and command test conditions described above represent the maximum HSD input and output requirements on the TCP. A slight additional TCP load

will exist when Viking high-rate (16 kb/s) data are output to the GCF Wideband Subsystem (GWB) by the Interdata-4 processor under control of the TCP. (The latter condition was not tested due to CTA 21 configurational limitations.)

The telemetry and command tests were performed only with the Viking TCP software module. However, the results can be considered as also representative of the performance to be expected for Pioneer and Helios telemetry and command processing.

2. Tracking and Monitor and Control Subsystems

a. Configuration and data types

DIS software: Multiple-mission radio metric and monitor and control (DOI-5046-OP-E)

GHS configuration: 7200 b/s

NOCC configuration: Block II Tracking Subsystem

Block III Monitor & Control Subsystem

A tracking and data handling (TDH) simulator provided 10 samples per second S-band and 10 samples per second X-band radio metric data inputs to the DIS. The normal DSS monitor interfaces from the Receiver-Exciter Subsystem, and the TCDs were also active.

b. *Test description.* The following operating conditions were tested with the DIS connected to the 7200-b/s GHS:

- (1) An NOCC transmission of sequence of event (SOE) text data was received and output to the line printer, while HSD output of maximum sample rate radio metric data and normal monitor data continued. The SOE transmission consisted of 158 HSD blocks, and all were received without errors. The radio metric and monitor data received at NOCC appeared to be satisfactory.
- (2) Floating-point tracking predicts were received from NOCC and output to a magpack tape, while HSD output of radio metric and monitor data continued satisfactorily. The predicts transmission consisted of 60 HSD blocks, and all were received without errors.
- (3) An Antenna Pointing Subsystem (APS) drive tape was generated on the DIS paper-tape punch and then verified. The HSD output continued to be satisfactory while these operations were performed.

c. *Discussion.* The DIS operating conditions tested are representative of the expected combinations of HSD input and output.

C. Telemetry Automatic Recall

Further tests were conducted on 16 June 1976 to evaluate the performance of the Automatic Total Recall System (ATRS-III) with the HSD line rate of 7200 b/s.

1. Configuration

TCP software: Viking Telemetry & Command
(DOI-5050-OP-C, Rev. A)
ATRS III (DOI-5082-OP-A)

NOCC configuration: Block III Data Records
Processor

2. **Test description.** Simulated Viking Orbiter telemetry data at 33-1/3 b/s uncoded and at 2 kb/s block coded were processed by the TCP and sent to NOCC on the 7200-b/s HSD line for a period of about 20 minutes.

A 7-track digital Original Data Record (ODR) was generated during the period of real-time processing. The ODR tape was rewound, and the ATRS-III program was loaded into the TCP and configured for remote control. The NOCC then recalled the complete ODR at the full 7200-b/s rate and recorded a Network Data Log (NDL) on the Network Log Processor (NLP). Later, an Intermediate Data Record (IDR) of these data was generated in the NOCC. The IDR summary indicated that there were no gaps on the NDL.

3. **Discussion.** The test confirmed that ODR recalls of HSD from the TCP can be performed at the full line rate of 7200 b/s.

D. Simulation Conversion Assembly Tests

1. **On-Site HSD test.** The CTA 21 on-site testing included a demonstration of satisfactory Simulation Conversion Assembly (SCA) XDS-910 performance with HSD input at 7200 b/s. The configuration and input loading were representative of the 26-meter DSS requirements, where all input is by HSD line and there is no wideband data (WBD) input.

2. **HSD and WBD test with MCCC.** Further SCA tests were conducted at CTA 21 on 16 June 1976 with "long-loop" data inputs from the Mission Control and Computing Center (MCCC) Simulation Center.

a. Configuration

HSD: 7200-b/s line rate
WBD 50-kb/s line rate

SCA software: Data routing version E (DOI-5089-TP-E), which permits 2400-bit WBD blocks to be processed along with 1200-bit HSD blocks

b. **Test description.** Satisfactory SCA performance was demonstrated with the following loading conditions:

- (1) WBD input: 16 kb/s to SCA Channel 1
HSD inputs: 2 kb/s to SCA Channel 2
33-1/3 b/s to SCA Channel 3
33-1/3 b/s to SCA Channel 4
- (2) HSD inputs: 2 kb/s to SCA Channel 1
2 kb/s to SCA Channel 2
33-1/3 b/s to SCA Channel 3
33-1/3 b/s to SCA Channel 4

(Note: Condition (2) exceeds the rate which could be carried on a 4800-b/s HSD line.)

The 2-kb/s block-coded data stream from SCA Channel 2 and a 33-1/3-b/s uncoded data stream were input to the DSS Telemetry Subsystem. These streams were processed by the TCD and returned to the MCCC for validation.

c. **Discussion.** Simulation Conversion Assembly performance with the 7200-b/s HSD interface is satisfactory when the concurrent WBD loading is limited to 16 kb/s. Performance with additional WBD input, such as required for 64-meter DSS support of Viking 3 spacecraft simulation, could not be tested at CTA 21. However, it is expected that the Viking Project will not require maximum-level long-loop simulation by the time the GHS equipment is converted to 7200 b/s.

E. Telemetry Processing Limit Test

CTA 21 testing on 16 June 1976 included an experiment to determine whether the 7200-b/s GHS might permit the TCD to handle 4-kb/s Viking data. SCA-generated data were used for the experiment.

It was found that the 26-meter DSS configuration of the TCD was able to process 4-kb/s *uncoded* data. The TCD was not able to handle 4-kb/s *block coded* data, however, because the coded symbol rate (21.333 ks/s) is too high for the Interdata-4 block decoding function.

The TCD was also tested in a 64-meter DSS configuration where the 4-kb/s block coded data were decoded by the Block Decoder Assembly (BDA), then output by an Interdata-4 Processor to the 7200-b/s HSD line satisfactorily. In this configuration the data would ordinarily be output to the WBD line.

III. Conclusions

On the basis of the foregoing analyses and test results, it was concluded that the conversion of the GCF HSD Subsystem (GHS) to a line rate of 7200 b/s will have no adverse effect on the DSS processing of telemetry, command, radio metric, monitor, and operations control data in the DSN Mark III-75 configuration.

The use of the 7200-b/s line rate will improve certain DSS functions. For example, the time required for ODR recall via HSD line will be appreciably reduced.

IV. Comments

On the basis of these test results, it was recommended that the implementation of the 7200-b/s GCF High-Speed Data Subsystem equipment in the DSN proceed as planned.

The 7200-b/s GCF High-Speed Subsystem has been implemented throughout the Network as scheduled, and is operating satisfactorily.

Acknowledgment

Richard Kee, DSN Network Operations Section, conducted the CTA 21 on-site tests and also contributed valuable support to the performance of the CTA 21 and NOCC interactive tests.

Reference

1. Glenn, M. S., "DSN Ground Communications Facility," in *The Deep Space Network Progress Report 42-36*, pp. 4-12, Jet Propulsion Laboratory, Pasadena, Calif., Dec. 15, 1976.

D119; 17, 17B

N77-19110

Baseband Recording and Playback

S. S. Kent

Radio Frequency and Microwave Subsystems Section

J. I. Molinder

Tracking and Data Acquisition Engineering Section

Analog recordings of spacecraft telemetry signals are made by Deep Space Network Deep Space Stations to provide backup for both spacecraft and ground station anomalies. In this article the requirements that must be met to insure successful baseband recording and playback are given. Recording and playback procedures are developed to insure that these requirements are met and performance results from tests conducted at the Compatibility Test Area (JPL) are tabulated.

I. Introduction

Analog recordings of spacecraft telemetry signals are made by Deep Space Network Deep Space Stations to provide backup for both spacecraft and ground station anomalies. These recordings can be made at various points along the telemetry string as shown in Fig 1. Both the effectiveness of the backup provided and the recording bandwidth required increase as the recording point moves upstream (toward the antenna). For example, an unanticipated change in spacecraft subcarrier frequency or data rate will cause the Subcarrier Demodulator Assembly (SDA) to lose lock. If this happens, no data can be recovered unless the recording is made upstream of the SDA. In addition, recording upstream of the SDA provides a backup in the event of a ground station failure or operator error affecting the SDA or other equipment further downstream. On the other hand, the recording bandwidth required just upstream of the SDA (baseband) is greater than that

required just downstream of the SDA (SDA output) by a factor of approximately the ratio of the spacecraft subcarrier frequency to half the data symbol rate. This ratio can easily be greater than ten. An even larger factor may result in the case of more than one subcarrier on a single carrier. Open-loop recording (Fig. 1) provides further backup since the receiver does not have to be in lock (as required for baseband recording) but increases the required recording bandwidth by a factor of two (the ratio of IF to baseband bandwidth) over that needed for baseband recording.

In this article the requirements that must be met to insure successful baseband recording and playback are given. Recording and playback procedures are developed to insure that these requirements are met and performance results from tests conducted at CTA 21 are tabulated.

II. Spectrum of Baseband Signal (Ref. 1)

The baseband signal $b(t)$ is given by

$$b(t) = Kd(t)s(t)$$

where

$s(t)$ = square wave subcarrier of unit amplitude and fundamental frequency f_{sc}

$d(t)$ = binary data waveform taking on the values of -1 and 1 with symbol rate f_d depending on whether the data symbol is 1 or 0 respectively

and

K = constant

Expanding $s(t)$ in a Fourier series (and without loss of generality choosing the reference such that $s(t)$ is even) yields

$$b(t) = Kd(t) \sum_{n=1}^{\infty} a_n \cos n2\pi f_{sc} t$$

where

$$a_n = \frac{4}{\pi n} \sin \frac{n\pi}{2} = \begin{cases} (-1)^{\frac{n-1}{2}} \frac{4}{n\pi} & n \text{ odd} \\ 0 & n \text{ even} \end{cases}$$

Thus the baseband spectrum consists of the data spectrum centered on the odd harmonics of the square-wave subcarrier.

III. Degradation Due to Loss of Subcarrier and Data Harmonics (Ref. 1)

Since $d(t)s(t)$ takes on only the values ± 1 , the available power in the baseband signal is K^2 . However, since the bandwidth of this signal is infinite, only a finite number of sidebands are actually preserved. The available power if subcarrier harmonics above the N th are filtered out (assuming the data spectrums around the N harmonics are preserved, i.e., data rate is low compared to subcarrier frequency) is given by

$$P_N = K^2 \frac{8}{\pi^2} \sum_{\substack{n=1 \\ (n \text{ odd})}}^N \frac{1}{n^2}$$

and thus the degradation in dB is

$$\rho_{dB} = 10 \log_{10} \frac{P_N}{K^2} = 10 \log_{10} \frac{8}{\pi^2} \sum_{\substack{n=1 \\ (n \text{ odd})}}^N \frac{1}{n^2}$$

Values of ρ_{dB} versus N are given in Table 1.

When the data rate is not small compared to the subcarrier frequency, additional degradation occurs due to loss of data sidebands around the subcarrier harmonic near the edge of the system passband. The amount of degradation can be approximated by assuming a symbol stream of alternating 1's and 0's (yielding the largest possible data bandwidth produced by a square wave of fundamental frequency $f_d/2$) and assuming only a finite number of upper data sidebands on the highest subcarrier harmonic are preserved (all the lower sidebands are assumed to be preserved). Under these assumptions the baseband signal $b(t)$ can be written

$$b(t) = Kd(t) \sum_{n=1}^{N-2} a_n \cos n2\pi f_{sc} t + K \left[a_N \cos N2\pi f_{sc} t \sum_{j=1}^{\infty} a_j \cos j\pi f_d t \right]^J$$

where

N = highest subcarrier harmonic preserved

$$a_j = \frac{4}{\pi j} \sin \frac{j\pi}{2} = \begin{cases} (-1)^{\frac{j-1}{2}} \frac{4}{\pi j} & j \text{ odd} \\ 0 & j \text{ even} \end{cases}$$

$[]^J$ = indicates that all data sidebands up to and including the J th upper sideband are preserved.

The available power is given by

$$P_{N,J} \cong K^2 \frac{8}{\pi^2} \sum_{\substack{n=1 \\ (n \text{ odd})}}^{N-2} \frac{1}{n^2} + K^2 \frac{8}{\pi^2 N^2} \left(0.5 + \frac{4}{\pi^2} \sum_{\substack{j=1 \\ (j \text{ odd})}}^J \frac{1}{j^2} \right)$$

and thus

$$\rho_{dB} = 10 \log_{10} \frac{P_{N,J}}{K^2}$$

$$= 10 \log_{10} \frac{8}{\pi^2} \left[\sum_{\substack{n=1 \\ (n \text{ odd})}}^{N-2} \frac{1}{n^2} + \frac{1}{N^2} \left(0.5 + \frac{4}{\pi^2} \sum_{j=1}^J \frac{1}{j^2} \right) \right]$$

Values of ρ_{dB} versus N and J are given in Table 2.

IV. Recorder Bandwidth and Phase Linearity Limitations

In general the tape recorder bandwidth is directly proportional to tape speed. For example, the Ampex FR 2000A and Honeywell 96 recorders have bandwidths of 500 kHz at 76.2 cm/s (30 ips), 1 MHz at 152.4 cm/s (60 ips), and 2 MHz at 304.8 cm/s (120 ips). Thus it is apparent that a tradeoff exists between data degradation and tape usage (at 304.8 cm/s (120 ips) a reel of tape lasts approximately 15 minutes).

In addition, because of the coherent detection process used in the DSN it is important to preserve the phase relationship of the subcarrier and data components. Derivation of degradation due to phase nonlinearities is given in Ref. 2. In selecting an appropriate speed, both the amplitude and phase response of the recorder as a function of tape speed must be considered.

V. Requirements to Minimize Degradation for a Given Recorder Bandwidth

The following requirements must be met to minimize degradation in the baseband recording and playback process for a given recorder bandwidth.

- (1) Linear operation and proper phasing of the receiver telemetry channel.
- (2) Linear operation of the recorder in both the record and playback modes.
- (3) Proper input levels to the Subcarrier Demodulator Assembly (SDA).
- (4) Sufficiently small variations in tape velocity to insure proper operation of downstream equipment requiring phase lock.

A recording and playback procedure to insure that these requirements are met is developed in the next section.

VI. Procedure

The development of the portion of the procedure to meet each requirement is given below. At the end of the section the overall procedure is summarized.

A. Requirement 1

The Block III receiver telemetry channel IF and video amplifiers are designed for maximum output levels of +6 dBm (sine, 50 Ω) and +10 dBm (sine, 50 Ω) respectively. Since, for equal rms levels, a noise waveform has 3 dB higher amplitude peaks (using a 95% of the peaks criteria) than does a sine wave, the output levels of the IF and video amplifiers should not exceed +3 and +7 dBm, respectively. Levels of 0 and +5 dBm are specified in the procedure to allow some safety margin.

The Block IV receiver telemetry channel uses an internal AGC to maintain linearity at an output level of approximately +10 dBm (50 Ω), and thus no adjustment is required.

Correct phasing of the phase detector in either the Block III or Block IV receivers must be insured by following the standard phasing procedures for the receiver. The Block III receiver must be rephased each time the telemetry bandwidth is changed, while the Block IV receiver has separate phase adjustments for each bandwidth and requires only one initial adjustment.

B. Requirement 2

Standard procedures for calibrating the analog recorder use a 1-V rms sine wave input (+13 dBm, 50 Ω). The record electronics are adjusted for 1% third harmonic distortion with this input. A +5-dBm (noise) input is specified in the procedure to insure the input level is well within the linear range of the recorder.

C. Requirement 3

The Block III and Block IV SDAs are designed to operate with signal levels of -75 dBm and -70 dBm, respectively, at the output of the modulation index (step) attenuator. With the attenuator set at 0, this corresponds to a "tape input" signal level of -29 dBm and -28 dBm for the Block III and Block IV SDAs, respectively. An input level of -28 dBm is selected as a standard. In addition, the total input (signal + noise) must not exceed ± 1.4 peak (+10 dBm noise into 50 Ω). Note that this means the minimum signal-to-noise ratio, $S/N = -28 - 10 = -38$ dB.

Given the value of ST_b/N_o in dB the signal-to-noise ratio out of the recorder can be determined by observing that

$$\frac{S}{N} = \frac{S}{N_o W} = \frac{ST_b}{N_b} \times \frac{1}{T_o W} = \frac{ST_b}{N_o} \times \frac{f_d}{W}$$

and thus,

$$\left(\frac{S}{N}\right)_{dB} = \left(\frac{ST_b}{N_o}\right)_{dB} + 10 \log_{10} f_d - 10 \log_{10} W$$

where $f_d = 1/T_b$ = data rate and W is either the telemetry noise bandwidth or twice the recorder noise bandwidth, whichever is smaller.

Denote the output level of the recorder in dBm as $R_o = S + N$. Thus,

$$\frac{S}{R_o} = \frac{S}{S+N} = \frac{S/N}{S/N+1}$$

Solving for S yields

$$S = \frac{R_o \times S/N}{S/N+1}$$

For most cases of interest

$$\frac{S}{N} \ll 1$$

and thus

$$S \cong R_o \times \frac{S}{N}$$

or in dBm

$$S = R_o + \left(\frac{S}{N}\right)_{dB}$$

The attenuator setting A necessary to reduce this level to the required value of -28 dBm can be determined by observing that

$$S - A = -28 \text{ dBm}$$

or, in dB

$$A = S + 28 = R_o + \left(\frac{S}{N}\right)_{dB} + 28$$

D. Requirement 4

A theoretical analysis of the effect of tape velocity errors on the operation of downstream equipment requiring phase lock (the SDA and SSA) is difficult and has not been attempted. Experience gained from tests at CTA 21 show that current generation instrumentation recorders (specifically the Ampex FR 2000A and Honeywell 96) have sufficiently low tape velocity variations to permit playback at signal-to-noise ratios approaching telemetry system threshold conditions. This is not true of older-generation recorders (such as the Ampex FR 1400 for example).

The recording and playback procedures can be summarized as follows:

1. Recording

- (1) Phase the telemetry string at the required telemetry bandwidth setting.
- (2) (Block III receiver only) With no signal applied to the receiver, set the manual gain control (MGC) to correspond to the predicted carrier level (for strong signal conditions the actual receiver input signal-to-noise ratio should be simulated). Using a true reading rms voltmeter terminated in 50 Ω , adjust the IF attenuator for 0 dBm (50 Ω) at the IF linear output port.
- (3) (Block III receiver only) With the IF attenuator set as determined in step 2, adjust the video output for 5 dBm (50 Ω) and connect to recorder input terminated in 50 Ω .
- (4) (Block IV receiver only) Attenuate the video output to a level of 5 dBm (50 Ω) and connect to recorder input terminated in 50 Ω .

2. Playback

- (1) Using a true reading rms voltmeter terminated in 50 Ω , measure the recorder reproduce output level in dBm. Call this level R_o .
- (2) Let W = either the telemetry noise bandwidth or twice the recorder bandwidth, whichever is smaller, and compute

$$\left(\frac{S}{N}\right)_{dB} = \left(\frac{ST_b}{N_o}\right)_{dB} + 10 \log_{10} f_d - 10 \log_{10} W$$

where f_d is the bit rate.

- (3) Insert attenuator between reproduce output and input to SDA balanced modulator and compute setting A in dB as follows:

$$A =_{dB} R_o + \left(\frac{S}{N} \right)_{dB} + 28$$

Set the SDA step attenuator at 0 dB.

3. Test Procedures and Results

A series of baseband recording and playback tests using the above procedures were conducted at CTA 21 using the Block III receiver and the following test procedure (see Fig 2).

- (1) Phase the telemetry string at the required telemetry bandwidth setting using standard procedures
- (2) With the Simulation Conversion Assembly (SCA) set for the desired data, subcarrier and modulation index, adjust the attenuator of the test transmitter for the desired ST_b/N_o using the Y-factor equipment.
- (3) Record the bit error rate (BER) in the direct "10 MHz" configuration and determine ST_b/N_o using the theoretical bit error rate curve (this also verifies the Y-factor setting of step 2).
- (4) With the simulated data applied, adjust the IF attenuator for a level of 0 dBm (50 Ω) at the output of the receiver IF amplifier and adjust the junction box preceding the video amplifier for a level of 5 dBm (50 Ω) at the output of the video amplifier.
- (5) Record the output of the video amplifier and simultaneously monitor the BER using the record and monitor configuration (output of the video amplifier properly attenuated and connected to the input of the SDA balanced modulator).
- (6) Play back the data recorded in step 5 through an attenuator connected to the SDA balanced modulator input (playback configuration). Record the BER and

determine ST_b/N_o using the theoretical bit error rate curve.

The results of these tests are tabulated in Tables 3 and 4. The direct "10 MHz" configuration is the normal real-time telemetry path whereas in the record and monitor configuration one output of the receiver video amplifier (baseband subcarrier + data) is connected to the input of the SDA balanced modulator and another to the recorder input. Comparing the record and monitor with the playback column gives the degradation due to the recorder alone. In some cases, the record and monitor configuration gives a higher signal-to-noise ratio than the direct "10 MHz" configuration. The probable cause is phase misalignment in the real-time (direct "10 MHz") path but this has not been verified. It should also be pointed out that the degradation is a function of signal-to-noise ratio with higher degradations expected at higher signal-to-noise ratios where the noise added by the recorder (both amplitude and phase) is a larger fraction of the total system noise.

V. Conclusions

A procedure to insure successful baseband recording and playback at signal-to-noise ratios (ST_b/N_o) approaching the threshold of the telemetry system has been developed. This procedure has been verified by extensive testing at CTA 21 and has been used for successful on-site playback of baseband recordings made during the Viking mission (Refs. 3-6; see also the article by G. Hamilton in this issue.) Theoretical analyses of the approximate data degradation due to limitations in bandwidth and phase linearity have been made. Since the tape recorder bandwidth is directly proportional to tape speed, a tradeoff must be made between allowable degradation and tape usage. This tradeoff is complicated by the fact that very little information on the recorder phase response is currently available, although some data have been derived from pulse response tests. Since the signal-to-noise ratio of the recorder is normally much higher (>20 dB) than the signal-to-noise ratio of the data typically recorded, it is believed that practically all of the data degradation is now due to limitations in bandwidth and phase linearity.

Acknowledgments

The efforts of J. McAllaster in maintaining the newly delivered Honeywell 96 recorder in operating condition, and the expertise and help of the Ampex representative, W. Snow, and the helpfulness, patience, and good humor of the CTA 21 station personnel are gratefully acknowledged.

References

1. Kent, S., and Molinder, J., *Telemetry Degradation Due to Loss of Subcarrier and Data Sidebands in Baseband Recording and Playback*, AE-76-193, Dec. 7, 1976 (JPL internal document).
2. Molinder, J., "Effect of Phase Distortion on Effective Signal Power — A Simple Mathematical Model," in *The Deep Space Network Progress Report 42-29*, Oct. 15, 1975, pp. 136-140, Jet Propulsion Laboratory, Pasadena, Calif.
3. Molinder, J., *Baseband Recording and Playback Procedures*, AE-76, April 15, 1976 (JPL internal document).
4. Johnston, D. W. H., private communication, August 26, 1976.
5. Caswell, R., Kent, S., and Molinder, J., *Baseband Recording and Playback Considerations*, AE-76-153, Sept. 17, 1976 (JPL internal document).
6. Caswell, R., *Baseband Recording Playback at the 64-meter Stations*, 376E-76-452, Oct. 14, 1976 (JPL internal document).

Table 1. Theoretical degradation versus highest subcarrier harmonic (N) preserved

N	ρ_{dB}
1	-0.91
3	-0.45
5	-0.30
7	-0.22
9	-0.18

Table 2. Theoretical degradation versus highest subcarrier harmonic (N) and highest square-wave upper data harmonic (J) preserved

N	J	ρ_{dB}
1	1	-1.34
1	3	-1.13
1	5	-1.06
3	1	-0.50

Table 3. CTA 21 Baseband recording and playback tests (Ampex FR 20002 A)

Date	Data rate	Subcarrier frequency	Tape speed, cm/s (in /s)	SNR (ST_b/N_o or ST_s/N_o), dB			Degradation, dB	
				Direct "10 MHz"	Record and Monitor Direct (TLM)	Playback	Total	Recorder
11-11-75	16 kbits/s (32,6) ¹	240 kHz	76.2 (30)		2.4	0.85		1.55
				4.15	3.9	2.75	1.4	1.15
					5.55	3.65		1.9
			152.4 (60)		3.75	3.15		0.6
			304.8 (120)		3.75	3.45		0.3
9-23-75	16 kbits/s (32,6)	240 kHz	76.2 (30)	3.45	3.75	2.7		1.05
			152.4 (60)		3.75	1.75		2.0
			304.8 (120)		3.8	2.7		1.1
8-7-75	64 bits/s (UC)	25.6 kHz	76.2 (30)	3.9	3.2	2.45	1.45	0.75
8-7-75	2048 bits/s (UC)	26.624 kHz	76.2 (30)	5.2	4.4	3.8	1.4	0.6
7-31-75	2048 bits/s (UC)	26.624 kHz	76.2 (30)	3.9	3.3	2.25	1.65	1.05
7-28-75	64 bits/s (UC)	25.6 kHz	76.2 (30)	3.9	2.5	1.1	2.8	1.4
7-28-75	64 bits/s (UC)	102.4 kHz	76.2 (30)		2.9	1.7		1.2
7-9-75	64 bits/s (UC)	25.6 kHz	76.2 (30)	3.65	2.65	0.7	2.95	1.95
7-9-75	16 kbits/s (UC)	240 kHz	152.4 (60)	5.4	4.95	4.5	0.9	0.45
7-8-75	64 bits/s (UC)	25.6 kHz	76.2 (30)		3.0	1.05		1.95

¹(32,6) Block coded UC = Uncoded

Table 4. CTA 21 baseband recording and playback tests (Honeywell 96)

Date	Data rate	Subcarrier frequency, kHz	Tape speed, cm/s (in /s)	SNR (ST_b/N_o or ST_s/N_o), dB			Degradation, dB	
				Direct "10 MHz"	Record and Monitor	Playback	Total	Recorder only
2-24-76 ↓	16 kbits/s (32,6) ¹ ↓	240 ↓	304.8 (120)		4.5	4.1		0.4
			152.4 (60)		5.0	4.55		0.45
			152.4 (60)		2.9	2.45		0.45
			76.2 (30)		5	3.45		1.55
3-2-76 ↓	16 kbits/s (32,6) ↓	240 ↓	152.4 (60)		4.25	3.45-3.75		0.8-0.5
			76.2 (30)		4.25	3.05		1.2
			76.2 (30)		4.3	2.95-3.15		1.35-1.15
3-23-76 ↓	16 kbits/s (32,6)	240	152.4 (60)		4.35	4.05		0.3
		360	152.4 (60)		4.3	3.65		0.65
	33-1/3 bits/s (UC)	24	38.1 (15)		6.75	5.85		0.9

¹(32,6) Block coded UC = Uncoded

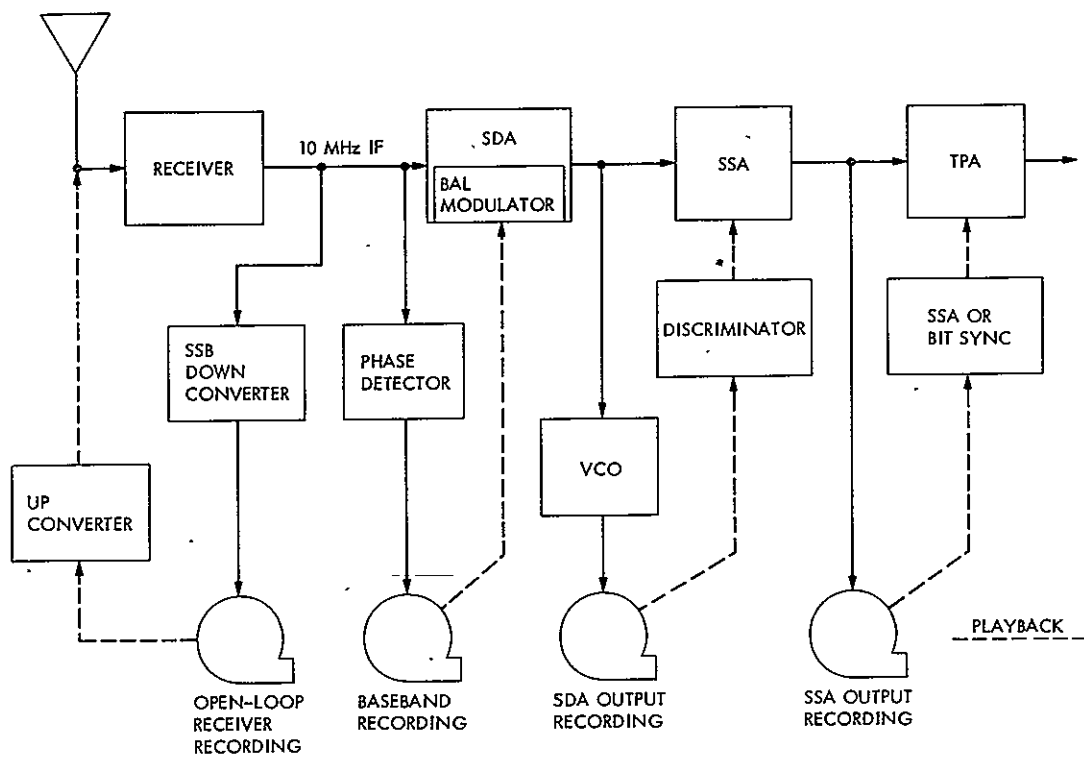


Fig. 1. Analog recording techniques

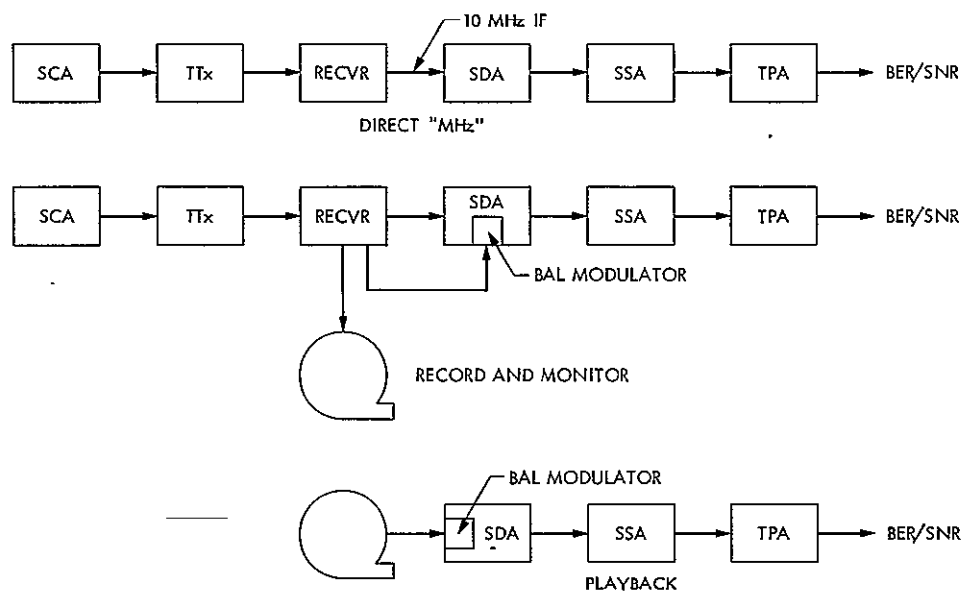


Fig. 2. Baseband recording and playback test configurations

D20 64, 12A

N77-19111

Simulation of Time Series by Distorted Gaussian Processes

C. A. Greenhall
TDA Engineering Office

Distorted stationary gaussian processes can be used to provide computer-generated imitations of experimental time series. A method of analyzing a source time series and synthesizing an imitation is shown, and an example using X-band radiometer data is given

I. Motivation

The simulation technique described here was motivated by the problem of weather-induced degradation of X- and K-band communication. A sequence of X-band noise temperature measurements is being gathered at Deep Space Station 13 (Goldstone); it is desired to use these data to study the effects of weather fluctuations on space communication. One can, for example, predict the percentage of time (out of a given year-quarter, for example) that the noise temperature exceeds a given level, but then no information about the variation of noise temperature with time is used. To study the effect of these fluctuations, one would like to have typical samples of noise temperature data to serve as inputs to communication system models. Computer-generated pseudorandom synthetic data have advantages over the real data, provided that the synthetic data preserve essential features of the real data: Such synthetic data can be controlled simply by changing parameters. As much (and only as much) data as needed can be generated. It is free of the inevitable bugs that infect the

data-gathering process (but see Sections V and VI). Moreover, the synthetic data are more *random* than the original data, in the sense that the original data, once gathered and plotted, are *known*, whereas the exact course of the synthetic data is not. To change the sample function entirely, one need only start the program's pseudorandom-number generator at a different place. As M. Easterling put it, the real data are never *typical*.¹

The noise temperature data are nowhere near gaussian. (Fig. 1.) This makes them more difficult to simulate. They motivate the search for a *general-purpose* simulation method, one that can be used to imitate a wide variety of time series. The method used here is: generate a stationary gaussian process having certain correlations, and distort it by a zero-memory nonlinearity so that the result has a desired marginal distribution. The problem is how to choose the correlations.

¹Private communication

II. Ideas Leading to Present Method

We wish to produce a random process Y_0, Y_1, \dots that in some way imitates a source time series y_1, y_2, \dots, y_N . There are two broad questions:

- (1) What statistical properties of the y_i are to be duplicated?
- (2) What class of processes shall the Y_i belong to?

The answers to these two questions depend on each other, of course. Let us start with some tentative answers: The process (Y_i) is stationary. Its marginal distribution function

$$P\{Y_i \leq y\}$$

and a certain number of correlations

$$\rho(Y_i, Y_{i+t}), \quad t = 1 \text{ to } n$$

agree with the sample distribution function and correlations of the source series. This leads to another question: Is there a stationary process having *arbitrary* prescribed marginal distribution function F (with finite second moment) and (non-negative definite) correlation function λ_1 to λ_n ? (Here, λ_t is the correlation for lag t .) The answer is quickly no, for if the distribution described by F is not symmetric about its mean², then there is a number $\lambda_{\min} > -1$ such that

$$\rho(Y_1, Y_2) \geq \lambda_{\min}$$

for any random variables Y_1, Y_2 whose marginal distributions are both F . For such F , the λ_t cannot be allowed to get too close to -1 . Given F , then, there is a set C_F of permissible correlation sequences $(\lambda_1, \dots, \lambda_n)$. However, it is unlikely, perhaps even impossible, that the sample correlations of (y_i) fall outside C_F for the sample distribution function F . So far, the proposed answer to questions (1) and (2) seems feasible.

It is time to restrict the answer to (2) to a class of processes that are easy to generate to order. We say that (Y_i) is a *stationary distorted gaussian process* if, for some function g ,

$$Y_i = g(X_i), \quad (1)$$

where X_1, X_2, \dots is a stationary *standard* (mean 0, variance 1) gaussian process. The function g can be chosen to give the

Y_i any desired marginal distribution function F . In fact, we can take

$$g(x) = F^{-1}(\Phi(x)), \quad (2)$$

where F^{-1} is the (generalized) inverse of F , and Φ is the standard gaussian distribution function. Then g is nondecreasing. There is an invertible function Λ_g such that the correlations λ_t of the Y_i are related to the correlations ρ_t of the X_i by

$$\lambda_t = \Lambda_g(\rho_t) \quad (3)$$

(Ref. 1). The program now appears to be: Given a distribution function F and a correlation sequence $(\lambda_1, \dots, \lambda_n)$ in C_F , let

$$\rho_t = \Lambda_g^{-1}(\lambda_t), \quad t = 1 \text{ to } n \quad (4)$$

Construct a stationary standard gaussian process (X_i) with correlations ρ_1 to ρ_n . Then the Y_i have the desired marginal F and correlations λ_t .

A program similar to this was carried out by Posner and Zeigler (Ref. 2), using $g(x) = |x|$ (not a monotonic function), and specifying two nonnegative correlations λ_1, λ_2 . They noted that they had not proven that *any* (nonnegative) (λ_1, λ_2) in C_F (where F is the distribution function of a "half-gaussian") can be reached by Eq. (3), where ρ_1, ρ_2 are the correlations of a gaussian process. This same question must be asked of the general program above. Another way to put it is: Given $(\lambda_1, \dots, \lambda_n)$ in C_F , define (ρ_1, \dots, ρ_n) by Eq. (4), and let $\rho_{-t} = \rho_t$. Is the sequence

$$\rho_{-n}, \dots, \rho_{-1}, 1, \rho_1, \dots, \rho_n$$

nonnegative definite? If it is not, the process (X_i) does not exist.

E. Rodemich found a counterexample that shows that the program fails in general. Consider the three-point sample space $\{1, 2, 3\}$, with $P\{i\} = 1/3$. For $i = 1$ to 3 , let $Y_i(\omega) = \sqrt{2}$ if $\omega = i$, and $Y_i(\omega) = -1/\sqrt{2}$ otherwise. Then Y_i is standard, and $EY_i Y_j = -1/2$ if $i \neq j$. Suppose that X_1, X_2 , and X_3 are *jointly* gaussian with standard marginals, and that g is a function such that $g(X_1), g(X_2), g(X_3)$ have the same marginals and correlations as the Y_i . Then with probability 1, $g(X_i)$ only takes values $\sqrt{2}$ and $-1/\sqrt{2}$, and

$$g(X_1) + g(X_2) + g(X_3) = 0 \quad (5)$$

²We owe this observation to E. Rodemich.

Let $A = \{x: g(x) = \sqrt{2}\}$. Then $P\{X_i \in A\} = 1/3$. The rank of the distribution of (X_1, X_2, X_3) must be 1, for suppose, say, that (X_1, X_2) had a density. Then $P\{X_i \in A, X_2 \in A\} > 0$, which is impossible, for if X_1 takes a value in A , then Eq. (5) implies that X_2 does not. On the other hand, if the rank is 1, then $X_2 = \pm X_1, X_3 = \pm X_1$; therefore at least two of the X_i are equal, which is again impossible. The process (Y_i) cannot be simulated by a stationary distorted Gaussian process. Notice, however, that we used a *process* instead of a *time series* for this example. The *finite* time series

$$(1/\sqrt{2})(2, -1, -1, 2, -1, -1, \dots, -1) \quad (6)$$

won't work for the example unless correlations are computed cyclically, which we don't want to do. We conjecture that the sample distribution and correlations of any finite time series can be obtained by a stationary distorted Gaussian process.

For the time being, we are stepping around the problem, instead of surmounting it. One can always specify the correlations of a gaussian process, as long as they are nonnegative definite. Therefore, let us take the source time series (y_i) , measure its sample distribution function F , and use F to compress the y_i into a time series (x_i) whose sample distribution function is approximately Φ . In fact, let

$$x_i = g^{-1}(y_i) = \Phi^{-1}(F(y_i)). \quad (7)$$

Measure the sample correlations ρ_1, \dots, ρ_n of the x_i . These will be nonnegative definite (if defined correctly), so a gaussian process (X_i) can be generated having these correlations. Finally, use Eq. (1) to expand the X_i into a process (Y_i) whose marginal distribution approximately equals the sample distribution of the y_i . Moreover, when (Y_i) and (y_i) are compressed by g^{-1} to (X_i) and (x_i) , respectively, the correlations of the X_i equal the sample correlations of the x_i . Note that (X_i) is a true gaussian process, whereas the *most* that can be said about the x_i is that their sample distribution is approximately gaussian.

III. Analysis of Source Time Series

The sample distribution function of the source time series y_1, \dots, y_N is given by

$$F(y) = (\text{number of } y_i \leq y) / N.$$

A bin-sort of the data will yield the values of F at the bin boundaries. If one agrees to interpolate F linearly between the

boundaries, then Eq. (7) yields a sequence (x_i) whose sample distribution function is a step-function approximation to Φ . To make this approximation good, the jumps of F should be small, and the bin boundaries close enough together to allow linear interpolation. In implementing Eq. (7), it is also a good idea to truncate Φ^{-1} at 4 and -4, say. This avoids the possibility of the linear interpolation producing grossly over-size x_i for those y_i that are very close to the maximum bin boundary.

One computes the sample mean, covariances, and correlations of the x_i :

$$\mu = (1/N) \sum x_i,$$

$$r_t = (1/N) \sum_{i=1}^{N-t} (x_i - \mu)(x_{i+t} - \mu),$$

$$\rho_t = r_t / r_0, \quad t = 0 \text{ to } n.$$

If the previous work was done well, μ should be close to 0, and r_0 to 1. The ρ_t are guaranteed to be nonnegative definite.

The functions F and ρ serve as inputs to the synthesis algorithm given in the next section.

IV. Synthesis of Artificial Time Series

We are given tabulated values of a distribution function F , and a sequence of correlations $\rho_0, \rho_1, \dots, \rho_n$, where $\rho_0 = 1$. The main job is to generate a stationary standard gaussian process X_0, X_1, \dots such that

$$EX_i X_{i+t} = \rho_t, \quad t = 0 \text{ to } n.$$

Then the process Y_0, Y_1, \dots that we seek is given by

$$Y_i = F^{-1}(\Phi(X_i)), \quad (8)$$

where F^{-1} is executed by linear interpolation in the F -table.

Here is an algorithm that generates the X_i as an autoregressive scheme. Let Z_0, Z_1, \dots be a sequence of independent standard gaussians. Execute the following steps in order:

Step 0. Set

$$g_0 = 1, c_{00} = 1, X_0 = Z_0$$

Step i , $i = 1$ to n . Set

$$a_j = \frac{1}{g_j} \sum_{k=0}^j \rho_{i-k} c_{jk}, \quad j = 0 \text{ to } i-1$$

$$g_i = 1 - \sum_{j=0}^{i-1} a_j^2 g_j$$

$$c_{ij} = - \sum_{k=j}^{i-1} a_k c_{kj}, \quad j = 0 \text{ to } i-1$$

$$c_{ii} = 1$$

$$X_i = \sqrt{g_i} Z_i - \sum_{j=0}^{i-1} c_{ij} X_j \quad (9)$$

Step i , $i > n$. Set

$$X_i = \sqrt{g_n} Z_i - \sum_{j=0}^{n-1} c_{nj} X_{i-n+j} \quad (10)$$

This algorithm constructs a lower triangular matrix $C = (c_{ij})$ and a nonnegative diagonal matrix $G = \text{diag}(g_0, \dots, g_n)$ such that $CRC^T = G$, where $R = (\rho_{i-j})$, with $\rho_{-i} = \rho_i$. The vectors (a_j) are the rows of C^{-1} .

The algorithm goes through if and only if R is nonnegative definite and has rank n or $n+1$. Otherwise, the algorithm will run into a negative g_i , in which case R is indefinite, or a $g_m = 0$ for some $m < n$, in which case $R_m = (\rho_{i-j})$, $i, j = 0$ to m is nonnegative definite and singular, and the full matrix R may or may not be nonnegative definite.

The synthesis procedure has been realized in a documented MBASIC program TSS (Time Series Synthesis).

V. Example

Figure 1 shows a plot of X-band noise temperature measurements made by a radiometer at the Goldstone DSCC from Day 207 to Day 214 of 1976. The data have pre-processed so that they represent noise temperature above quiescent as seen at zenith. The data come once every two minutes, but the plot samples them only once every 20 minutes. The gaps indicate missing data; the program that computes correlations maintains the correct time relationships

among the rest of the data. The sharp negative peaks are caused by equipment malfunction; nevertheless, for the purpose of this exercise, they were not excised.

Figure 2 shows five weeks worth of output of the Time Series Synthesis program, whose inputs were the distribution function and correlations obtained by the procedure of Section III from the data of Fig. 1. Only the correlations $\rho_{20k \text{ min}}$, $k = 1$ to 13, were used; thus the order n of the autoregression is 13, and the output of the program represents 20-minute samples.

VI. Remarks

Comparing Figs. 1 and 2, we see that the synthesis program does produce sharp irregular peaks resembling those of the source data. The peaks of the synthetic data seem to be more clumped together than those of the source data, and the quiet periods of the synthetic data are noisier than those of the source. The spurious negative peaks of the source cause strange-looking clumps of negative excursions in the synthetic data. Obviously, bad points should be removed when putting a time series through the analysis procedure; alternatively, the distribution function can be fixed before giving it to the synthesis program.

Some objections to the technique come to mind.

First, there is no objective criterion for acceptance of the output of the synthesis program. It does have certain statistical properties in common with the source time series, the ones it was designed to have, but other than that, one can perhaps only ask whether it "looks right."

The second objection applies to radiometer data. The important features of Fig. 1 are the large positive peaks, for during these periods, X-band communication is considerably degraded. This time series is severely compressed by Eq. (7) into a gaussian mold; the peaks become insignificant and can affect the correlations of the compressed series only very little. Most of the information in the correlations comes from the uninteresting quiet periods. Yet, these correlations strongly affect the peaks of the synthetic data. Perhaps this is why the peaks of the synthetic data tend to come in clumps. Actually, the peaks of the source data are probably caused by phenomena (clouds or rain) that are independent of the phenomena that cause the small fluctuations of the quiet periods. We may be fooling ourselves if we treat these data as a *single* time series.

Third, it has been objected that the compression-plus-correlation technique requires that the source time series be saved in case one wants to improve the distribution function

and correlations by using additional source series. As an illustration, consider two source series y_1, \dots, y_N and y'_1, \dots, y'_N of the same length, which give rise to compressed series (x_i) and (x'_i) , distribution functions F and F' , and correlations ρ and ρ' . The distribution function of the combined source series is $F'' = (F + F')/2$. One should use F'' to compress $y_1, \dots, y_N, y'_1, \dots, y'_N$ to a series

$$x''_1, \dots, x''_N - \text{gap} - x''_{N+1}, \dots, x''_{2N}.$$

Then the correlation function ρ'' of the x''_i would be computed. However, this may not be necessary. The x_i and x'_i series both have an approximately gaussian sample distribution; it seems reasonable to use the series

$$(x'''_i) = (x_1, \dots, x_N - \text{gap} - x'_1, \dots, x'_N)$$

in place of (x''_i) for computing the new correlations. If the sample means and variances of (x_i) and (x'_i) are close to 0 and 1, respectively, then the sample correlation of (x'''_i) is close to

$(\rho + \rho')/2$. In this case, it is sufficient to save only F and ρ , instead of the source series.

Finally, it must be admitted that the idea of computing correlations after compressing is an expediency created to dodge a difficult mathematical problem, the relationship between marginals and correlations for nongaussian processes and finite time series. In fact, the dodge itself may be illusory; our "gaussian correlation" technique will not work at all well on the time series of Eq. (6). But this time series comes from the very counterexample which we used as an excuse to go to the gaussian correlation technique. Perhaps what we are *really* dodging is the numerical evaluation of Λ_g^{-1} in Eq. (4). More mathematical effort is needed to clarify the situation. In the meantime, the present method works in practice.

The conjecture that appears after (6) is false. Provided that (6) is long enough, no stationary distorted gaussian process with nondecreasing distortion function g can have the same distribution and correlations as (6). This fact makes the compression-plus-correlation technique more attractive, for we can guarantee that the analysis and synthesis procedures can be carried out, whatever the source time series (y_i) . However, for pathological examples such as (6), the sample distribution function of the compressed series (x_i) will not be close to Φ .

References

1. Rodemich, E. R., "Spectral Estimates Using Nonlinear Functions," *Annals of Mathematical Statistics*, Vol. 37, No. 5, October 1965.
2. Posner, E. C., and Zeigler, F. J., "A Technique for Generating Correlated X-band Weather Degradation Statistics," in *The Deep Space Network Progress Report 42-35*, Jet Propulsion Laboratory, Pasadena, Calif., Oct. 15, 1976.

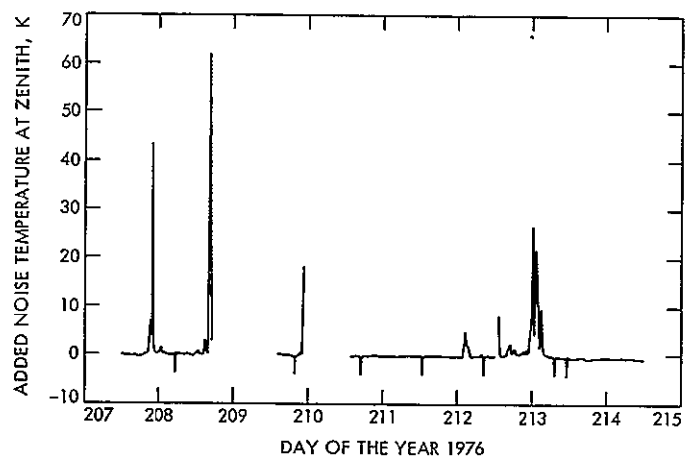


Fig. 1. One week of X-band radiometer data

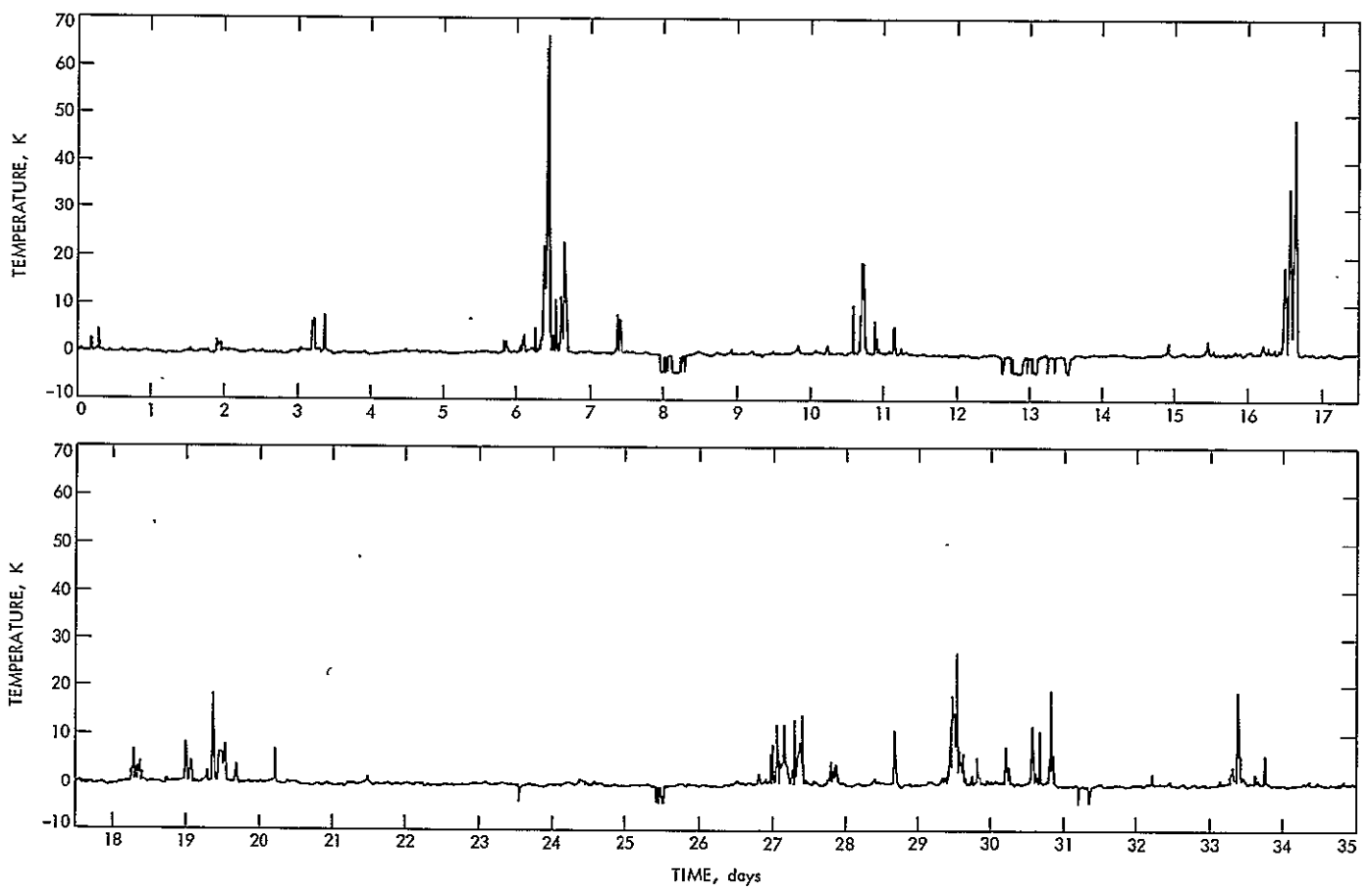


Fig. 2. Five weeks of synthetic data

N77-19112

Computer Modeling of a Regenerative Solar-Assisted Rankine Power Cycle

F. L. Lansing
DSN Engineering Section

Advanced solar-driven thermodynamic cycles for electric power generation are under study for application of the DSN Energy Conservation Project at Goldstone, California. This article presents a detailed interpretation of the computer program that describes the performance of one of these cycles; namely, a regenerative Rankine power cycle. Water is used as the working medium throughout the cycle. The solar energy collected at relatively low temperature level presents 75 to 80 % of the total heat demand and provides mainly the latent heat of vaporization. Another energy source at high temperature level superheats the steam and supplements the solar energy share. A program summary and a numerical example showing the sequence of computations are included. The outcome from the model comprises line temperatures, pressures, component heat rates, specific steam consumption, percentage of solar energy contribution, and the overall thermal efficiency.

I. Introduction

One of the problems associated with the effort to convert solar thermal energy to electric power via power cycles, is the low conversion efficiency. Solar energy collected by low cost flat plate collectors can inefficiently reach a temperature level of about 100°C. Such a temperature makes the thermal-to-mechanical energy conversion efficiency on the order of 10 %. On the other hand, expensive solar concentrators (ranging from 2 to 10 times the cost of flat plate collectors) can achieve much higher temperatures with a conversion efficiency in the order of 20 %.

As a candidate solution to the efficiency versus cost problem, several investigators (Refs. 1, 2 and 3) have recently studied an advanced solar-assisted Rankine cycle with two regenerators. In this advanced cycle, solar energy is used as the

primary source of heat for supplying the latent heat of vaporization for the working fluid. Evaporation temperatures consistent with the capability of low-cost solar collectors are sufficient. This means that the evaporation temperature will range from 90°C for flat plate collectors to 160°C for low concentration ratio¹ types.

A thermal superheater utilizing a secondary source of energy at a high temperature level is added. The superheater will supplement the solar energy share and will elevate the maximum cycle temperature to that attained in commercial power plants.

¹There are several definitions in the literature for this ratio. The concentration ratio in this work refers to the ratio of the projected area of the opening receiving the Sun rays to the projected area of the absorbing tube(s).

The choice of the working fluid in this cycle is restricted to water only. The chemical instability of other candidates of organic working fluids prohibits their application at temperatures above 300°C. Water is also a nonhazard material; it is nontoxic, easily detectable and nonflammable. Moreover, the latent heat of water is the largest quantity of energy compared with liquid sensible heat or vapor superheat. This advantage makes the superheat share supplied by the secondary energy source small compared to the latent heat share contributed by the Sun. The overall arrangement of the advanced cycle results in a significantly higher thermal efficiency (about double) and a reduction of collector size (about one half) compared with a simple Rankine cycle without superheat that is 100 % powered by solar energy.

Definitions of terms used appear at the end of this article.

II. Thermodynamic Cycle

The system components and the states of the working fluid are shown in the flow diagram (Fig. 1) on the temperature entropy diagram (Fig. 2) and the enthalpy-entropy (Mollier) diagram (Fig. 3). The advanced Rankine power cycle is composed of the same simple Rankine cycle components; namely, a boiler, a superheater, a turbine, a condenser and a pump, in addition to two extra heat exchangers; a vapor-vapor regenerator and a vapor-liquid regenerator.

The cycle of events is described as follows. Starting from the condenser end as shown in Fig. 1, the condensate (state 1) as saturated water is pumped to state 2 from the condenser pressure, P_c , to the evaporation pressure, P_e , in the boiler. Prior to the boiler entrance section (state 3), the water passes through the vapor-liquid heat exchanger and picks up some regenerative heat. In the solar powered boiler, the accumulated solar energy provides the latent heat of vaporization at the corresponding boiler pressure. A set of low-cost high-temperature flat-plate collectors or low-to-medium concentration ratio types can be used as the boiler. The evaporation temperature, t_e , can vary from 90°C for flat-plate types to 160°C for medium concentration types. The evaporation pressure will vary from 0.7 to 6 atm depending on the above collection temperature. It is important to note that the cycle can also be operated as a "waste-heat assisted" Rankine cycle by replacing the low-level-temperature solar heat by any other source of waste heat such as engine exhaust gases if available.

The dry and saturated water vapor (state 4), leaves the boiler for the vapor-vapor heat exchanger where it is superheated with regenerative heat to state 5. The high temperature superheater then follows to raise the maximum cycle temperature to around 600°C (state 6) where the heat is added by the

secondary source of energy. The fuel used in the superheater can be of any phase (solid, liquid, or gaseous) and it presents a small fraction (20 to 25 %) of the total external heat added to the cycle.

Adiabatic expansion of the superheated steam in the turbine will produce the mechanical work required. The turbine exhaust steam (state 7), still at high temperature, is used to supply the two regenerative heat quantities; in the vapor-vapor heat exchanger to state 8 and in the vapor-liquid heat exchanger to state 9. The only heat rejection process in the cycle takes place in the condenser from state 9 to state 1 and the cycle is repeated.

The operational function of the two extra regenerators in the cycle is to reduce the heat input without affecting the network output. This function results in a large increase in the thermal efficiency.

III. Thermodynamic Properties

A. Enthalpy Scale

The enthalpy of water is calculated based on a reference temperature of 0°C, i.e., the enthalpy of saturated water at 0°C is 0 kcal/kg. The following are expressions used to construct the enthalpy scale.

- (1) By approximating the specific heat of water liquid in the range of operating temperatures (up to 160°C) to be 1 kcal/kg°C, the enthalpy of saturated water liquid at $t^\circ\text{C}$ is equal to

$$H_f = t, \text{ kcal/kg} \quad (1)$$

- (2) The latent heat of evaporation expression for water in kcal/kg is

$$H_{fg} = 597.8 - 0.583 t \quad (2)$$

where t is the saturation temperature in °C, or

$$H_{fg} = 757.05 - 0.583 T \quad (3)$$

where T is the saturation temperature in K. The error in both expressions, Eqs. (2) and (3), is found to be ± 0.4 kcal/kg

- (3) From Eqs. (1) and (2), the enthalpy of saturated water vapor at temperature $t^\circ\text{C}$ is given by

$$H_g = 597.8 + 0.417 t, \text{ kcal/kg} \quad (4)$$

- (4) The specific heat at constant pressure of superheated steam can be expressed approximately by a linear relationship with the absolute temperature T ,

$$C = a + bT \quad (5a)$$

The mean specific heat value between temperatures T_1 and T_2 is determined from

$$C_{1,2} = \frac{1}{(T_2 - T_1)} \int_{T_1}^{T_2} C dT$$

or

$$C_{1,2} = a + \frac{b}{2} (T_1 + T_2) \quad (5b)$$

The values of a and b for steam at atmospheric pressure and in the temperature range from 400 to 1000 K, are calculated using Ref. 4, thus

$$\begin{aligned} a &= 0.3924, \text{ kcal/kg K} \\ b &= 15 \times 10^{-5}, \text{ kcal/kg K}^2 \end{aligned} \quad (6)$$

- (5) The enthalpy of superheated steam at temperature $t^\circ\text{C}$ and at a pressure equal to the saturation pressure of steam at temperature $t_s^\circ\text{C}$ is

$$H_{t,ts} = (597.8 + 0.417 t_s) + C_{t,ts} (t - t_s), \text{ kcal/kg} \quad (7)$$

where $C_{t,ts}$ is the mean value of specific heat of the superheated steam between temperatures t and t_s as determined by Eq. (5b).

B. Entropy Scale

Having established an enthalpy scale, the entropy scale can be constructed by taking an entropy datum ($s = 0$) for satu-

rated water liquid at 0°C (273.15-K). The following entropy expressions are then made:

- (1) With a liquid specific heat of $1 \text{ kcal/kg}^\circ\text{C}$, the entropy of saturated water liquid at $T \text{ K}$ is

$$S_f = \ln \frac{T}{273.15}, \text{ kcal/kg}^\circ\text{C} \quad (8)$$

- (2) Entropy of saturated steam at temperature $t_s^\circ\text{C}$ ($T_s \text{ K}$) is calculated using Eqs. (3) and (8) as

$$S_g = \ln \frac{T_s}{273.15} + \frac{(757.05 - 0.583 T_s)}{T_s} \quad (9)$$

- (3) Entropy of superheated steam at temperature $T \text{ K}$ and at a pressure equal to the saturation pressure of steam at temperature $T_s \text{ K}$ is

$$S_{t,ts} = S_g (\text{at } T_s) + \int_{T_s}^T C \frac{dT}{T}$$

or by using Eq. (5a)

$$\begin{aligned} S_{t,ts} &= \ln \frac{T_s}{273.15} + \frac{(757.05 - 0.583 T_s)}{T_s} \\ &+ a \ln \frac{T}{T_s} + b (T - T_s) \end{aligned} \quad (10)$$

where a, b are given by Eq. (6).

C. Saturation Pressure

The saturated water vapor pressure P in a millimeter of mercury (mm Hg) corresponding to a saturation temperature $T \text{ K}$ can be expressed by the formula

$$P = \text{antilog} \left[7.8553 - \frac{1555}{T} - \frac{11.2414 \times 10^{-4}}{T^2} \right] \quad (11)$$

IV. Performance Calculations

To determine the thermodynamic properties of each state and the rates of heat and work exchanged for each process in the cycle, the following set of parameters should be given:

- | | | |
|----------------------|---|--|
| Temperatures | { | 1. Evaporation temperature in the boiler, t_e °C |
| | | 2. Condensation temperature, t_c °C |
| | | 3. Maximum cycle temperature leaving the superheater, T_6 °C |
| Component Efficiency | { | 4. Isentropic efficiency of the feed water pump, E_p |
| | | 5. Isentropic efficiency of the turbine, E_T |
| | | 6. Effectiveness of the vapor-vapor heat exchanger, E_{VV} |
| | | 7. Effectiveness of the vapor-liquid heat exchanger, E_{VL} |

As mentioned before, the evaporation temperature, t_e , may vary from 90°C to 160°C, according to the collector type. The condensation temperature, t_c , depends entirely on the type of cooling medium used. It varies from 25°C (77°F) for water cooled condensers to 40°C (104°F) for air-cooled ones. The maximum cycle temperature, T_6 in Fig. 2 has a ceiling value limited by the phenomenon of creep and other metallurgical effects on materials subjected to high temperature. A design value for the temperature t_e should not exceed 600°C (1112°F) for a continuous safe operation.

Regarding the load versus the steam flow-rate control mechanism, the present study considers a "nozzle cut-off" in the turbine that is actuated by the turbine speed. The "throttling" control mechanism, on the other hand, is not recommended for its irreversibility and the associated changes in cycle configuration. Therefore, the above set of input parameters will be kept unchanged during load variations, and the only expected variation is the steam flow rate.

Considering a unit mass (1 kg) of steam flowing in the cycle, the following is an ordered sequence of calculation steps, which also presents the computer program sequence.

A. Cycle Limiting Pressures

This is determined by using Eq. (11) and the temperatures t_e and t_c for the pressures P_e and P_c , respectively.

B. Turbine Isentropic End Temperature

The turbine exit temperature in case of isentropic expansion (state 7' on Figs. 2 and 3) has to be determined first before applying the turbine isentropic efficiency E_T . There exist several approaches to solve for state 7', and all of them allow for a trial-and-error procedure. Two of these approaches are:

Approach 1: This assumes that the superheated steam follows the ideal gas relations. Accordingly, in the isentropic process from state 6 to state 7', the temperature $T_{7'}$ is determined from

$$\frac{T_{7'}}{T_6} = \left(\frac{P_c}{P_e} \right)^{\gamma - 1/\gamma} \quad (12)$$

where γ is the mean specific heat ratio between temperatures T_6 and $T_{7'}$. A first estimate of γ can be taken as 1.3 for superheated steam. The second corrected estimate of γ will be calculated after calculating the temperature $T_{7'}$ using Eq. (12), and the mean specific heat at constant pressure $C_{p,7'}$ using Eq. (5b). Usually, this approach converges very rapidly to the true temperature required, and either one or two trials is enough for engineering purposes.

Approach 2: In this approach, the entropy of states 6 and 7' are set equal using Eq. (10). The temperature $T_{7'}$ is then found by trial and error as follows:

$$S_6 = \ln \frac{T_e}{273.15} + \left(\frac{757.05}{T_e} - 0.583 \right) + a \ln \frac{T_6}{T_e} + b (T_6 - T_e)$$

$$S_{7'} = \ln \frac{T_c}{273.15} + \left(\frac{757.05}{T_c} - 0.583 \right) + a \ln \frac{T_{7'}}{T_c} + b (T_{7'} - T_c)$$

with the equality

$$S_6 = S_{7'}$$

and dividing by a for both sides, then

$$\begin{aligned} \frac{1}{a} \ln \left(\frac{T_e}{T_c} \right) + \ln \left(\frac{T_6 T_c}{T_e} \right) + \frac{757.05}{a} \left(\frac{1}{T_e} - \frac{1}{T_c} \right) + \frac{b}{a} (T_6 - T_e + T_c) \\ - \frac{b}{a} T_{7'} = \ln T_{7'} \end{aligned} \quad (13)$$

By raising both sides of Eq. (13) to the base e , and rearranging the terms, then

$$T_7' = \frac{\left(\frac{T_c T_6}{T_e}\right) \left(\frac{T_e}{T_c}\right)^{1/a}}{\exp\left[\frac{757.05}{a} \left(\frac{1}{T_c} - \frac{1}{T_e}\right) - \frac{b}{a} (T_6 + T_c - T_e)\right]} \exp\left(-\frac{b T_7'}{a}\right) \quad (14)$$

The values of a and b from Eq. (6) are substituted in Eq. (14) to yield

$$T_7' = \frac{T_6 \cdot \left(\frac{T_e}{T_c}\right)^{1.5484}}{\exp\left[1929.3 \left(\frac{1}{T_c} - \frac{1}{T_e}\right) - \frac{(T_6 + T_c - T_e)}{2616}\right]} \exp\left(-\frac{T_7'}{2616}\right) \quad (15)$$

The temperature T_7' is found by substituting an initial estimate of T_7' in the right-hand side of Eq. (15) and getting the corrected value from the left-hand side of Eq. (15), and repeating the procedure. The convergence of this approach is also rapid but needs more than three trials, as will be shown later in an example

C. Actual Turbine End-Temperature

The turbine isentropic efficiency E_T is defined as the ratio

$$E_T = \frac{\text{actual turbine work}}{\text{isentropic turbine work}} = \frac{H_6 - H_7}{H_6 - H_7'} \approx \frac{T_6 - T_7}{T_6 - T_7'} \quad (16)$$

since the expansion process lies entirely in the superheat region, the above approximation simply means that the mean value of specific heat for the isentropic and actual expansion processes $C_{6,7'}$ and $C_{6,7}$ are equal.

The actual turbine end temperature T_7 is then found from Eq. (16) as

$$T_7 = T_6 - E_T (T_6 - T_7') \quad (17)$$

D. Turbine Work

This is calculated from

$$W_T = C_{6,7} (T_6 - T_7) \quad (18)$$

where $C_{6,7}$ is the mean specific heat at constant pressure between temperatures T_6 and T_7 .

E. Pump Work

The pump work is usually very small compared with the turbine work and is sometimes neglected in most Rankine cycle analyses. However, it will be calculated in this program to size the pump and the driving motor. The actual pump work is given the enthalpy difference of states 1 and 2 as

$$\begin{aligned} W_P &= (H_2 - H_1) = (P_e - P_c) \\ &\times \left(\frac{1 \text{ atm}}{760 \text{ mm Hg}}\right) \left(\frac{1.033 \text{ kg}_f/\text{cm}^2}{1 \text{ atm}}\right) \left(\frac{10^4 \text{ cm}^2}{\text{m}^2}\right) \\ &\times \left(\frac{\text{kcal}}{427 \text{ kg}_f \cdot \text{m}}\right) \cdot \frac{V_1}{E_P}, \text{ kcal/kg} \end{aligned} \quad (19)$$

where V_1 is the specific volume of saturated water in m^3/kg at temperature t_c , E_P is the pump isentropic efficiency, and P_e and P_c are the evaporation and condenser pressures in mm Hg, respectively. The specific volume V_1 is considered uniform at $0.001 \text{ m}^3/\text{kg}$ and Eq. (19) is reduced to

$$W_P = \frac{(P_e - P_c) \text{ in mm Hg}}{31415 E_P}, \text{ kcal/kg} \quad (20)$$

Also, the temperature of compressed liquid water leaving the pump is taken as the condenser temperature for heat exchange calculations

$$T_2 \approx T_1 = T_c \quad (21)$$

F. Vapor-Vapor Heat Exchanger

This is the device that transfers heat to the superheated steam from state 4 to state 5 by cooling the turbine exhaust from state 7 to state 8. It is considered a "balanced" counter-flow heat exchanger, since the two heat transfer fluids possess the same heat capacity.

The temperature pattern of each heat transfer fluid is represented by two straight lines as shown in Fig. 4. The effectiveness expression E_{VV} is written as (Ref. 5)

$$E_{VV} = \frac{T_7 - T_8}{T_7 - T_e} = \frac{T_5 - T_e}{T_7 - T_e} \quad (22)$$

from which the temperatures T_5 and T_8 are calculated.

$$T_5 = T_e + E_{VV} (T_7 - T_e) \quad (23)$$

$$T_8 = T_7 - E_{VV} (T_7 - T_e) \quad (24)$$

G. Vapor-liquid Heat Exchanger

This heat exchanger acts as a "feed water heater" from state 2 to state 3 by utilizing the exhaust steam leaving the vapor-vapor heat exchanger. The temperature pattern is sketched in Fig. 5. The heat exchanger is considered an "unbalanced" counterflow type since the heat capacities of the two heat transfer fluids are unequal. The effectiveness expression E_{VL} is based on the minimum heat capacity fluid (the vapor in this case) as

$$E_{VL} = \frac{(T_8 - T_9)}{(T_8 - T_c)} = \frac{C_{2,3}(T_3 - T_c)}{C_{8,9}(T_8 - T_c)} \quad (25)$$

where $C_{2,3}$ is the mean specific heat of liquid water in the range of temperatures from T_2 to T_3 and $C_{8,9}$ is that for superheated steam in the range of temperatures T_8 to T_9 . By taking $C_{2,3}$ as 1 kcal/kg°C, the temperatures T_3 and T_9 are then written as

$$T_9 = T_8 - E_{VL} (T_8 - T_c) \quad (26)$$

$$T_3 = T_c + C_{8,9} \cdot (T_8 - T_c) \cdot E_{VL} \quad (27)$$

In the computer model, the ceiling value of the temperature T_3 is assigned the evaporation temperature T_e . This means that if the temperature T_3 , when computed from Eq. (27), exceeds the temperature T_e , then T_3 will be set equal to T_e as a maximum value. The enthalpy H_3 is calculated using Eq. (1).

H. Cycle Performance

The cycle performance characteristics and heat rates are determined as follows:

- (1) The heat supplied by solar energy

$$Q_s = (H_4 - H_3)$$

$$Q_s = (597.8 + 0.417 t_e) - t_3$$

or

$$Q_s = (757.05 + 0.417 T_e - T_3) \quad (28)$$

- (2) The heat supplied by the external fuel for superheat

$$Q_{ex} = (H_6 - H_5)$$

$$Q_{ex} = C_{5,6}(T_6 - T_5) \quad (29)$$

where $C_{5,6}$ is the mean specific heat between states 5 and 6 as determined from Eq. (5).

- (3) Total heat added to the cycle

$$Q_{add} = Q_s + Q_{ex}$$

- (4) The percentage of fuel heat added to total heat added

$$\lambda_s = Q_s / Q_{add}$$

- (5) Net work done per unit mass of steam

$$W_{net} = (W_T - W_P)$$

- (6) Rankine thermal efficiency

$$W_{rankine} = \frac{W_{net}}{Q_{add}}$$

- (7) Specific Stream Consumption (SSC)

This is the amount of steam rate in kg/hr necessary to produce a net one horsepower output.

$$SSC = \frac{632}{W_{net}} \text{ kg/hp hr}$$

- (8) Carnot efficiency based on the cycle minimum and maximum temperatures T_c and T_6

$$E_{\text{Carnot}} = 1 - \frac{T_c}{T_6}$$

- (9) Relative efficiency which measures the deviation from the ideal cycle

$$E_{\text{relative}} = E_{\text{rankine}} / E_{\text{carnot}}$$

V. Summary of Program Steps

The following is an ordered list of the program sequence with the necessary repetitive or conditional commands.

A. Input Data

A.1. Input temperatures

A.1.1 Evaporation temperature, t_e °C

A.1.2 Condenser temperature, t_c °C

A.1.3 Maximum superheat temperature, t_6 °C

A.2. Input component efficiency

A.2.1 Pump isentropic efficiency, E_p

A.2.2 Turbine isentropic efficiency, E_T

A.2.3 Vapor-vapor heat exchanger effectiveness, E_{VV}

A.2.4 Vapor-liquid heat exchanger effectiveness, E_{VL}

B. Pressure Calculations

$$B.1 \quad T_e = t_e + 273.15$$

$$T_c = t_c + 273.15$$

$$T_6 = t_6 + 273.15$$

$$B.2 \quad P_e = \text{antilog} \left[7.8553 - \frac{1555}{T_e} - \frac{11.2414}{(T_e/100)^2} \right] \text{ mm Hg}$$

$$B.3 \quad P_c = \text{antilog} \left[7.8553 - \frac{1555}{T_c} - \frac{11.2414}{(T_c/100)^2} \right] \text{ mm Hg}$$

$$B.4 \quad W_P = \frac{(P_e - P_c)}{31415 E_p}, \text{ kcal/kg}$$

Next, either one of the following two approaches should be used to determine the isentropic turbine-end temperature.

C. Approach 1, by Ideal Gas Relations

C.1 Initiate a DO LOOP COMMAND

C.2 Set an initial value for $\gamma^{(0)} = 1.30$ or an initial value for the parameter $X = \gamma - 1/\gamma$ i.e., $X^{(0)} = 0.2308$ (based on $\gamma^{(0)} = 1.3$)

$$C.3 \quad T_{7'} = T_6 \left(\frac{P_c}{P_e} \right)^X, \text{ } ^\circ\text{K}$$

$$C.4 \quad C_{6,7'} = 0.3924 + 7.5 \times 10^{-5} (T_6 + T_{7'}), \text{ kcal/kg K}$$

$$C.5 \quad X = \frac{0.11024}{C_{6,7'}} \quad [\text{This is an updated value for } X]$$

[The gas constant for superheated steam = 0.11024 kcal/kg K]

C.6 GO TO STEP C.3. Either repeat the procedure three or four times only since the convergence is rapid, or repeat until two consecutive values of X differ by a preassigned error.

C.7 Exit from the loop with the final value of $T_{7'}$.

D. Approach 2, by Equating the Entropy

D.1 Initiate a DO LOOP COMMAND

D.2 Set an initial value of $T_{7'}$. This could be taken as T_6 , i.e., $T_{7'}^{(0)} = T_6$

$$D.3 \quad T_{7'} = \frac{T_6 \left(\frac{T_e}{T_c} \right)^{1.54842}}{\exp \left[1929.3 \left(\frac{1}{T_c} - \frac{1}{T_e} \right) - \left(\frac{T_6 + T_c - T_e}{2616} \right) \right]} \times \exp \left(\frac{-T_{7'}}{2616} \right)$$

This is an updated value of $T_{7'}$.

D.4 GO TO STEP D.3. Either repeat the procedure six or seven times or repeat until two consecutive values of T_7' differ by a preassigned error.

D.5 Exit from the loop with the final value of T_7' .

E: Heat Exchangers and Cycle Performance

Having calculated T_7' by either approach (1) or (2), then

$$E.1 \quad T_7 = T_6 - E_T (T_6 - T_7'), \text{ K}$$

E.2 Conditional command: IF $T_7 < T_e$ STOP ELSE proceed.

$$E.3 \quad C_{6,7} = 0.3924 + 7.5 \times 10^{-5} (T_6 + T_7), \text{ kcal/kg K}$$

$$E.4 \quad W_T = C_{6,7} (T_6 - T_7), \text{ kcal/kg}$$

$$E.5 \quad T_5 = T_e + E_{VV} (T_7 - T_e), \text{ K}$$

$$E.6 \quad T_8 = T_7 - E_{VV} (T_7 - T_e), \text{ K}$$

$$E.7 \quad T_9 = T_8 - E_{VL} (T_8 - T_e), \text{ K}$$

$$E.8 \quad C_{8,9} = 0.3924 + 7.5 \times 10^{-5} (T_8 + T_9), \text{ kcal/kg K}$$

$$E.9 \quad T_3 = T_e + C_{8,9} \cdot E_{VL} (T_8 - T_e), \text{ K}$$

E.10 Conditional Command. IF $T_3 > T_e$ THEN assign $T_3 = T_e$ ELSE proceed

$$E.11 \quad Q_s = 757.05 + 0.417 T_e - T_3, \text{ kcal/kg}$$

$$E.12 \quad Q_{ex} = 0.3924 (T_6 - T_5) + 7.5 \times 10^{-5} (T_6^2 - T_5^2), \text{ kcal/kg}$$

$$E.13 \quad Q_{add} = Q_s + Q_{ex}, \text{ kcal/kg}$$

$$E.14 \quad \lambda_s = \frac{Q_s}{Q_{add}}$$

$$E.15 \quad W_{net} = W_T - W_P, \text{ kcal/kg}$$

$$E.16 \quad E_{rankine} = W_{net} / Q_{add}$$

$$E.17 \quad E_{carnot} = 1 - (T_e / T_6)$$

$$E.18 \quad E_{relative} = E_{rankine} / E_{carnot}$$

$$E.19 \quad SSC = \frac{632}{W_{net}}, \text{ kg/hp hr}$$

VI. Example of Calculations

The following numerical example is given to show the relative weight of each property involved in the calculations and to identify the order of execution steps.

A. Input Temperatures

$t_e = 90^\circ\text{C}$, evaporation temperature

$t_c = 40^\circ\text{C}$, condenser temperature

$t_6 = 600^\circ\text{C}$, maximum cycle temperature

B. Input Component Efficiencies

$E_P = 0.60$, for the pump

$E_T = 0.75$, for the turbine

$E_{VV} = 0.80$, for the vapor-vapor heat exchanger

$E_{VL} = 0.80$, for the vapor-liquid heat exchanger

C. Program Steps

$$T_e = 363.15 \text{ K}$$

$$T_c = 313.15 \text{ K}$$

$$T_6 = 873.15 \text{ K}$$

$$P_e = 525.91, \text{ mm Hg}$$

$$P_c = 55.37, \text{ mm Hg}$$

$$W_P = 0.025, \text{ kcal/kg}$$

D. If Approach 1 Is Selected, Then

$$X^{(0)} = 0.2308$$

$$T_{7'}^{(1)} = 519.34 \text{ K}$$

$$C_{6,7}^{(1)} = 0.4968 \text{ kcal/kg K}$$

$$X^{(1)} = 0.2219$$

$$T_{7'}^{(2)} = 529.87 \text{ K}$$

$$C_{6,7}^{(2)} = 0.4976$$

$$X^{(2)} = 0.2215$$

$$T_{7'}^{(3)} = 530.29 \text{ K}$$

$$C_{6,7}^{(3)} = 0.4976$$

$$X^{(3)} = 0.2215$$

$$\text{Final temperature } T_{7'} = 530.29 \text{ K}$$

E. If Approach 2 Is Selected, Then

$$T_{7'} = 644.1140 \exp\left(\frac{-\dot{T}_{7'}}{2616}\right)$$

$$T_{7'}^{(0)} = 873.15$$

$$T_{7'}^{(1)} = 461.32$$

$$T_{7'}^{(2)} = 539.98$$

$$T_{7'}^{(3)} = 523.98$$

$$T_{7'}^{(4)} = 527.20$$

$$T_{7'}^{(5)} = 526.55$$

$$T_{7'}^{(6)} = 526.68$$

$$T_{7'}^{(7)} = 526.65$$

$$\text{Final temperature } T_{7'}^{(8)} = 526.66 \text{ K}$$

The error between the two approaches is negligible in the final answers. Let us complete the program steps as if Approach 1 was chosen.

$$T_7 = 616.00 \text{ K}, \quad T_7 > T_e$$

$$C_{6,7} = 0.5041, \text{ kcal/kg K}$$

$$W_T = 129.63, \text{ kcal/kg}$$

$$T_5 = 565.43 \text{ K}$$

$$T_8 = 413.72 \text{ K}$$

$$T_9 = 333.26 \text{ K}$$

$$C_{8,9} = 0.4484, \text{ kcal/kg}^\circ\text{C}$$

$$T_3 = 349.21 \text{ K}$$

$$\text{Note } T_3 < T_e$$

$$Q_s = 559.27, \text{ kcal/kg}$$

$$Q_{ex} = 153.95, \text{ kcal/kg}$$

$$Q_{add} = 713.22, \text{ kcal/kg}$$

$$\lambda_s = 0.7841 \quad \left\{ \begin{array}{l} \text{i.e., 78.41\% solar} \\ 21.59\% \text{ fuel} \end{array} \right.$$

$$W_{net} = 129.605, \text{ kcal/kg}$$

$$E_{rankine} = 0.1817 \quad \text{i.e., 18.17\%}$$

$$E_{carnot} = 0.6414 \quad 64.14\%$$

$$E_{relative} = 0.2833$$

$$SSC = 4.8764, \text{ kg/hp hr}$$

A short computer program was written based on the above sequence of cycle calculations. Several runs were made with the condenser temperature and the evaporator temperature as parameters, keeping the component efficiencies and the maximum cycle temperature fixed. The results are plotted in Figs 6 and 7 to form a performance map to help the system

The component efficiencies were arbitrarily selected to be as close as possible to practical values. The specific steam

trade-off would then have to be made for the selection of the optimum design point that solves the thermal efficiency versus operation costs problem.

Definition of Terms

a, b	specific heat constants	T	absolute temperature, K
C	specific heat at constant pressure, kcal/kg°C	W	mechanical work, kcal/kg
E_p	pump isentropic efficiency	λ_s	percentage of solar heat to total heat added
E_T	turbine isentropic efficiency		
E_{VL}	vapor-liquid heat exchanger effectiveness		
E_{VV}	vapor-vapor heat exchanger effectiveness	Subscripts	
H	specific enthalpy, kcal/kg	c	condenser
P	pressure, mm Hg	e	evaporation
Q	heat rate	ex	extra for superheat
S	entropy, kcal/kg K	f	liquid phase
SSC	specific steam consumption, kg/hp hr	g	gas phase
t	temperature, °C	s	solar share

References

1. Curran, H. M., and Miller, M., "Evaluation of Solar-Assisted Rankine Cycle Concept for the Cooling of Buildings," *IECEC 75 Record*, pp. 1391-1398.
2. Curran, H. M., "Assessment of Solar Cooling," *Proceedings of the Second Workshop on The Use of Solar Energy for the Cooling of Buildings*, held at University of California, Los Angeles, August 1975, pp. 18-25.
3. Lior, N., "Solar Rankine Cycle (steam) Drive and Assistance to Heat Pump Systems," in *Workshop Proceedings, Solar Energy Heat Pump Systems for Heating and Cooling Buildings*, Pennsylvania State University, College of Engineering, June 1975, pp. 213-221.
4. *JANAF Thermochemical Tables*, U.S. Department of Commerce, NBS Institute for Applied Technology, August 1965.
5. Kays, W. M., and London, A. L., *Compact Heat Exchangers*, McGraw Hill Book Company, Inc., New York, 1958.



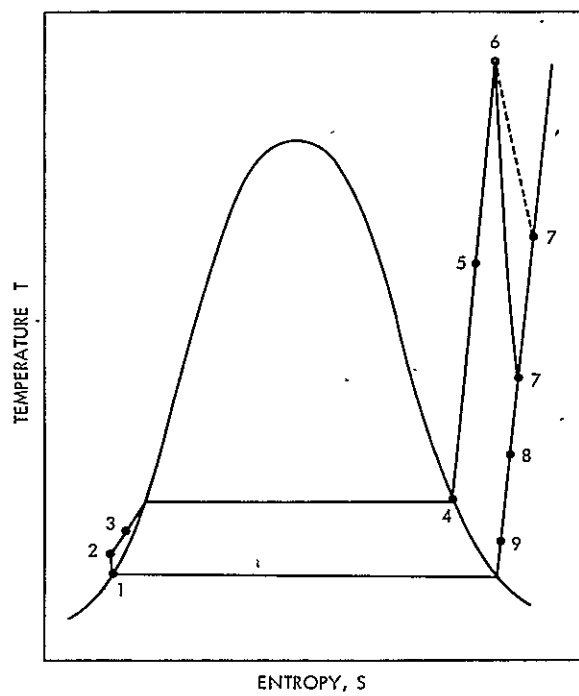


Fig. 2. Temperature entropy diagram for steam showing the states of the regenerative Rankine cycle (not to scale)

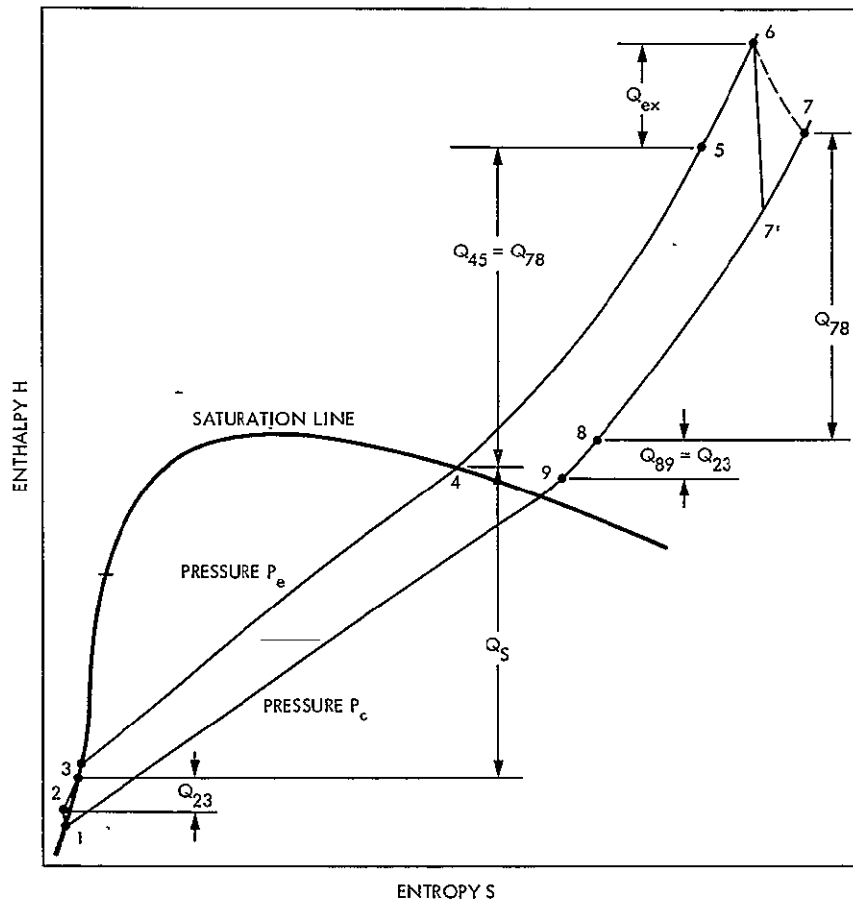


Fig. 3. Enthalpy-entropy (Mollier) diagram for steam showing the states of the regenerative Rankine cycle (not to scale)

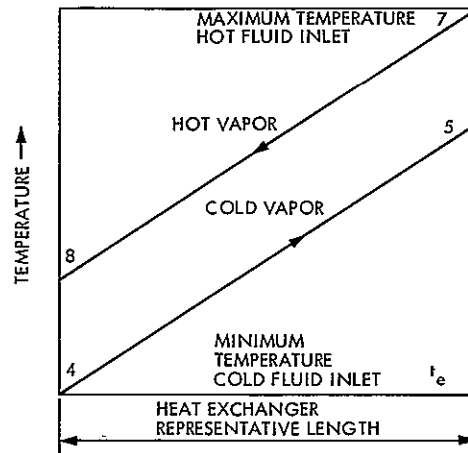


Fig. 4. Vapor-vapor heat-exchanger temperature pattern

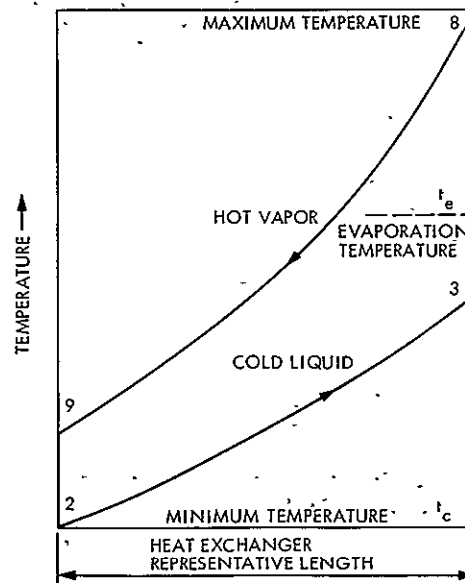


Fig. 5. Vapor-liquid heat-exchanger temperature pattern

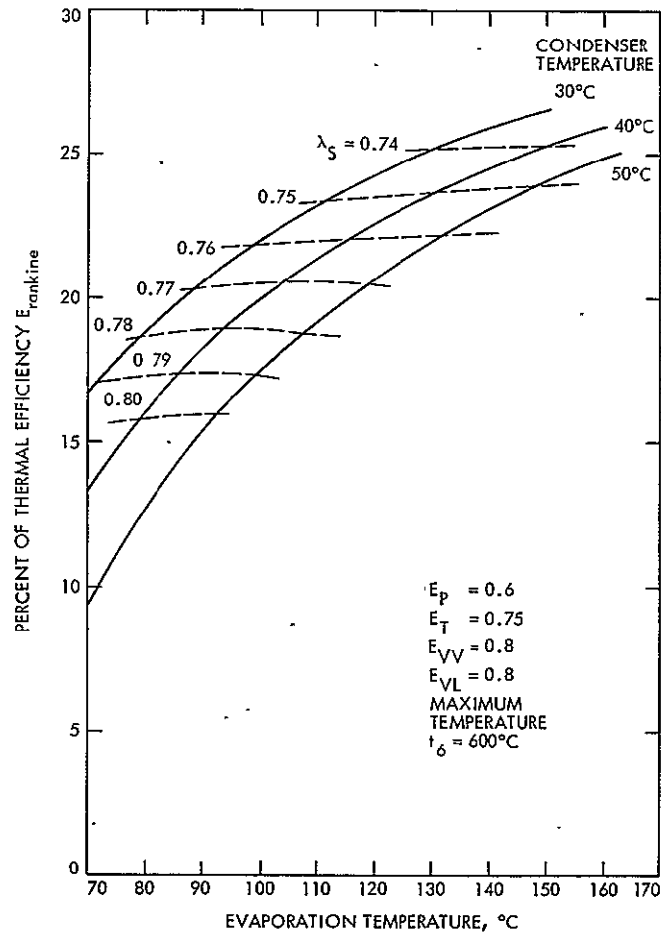


Fig. 6. Rankine efficiency and percentage of solar share versus the evaporation temperature

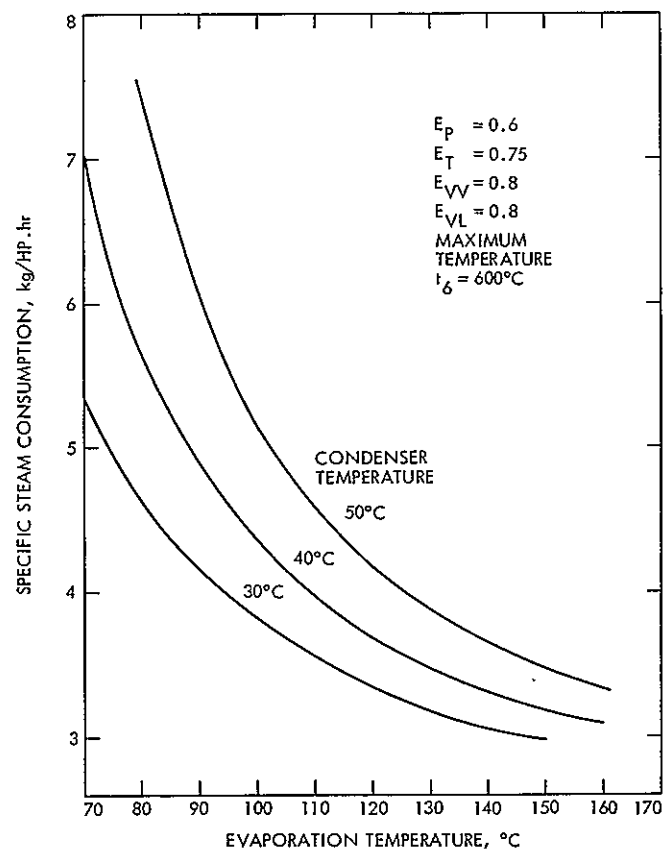


Fig. 7. Specific steam consumption versus the evaporation temperature for variable condenser temperatures

N77-19113

Precision Insolation Measurement Under Field Conditions

M. S. Reid and R. A. Gardner
Radio Frequency and Microwave Subsystems Section

C. M. Berdahl
Instrumentation Section

A solar energy instrumentation project was started at Goldstone to support the DSN energy conservation project. The objective is to help provide an adequate technological foundation for supporting a solar energy based facilities design at Goldstone. The lack of historical records of insolation for the Goldstone area required that a program of instrumentation development and solar data recording be started as quickly as possible. Prior NASA-supported work at the Jet Propulsion Laboratory had resulted in the development of a primary absolute cavity radiometer (PACRAD), which was recently accepted as an international standard of irradiance. This report discusses the development of an all-weather, field-worthy solar radiometer based on the PACRAD, and describes its calibration stability over a two-year period in the field.

I. Introduction

A solar energy instrumentation project was started at Goldstone to support the DSN energy conservation project. The objective is to help provide an adequate technological foundation for supporting a solar energy based facilities design at Goldstone. The lack of accurate historical records of insolation (Ref. 1) for the Goldstone area required that a program of instrumentation development and solar data recording be started as quickly as possible.

At the time the solar energy instrumentation project (which has been described elsewhere (Refs. 2 and 3) was started in 1973, no high-precision, field-worthy instrument was available for unattended insolation survey work. Prior NASA-supported work under a different program at the Jet Propulsion Laboratory (JPL) had resulted in the development of a

primary absolute cavity radiometer (PACRAD), which was recently accepted as an international standard of irradiance. This report discusses the development of an all-weather, field-worthy solar radiometer based on the PACRAD, and describes its calibration stability over a two-year period in the field. This work was completed by 1 October 1976.

II. An Absolute Calibration Standard

In the mid-1960s, an anomaly in the equilibrium temperature of spacecraft in flight, from that which was predicted from solar simulation testing, encouraged instrumentation engineers at JPL to investigate the validity of irradiance measurements with respect to the absolute scale of energy. Instruments that were used to measure synthesized solar irradiance were scaled to agree with the International Pyrhelio-

metric Scale (I.P.S.). This scale was recommended by the International Radiation Conference in Davos, Switzerland, in 1956 and referred to the Ångström Pyrheliometer maintained at the World Radiation Center in Davos. Although the Ångström instrument was originally intended to represent the absolute scale of units, it has been used only in a relative reference capacity to achieve agreement of radiometric measurements made throughout the world.

In the later 1960s a standard absolute cavity radiometer was developed for solar simulated irradiance measurement (Ref. 4). This instrument is a primary standard since its calibration depends only on dimensions, arrangement of components, and electrical measurements. Sensor absorptivity was enhanced by using a cavity receptor that greatly decreased the measurement uncertainty over previously built instruments. Proof of measurement accuracy has been ascertained experimentally by its use in the determination of the Stephan-Boltzmann constant, and verified by the accuracy with which spacecraft equilibrium temperatures may now be determined prior to flight (Ref. 4).

Modification of the standard absolute cavity radiometer with a view limiting aperture provided an instrument for measuring direct normal incidence solar irradiance (Ref. 5). This instrument, the primary absolute cavity radiometer (PACRAD) was compared with the Ångström I.P.S. in Davos and found to give readings in the order of two percent higher. The same instrument, the PACRAD III, was used in International Pyrheliometric Comparisons (I.P.C.) at Davos in 1970 and 1975 (Ref. 6). Because of its extreme stability and the agreement with similar cavity type instruments, it was recommended and accepted as an international reference for the absolute scale of units. The PACRAD has a windowless black cavity receptor mounted in a massive heatsink, and has equal sensitivity to ultraviolet, visible, and infrared radiation. The incoming radiation is absorbed and converted into heat that flows through a metallic thermal resistor to the massive heatsink to produce a temperature difference of about one Kelvin. This difference is measured by a thermopile. A totally enclosed electric heater winding serves as a source of cavity heating accurately equivalent to radiation heating, and provides a built-in means of calibration. There is no temperature to control or measure. By measuring the voltage and current to the heater, a known amount of equivalent power is applied to the cavity. Thermopile output is measured to give an accurate calibration of the radiometer. The design, which includes a compensating cavity and thermal resistor, minimizes all unwanted heat transfers. The view-limiting aperture is normally set to 5-deg total angle, but can be opened to a maximum of 15-deg total angle or greater, depending on the desired use. The PACRAD has been described in detail elsewhere (Ref. 5), and is shown in Fig. 1.

III. An All-Weather, Field-Worthy Radiometer

The PACRAD III, and other copies of it that have recently been built, are primary standards of reference. They are used in intercomparisons for absolute calibrations and are not suitable for extended field operations. Further instrument development work began in 1973 in response to the requirements of a solar energy based facility design study at the Goldstone Deep Space Communications Complex (GDSCC), as described above (Refs. 3 and 7). The lack of precision historical insolation data clearly pointed to the need for an accurate and stable field instrument. The result of this instrument research was the development of an all-weather, field-worthy version of the PACRAD. This field instrument, designated the Kendall Radiometer System Mark 3, is identical to the PACRAD except for a modification to ensure all-weather operation.

The Mark 3 radiometer has a flat quartz window to seal the cavity aperture and is dry nitrogen filled to avoid dew formation on the glass. The instrument is mounted on a continuously tracking mount and the view angle has been opened to 15 deg to permit reasonable tracking errors. The quartz window adds approximately 7-percent attenuation that is not present in the PACRAD, but this has been compensated for. Two Mark 3 radiometers have been in service side by side at GDSCC for over two years and are continuing to provide data that are within plus and minus one percent of the absolute value. The Mark 3 radiometers, both with and without their quartz windows, were extensively calibrated against the PACRAD II prior to installation in the field. Figures 2 and 3 are photographs of the Kendall Radiometer System Mark 3.

IV. Stability Analysis of the Mark 3 Systems

Two Mark 3 systems and several commercial pyranometers were installed at GDSCC in mid-1974. The objectives are to initiate and operate a solar (and meteorological, including wind) measurement program at GDSCC using high-precision instrumentation and to archive the data on magnetic tape (Ref. 3). Further objectives are to combine these data into a mathematical model of solar energy for the GDSCC (Mojave Desert) area (Ref. 7), and to test the long-term stability and accuracy of the Kendall Radiometer System Mark 3.

Normal incidence pyrheliometer data from the Mark 3 systems have been collected on magnetic tape for approximately two years. During this time the Mark 3s were operated continuously and were subjected to ambient temperatures

ranging from -7.5°C to 48°C , and rain, snow, wind, and dust. Declination settings were manually adjusted approximately once per week, at which times the quartz windows were cleaned, if necessary.

On 28 April 1976 one of the GDSCC Mark 3 systems (serial number 6) was taken to the Table Mountain (TM) facility for calibration against an absolute standard. The TM facility has been used since 1923 as an optical calibration and operational site because of its high altitude and stable and clear atmosphere. The absolute reference standard was a commercially built instrument* equivalent to the PACRAD. The outputs from the Mark 3 serial number 6 and the absolute instrument were fed into an automatic data acquisition system that recorded one simultaneous data set every 30 seconds. Several data sets of measurements and calibrations, of varying lengths up to 20 minutes, were recorded around solar noon. Zero calibration runs were made by covering the instruments with shielded black bodies, and the data system was calibrated by electrically short-circuiting the output terminals of the instruments. The details of the calibration method have been described elsewhere (Ref. 5). Data from the initial settings show that the two instruments' outputs differ by less than 0.5 percent. The Mark 3 system recorded the higher output. This might be explained by the differing view angles of the two instruments — 15 deg and 5 deg. The Mark 3's 15-deg view angle may have detected some additional circumsolar radiation that was not in the 5-deg view angle. Circumsolar radiation was not separately measured.

After the calibrations at the TM station were complete, the calibration factor of the Mark 3 serial number 6 was adjusted to coincide with the absolute instrument. It was then returned to the GDSCC station, where it agreed with the second Mark 3 (serial number 1) within 0.5 percent.

On 16 September 1976 a standard calibration instrument, the PACRAD II, was taken to the GDSCC station. Both

Mark 3 radiometers (serial numbers 1 and 6) were calibrated against the PACRAD in good weather using the same techniques as described above. The results of these intercomparisons showed that both Mark 3 instruments were within 0.5 percent of the PACRAD II.

Both the absolute calibration standards used in these intercomparisons are continually compared with the PACRAD, which was present at Davos in 1970 and 1975; they are, therefore, both traceable to IPC IV (1975). Two Kendall Radiometer Systems Mark 3 have therefore demonstrated stability of calibration to 0.5 percent for over two years in the field.

V. Data Bank

The data from the two Mark 3 pyrheliometers and several commercial pyranometers, together with conventional ground-level meteorological data, are fed into a data acquisition system for recording on magnetic tape. One data set is recorded every two minutes, the value of the parameters being the average over two minutes. This data bank is therefore accumulating insolation records typical of the Mojave Desert area and calibrated to the International Standard.

VI. Conclusions

The Mark 3 Kendall Radiometer System is an all-weather insolation radiometer that has demonstrated extraordinary stability in severe environments over an extended period of time. The instrument may therefore be considered a transfer standard as well as a field-worthy radiometer of unique precision and accuracy. A simple improvement to the tracking system would eliminate the need for weekly manual declination adjustments. Experience with these instruments has shown that the 15-deg view angle could be reduced considerably without compromising the tracking accuracy.

*Built by Technical Measurements Inc., under license from the California Institute of Technology.

References

1. Durrenberger, R. W., and Brazel, A. J., "Need for a Better Solar Radiation Data Base," *Science*, Vol. 193, 17 Sept. 1976, pp. 1154-1155.
2. Reid, M. S., Gardner, R. A., and Parham, O. B., "Goldstone Solar Energy Instrumentation Project: Description, Instrumentation, and Preliminary Results," in *The Deep Space Network Progress Report 42-26*, pp. 133-144, Jet Propulsion Laboratory, Pasadena, Calif., April 15, 1975.
3. Reid, M. S., and Gardner, R. A., "A Versatile Data Acquisition System for Goldstone," in *The Deep Space Network Progress Report 42-30*, pp. 132-143, Jet Propulsion Laboratory, Pasadena, Calif., Dec. 15, 1975.
4. Kendall, J. M., Sr., and Berdahl, C. M., "Two Black-body Radiometers of High Accuracy," *Applied Optics*, Vol. 9, No. 5, May 1970.
5. Kendall, J. M., Sr., *Primary Absolute Cavity Radiometer*, Technical Report 32-1396, Jet Propulsion Laboratory, Pasadena, Calif., July 1969.
6. Frolich, C., "The Third International Comparisons of Pyrheliometers and a Comparison of Radiometric Scales," *Solar Energy*, Vol. 14, No. 2, 1973, pp. 157-166.
7. Hamilton, C. L., and Reid, M. S., "Toward a Mathematical Model of Solar Radiation for Engineering Analysis of Solar Energy Systems," in *The Deep Space Network Progress Report 42-34*, pp. 147-151, Jet Propulsion Laboratory, Pasadena, Calif., Aug. 15, 1976.

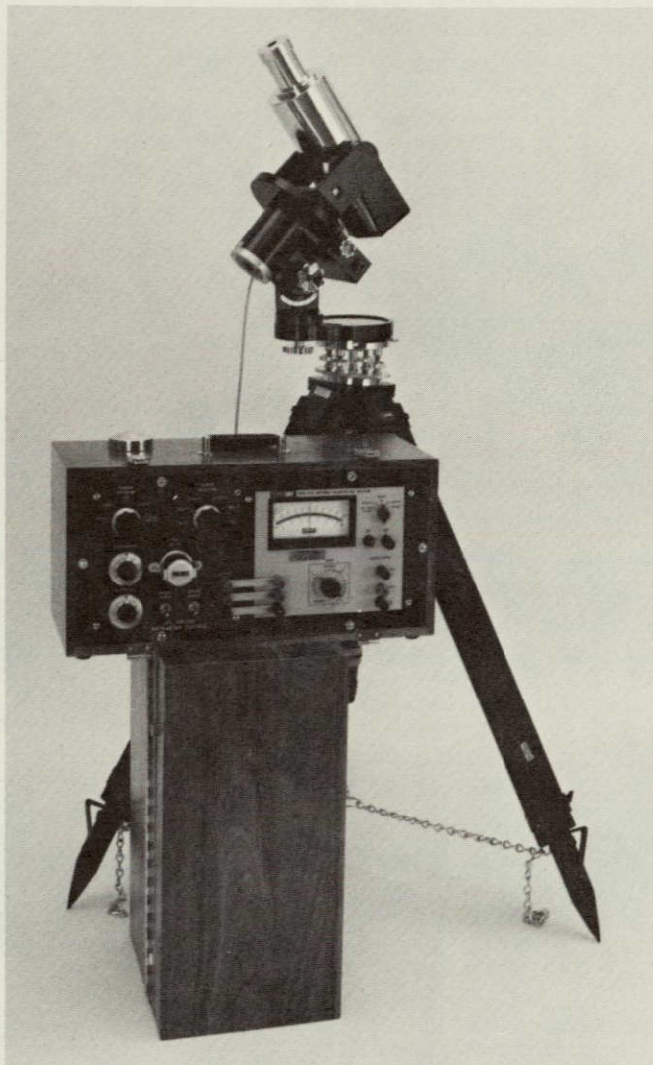


Fig. 1. Primary absolute cavity radiometer

REPRODUCIBILITY OF THE
ORIGINAL PAGE IS POOR

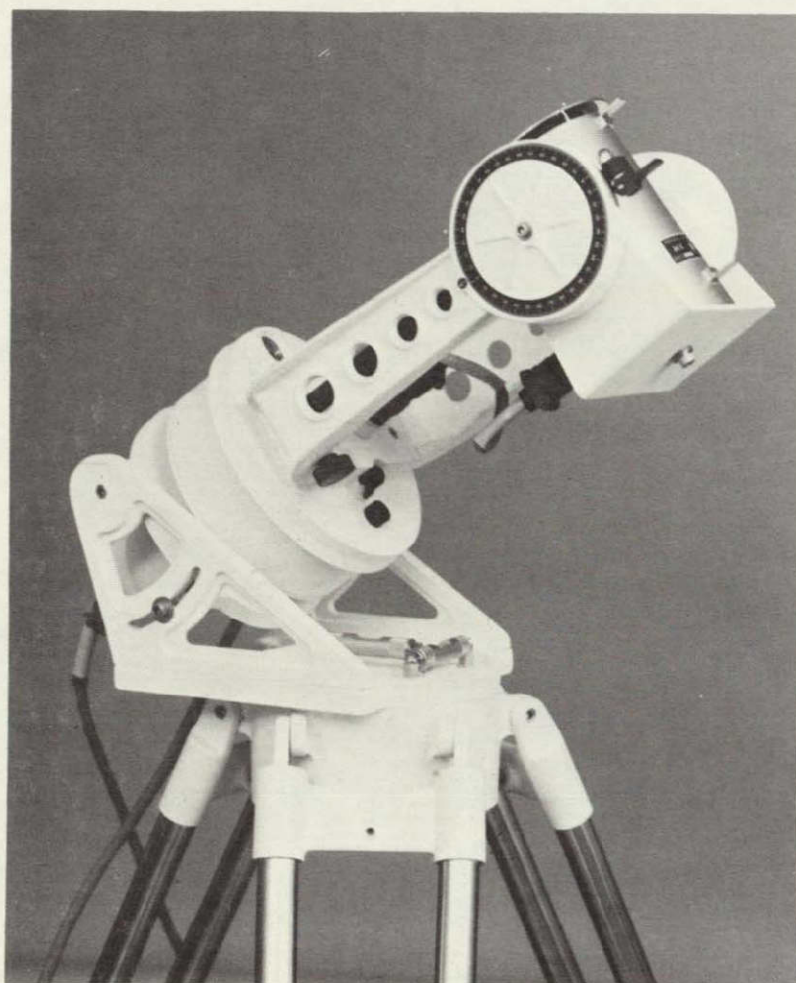


Fig. 2. Kendall Radiometer System Mark 3, closeup view

REPRODUCIBILITY OF THE
ORIGINAL PAGE IS POOR

ORIGINAL PAGE IS
OF POOR QUALITY

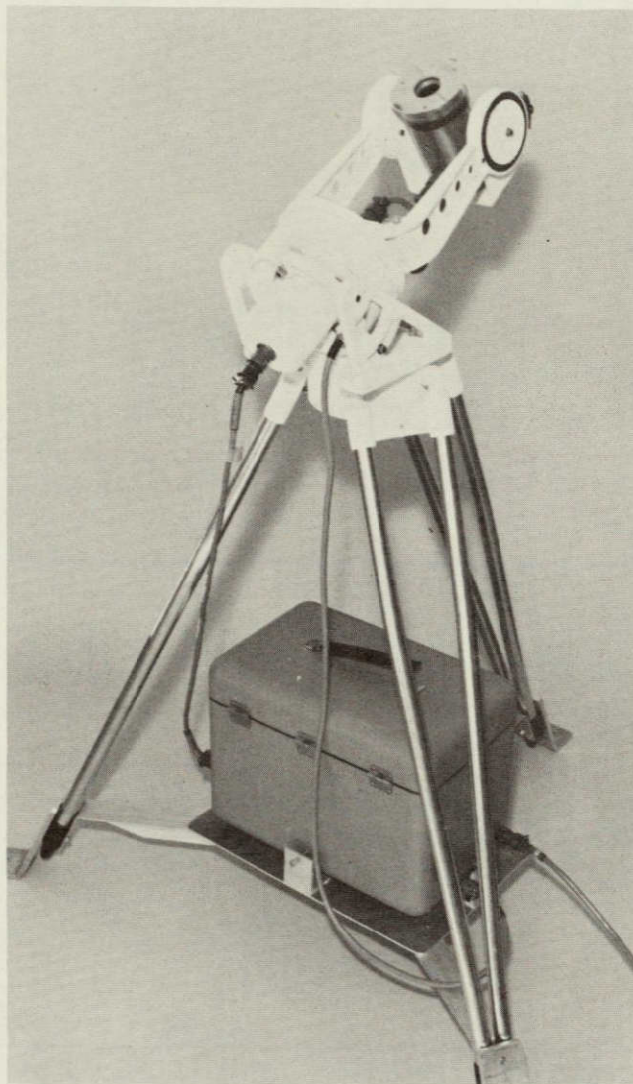


Fig. 3. Kendall Radiometer System Mark 3, overall view

N77-19114

Implementation of a Maximum Likelihood Convolutional Decoder in the DSN

M. E. Alberda
DSN Data Systems Section

The DSN is implementing a high data rate convolutional decoder capability for mission support starting in 1977. This article describes the development status of this decoder and the factors which were considered in defining the specific functional requirements. The design is discussed to the block diagram level. A description of the detailed design is provided, along with a description of the test software developed and a brief summary of the performance evaluation testing completed so far.

I. Introduction

Beginning in late 1976, a new telemetry convolutional decoding capability will be implemented throughout the Deep Space Network (DSN) at the nine Deep Space Stations (DSSs), in response to data system requirements specified for supporting the Mariner Jupiter-Saturn (MJS'77) flight project. This new decoder, called the Maximum Likelihood Convolutional Decoder (MCD), utilizes the Viterbi decoding algorithm, and operates on short constraint length ($K = 7$) convolutional codes, providing a coding gain of about 5 dB (over uncoded data), at data rates from 10 to 250,000 bits per second. This maximum rate is significantly higher than the maximum convolutional coded data rate of 2048 bits per second presently available throughout the DSN, using sequential decoding and the Fano algorithm, as implemented in the Data

Decoder Assembly (DDA). Maximum likelihood decoding allows higher data rates because a large part of the required computations can be performed in parallel.

The MCD is a special-purpose digital computing device which decodes in real-time, high-rate, short-constraint length convolutionally encoded data received from a spacecraft at a DSS. It operates as a component within the DSS Telemetry Subsystem, receiving coded, quantized symbols from a Symbol Synchronizer Assembly (SSA) and outputting decoded data to the Telemetry Processor Assembly (TPA). The TPA formats and outputs this data stream to the Mission Control Center via the Ground Communication Subsystem. The TPA controls and monitors the operation of the MCD, as well as receiving its decoded data.

II. Specific Functional Requirements

The selection of the required codes and code rates, maximum data rate, and system interconnections was completed very early in the overall effort (Ref. 1). Alternate symbol inversion was an added requirement imposed during the development phase to assure adequate symbol transition density.

The salient functional requirements defined for the MCD, and the factors used in their selection, are discussed briefly below.

A. Codes and Code Rates

1. Short constraint length ($K = 7$). Provides simplified encoder design, adequate decoding performance and reasonable computational load (proportional to 2^K).

2. Transparent codes. Provide minimum length initialization interval (called node synchronization or proper grouping of incoming symbols into pairs, for code rate 1/2, or triplets for code rate 1/3).

Transparency indicates that either inverted or non-inverted input symbols are acceptable and produce correspondingly inverted or non-inverted decoded data.

3. Code rates 1/2 and 1/3. Both rates are provided, 1/2 to satisfy a current flight project requirement and 1/3 to provide growth capability for future requirements. (Rate 1/3 offers about a 0.3-dB improvement over rate 1/2, but at the expense of reduced data rate, for a given symbol rate.)

B. Maximum Data Rate—250 kilobits/second

Selected to be roughly double the existing SSA maximum symbol rate capability, to provide for future SSA rate increases, if required.

C. Decoder Bit Error Rate

Provides current state-of-the-art performance capability, as tabulated below.

Bit error rate	Code 7-1/2 E_B/N_0 , dB	Code 7-1/3 E_B/N_0 , dB
10^{-3}	3.0	2.7
10^{-4}	3.8	3.5
10^{-5}	4.5	4.2
10^{-6}	5.2	4.9

D. Built-In Hardware Self-Test

Provides a rapid pass/fail check of decoder operability, for both code rates.

E. System Interfaces

1. Symbol inputs. Received from the Symbol Synchronizer Assembly (SSA), in the form of 5-bit parallel binary numbers (quantized to 1 of 8 levels).

2. Data output and control. The MCD communicates with the TPA via built-in circuitry that satisfied the JPL standard 14-line interface requirement (as defined per Ref. 2), receiving mode commands from the TPA, and sending interleaved status and data bytes (8 bits per byte) to the TPA.

III. Detailed Design Description

A brief summary of the design is presented as follows. A detailed design description is provided in the MCD Instruction Manual (Ref. 3).

A. System Interfaces (see Fig. 1)

A block diagram of the MCD system interconnections is shown in Fig. 1, with the interfaces as previously mentioned.

B. Input/Output Section (see Fig. 2)

The following subsections are provided:

- (1) Symbol input receivers and converter, for SSA inputs.
- (2) Data output register and drivers, to DDA.
- (3) Standard interface receivers, drivers, registers and control logic provided for TPA communication.

C. Decoder Section (see Fig. 3)

1. Input processor. Generates the branch metric values associated with the allowable branches through the decoder trellis diagram. There are 128 allowable branches for each input symbol pair (code rate 1/2). The lower the branch metric value, the better is the correlation between the possible branch and the quantized symbol pair received.

2. Arithmetic processor and state metric memory. The arithmetic processor, operating with the state metric memory, updates each of the 2^{K-1} , or 64, decoder states for each symbol pair received, by adding the appropriate branch metric values to the previously computed and stored state metric values, and then storing the better (or lesser) of the two sums

as the new state metric value. This is equivalent to selecting and storing the most likely of the two possible branches for entering each decoder state.

3. **Path memory.** For each state, a path history consisting of the most recent 64 bits that define the best path leading to that state is also stored in the path memory. It is the oldest path bit, of the state with the lowest accumulated state metric value, that is the decoded data bit output by the decoder after each symbol pair is received.

4. **Node synchronization.** The node synchronization circuitry performs the function of properly grouping the incoming symbols into pairs (code rate 1/2). It does this by grouping so that all state metric values build up at the slower of two rates, as detected by the rate of the state metric normalization counter. All state metrics are normalized by subtracting a fixed constant from each metric whenever all metrics are above a certain threshold value. This normalization rate is an indicator of the quality of input symbols, or symbol error rate, being input to the MCD, and also roughly indicates decoder output bit error rate (BER). This rate is output from the MCD as a 4-bit number, within the 8-bit status byte.

D. Self-Test Section (see Fig. 4)

Whenever the MCD is commanded to enter the self-test mode, a procedure consisting of three phases is automatically performed. The first phase consists of initializing and/or clearing all control, state metric, and path memory values to predetermined values. In the next two phases the decoder operates in its normal decoding manner, utilizing simulated input symbols derived from a self-contained PN sequence generator. The number of decoded 1's is counted during these two phases, (one phase for code rate 1/2, and one phase for code rate 1/3), and the total at the end of the test is compared with a prestored value. This value is known because the PN sequence is random but exactly repeatable. A status bit is set at the end of the test, indicating the result of the test.

E. Physical Characteristics

- (1) Size: rack-mounted unit, 13.3 cm (5-1/4 inches) high, 37.5 cm (14-3/4 inches) deep, 48.3 cm (19 inches) wide.
- (2) Weight: 6.7 kg (14-3/4 lb).
- (3) Power consumption. 100 watts (max), 120 Vac ($\pm 10\%$).
- (4) Operating temperature (ambient): 13°-38°C (55°-100°F).

- (5) Cooling: self contained internal fan.
- (6) Reliability: computed mean time between failures (MTBF) greater than 8000 hours, using MIL-HDBK-217B, based on a total IC count of 154 units, all of MIL-STD 883 Level B quality.
- (7) Operating life: 10 years minimum.

IV. Testing and Evaluation

A. Acceptance Testing

A typical acceptance test data sheet is shown as Fig. 5.

B. Test Software

1. **MCD Test Program.** This program was developed during the same time span as that allotted for the prototype MCD development, using the MCD simulator as a tool for program checkout. Using this parallel approach, the program was almost totally checked out and operable at the time that the prototype unit was delivered.

The program resides in the TPA. Its primary functions are:

- (1) To evaluate and verify the modes of MCD operation, including *self-test* and *operate*, for both code rates.
- (2) To validate all modes of communication between the MCD and TPA, including interleaved *commands*, *status*, and *data* transfers.
- (3) To monitor and report on MCD status, including validation of both types of MCD status outputs (responses to read status commands from the TPA, and also self-generated status outputs whenever an MCD internal sync change occurs in response to a high normalization rate condition).

In order to accomplish these functions, the program performs the following sequence of operations.

- (1) Commands the MCD to the *operate* and then to the *self-test* modes.
- (2) Receives and stores about 4000 bits of the PN sequence received from the MCD during *self-test*.
- (3) Examines the stored data sequence to find the frame sync reference (127 consecutive 0's), and then compares each bit following frame sync with a stored reference pattern.

- (4) Monitors and evaluates both types of MCD status outputs.
- (5) Outputs pass/fail messages to the Terminate at the end of the test.

This program is intended to be used as a convenient tool for performing a rapid GO-NO GO test to verify the operational readiness of the MCD and its operation with the TPA. It is used both at JPL and at the DSN integration contractor (Univac) for this purpose.

2. **MCD Performance Evaluation Program (MCDPEP).** This program was developed early in 1976 to support extensive performance evaluations of the MCD, while operating within a typical telemetry string (Receiver-Subcarrier Demodulator-SSA-MCD-TPA), with simulated encoded data provided from the Simulation Conversion Assembly (SCA). These tests were performed at the JPL Compatibility Test Area (CTA 21) and the results were evaluated using a companion data reduction program called MCD DAP (Data Analysis Program). This latter program was used to compute and output MCD burst error statistics as well as error-free run length and other performance statistics, including BER versus input symbol error rate (SER).

Extensive testing was done at CTA 21 to evaluate many different combinations of data rates (from 115.2 to 44.8

kilobits per second), with the Block 4 Receiver operating in both S- and X-band modes, at various signal levels (E_s/N_o) and Receiver and Subcarrier Demodulator bandwidth settings. The results obtained are in close agreement with the nominal MCD bit error rate performance. These results are summarized in Ref. 4.

C. Other MCD Testing

Late in 1975 a production MCD was provided to the JPL Spacecraft Telecommunications Systems Section where extensive MCD performance evaluation tests were performed in the Telemetry Development Laboratory, with the MCD operating with a Receiver-Subcarrier Demodulator-SSA.

The results of these tests were entirely satisfactory, with the MCD meeting (or exceeding) the BER performance requirements specified in the TRD.

V. Conclusion

The entire MCD development effort has proceeded in an orderly and satisfactory manner, with relatively few changes of any kind required, and has closely followed all aspects of the original development plan including cost, delivery schedule, and meeting of performance requirements.

References

1. Alberda, M. E., *Technical Requirements Document for Maximum Likelihood Convolutional Decoder (MCD)*, JPL TRD 338-256, Rev. E, November 1975 (JPL internal document).
2. *Detailed Specification for Deep Space Network Standard Interface*, JPL Equipment Specification, ES 508534, Rev. B, November 1974 (JPL internal document).
3. *Instruction Manual, Maximum Likelihood Convolutional Decoder (MCD) LV 7035 Viterbi Decoder*, Linkabit Corp., San Diego, CA, January 1976.
4. Benjauthrit, B., et al., "DSN Telemetry System Performance With Convolutionally Coded Data Using Operational Maximum-Likelihood Convolutional Decoders," in *The Deep Space Network Progress Report 42-36*, pp. 81-101, Jet Propulsion Laboratory, Pasadena, Calif., Dec. 15, 1976.

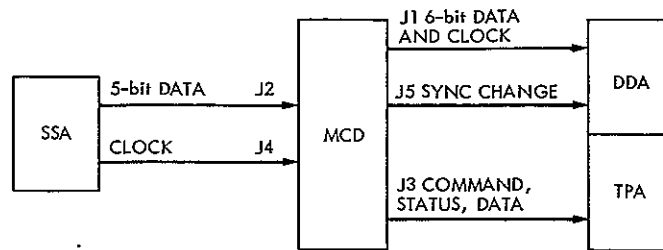


Fig. 1. MCD system block diagram

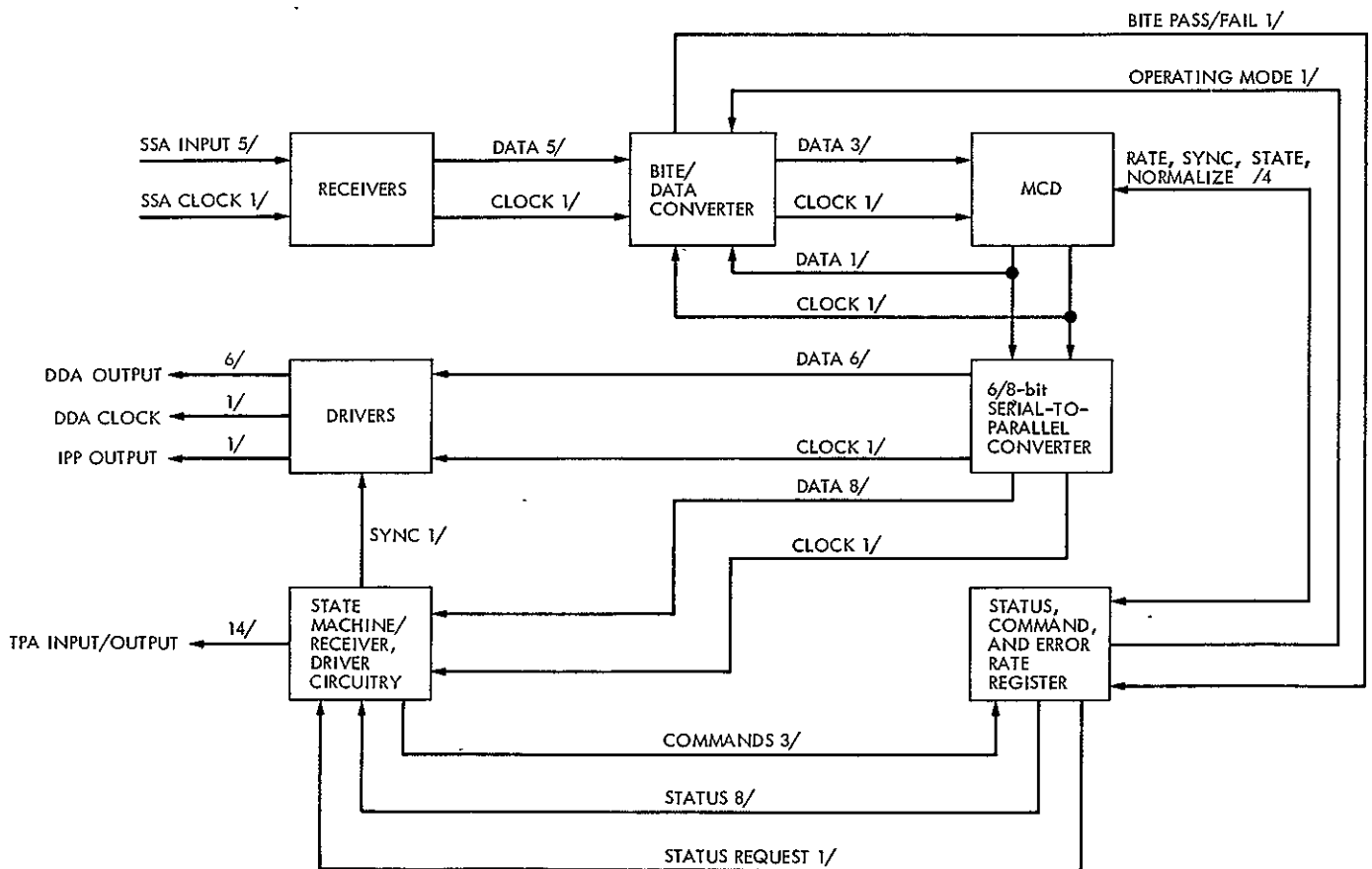


Fig. 2. MCD input/output section block diagram

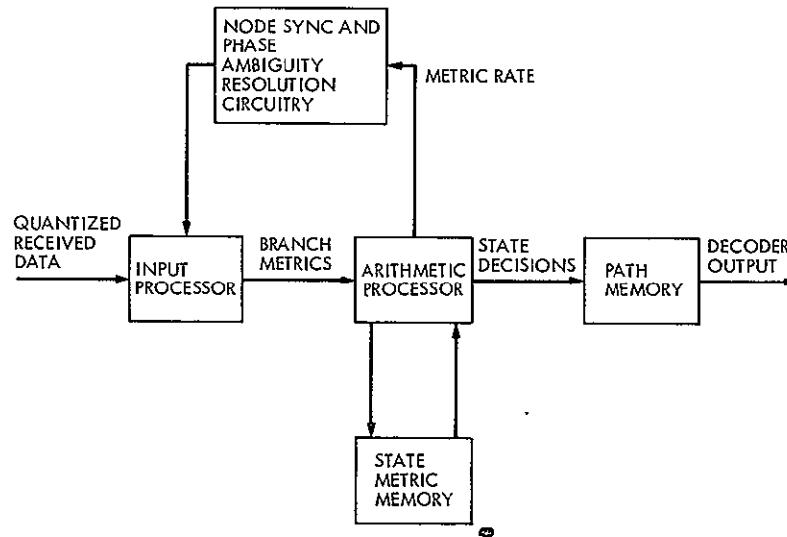


Fig. 3. MCD decoder block diagram

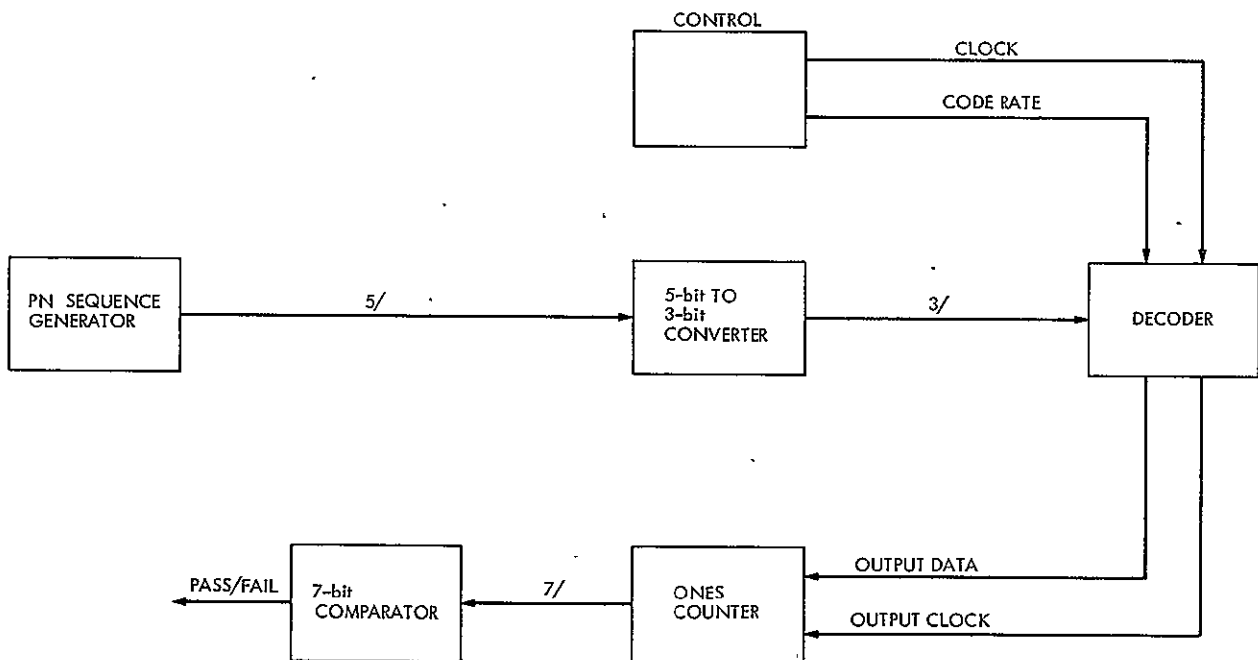


Fig. 4. MCD self-test block diagram

TESTING DATE							
10NOV75							
SERIAL NO.							
0002							
(3.1) TESTER BUILT-IN TEST							
OBSERVED		REQUIRED		PASSED		FAILED	
00A3		00A3		X			
(3.2) ERROR RATE PERFORMANCE							
MCD-TPA							
RATE	EB/NO	NO. BITS	NO. ERRORS	ERROR RATE	UPPER BOUND	PASSED	FAILED
1/2	3.0	0.4096E 07	3028	0.7392E-03	0.9000E-03	X	
1/2	4.0	0.4096E 08	1621	0.3957E-04	0.6000E-04	X	
1/2	5.0	0.6553E 08	89	0.1358E-05	0.2500E-05	X	
1/3	3.0	0.4096E 07	1107	0.2702E-03	0.3600E-03	X	
1/3	3.5	0.4096E 08	2901	0.7082E-04	0.1000E-03	X	
1/3	4.5	0.4096E 08	103	0.2514E-05	0.7000E-05	X	
MCD-DDA							
1/3	3.0	0.4096E 07	1234	0.3012E-03	0.3600E-03	X	
(3.3) MCD SYMBOL SYNCHRONIZATION RECOVERY							
SYMBOLS DROPPED		NO. SYMBOLS TO RECOVERY		PASSED		FAILED	
RATE 1/2							
1		162		X			
1		186		X			
1		186		X			
1		198		X			
1		186		X			
1		192		X			
1		192		X			
1		186		X			
1		192		X			
1		174		X			
RATE 1/3							
1		156		X			
1		144		X			
1		138		X			
1		132		X			
1		144		X			
2		318		X			
2		318		X			
2		282		X			
2		312		X			
2		282		X			

Fig. 5. MCD acceptance test data sheet (typical)

(3.4) MCD BUILT-IN TEST EQUIPMENT							
FAULT INSERTED		BITE VALUE		PASSED	FAILED		
NO		1		X			
YES		0		X			
(3.5) CHANNEL ERROR RATE TEST							
RATE	ED/NO	AVERAGE	LOWER BOUND	UPPER BOUND	PASSED	FAILED	
1/2	3.0	11.0	10	13	X		
1/2	4.0	8.4	7	9	X		
1/2	5.0	4.6	4	6	X		
1/3	3.0	10.5	10	12	X		
1/3	3.5	10.0	9	11	X		
1/3	4.5	7.1	6	8	X		
(3.6) CODE RATE AND MODE STATUS INDICATORS							
OBSERVED	D3	D4	REQUIRED	D3	D4	PASSED	FAILED
		0			0	X	
		1			1	X	
	0			0		X	
	1			1		X	
TESTED BY- <i>Jim L...</i>							
PRODUCT ASSURANCE- <i>R.D. Bleckhoff 10-75</i>							
JPL REPRESENTATIVE- <i>ME Alberda 11/10/75</i>							

Fig. 5 (contd)

D24 17, 17B

N77-19115

Implementation of New-Generation Recorders/Reproducers Into the DSN

G. B. Hamilton
DSN Data Systems Section

New-generation recorder/reproducers are being installed in the Pre/Post-Detection Recording Subsystem at DSSs 14 (Goldstone), 43 (Australia), 63 (Spain), and the JPL Compatibility Test Area CTA 21. The performance of these new-generation machines is discussed, and representative corroborating data acquired at CTA 21 are presented.

I. Introduction

New-generation high-performance instrumentation recorder/reproducers have been introduced into the Pre/Post-Detection Recording Subsystem (PPR) in the DSN. The PPR has been committed to recovery or playback of baseband data recordings with a maximum degradation of 2 dB at encounter signal-to-noise ratios. Use of the new-generation recorders enables the PPR to meet this commitment. This report will discuss the results of performance tests that have been conducted on these machines at CTA 21. Conclusions from results of these tests will be discussed.

II. Objective

The purpose of performing these evaluation tests was twofold: first, a recording and playback procedure for baseband data was developed and proven; second, limits of baseband data recovery and degradation were established. The design review for the PPR produced a commitment to recover

baseband data down to telemetry threshold ($-5 \text{ dB ST}_S/N_0$) with 2 dB degradation. This means that the actual playback telemetry threshold is $-3 \text{ dB ST}_S/N_0$. Thus if the real-time normal path data SNR were at threshold and it was required to insure playback recovery, it would be necessary to decrease the data rate to allow for degradation loss. It becomes important, therefore, for this reason alone, to seek ways to predict and minimize degradation losses due to the entire playback process.

At the present time, data are recorded on the DSS FR 1400s and recovered, when necessary, on a new-generation recorder. A large time base error on the FR 1400s precludes their use as playback machines. A large dynamic skew from the FR 1400 recording inherent in these tapes, even when played back on a newer recorder, contributes to a 2-dB or greater degradation. Procurement is in process for additional new-generation recorders at 64-m stations to replace the FR 1400s. These will minimize time base error and dynamic skew at the 64-m stations.

III. Test Configuration

Figure 1 is a block diagram showing the record and reproduce configuration used to acquire the data and support the conclusions reported here. Baseband data were recorded in the direct record mode on a track adjacent (within the same head stack) to a servo control signal track. This proximity minimizes dynamic skew. Signal levels, telemetry channel settings, and the record/reproduce procedure used are derived and presented in the report by John Molinder in this issue of the Progress Report. When recovering data, it is essential that the servo control signal be used to obtain recorder servo lock in order to minimize time base error or jitter of the data.

IV. Test Results

Tests indicate that under laboratory conditions, degradation on the order of 1 dB or less can be obtained if the 3rd harmonic of the subcarrier plus data can be accommodated within the bandwidth of the recorder. This is subject to the restriction that the components of the subcarrier plus data signal fall upon a linear portion of the phase response curve of the recorder system being used. In practice, this means that performance at a new subcarrier and data rate is difficult to predict and should be tested at various tape speeds. It may well be, and has happened, that less degradation results from discarding the 3rd harmonic by limiting tape speed than by including it in an out-of-phase condition.

Other factors involved which may preclude the direct transfer of laboratory results to DSN use should be mentioned. In addition to losses suffered due to bandwidth limitations are those due to skew and time base error of the recorder. For this discussion, these may be assumed to be interchangeable and cumulative. Tests have been conducted showing that as dynamic skew is increased, degradation increases until finally loss of lock occurs. Such a small matter as removing the tape from the recording machine and replacing it for reproduction, or reproducing the tape on a second machine, increases time base error and skew. In general, it would seem that phase error

also must be affected by reproducing on another machine. As a practical matter, removal and replacement of tape is unavoidable in DSN use. On new-generation tape recorders, cleanliness of the tape path, especially the vacuum chamber, affects the skew and time base error directly.

During testing, using essentially the same type of tape, it was observed that a reel of tape failed to lock up the system. No visible defect was noted. As a last resort, a different reel of tape was used and lockup achieved. This is mentioned to stress the necessity of good tape as a prerequisite for successful recovery of data.

Reliance is placed upon the one-to-one correspondence of machines when recording and reproducing in the direct record mode. (FM recording is impractical because of bandwidth and tape speed limitations.) A standard calibration of the tape recorders is specified and agreed upon as a baseline such that signals recorded on one machine, when reproduced on another machine, agree in amplitude and wave shape. This uniform calibration is important to baseband recovery in the DSN. Representative laboratory results of data recovery are given in Table 1. More extensive tables are presented in John Molinder's article.

V. Conclusions

Results of tests at CTA 21 and actual data recovery in the DSS indicate that the commitment of a maximum degradation of 2 dB on encounter-level baseband recovery can be met using new-generation recorders at a reasonable tape speed. Constraints are the requirements for good maintenance, including receiver phasing, tape path cleaning, and recorder calibration, and the necessity for good tape and strict adherence to record/reproduce procedures. It is expected that, with further practice, more confidence, and more convenient and uniform calibration of the recorders, the 2-dB degradation figure may be improved.

Table 1. Representative baseband recovery data

Subcarrier, kHz	Data (coding)	Tape speed and bandwidth	SNR (ST_B/N_0 or $ST_S N_0$), dB		Degradation, ^a dB	Comments
			Direct	Playback		
360	16 kb/s (32,6)	60 i/s, 1 MHz	4.35	4.05	0.03	
240	16 kb/s (32,6)	60 i/s, 1 MHz	2.9	2.45	0.45	
240	16 kb/s (32,6)	30 i/s, 500 kHz	5	3.45	1.55	Bandwidth limited.
24	33-1/3 b/s (UC)	15 i/s, 250 kHz	6.75	5.85	0.9	Strong signal and increasing skew.

^aThe path chosen for comparison or "direct" includes the SDA up converter, so the degradation contributed by it (normally about 0.5 dB) is chargeable to the recovery process and should be added to the above playback degradation in order to arrive at an estimate of the degradation compared to the normal real-time telemetry SNR.

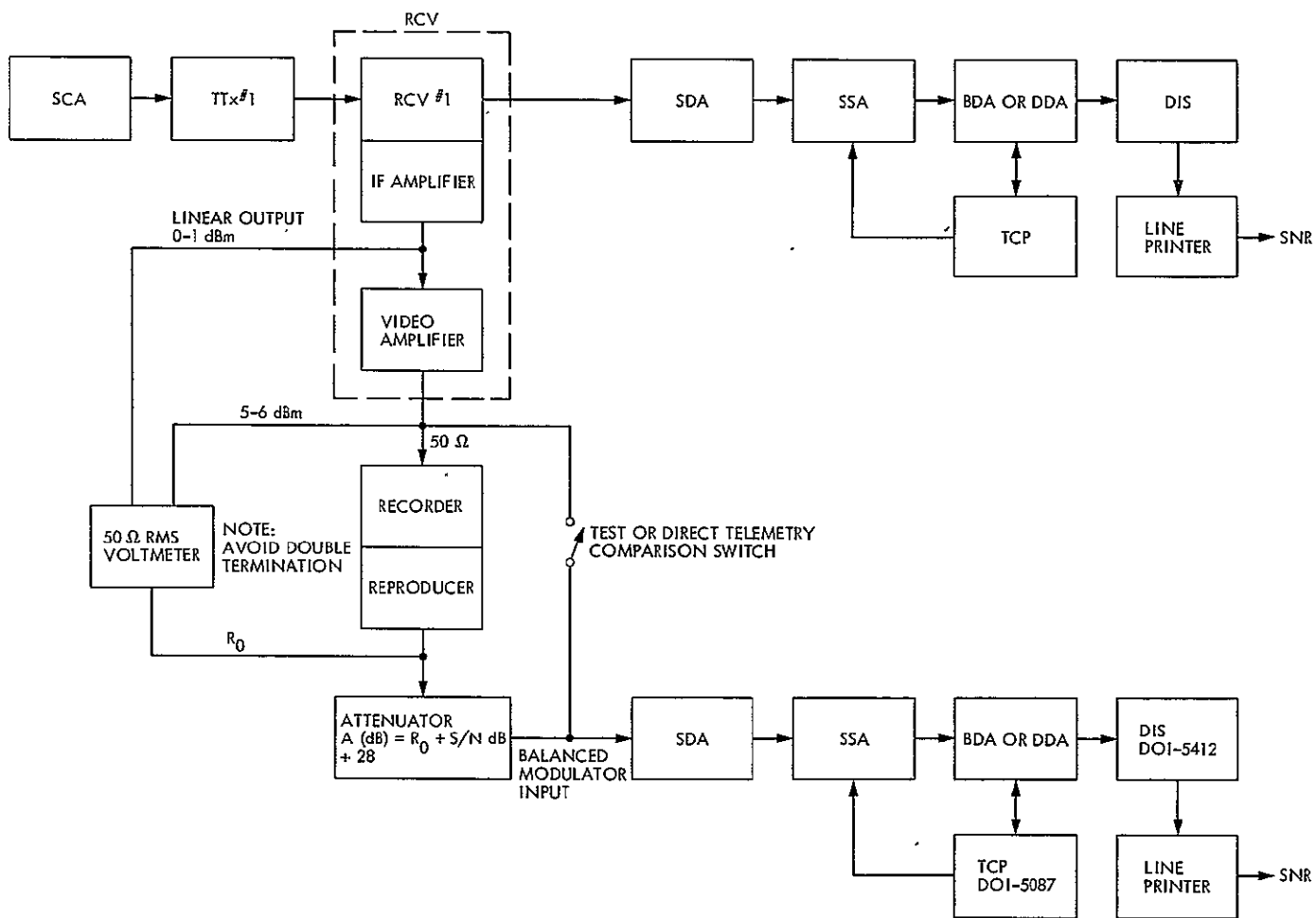


Fig. 1. Baseband record/reproduce configuration

N77-19116

Calibration of Block 4 Translator Path Delays at DSS 14 and CTA 21

T. Y. Otoshi, P. D. Batelaan, and K. B. Wallace
Radio Frequency and Microwave Subsystems Section

F. Ibanez
MCCC Development Section

Ground station range delays are currently being performed at 64-m stations in the DSN by use of the "Translator Method." This method requires the absolute calibrations of the delays of the Block 4 Doppler Translator Assembly as well as the cables connecting it to the high-power coupler uplink sampling point and the downlink injection points into S- and X-band masers.

In this article the techniques for calibrating the translator path by means of a portable zero delay device are described. In addition, some translator path data taken at DSS 14, Goldstone, over a period of about one year is presented.

I. Introduction

Ground station delay calibrations are currently being performed by the "Dish-Mounted Zero Delay Device (ZDD) Method" for 26-m antenna Deep Space Stations (DSSs), and the "Translator Method" for 64-m antenna DSS. The Z-corrections required for referring these calibrations to the DSS reference locations have been discussed in Ref. 1 for each of these methods.

The Translator Method requires periodic calibration of the total translator path delay between an uplink sampling point and the downlink signal injection points into S- and X-band masers. The purpose of this article is to describe the procedure

that has been used to calibrate the translator path delay with an R&D Portable ZDD and to present some previous and recent data obtained at the Goldstone Mars Station, DSS 14, and the JPL Compatibility Test Area, CTA 21.

II. Method for Calibrating Translator Delay

The Translator Method involves the sampling of an uplink range-coded transmitter signal from a 54-dB high-power directional coupler. This sampled uplink signal is coherently translated to S- and X-band downlink signals by the Block 4 Doppler Translator installed at all 64-m antenna DSSs. The downlink signals are injected into respective S- and X-band masers via directional couplers.

A simplified block diagram of the translator path between the high-power coupler and maser injection point is depicted in Fig. 1. In the actual installation, the translator path is more complex and includes the following:

- (1) Level Set Attenuator Assembly.
- (2) Uplink Sample Distribution Box.
- (3) Block 4 Doppler Translator Assembly (See Fig. 2).
- (4) Test Signal Control Assembly.
- (5) Noise Box.
- (6) Coaxial to waveguide transitions.
- (7) Interconnecting cables and waveguides.

As explained in Ref. 1, this translator path is in the DSS calibration path, but not in the path when ranging to a spacecraft. Therefore, this delay must be calibrated. The method currently being used to calibrate this path will now be described.

The calibration of the translator path involves two measurements as depicted in Fig. 1. In the first measurement, the Doppler Translator path between the uplink sampling point and the maser injection points are replaced by a portable ZDD and its associated test cables and attenuators. With the ZDD installed, as shown by the dashed lines in Fig. 1, ranging measurements are made and noted on the test data sheet as D_{ZDD} . It should be understood that there is a measured value for S-band and another for X-band but for brevity they will be considered to be those of a single measurement. The second measurement consists of changing the delay path back to the normal translator path with the exception that the ZDD test cables and attenuators are connected in series with the normal translator path cables. The ZDD adjustable attenuators are set to zero and the fixed pads are replaced by pads of lower value to produce received signal levels the same (as nearly as possible) as those of the first measurement. Range measurements are again made and noted on the test data sheet as D'_{XLTR} . The translator path delay can now be determined from subtraction of the first measurement from the second and adding in the delay of the portable ZDD.

Using the equations and terminology proposed in Ref. 1, the procedure can be expressed mathematically as follows.

In the first measurement, the measured range delay with the portable ZDD is

$$D_{ZDD} = \tau_1 + \tau_{ZDD} + \tau_{CABLE} + \tau_2 \quad (1)$$

In the second measurement, the measured range delay of the translator path with ZDD cable is:

$$D'_{XLTR} = \tau_1 + \tau_{XLTR} + \tau_{CABLE} + \tau_2 \quad (2)$$

where

τ_1 = DSS uplink delay from the ranging machine to the high-power coupler sampling point. This delay includes delays of the Block 4 exciter, klystron, filters, and waveguide up to the sampling point.

τ_2 = DSS downlink delay from the downlink maser injection point to the ranging machine. This delay includes delays of the maser, Block 4 receiver and any postamplifiers in the ranging path.

Differencing Eqs. (1) and (2) and rearrangement of terms give

$$\tau_{XLTR} = D'_{XLTR} - D_{ZDD} + \tau_{ZDD} \quad (3)$$

where τ_{ZDD} is the premeasured calibration delay of the portable ZDD without its external cables and is information supplied with the device. It can be seen that the procedure does not require knowledge of τ_{CABLE} which is the delay of the external ZDD cables and pads. If the same cables and equal length pads are common to both measurements, their delays will cancel out in the differencing calculation. This procedure allows the user to use additional lengths of station-available cables if necessary to reach the connection points.

The quantity of interest is τ_{XLTR} , the range delay of the total Block 4 translator path as defined from the high-power coupler to the maser injection point. Equation (3) is for the general case and applies to the procedure for measurement of either the (S, S) and (S, X) translator path delays. For convenience and brevity (S, S) and (S, X) are used throughout this article to denote S- to S-band and S- to X-band translations.

In practice, it is not possible to connect the ZDD cables all the way to the maser injection point.* Therefore, connections are made to the closest available connection point to the maser. In the case of the S-Band Polarization Diversity (SPD) cone at DSS 14, this connection point is a WR 430-to-type N transition on the coupling arm of a 30-dB directional coupler directly in front of the maser. In the case of the X-Band Receive Only (XRO) cone, this connection point is the input

*The maser injection point is currently defined as the midpoint of the cross-guide coupler installed directly in front of the maser.

to the XRO noise box. A correction must therefore be made for the additional lengths of waveguide from the measurement point to the maser injection point. These corrections are calculated from measured physical lengths of waveguide and theoretical group velocity of rectangular waveguide. In the case of the SPD cone, this correction is small (~ 1 ns), but for the XRO cone it is significantly larger (~ 6 ns) because of the noise box path.

The τ_{XLTR} measurement should be performed periodically (semiannually). It is also mandatory that it be performed (1) whenever any new equipment is installed, thus altering the translator path length, and (2) when a subassembly in the translator path be replaced. Absolute configuration control is mandatory. Any change in the translator path will invalidate the measurements.

III. Portable Zero Delay Device

The R&D Portable ZDD that has been used to calibrate Block 4 Translator paths at DSSs 14, 43 (Australia), and 63 (Spain), is shown in Fig. 3. A power splitter at the input permits the uplink signal to simultaneously feed the (S, S) and (S, X) band mixers. The local oscillator (LO) drive for the portable ZDD is supplied by the Block 4 Doppler Translator Assembly. The portable ZDD is basically a miniature Block 4 Translator without remotely controllable attenuators, filters, internal LO drives, etc. Therefore, its delay is small (typically less than 2 ns) and can be calibrated precisely in the laboratory with best available state-of-the-art techniques.

The portable ZDD contains a mixer assembly whose absolute delay is difficult to calibrate. Although different techniques were tried, the best result was obtained from a technique where two identical assemblies were cascaded back-to-back. The total measured delay is divided by two. The total present accuracy of the portable ZDD is estimated to be ± 1.5 ns (3σ).

The state-of-the-art of mixer delay measurement is currently not sufficiently advanced, so it is not clear whether the present accuracy of ZDD calibrations can be improved further without considerable development effort and cost.

Tests were made on the portable ZDD by use of a demonstration model "Microwave Link Analyzer" manufactured by Hewlett-Packard. Absolute delays of translators cannot be calibrated by the Link Analyzer, but relative delay changes can be calibrated to better than ± 1.0 ns. The tests showed that the portable ZDD delays were constant, with

frequency to within ± 1.0 ns over a 50-MHz bandwidth at the center transmit and S and X receive frequencies for the DSN.

The R&D ZDD shown in Fig. 3 has been used in the past to calibrate translator paths for all 64-m antenna DSS. In the future, 64-m stations will be supplied with their own calibrated portable ZDD.

IV. Test Results

A. Measurement of D_{ZDD} and D'_{XLTR}

To illustrate the measurement technique described in the previous section, some test data of D_{ZDD} and D'_{XLTR} at DSS 14 are shown in Figs. 4 through 7. The data were taken at different time periods and taken at several frequencies. These frequencies are indicated by transmitter voltage controlled oscillator (VCO) channel numbers. The relationship of channel number to microwave transmit (uplink) and receive (downlink) S- and X-band frequencies may be seen in Table 1.

Most of the slow upward trend seen in D_{ZDD} and D'_{XLTR} as a function of channel number is attributed to changes of klystron, exciter, maser, and receiver delays as a function of frequency. Since most of the delay changes with frequency are common to both measurements, they should cancel out in the differencing calculations. The individual amounts that various mentioned assemblies contribute to delay changes with frequency have been investigated and will be reported upon in a future DSN Progress Report.

B. Calibration of τ_{XLTR}

Figure 8 shows the calibrated translator delays τ_{XLTR} as determined from the D_{ZDD} and D'_{XLTR} measurements and use of Eq. (3). The calibrations done at different times were all performed using the same R&D portable ZDD shown in Fig. 3. Slight modifications to the portable ZDD were made at different times, but these have been accounted for in the updated values of τ_{ZDD} furnished with the device each time.

Figures 8a and 8b, respectively, show τ_{XLTR} values for the (S, S)-band path and (S, X)-band path at DSS 14. The measurements were made on October 23, 1975, May 16, 1976, and December 10, 1976.

It can be seen in Fig. 8a that the (S, S) translator delay values agree closely for October 23, 1975, and December 10, 1976, but the delay value for May 16, 1976, does not agree well. In the May 16 data, however, there is a cyclical variation in both the (S, S) and (S, X) data that indicates that there

could have been a leakage problem on the uplink similar to a multipath effect. Some tests and analysis of data made to explain these data are discussed in Part 5 of this article.

Figure 8b (S, X) delays on October 23, 1975, disagree with the other results by about 10 ns. The December 10 data showed that most of the cyclic variation seen on May 16 had disappeared. It is of interest to note that the (S, X) delays do not show an upward trend with frequency as do the (S, S) delays in Fig. 8a.

Figure 8c shows test data taken of a similar Block 4 Doppler Translator Assembly at CTA 21. The data show some cyclic variation, but some of this is attributed to measurement noise and nonrepeatability. There are two 13-pole filters and significant lengths of cable, and a number of components (such as switches and remotely controllable attenuators) to explain the large delays of about 80 to 90 ns. The filters are reasonably broadband and hence do not cause a significant variation of delay with frequency.

V. Analysis of the Leakage Problem

Tests were subsequently performed at DSS 14 during November and December, 1976, to pinpoint the cause of the large cyclic variations in translator delays seen on May 16, 1976. One test performed was a multipath test, which involved moving the subreflector through 6 inches of travel and observing variations in ground station delay. The test results showed less than 2 ns peak-to-peak (p-p) change on either (S, S) or (S, X) range delays. The 2 ns p-p was about the same as the noise on the measurement and repeatability. Since the Block 4 translator method uses directional couplers to obtain the uplink sample and couplers to inject downlink signals, the DSS calibrations by this method are significantly isolated from multiple-reflected signals that radiate back into the horn from the external antenna structure. Most portions of the uplink signals that reflect back into the horn are absorbed by the klystron. Due to the high directivity of the sampling coupler, very little reflection gets coupled back into the translator.

Analysis made of the May 16 data shows a possible explanation of the cyclic variations. Referring to measurements of D_{ZDD} and D'_{XLTR} values shown in Figs. 4 through 7, it can be seen that the cyclic variation appears only on the measurements of D_{ZDD} made on May 16, 1976. This type of behavior can be due to a leakage problem. Because of the similarity of the (S, S) and (S, X) data for D_{ZDD} , it is probable that the leakage was on the uplink path only. A loose connection probably occurred between the short 8-ft. uplink cable (supplied with the ZDD) and the high-power coupler.

VI. Evaluation of the Calibration Method and Results

The Translator Method was proposed initially as an interim solution to meet the immediate requirement by the Viking Project for a 5-m overall range accuracy. Serious calibration errors on 64-m antennas through the airpath were known to exist due to multipath and were reported in Ref. 2. The translator method was proposed as a satisfactory and economical interim solution for 64-m antenna DSS delay calibrations.

Experimental work is progressing on evaluating the absolute accuracy of this method. There are several known problems and disadvantages of this method. Some of the problems are:

- (1) The translator path delay is large and varies with frequency. The number of subassemblies (See Part 2 of this article) in the translator path make it difficult to keep it from being frequency and temperature sensitive.
- (2) Rigid configuration control and monitoring is required. A DSS must report when a component is replaced in the translator path or if any new cable is installed and recalibration is necessary.
- (3) The DSS 14 S-band translator path is different from that of DSS 43 and 63 due to a nonstandard SPD cone and noise box. A significant difference in the DSS 14 (S, S) translator path delay leads to suspicion concerning the validity of measurement accuracy.
- (4) The sampling and injection points are too far from the feed horn.
- (5) There is a slight difference in uplink delay through the "Level Set Attenuator Assembly" in the translator path for the 400-kW and 20-kW klystron operation modes.
- (6) The actual translator delay measurement can be made (conveniently) only up to the last coaxial connection point. In the XRO cone, the actual delay measurement stops at the input to the XRO noise box.
- (7) Leakage problems can occur. The measurements require special care by station personnel to use good laboratory techniques such as putting terminations on unused ports and cables and making sure that all connections are tight. Due to the stiffness of RG 252 cable, disconnection of this cable sometimes leads to loosening of other component connections in the system.
- (8) Some drift in system delay can occur between measurements of D_{ZDD} and D'_{XLTR} producing an error. This drift can be of the order of ± 5 ns.

Some recommendations for improving quality of data from this method are:

- (1) Repeat initial measurements to check for drift.
- (2) Go back to standard translator configuration without the ZDD cables and measure D_{XLTR} . The difference between D'_{XLTR} and D_{XLTR} should be the total ZDD cable delay and agree with calculable values to within ± 2 ns.

VII. Summary and Conclusions

The Translator path delay Measurement Technique has been described. Some data taken at DSS 14 pointed up some measurement problems, but in general it can be concluded that the translator path delay is probably stable with time to within ± 7 ns. The (S, S) delay varies about 12 ns with frequency from channel 5 to channel 29. The cause of this frequency variation

is not presently understood. Measurements made at CTA 21 showed that the Doppler Translator Assembly itself does not have significant variation of delay with frequency. Some similar measurements should be done at DSS 43 and DSS 63 to see if this frequency variation of translator path delays occurs at other 64-m stations.

Although the Block 4 Translator method has many problems and disadvantages, it is superior in accuracy to the airpath method, which has large multipath errors. It should be pointed out that multipath errors are also frequency sensitive. The "Translator Method" could be improved if there were a separate translator (simpler than the Block 4 Translator), and shorter paths and connection points dedicated specifically to ranging calibrations. A proposal for future consideration is to use a permanently installed portable ZDD, such as described in this article.

Acknowledgments

R. Coffin (formerly of the R. F. Systems Development Section) assisted in the development of the Translator Method and transfer of technology to Network Operations. M. Franco of the Radio Frequency and Microwave Subsystems Section assisted in the recent measurements at DSS 14.

References

1. Komarek, T., and Otoshi, T. "Terminology of Ranging Measurements and DSS Calibrations" in *The Deep Space Network Progress Report 42-36*, pp. 35-40, Jet Propulsion Laboratory, Pasadena, Calif., Dec. 15, 1976.
2. *A Collection of Articles on S/X-Band Experiment Zero Delay Ranging Tests*, Technical Memorandum 33-747, Vol. 1, pp. 114-126, edited by T. Y. Otoshi, Jet Propulsion Laboratory, Pasadena, Calif., Nov. 1975.

Table 1. Transmitter VCO channel vs. transmit and receive frequencies ^a

Channel number	S-Band transmit frequency, MHz	S-band receive frequency, MHz	X-band receive frequency, MHz
5	2110.243	2291.667	8402.778
10	2111.948	2293.519	8409.568
15	2113.654	2295.370	8416.358
20	2115.359	2297.222	8423.148
25	2117.064	2299.074	8429.938
30	2118.769	2300.926	8436.728

^aThe channel number versus transmit/receive frequency curve is linear.

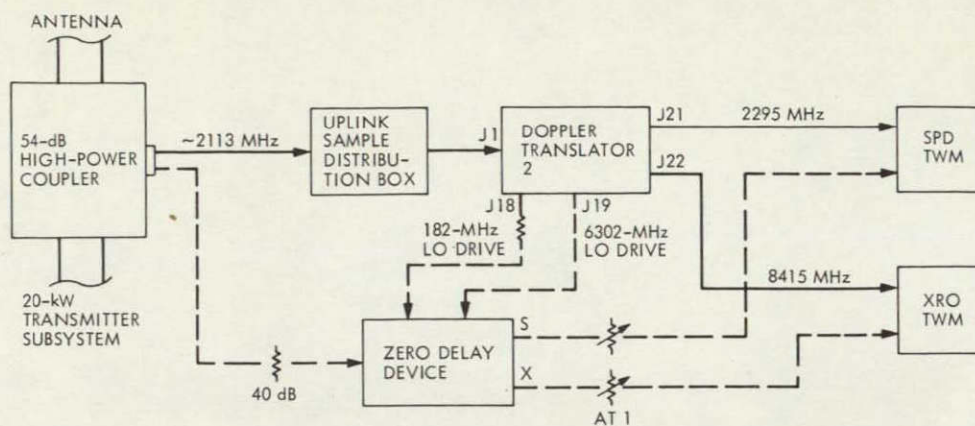


Fig. 1. Configuration for translator path delay calibration

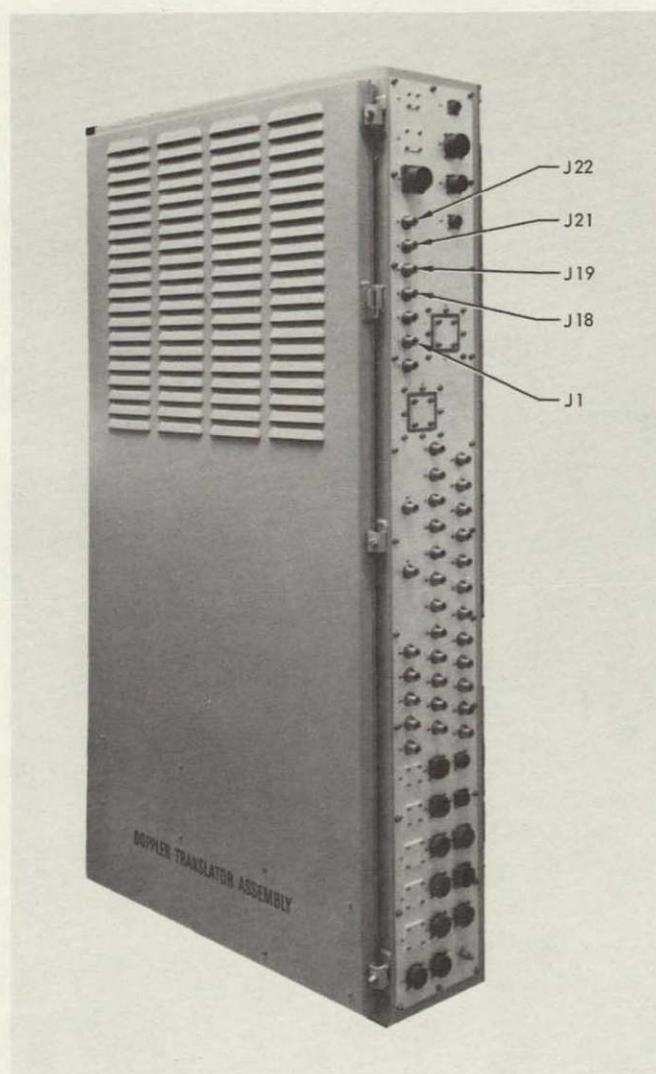


Fig. 2. Block 4 Doppler Translator Assembly (port numbers identify connection points shown in Fig. 1)

ORIGINAL PAGE IS
OF POOR QUALITY

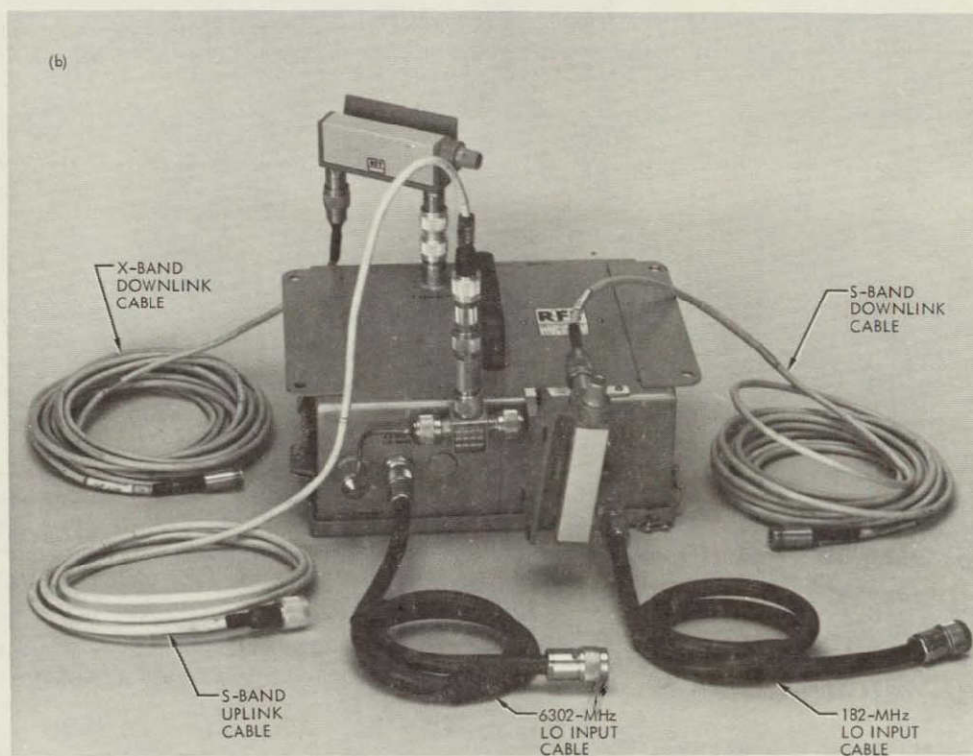


Fig. 3. R&D portable zero delay device: (a) without external test cables and attenuators, (b) with external test cables and attenuators

REPRODUCIBILITY OF THE
ORIGINAL PAGE IS POOR

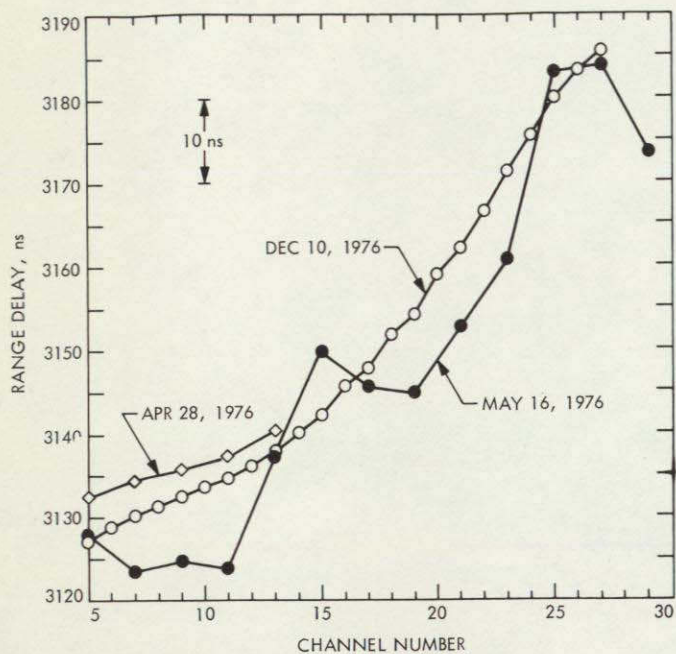


Fig. 4. Measurements of D_{ZDD} versus frequency at DSS 14 for the S-band uplink and S-band downlink path

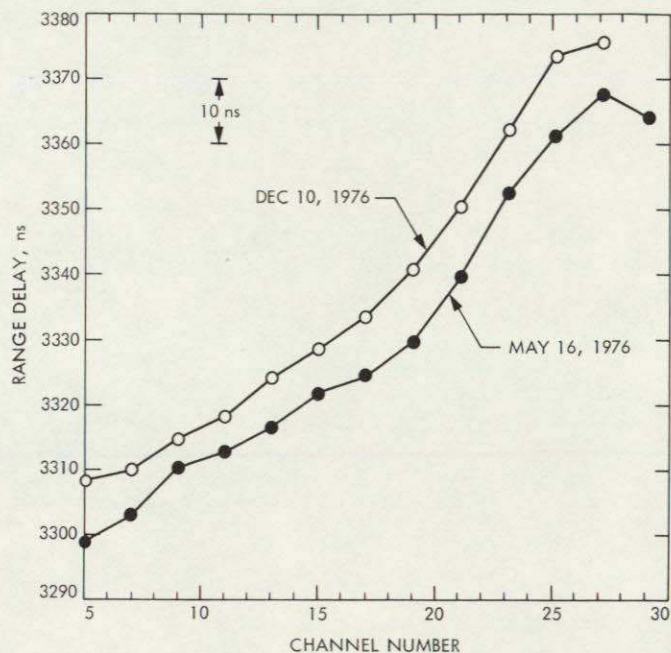


Fig. 6. Measurements of D'_{XLTR} versus frequency at DSS 14 for the S-band uplink and S-band downlink path

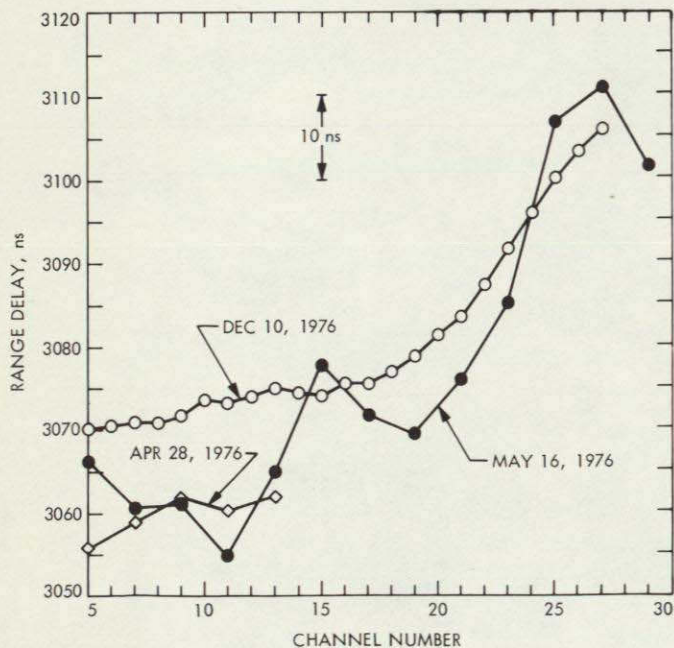


Fig. 5. Measurements of D_{ZDD} versus frequency at DSS 14 for the S-band uplink and X-band downlink path

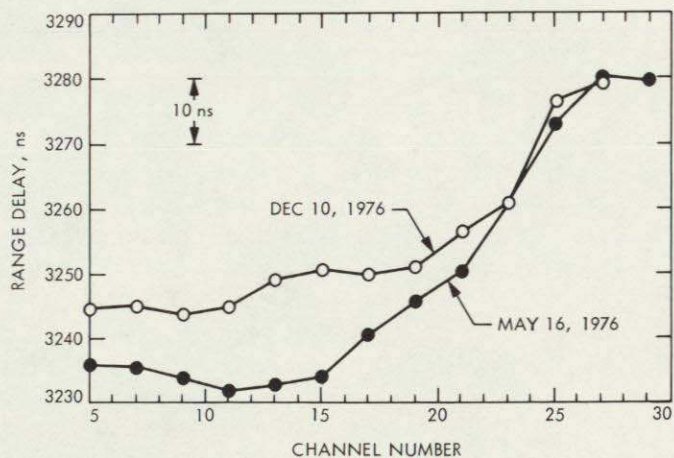


Fig. 7. Measurements of D'_{XLTR} versus frequency at DSS 14 for the S-band uplink and X-band downlink path

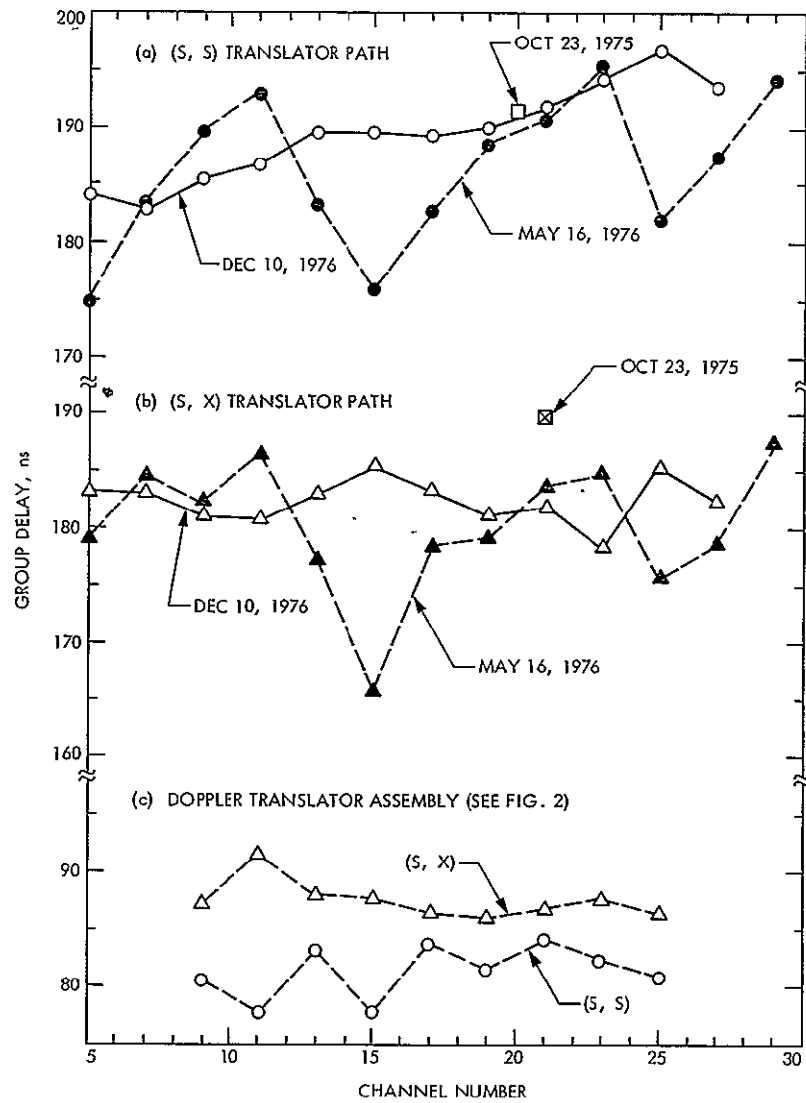


Fig. 8. Block 4 translator delay measurements: (a) (S, S) τ_{XLTR} values for DSS 14, (b) (S, X) τ_{XLTR} values for DSS 14, (c) Doppler Translator Assembly (Fig. 2) delay measured at CTA 21 on October 11, 1976

Page 14, 22D

N77-19117

Phase and Group Delay of S-Band Megawatt Cassegrain Diplexer and S-Band Megawatt Transmit Filter

R. Lay

Radio Frequency and Microwave Subsystems Section

This article reports the phase characteristic and group delay of the S-band Megawatt Cassegrain Diplexer (MCD) and S-band Megawatt Transmit Filter (MTF). These phase measurements on the MCD and MTF were done in response to the need to obtain the total DSS hardware ground delay required for very long baseline interferometry (VLBI) and ranging radio metric measurements

I. Introduction

As part of an effort to come up with the total ground delay at the 64-m stations for VLBI and ranging radio metric measurements, phase measurements on the S-band Megawatt Cassegrain Diplexer (MCD) have been made over both the transmitter frequency range (2100-2120 MHz) and the receiver frequency range (2270-2300 MHz). Phase measurements have also been made on the S-band Megawatt Transmit Filter (MTF) over the transmitter frequency range (2100-2120 MHz). The group delay for both the MCD and MTF are calculated using the results of these phase measurements.

II. Hardware Description

The S-band Megawatt Cassegrain Diplexer is shown in Fig. 1. It consists of two straight narrow-width waveguide

sections coupled together with waveguide hybrids. The straight narrow-width waveguide sections have a cutoff frequency of 2200 MHz; thus the MCD will pass signals through at the receive frequency of 2285 MHz and reject all signals from the transmitter which are transmitted to the antenna at a frequency of 2110 MHz.

The S-band Megawatt Transmit Filter is shown in Fig. 2. The MTF is a band reject filter with six cavities tuned to the receive frequency, providing a rejection of more than 90 dB at 2285 ± 15 MHz, while passing a frequency of 2110 ± 10 MHz.

Instrumentation methods of the VSWR and isolation recordings of both the MCD and MTF are described in Refs. 1 and 2. The results of these measurements are tabulated in Tables 1 and 2.

III. Phase Measurement Procedures

The phase measurement test configurations for either the MCD or MTF are shown in Figs. 3 and 4. Prior to recording any phase characteristics versus frequency on the X-Y plotter, it would be desirable to have a horizontal phase characteristic for the reference phase. This is achieved by having the same length for both the reference signal path and the test signal path using the test configuration shown in Fig. 3. The relative phase plots versus frequency obtained from the X-Y plotter are shown in Figs. 5, 6, and 7 for both the MCD and MTF. These relative phase plots were obtained using the test configuration shown in Fig. 4.

The values for $\Delta\phi$ and Δf can be obtained from the relative phase versus frequency plots (Figs. 5, 6, and 7). Referring to Fig. 5, for an incremental frequency change ($f_2 - f_1$), there will be a corresponding phase change ($\phi_{2 \text{ test}} - \phi_{1 \text{ test}}$) and ($\phi_{2 \text{ ref}} - \phi_{1 \text{ ref}}$). Thus the expression for the group delay may alternatively be written as

$$td = \frac{[(\phi_{2 \text{ test}} - \phi_{1 \text{ test}}) - (\phi_{2 \text{ ref}} - \phi_{1 \text{ ref}})]}{360^\circ \times [(f_2 - f_1) \text{ GHz}]} \text{ ns}$$

IV. Group Delay Results

The group delay is defined as the time required for a signal to propagate through a system, and it is simply given by

$$td = \frac{\Delta\phi}{360 \times \Delta f (\text{GHz})} \text{ ns}$$

The group delay for the MCD turned out to be 6.250 ns over the transmitter frequency range (2100-2120 MHz) and 14.815 ns over the receiver frequency range (2270-2300 MHz). The group delay for the MTF is 13.640 ns over the transmitter frequency range (2110-2120 MHz).

References

1. Hartop, R., JPL Test Procedure No. DMX-1370-TPA, *S-Band Megawatt Cassegrain Diplexer*, 25 September 1968.
2. Hartop, R., JPL Test Procedure No. DMX-1369-TPA, *S-Band Megawatt Transmit Filter*, 25 September 1968.

Table 1. VSWR, insertion loss, and isolation test data of Megawatt Cassegrain Diplexer

a. Insertion loss

Frequency, MHz	Insertion Loss, dB
2110	0.02460
2270	0.05626
2285	0.05517
2300	0.05019

b. VSWR and isolation

Test	Ports	Frequency, MHz					
		2100	2110	2120	2270	2285	2300
VSWR	TRANS	1.03	1.02	1.035			
VSWR	ANT	1.04	1.03	1.045	1.035	1.03	1.035
VSWR	RCVR				1.03	1.035	1.035
Rejection	Receive band				34.5	36	38.5
Rejection	Transmit band	99	96	90			

Table 2. VSWR, insertion loss, and isolation test data of Megawatt Transmit Filter

a. VSWR

Frequency, MHz	VSWR
2100	1.03
2110	1.02
2120	1.05

b. Insertion Loss

Frequency, MHz	Insertion Loss, dB
2100	0.03677
2110	0.03360
2120	0.03811

c. Rejection

Frequency, MHz	Rejection, dB
2259.0	80
2260.0	90
2261.5	100
2263.0	110
2270.0	110
2275.0	110
2280.0	110
2285.0	110
2290.0	110
2293.0	110
2295.0	100
2299.5	100
2301.5	90
2303.5	80

Table 3. Group delay of S-band Megawatt Cassegrain Diplexer and S-band Megawatt Transmit Filter

a. MCD over transmit band

Frequency, MHz	<i>td</i> , n-s
2110	6.250
2120	

b. MCD over receiver band

Frequency, MHz	<i>td</i> , n-s
2270	14.815
2300	

c. MTF over transmit band

Frequency, MHz	<i>td</i> , n-s
2110	13.640
2120	

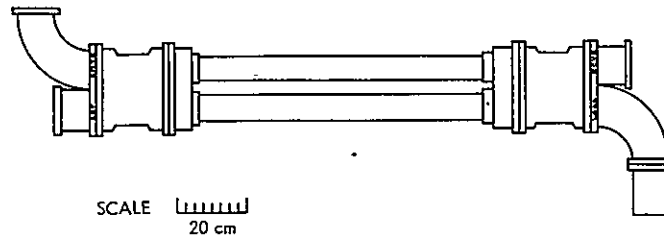


Fig. 1. S-band Megawatt Cassegrain Diplexer

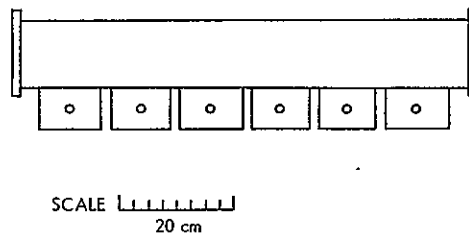


Fig. 2. S-band Megawatt Transmit Filter

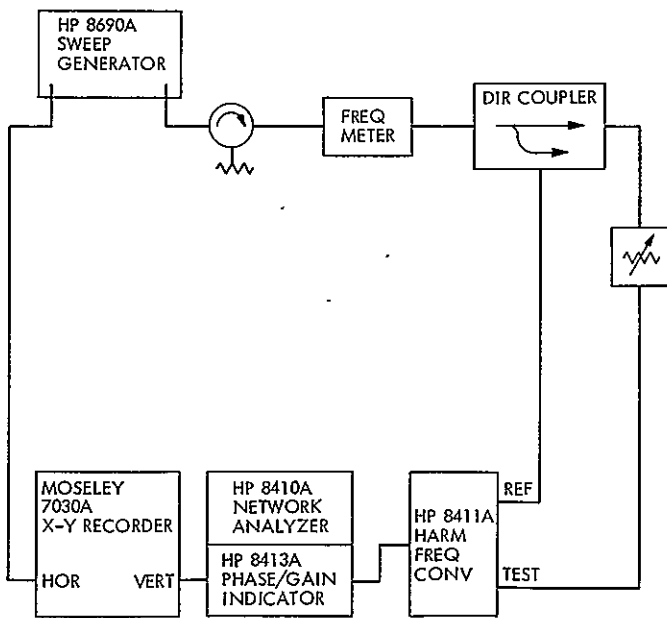


Fig. 3. Test configuration for reference phase

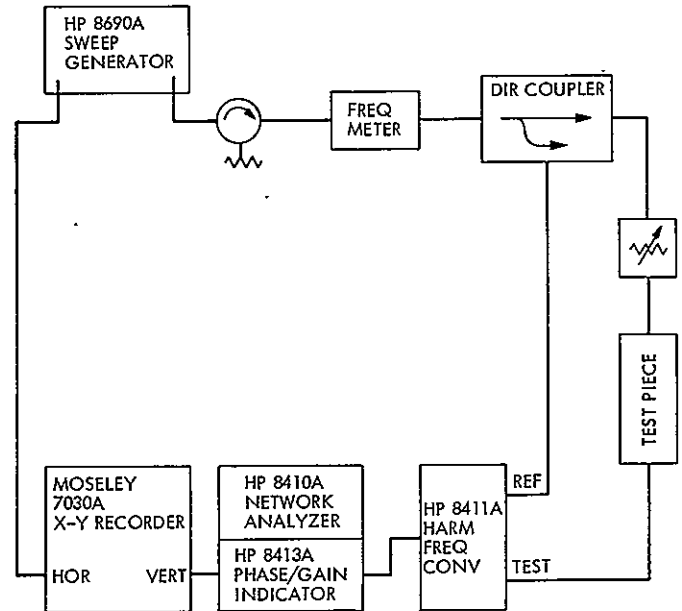


Fig. 4. Test configuration for relative phase of test device (MCD or MTF)

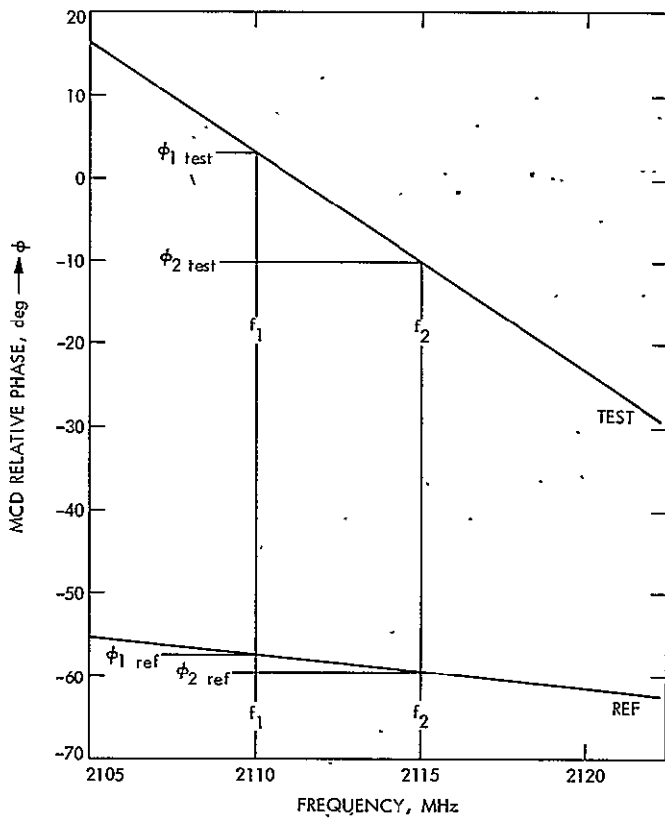


Fig. 5. Relative phase of MCD over transmit frequency range

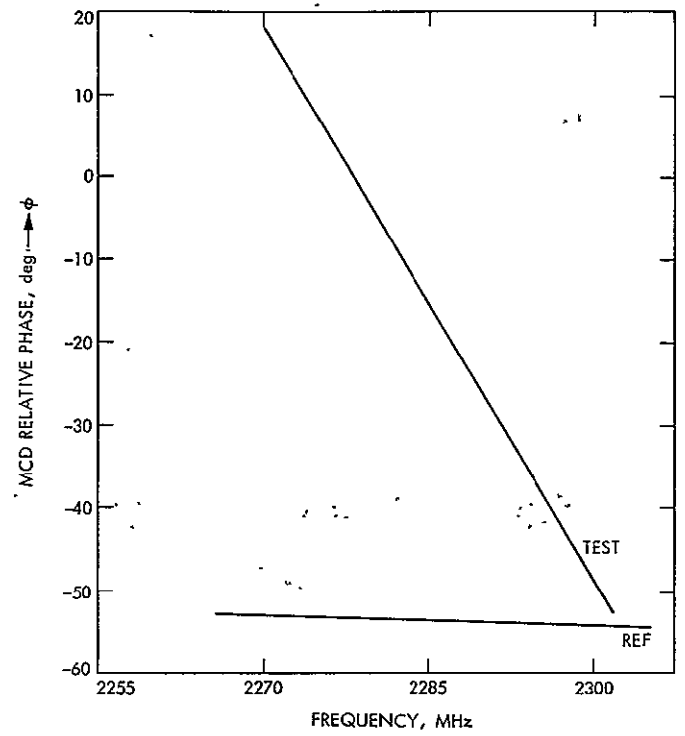


Fig. 6. Relative phase of MCD over receive frequency range

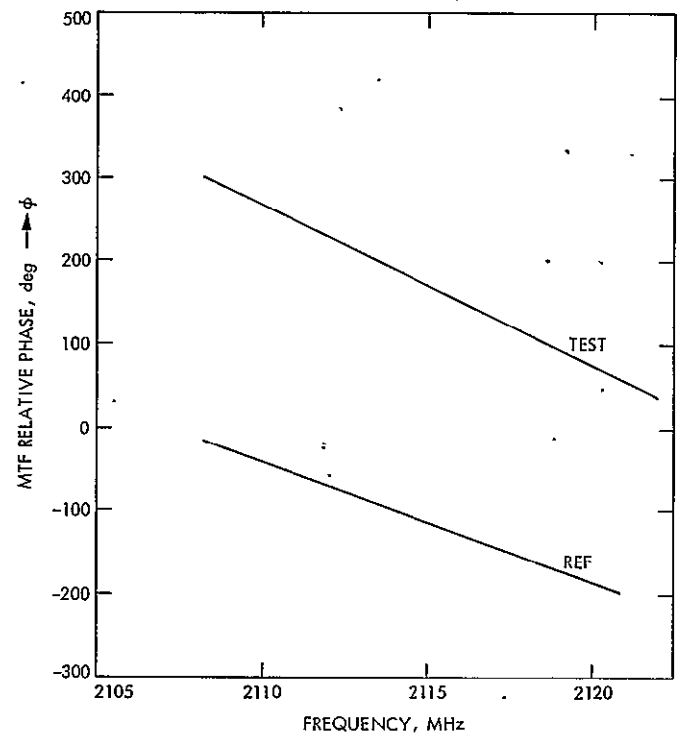


Fig. 7. Relative phase of MTF over transmit frequency range

N77-19118

Solar Plasma: Viking 1975 Interplanetary Spacecraft Dual-Frequency Doppler Data

S. C. Wu and F. B. Winn
Tracking Systems and Applications Section

K. B. W. Yip
Navigation Systems Section

Viking 1975 interplanetary S- and X-band doppler data are surveyed. These data show consistency with differenced range versus integrated doppler (DRVID) data when there is solar plasma and with Faraday rotation data otherwise. An increase of solar plasma effects with decreasing Sun-Earth-probe (SEP) angle (approaching Mars orbit insertion) is demonstrated. The 2-way/3-way data indicate a homogeneous solar plasma structure over a 8000-km spread. Occasional cycle slips in the data are pinpointed and tabulated.

I. Introduction

S- and X-band doppler data are valuable to the investigation of solar plasma activities and, consequently, to deep-space navigation. Since the beginning of the Viking 1975 (VK'75) mission, hundreds of good-quality data passes have been collected. This is the first time such abundance of good-quality S- and X-band doppler data have been available. With this data bank, an extensive study of the solar plasma can be made, and models can be constructed to predict the accuracy of uplink calibration from downlink data alone.

This article provides an overview of the VK'75 interplanetary S- and X-band doppler data. The data acquired after Mars orbit insertion (MOI) will be reported in the near future. The electrical phase changes are plotted to show the history of the line-of-sight charged-particle variations. Agreements with Faraday rotation and differenced range versus integrated doppler

(DRVID) data are illustrated. A calibration demonstration (Ref. 1) using the S- and X-band doppler data shows a three-fold reduction in the uncertainty of Mars probe encounter position estimates, a two-fold reduction in the rms doppler residuals and an approximate 80-km agreement with the "radio-only" long arc estimates. Solar plasma activities are shown increasing with decreasing Sun-Earth-probe (SEP) angle while approaching MOI. A segment of 2-way/3-way data is studied to demonstrate an approximate 8000-km homogeneity in solar plasma structure.

II. Background

Radio metric doppler is one of the prime data types for interplanetary navigation. During the VK'75 missions, S-band (~2.1 GHz) carriers are transmitted from Deep Space Stations (DSSs) to spacecraft in deep space. On each spacecraft, the

S-band carrier is multiplied by a factor of 240/221 and retransmitted back to the DSS; at the same time an experimental X-band signal, obtained by multiplying the uplink S-band carrier by a factor of 880/221, is also transmitted parallel to the downlink S-band carrier. These radio transmissions are corrupted by the charged particles in solar plasma and ionosphere. In particular, the amount of phase change $\Delta\Phi$ is directly proportional to the net change of the line-of-sight electron content and inversely proportional to the carrier frequency squared (Ref. 2):

$$\Delta\Phi = \frac{e^2(\Delta N)}{8\pi^2\epsilon_0 m f^2} \text{ (meters)}$$

where

e = electron charge (-1.602×10^{-19} coulomb)

ϵ_0 = free-space permittivity (8.854×10^{-12} farad/m)

m = electron mass (9.109×10^{-31} kg)

f = carrier frequency (Hz)

ΔN = net change in line-of-sight electron content (m^{-2})

The observables of the S- and X-band doppler data are the accumulated S- and X-band carrier cycles. These are directly reducible into S- and X-band phase changes, $\Delta\Phi_s$ and $\Delta\Phi_x$. When these two observables are differenced, the effects of spacecraft motion and of troposphere, being common to both S- and X-band transmissions, are cancelled out, leaving the charged-particle effects behind. With the S- and X-band carrier frequencies specified above, the S-band phase change due to charged particles can be expressed as (Ref. 3):

$$\Delta\Phi = 1.08 (\Delta\Phi_s - \frac{3}{11} \Delta\Phi_x)$$

Hence, the effects on the doppler data of the charged particles alone can be determined and calibrated.

III. Charged-Particle Effects

X-band receivers are installed only at DSSs 14, 43, and 63. Hence, S- and X-band doppler data are available only at these stations. During the VK'75 cruises, hundreds of data passes were collected. The chronological spans for these data passes up to the second MOI (August 7, 1976) are displayed in Fig. 1.

Figures 2 and 3 are the accumulated phase changes due to line-of-sight charged particles for the two spacecraft, each up to its MOI (the first being on June 19, 1976). In the calculation of these phase changes, a threshold is set to remove unrealistic rates of phase change and multiple S-band cycle slips (see Section VI). This threshold is set at 1 meter/minute: a threshold large enough to include plasma variations encountered but small enough to exclude "blunders." Also, accumulated phase changes are shown with each pass starting from zero phase. Only relative phase changes can be observed. To recover absolute phase changes, range data would be required.

Figure 4 compares five December 1975 passes with Faraday rotation¹ and DRVID² results. Figures 4a-d are typical no-solar-plasma passes in which all three data types agree well. Figure 4e is an example of a solar-plasma-affected pass. Here S- and X-band doppler and DRVID data still are consistent but differ from Faraday rotation data.

Figure 5 shows the maximum phase change (upper plot) and the corresponding mean rate of change (lower plot) for each of the passes. Here, further comparison with DRVID results is presented. This comparison indicates consistency in the general trend of the variations of charged-particle effects. The occasional differences between these two results are due to (1) the two data sets not being taken in the same period of time, and (2) the DRVID data being represented by a polynomial.

IV. Solar Plasma Effects

In the above section we have shown the effects of total line-of-sight charged particles on the S- and X-band doppler data. These effects include both the solar plasma and the ionospheric activities. The ionosphere is a relatively well known and stable component. The highly variable solar plasma activities have a significant effect on deep space radio metric data and limit the DSN navigation capability. To facilitate the investigation of the solar plasma activities, it is desirable to isolate its effects on the S- and X-band doppler data from the ionospheric effects.

The ionospheric effects are determined by observing the Faraday rotation effects at the DSS, using the signals transmitted from geo-stationary satellites and then mapped to the directions of the two Viking spacecraft. Since the solar plasma effects and the ionospheric effects are additive, the

¹Faraday rotation data, provided by K. S. Lambert of Section 314, measure the Earth's ionospheric electron content only.

²DRVID (differenced range versus integrated doppler) data are provided by V. W. Lam and H. N. Royden.

former can be extracted from the S- and X-band doppler data by subtracting out the latter.

Figures 6 and 7 are the accumulated phase changes due to the solar plasma activities for the two spacecraft. A comparison with Figs. 2 and 3 reveals that they differ only by small drifts near the beginnings and ends of the passes. This is mainly because of large line-of-sight mass for the ionosphere at the lower elevation angles. This indicates the dominance of the solar plasma dynamics over the ionosphere, as expected. From these figures (and Figs. 2 and 3 as well) it is easily observed that the charged-particle effects increase when approaching MOI. This is expected since the SEP angles become smaller as the time elapses, as shown in Fig. 8.

V. Two-Way/Three-Way Tracking Data

During a transmission handover between two DSSs, often there is a period in which both DSSs are receiving the same signal transmitted back from the spacecraft. The data received by the transmitting DSS are called 2-way data while those received by the other DSS are labeled 3-way data. These data contain useful information on solar plasma structure.

Figure 9 is an expanded segment of Fig. 6, which contains a relatively longer span of 2-way/3-way data. The resemblance in phase changes between the two DSSs indicates a homogeneous solar plasma over a distance between the two ray paths (~ 8000 km). Figure 10 is the difference between the two phase changes. The ± 0.3 -meter residual is within the limit of the mapped Faraday rotation data³ and should not be considered as the real difference in solar plasma effects.

³The uncertainty of the mapped Faraday rotation data at elevation angles below 30 degrees is typically 0.5 meter (Ref. 4).

VI. Cycle Slips

During the acquisition of the S- and X-band doppler data, there were intermittent cycle slips. Those multiple slips, which appear as phase changes greater than 1 meter, have been discarded as erroneous data. The remaining ones appear as phase jumps in Figs. 2, 3, 6, and 7. The effect of X-band cycle slips is too small to be detected; S-band cycle slips during strong solar plasma activities are also hard to detect. Those which are detectable are listed in Tables 1 and 2. These will be helpful in studying the causes and the remedy of the cycle slips.

In future studies of solar plasma structure through S- and X-band doppler data, any detectable cycle slips will have to be removed. This can be done by either of the two following schemes: (1) manually locate the cycle slips and set a suitable lower threshold; (2) automatically vary the threshold by examining phase changes for previous points.

VII. Conclusions

S- and X-band dual-frequency doppler data, unprecedented both in quality and quantity, have been collected during the VK'75 mission. They are consistent with Faraday rotation data (when there is no solar plasma) and consistent with DRVID data. A steady increase of solar plasma dynamics has been demonstrated as the angular separation between probes and the Sun decreased. The 2-way/3-way data have indicated a solar plasma homogeneous over an approximate 8000-km distance.

References

1. Yip, K. W., Winn, F. B., and Wu, S. C., "Viking I S/X Dual Doppler Demonstration," to be published.
2. Laurence, R. S., Little, C. G., and Chivers, H. J. A., "A Survey of Ionospheric Effects upon Earth-Space Radio Propagation," *Proc. IEEE*, Jan. 1964.
3. Winn, F. B., Reinbold, S. R., Yip, K. W., Koch, R. E., and Lubeley, A., "Corruption of Radio Metric Doppler Due to Solar Plasma Dynamics: S/X Dual-Frequency Doppler Calibration for These Effects," in *The Deep Space Network Progress Report 42-30*, pp. 88-101, Jet Propulsion Laboratory, Pasadena, Calif., Dec. 15, 1975.
4. Yip, K. W., and Mulhall, B. D., "A System Analysis of Error Sources in the Technique Used for Ionospheric Calibration of Deep Space Probe Radio Metric Data," in *The Deep Space Network Progress Report*, Technical Report 32-1526, Vol. XVII, pp. 48-67, Jet Propulsion Laboratory, Pasadena, Calif., Oct. 15, 1973.

Table 1. Detectable S-band Cycle Slips in S- and X-band doppler data (Viking A)

Date	DSS	Number of slips	Span hours	Slips/hour
2/16/76	14	2	7.9	0.253
3/22	63	10	9.8	1.020
3/24	14	1	8.6	0.116
3/26	14	8	7.5	1.067
3/26	43	10	7.6	1.316
3/29	63	1	8.3	0.120
4/2	63	1	8.2	0.122
4/6	63	2	9.5	0.211
4/23	63	1	11.0	0.091
4/24	63	1	12.6	0.079
4/25	63	1	7.7	0.130
5/5	14	3	7.6	0.395
5/6	63	1	13.0	0.077
5/6	14	19	4.2	4.524
5/7	43	1	5.9	0.169
5/10	63	6	7.8	0.769
5/11	63	MANY	8.4	?
5/15	14	2	9.4	0.213
5/18	43	3	5.4	0.556
5/19	43	8	8.6	0.930
5/20	63	1	11.8	0.085
5/21	63	1	12.7	0.079
5/25	63	2	9.7	0.206
5/25	14	1	6.9	0.145
5/27	63	4	8.6	0.465
5/28	63	2	8.2	0.224
5/29	63	7	11.5	0.609
5/30	63	4	12.9	0.310
5/31	14	1	1.2	0.833
6/4	63	1	12.7	0.079
6/5	63	1	12.6	0.079
6/6	43	1	8.7	0.115
6/6	63	2	13.0	0.154
6/8	43	4	5.5	0.727
6/8	63	2	12.4	0.161
6/9	43	1	9.1	0.110
6/9	14	1	12.2	0.082
6/10	43	1	4.7	0.213
6/11	43	2	7.2	0.278
6/13	43	1	5.6	0.179
6/13	63	1	12.4	0.081
6/14	43	2	9.0	0.222
6/15	43	1	9.6	0.104
6/15	63	3	12.5	0.240
6/16	43	1	9.7	0.103
6/16	14	1	2.2	0.455
6/17	63	1	12.4	0.081
6/18	63	1	8.9	0.112
6/18	14	6	11.7	0.513
6/19	14	2	3.4	0.588

Table 2. Detectable S-band cycle slips in S- and X-band doppler data (Viking B)

Date	DSS	Number of slips	Span hours	Slips/hour
3/17/76	63	1	13.0	0.077
3/24	63	2	9.2	0.217
3/31	63	2	8.8	0.227
4/7	63	1	8.2	0.122
4/10	63	1	10.2	0.098
4/16	63	2	12.0	0.167
4/22	63	4	7.9	0.506
5/9	63	5	6.8	0.735
5/15	43	3	6.9	0.435
5/15	63	2	12.4	0.161
5/16	63	1	12.7	0.079
5/21	14	1	8.9	0.112
5/24	63	2	11.4	0.175
5/31	63	2	8.2	0.244
6/1	43	1	4.2	0.238
6/1	63	1	12.4	0.081
6/2	43	3	10.4	0.288
6/12	63	1	11.5	0.087
7/8	63	1	2.9	0.345
7/12	63	1	2.6	0.385
7/15	14	2	3.4	0.588
7/17	14	2	2.9	0.690
7/21	14	1	6.3	0.159
7/22	14	1	2.6	0.385
7/30	63	1	3.2	0.313
8/6	43	6	9.9	0.606
8/8	14	2	10.1	0.198
8/9	43	1	8.0	0.125

		DECEMBER/1975																			
VIKING	DSS	5	6	7	8	9	10	11	12	13	14	15	16	17	18	19	20	21	22	23	
A	14	—				—					—	—							—		
A	43																				
A	63																				
B	14																				
B	43																				
B	63																				

															FEBRUARY						
17	18	19	20	21	22	23	24	25	26	27	28	29	30	31	1	2	3	4	5	6	7

3	4	5	6	7	8	9	10	11	12	13	14	15	16	17	18	19	20	21	22	23	24
---	---	---	---	---	---	---	----	----	----	----	----	----	----	----	----	----	----	----	----	----	----

															MAY						
18	19	20	21	22	23	24	25	26	27	28	29	30	1	2	3	4	5	6	7	8	9

3	4	5	6	7	8	9	10	11	12	13	14	15	16	17	18	19	20	21	22	23	24
---	---	---	---	---	---	---	----	----	----	----	----	----	----	----	----	----	----	----	----	----	----

													AUGUST							
19	20	21	22	23	24	25	26	27	28	29	30	31	1	2	3	4	5	6	7	8

Preceding page blank

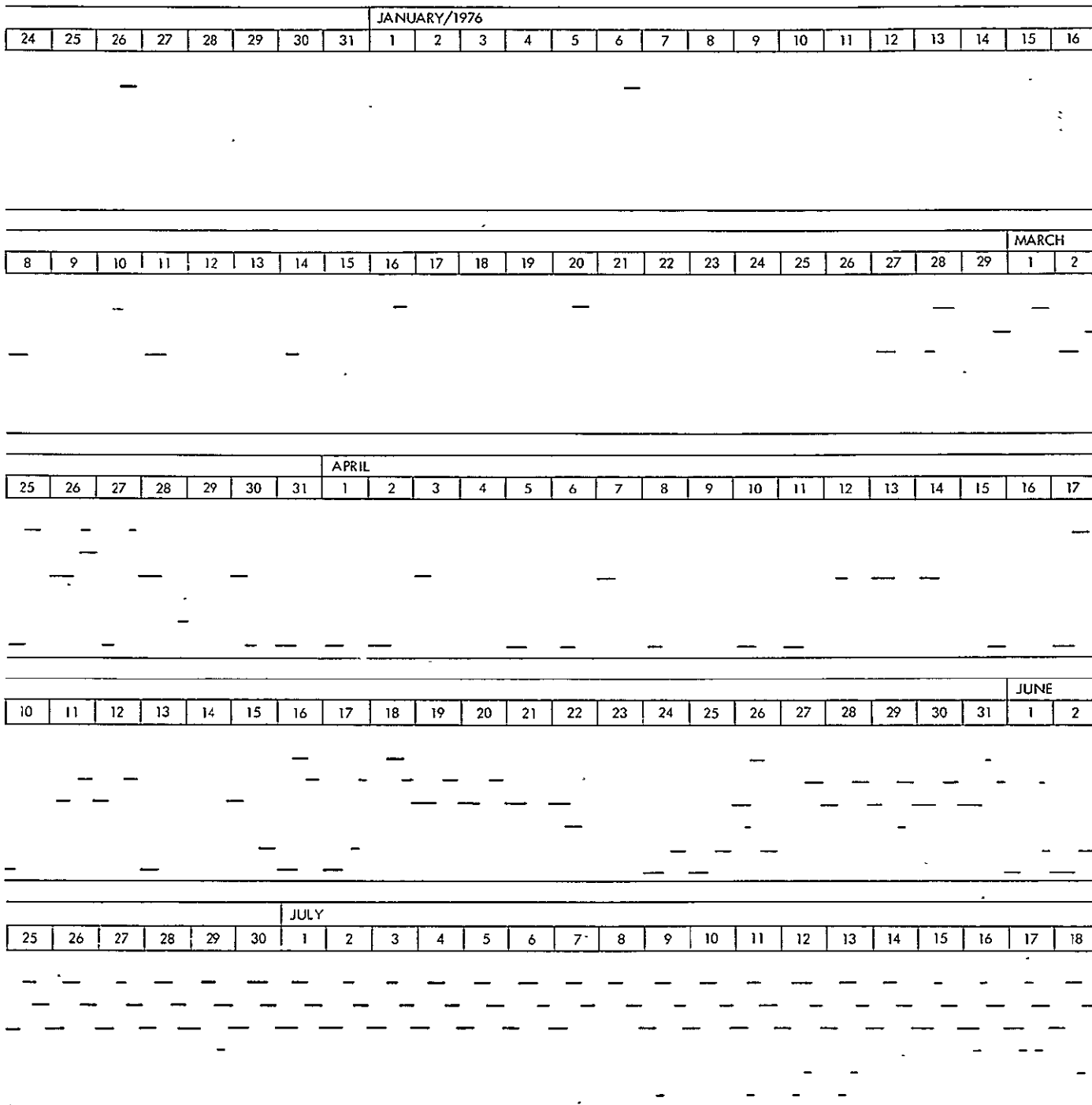
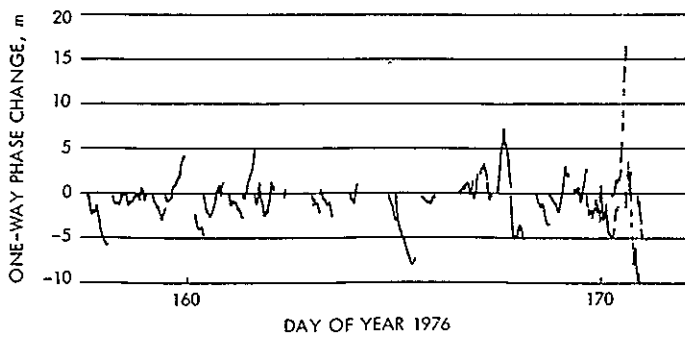
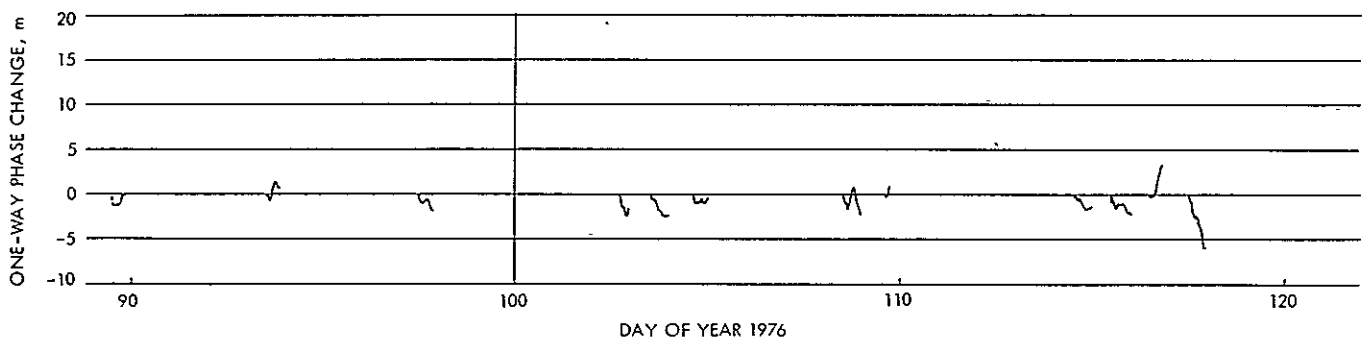
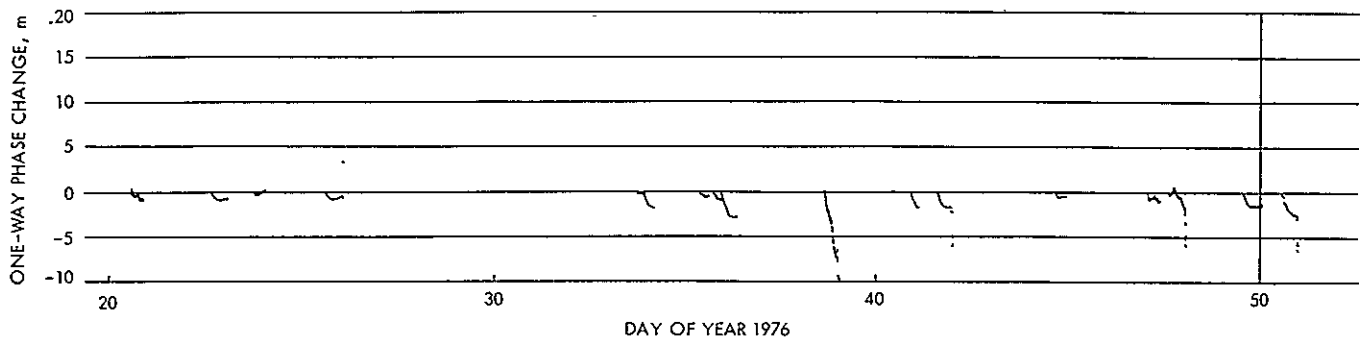
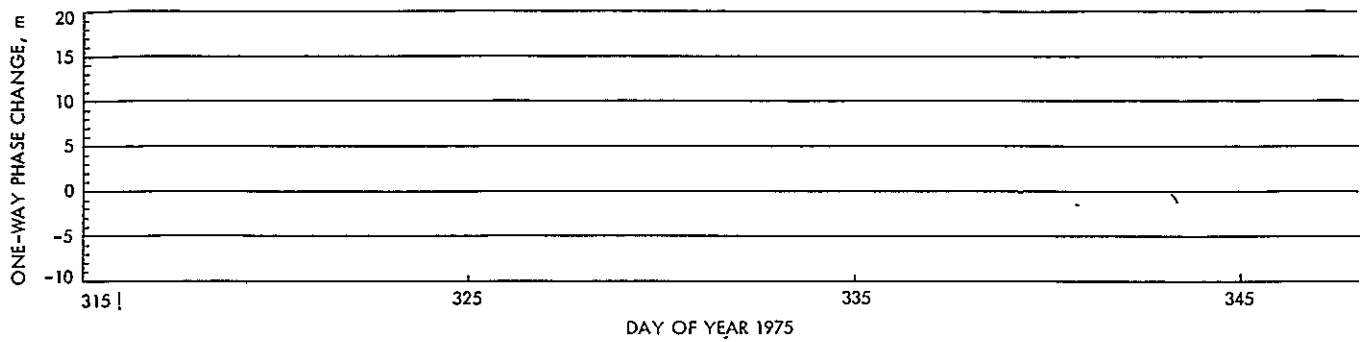


Fig. 1. Chronological spans for S- and X-band doppler data for Viking 1975



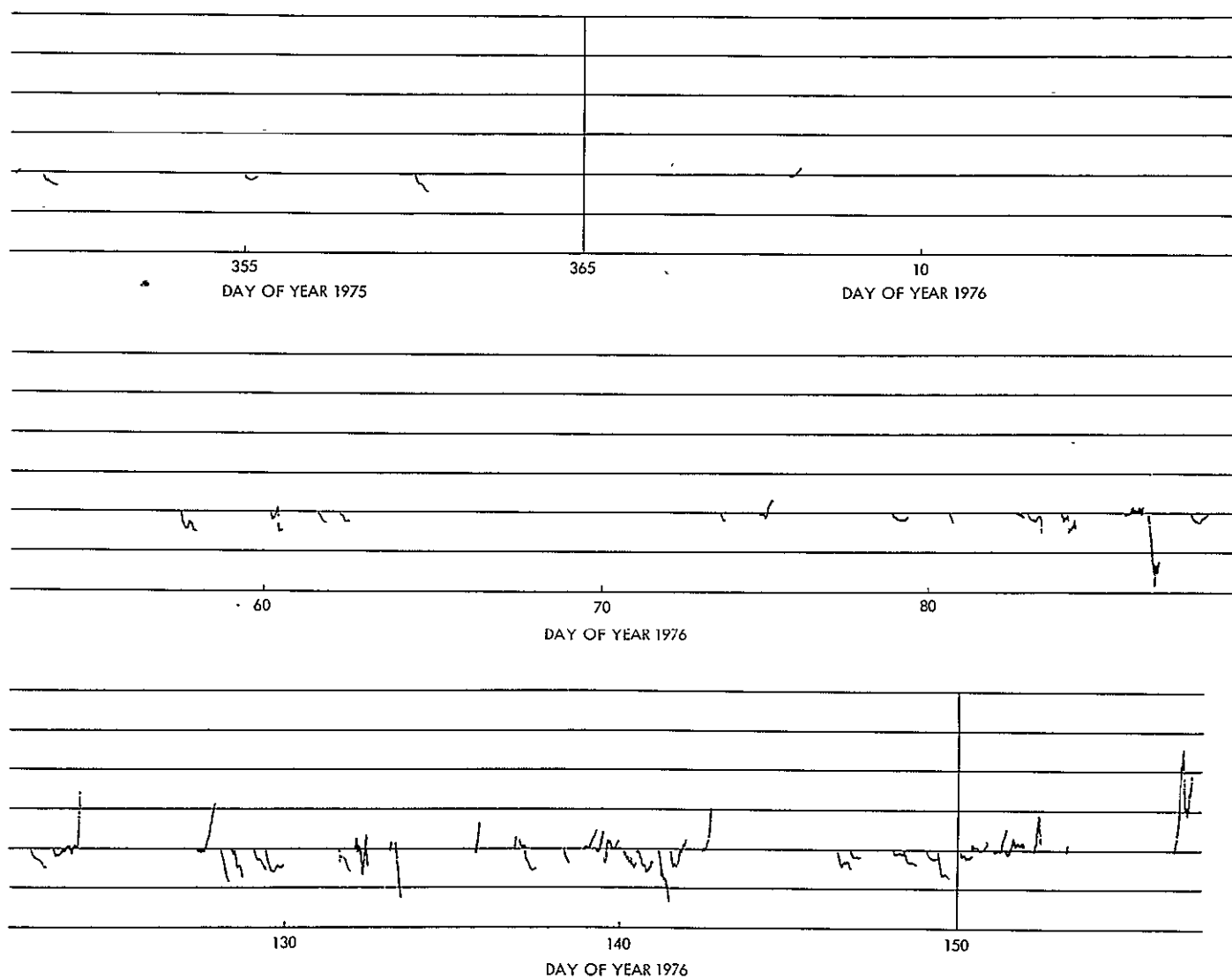
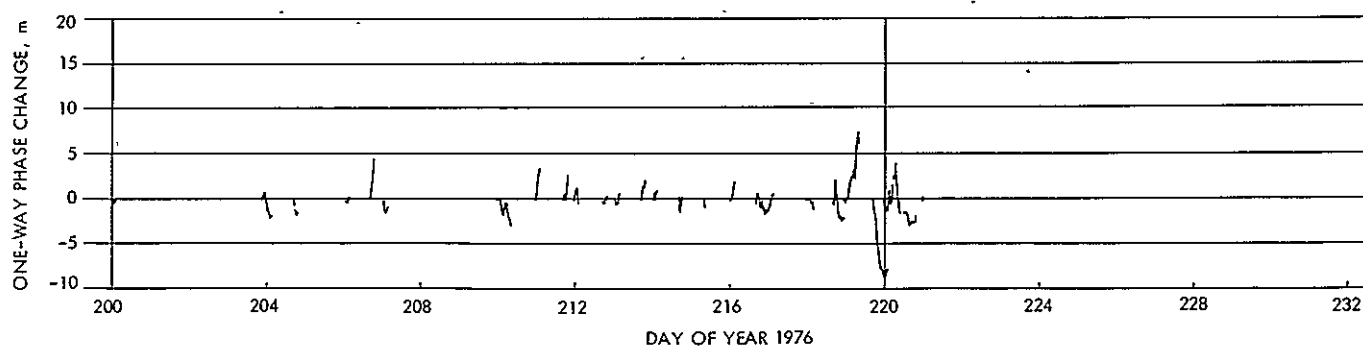
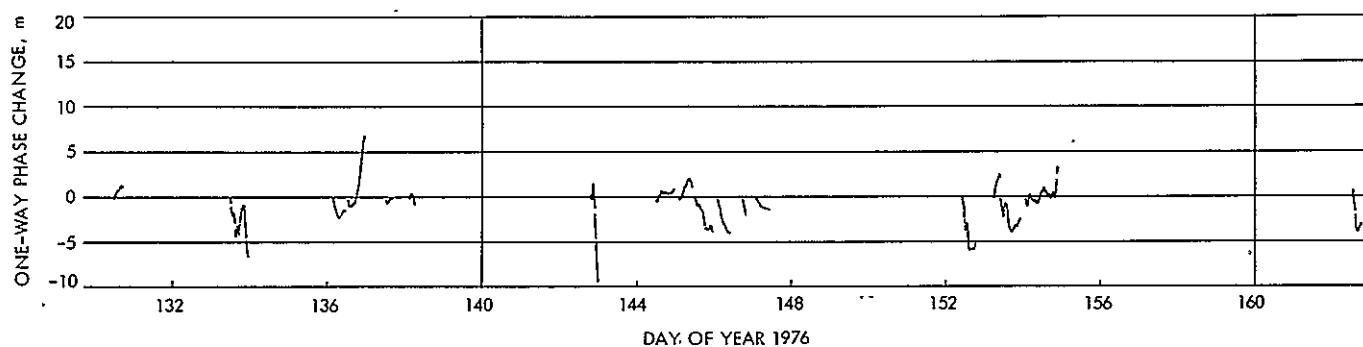
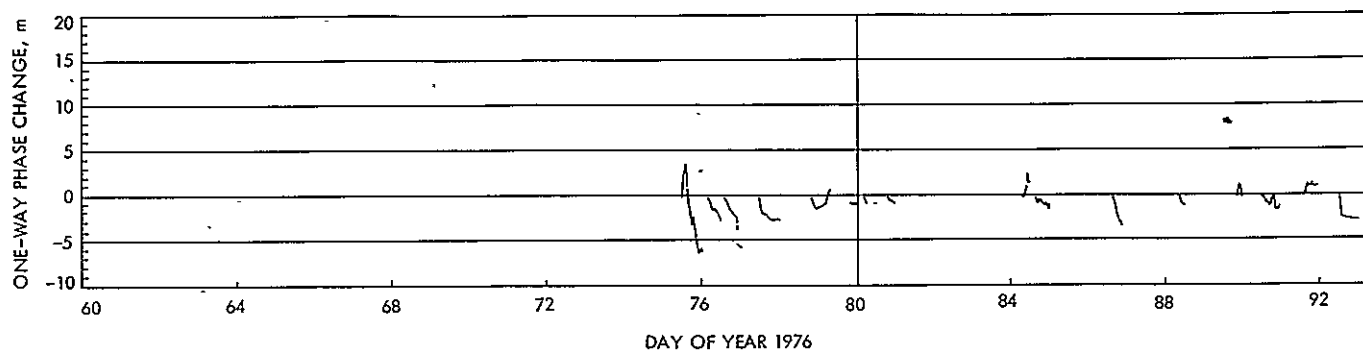


Fig. 2. Cumulative one-way phase change due to line-of-sight charged-particle dynamics (Viking A)



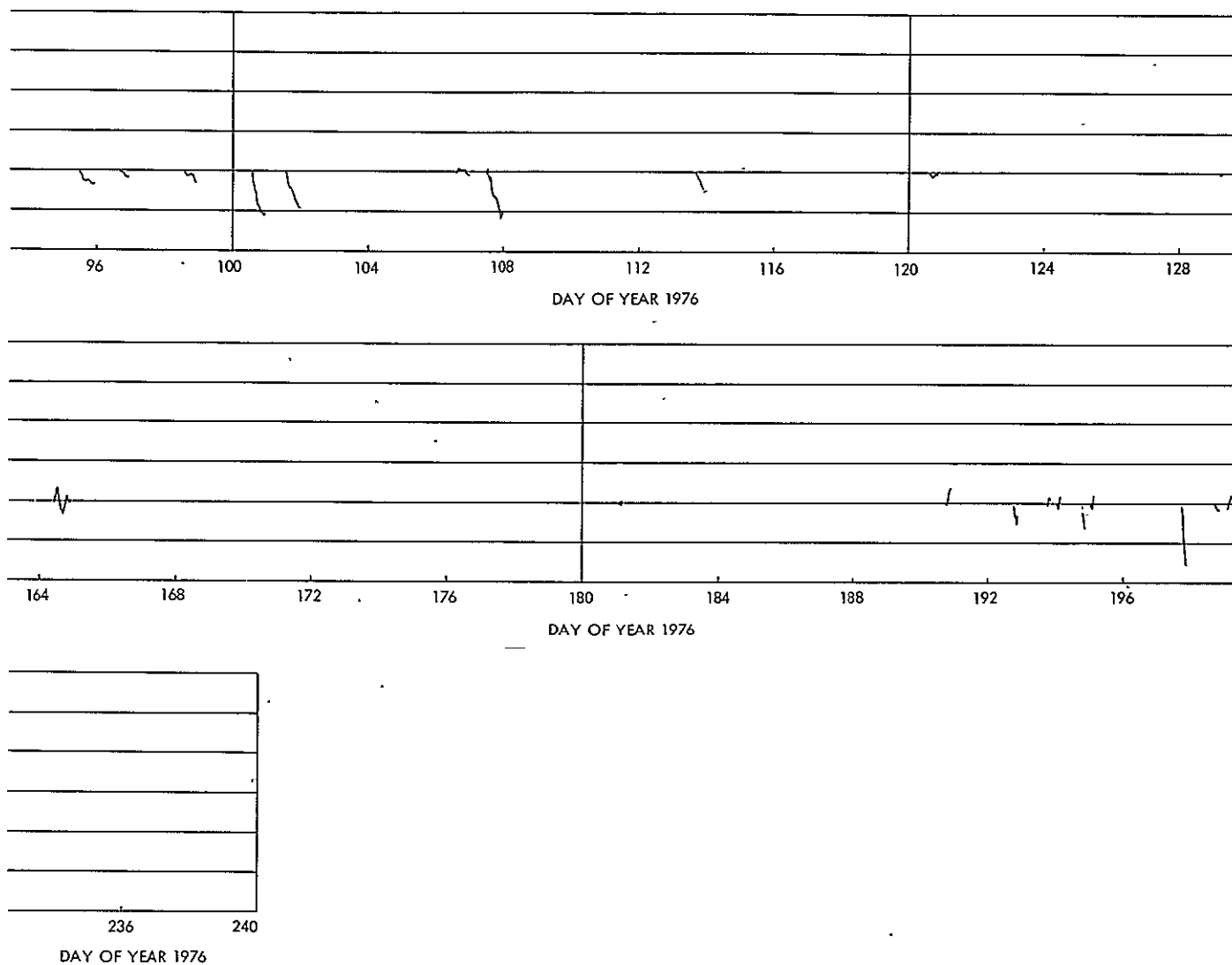


Fig. 3. Cumulative one-way phase change due to line-of-sight charged-particle dynamics (Viking B)

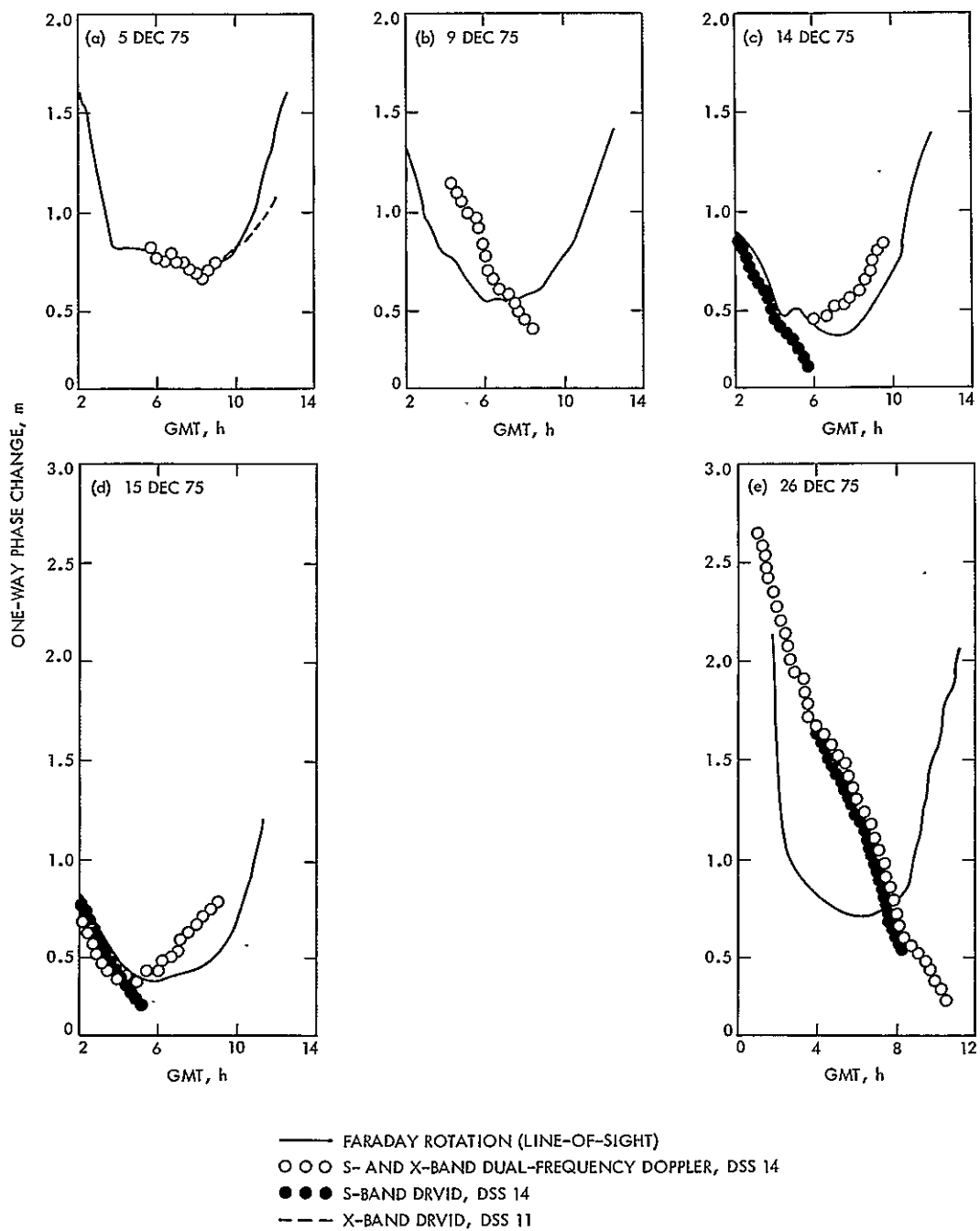


Fig. 4. Comparison of charged-particle effects

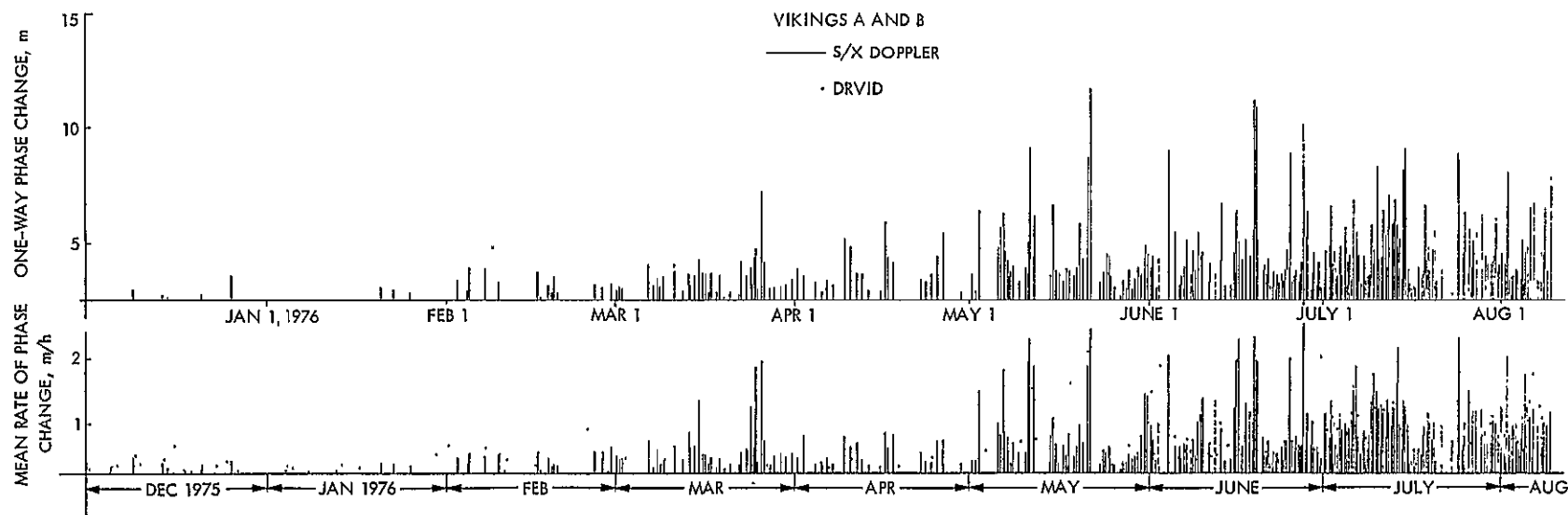
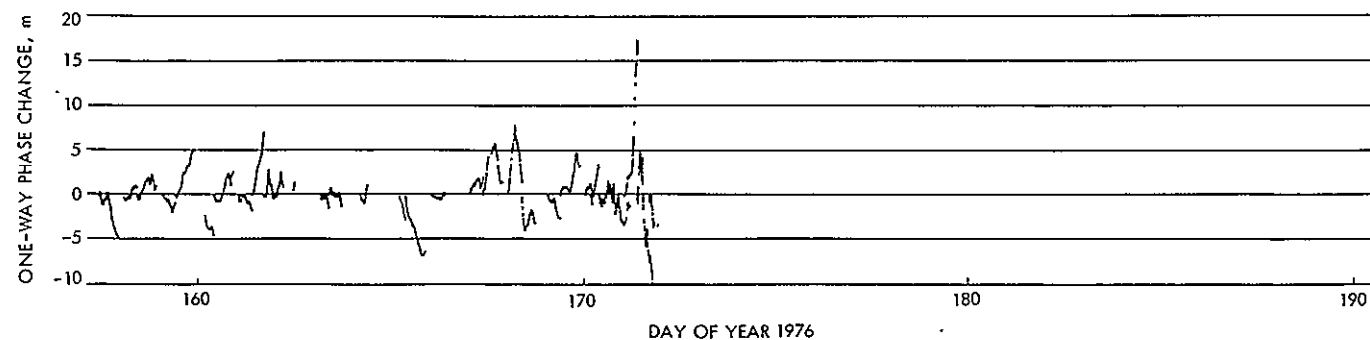
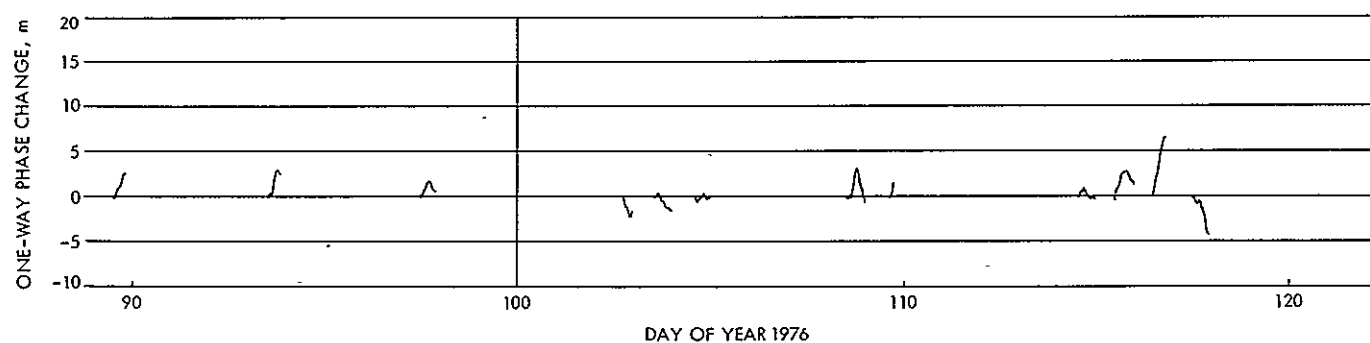
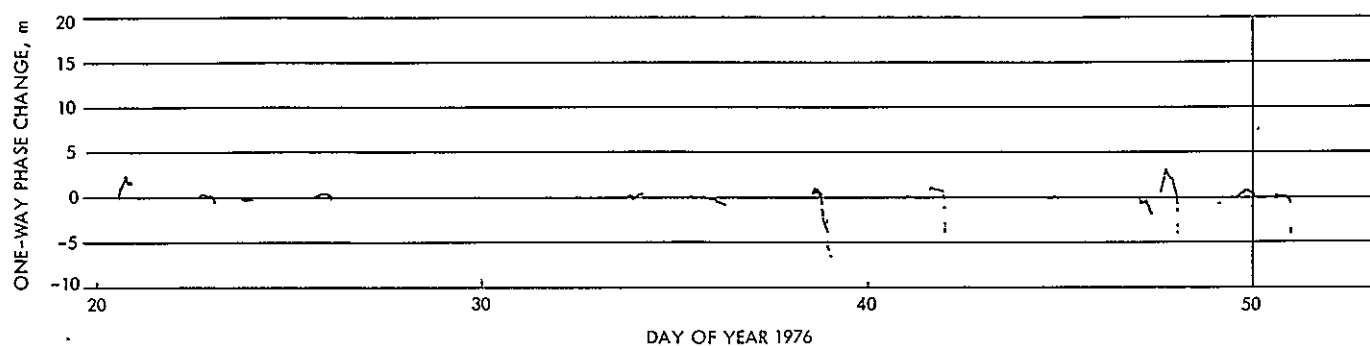
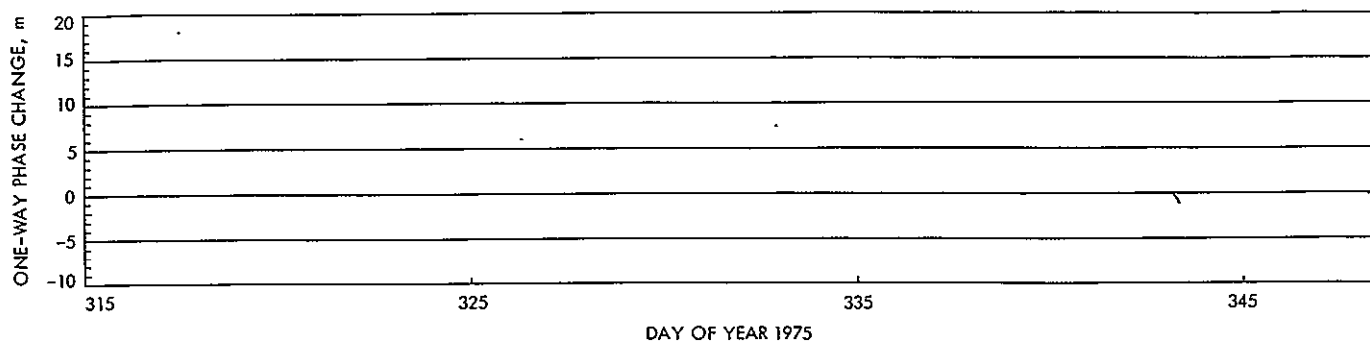


Fig. 5. Maximum phase change and corresponding mean rate of change



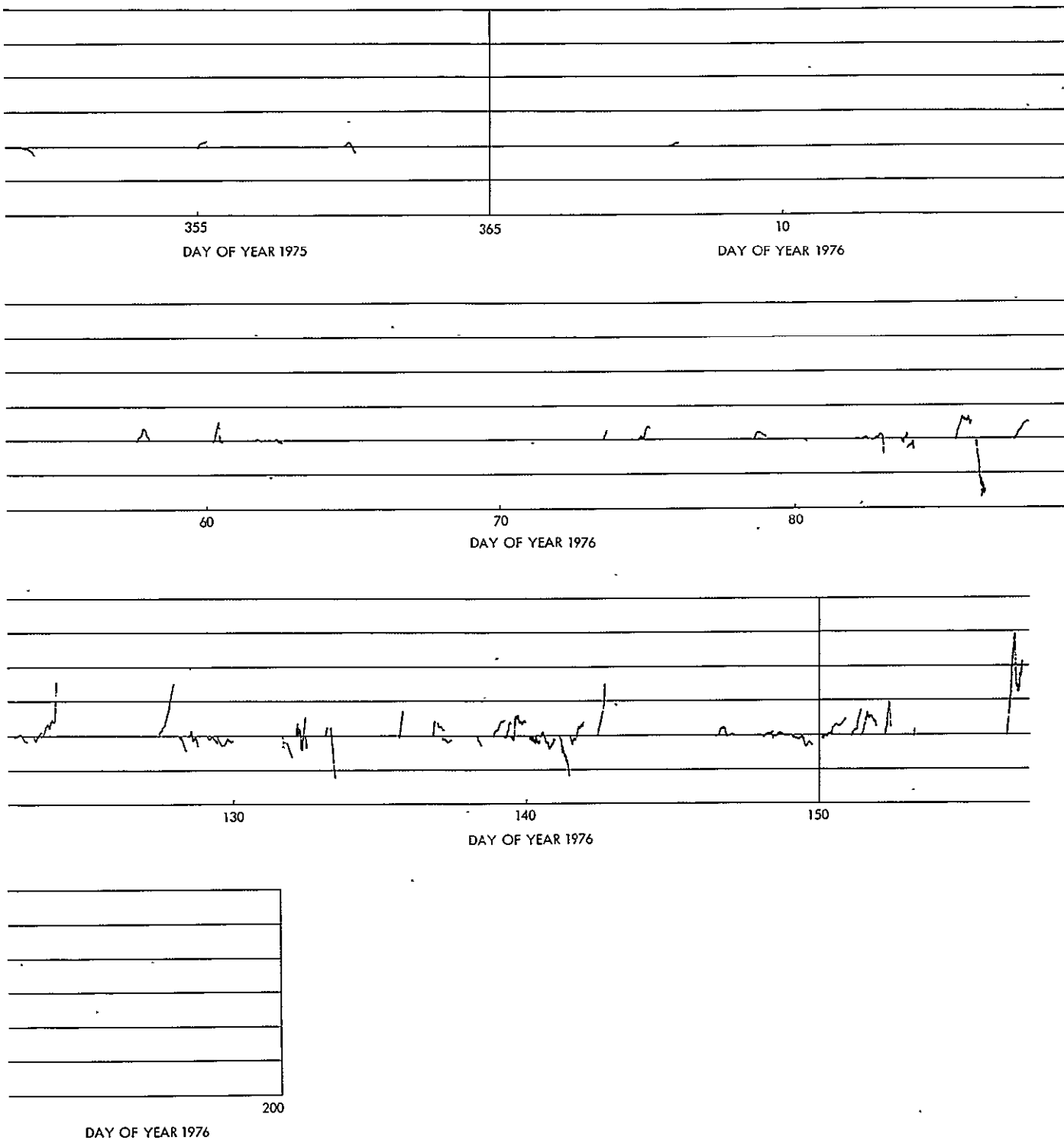
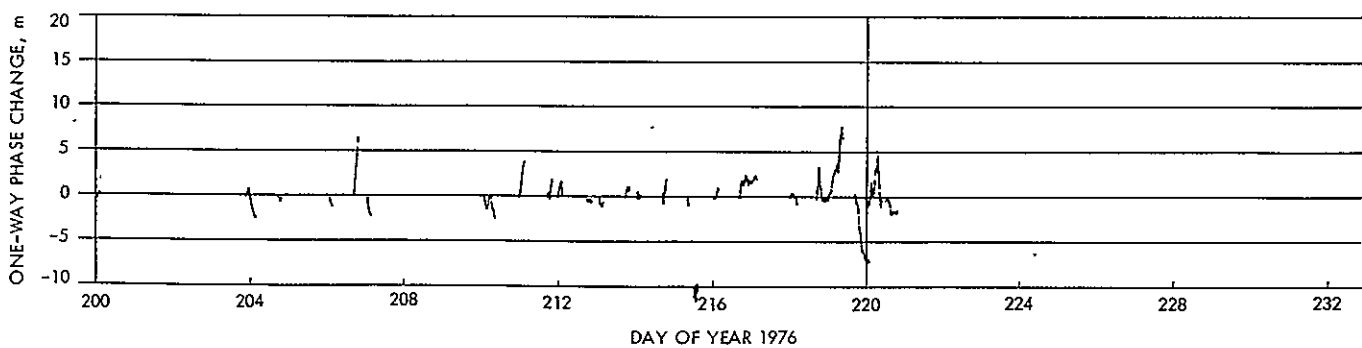
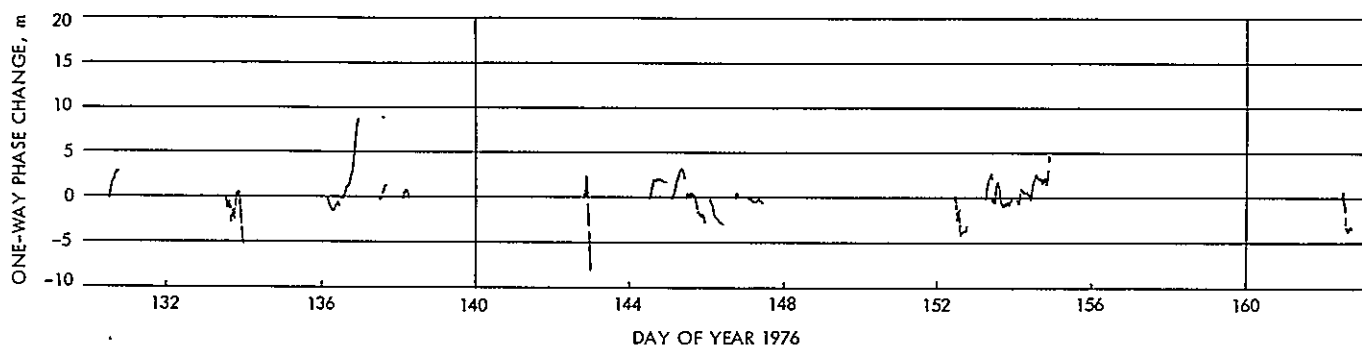
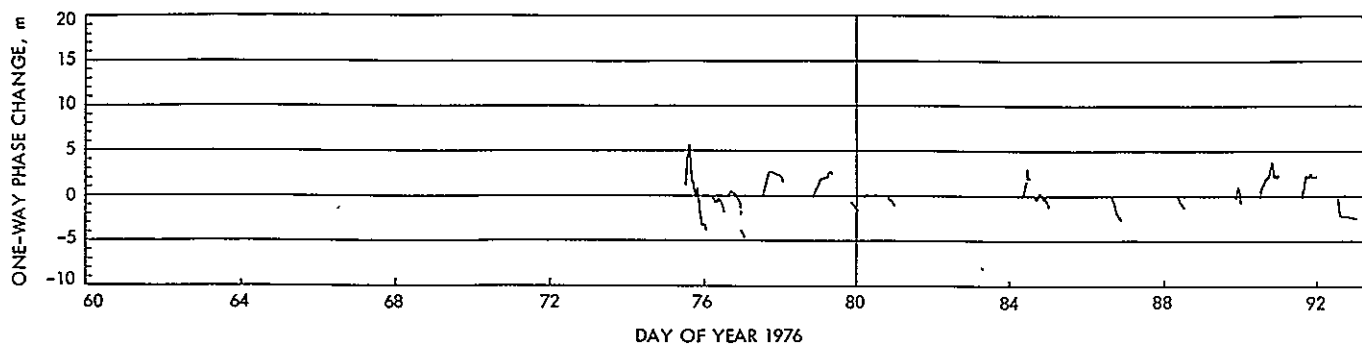


Fig. 6. Cumulative one-way phase change due to line-of-sight solar plasma dynamics (Viking A)



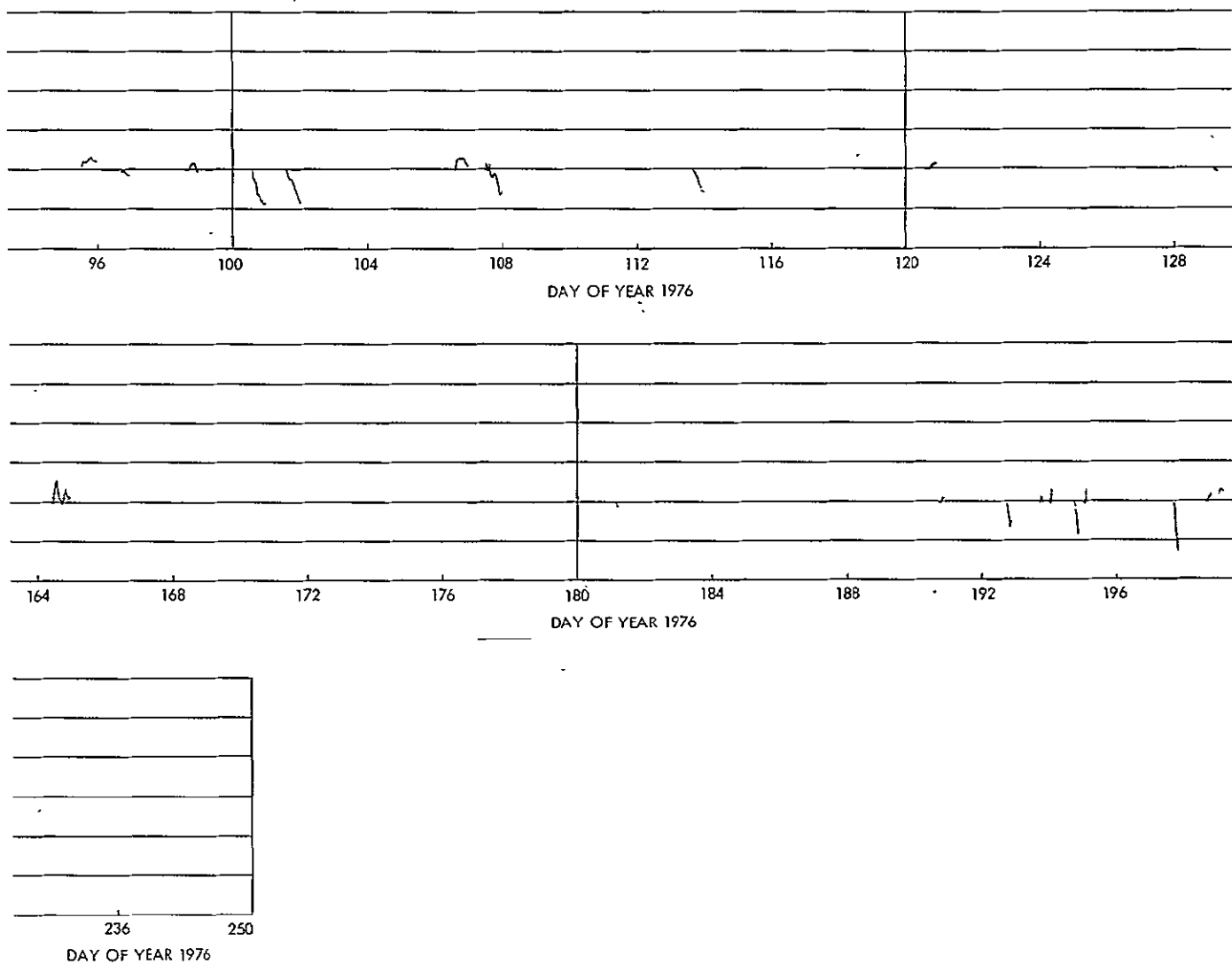


Fig. 7. Cumulative one-way phase change due to line-of-sight solar plasma dynamics (Viking B)

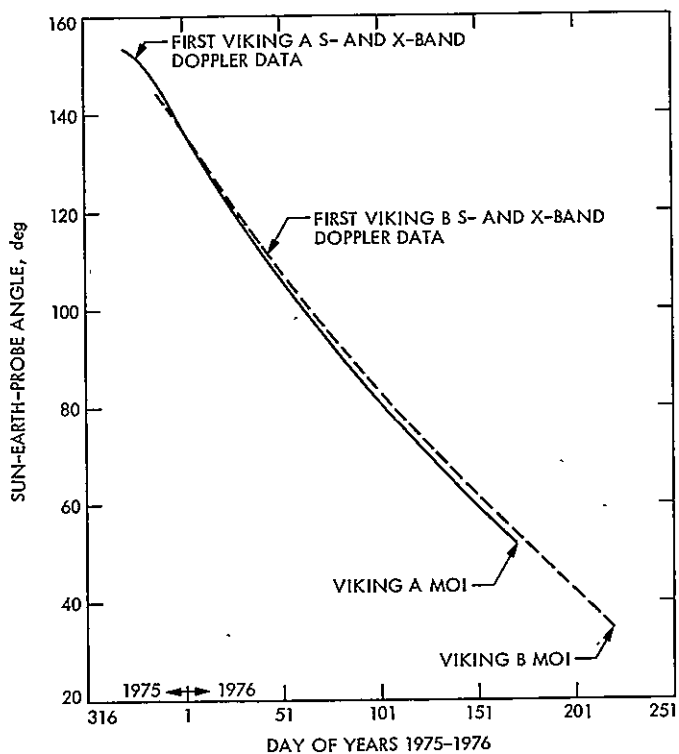


Fig. 8. Sun-Earth-probe angles of Viking spacecraft

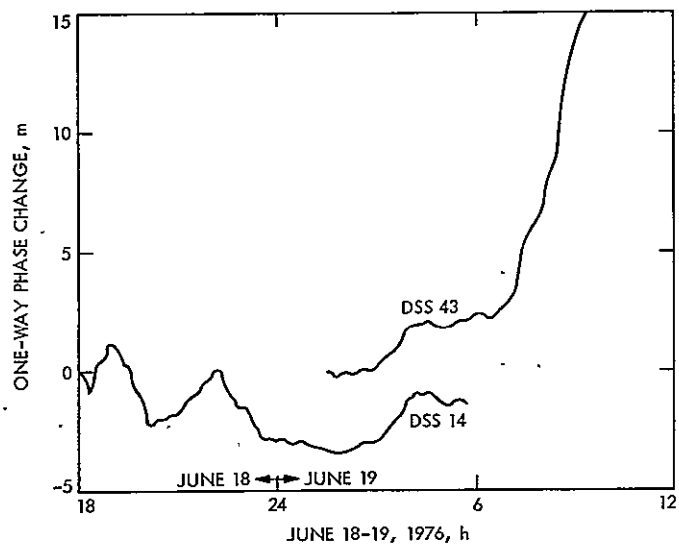


Fig. 9. Two-way/three-way tracking data

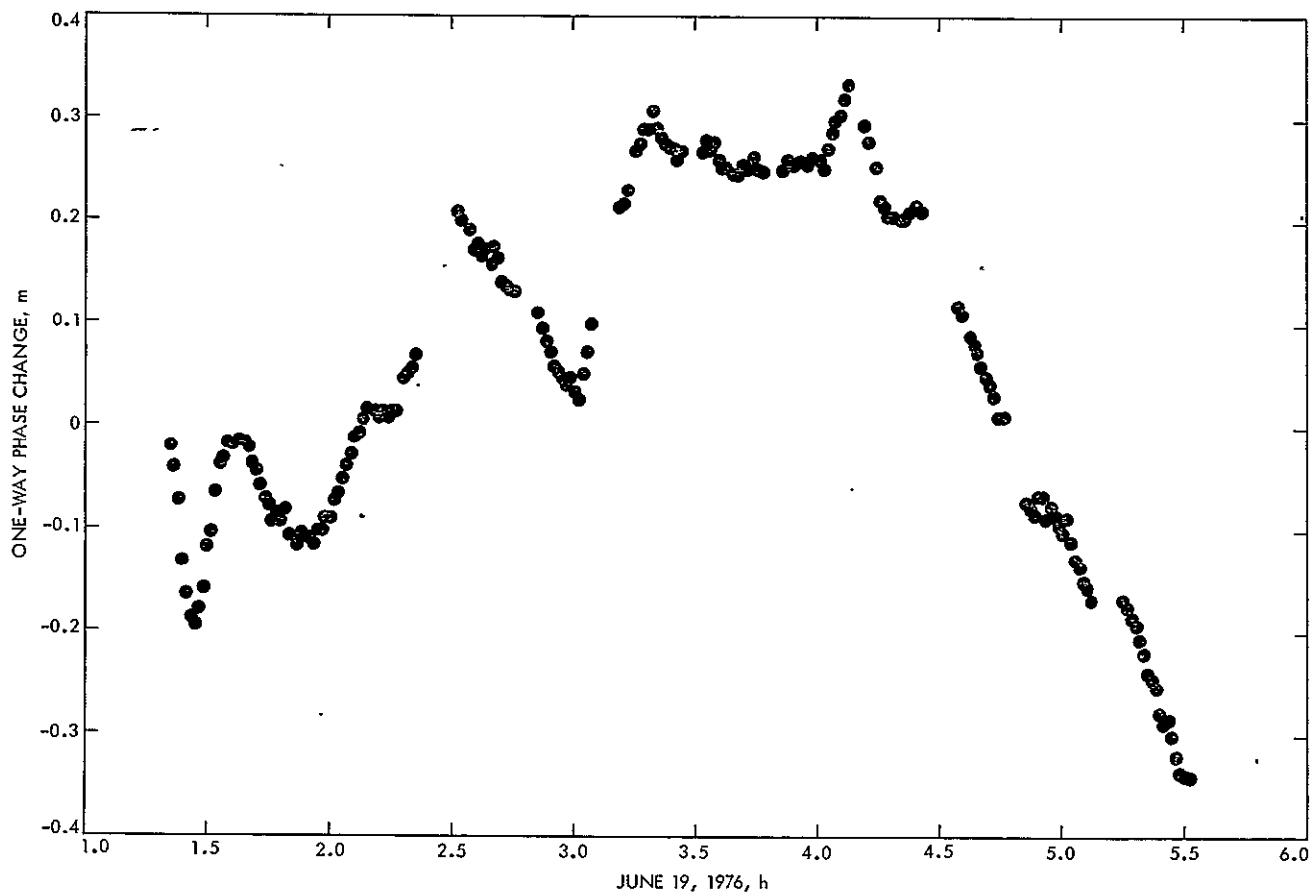


Fig. 10. Difference between two-way and three-way phase changes

D28 14, 22D

N77-19119

A Comprehensive Two-Way Doppler Noise Model for Near-Real-Time Validation of Doppler Data

A. L. Berman
DSN Network Operations Section

Recent articles have described the functional dependence of plasma-induced doppler noise ("media" noise) upon geometric parameters which approximate integrated signal path electron density (the "ISED" model). In this article, doppler noise generated within the tracking system ("system" noise) is modeled as a function of the dominant variable – doppler sample interval. Additionally, the relationship between media noise and doppler sample interval is empirically determined, and the ratio of media noise for S- and X-band downlinks is solved for. These functional relationships are incorporated into the previous media noise modeling to obtain a comprehensive two-way doppler noise model – ISEDC.

I. Introduction

Doppler noise has for some time been considered the strongest indicator of tracking system performance, and nothing appears likely to soon usurp that position. Doppler noise can be conveniently divided into two broad and very different categories: noise generated within the tracking system ("system" noise) and noise induced by the media being traversed ("media" noise). The last two years have seen an intensive effort mounted to model media noise (the ISED model, see Refs. 1-6). The reason why resources were first directed towards modeling the media noise is apparent from a comparison of the regions of interest for system noise and media noise, here roughly considered to be (rms phase jitter)

$$10 \text{ deg} \leq \text{system noise} \leq 100 \text{ deg}$$

$$100 \text{ deg} \leq \text{media noise} \leq 100,000 \text{ deg}$$

or for 60-second sample interval noise¹:

$$0.0005 \text{ Hz} \leq \text{system noise} \leq 0.005 \text{ Hz}$$

$$0.005 \text{ Hz} \leq \text{media noise} \leq 5.000 \text{ Hz}$$

Obviously, modeling media noise was a higher priority as it occupies the highest three orders of magnitude of the four orders of magnitude that doppler noise is commonly observed to span. With the media noise modeling nearing completion, it seems appropriate to address the question of system noise modeling.

¹For convenience, all expressions in rms phase jitter (degrees) will also be given in equivalent 60-second sample interval noise (Hz).

The most important functional parameter which describes system noise is doppler sample interval, and, therefore, tests were conceived and executed to empirically obtain this relationship. In addition, the relationship between media noise and doppler sample interval is obtained, as is the ratio of media noise for S-band and X-band downlinks. Finally, these relationships are incorporated into the ISED media noise model to yield a comprehensive two-way doppler noise model.

II. Tracking System Doppler Noise Dependence Upon Doppler Sample Interval

The only doppler system noise model known to DSN Network Operations, since at least the beginning of this decade, is as follows:²

$$\text{Rms phase jitter} = \left\{ (B_0 + C_0)^2 \tau^2 + (B_1 + C_1)^2 + \frac{(B_2 + C_2)^2}{(B_3 + C_3)^2} \right\}^{1/2}$$

or

$$\text{Noise} = \left\{ (B'_0 + C'_0)^2 + \frac{(B'_1 + C'_1)^2}{\tau^2} + \frac{(B'_2 + C'_2)^2}{(B'_3 + C'_3)^2 \tau^2} \right\}^{1/2}$$

where

B_n, B'_n = tracking station constants

C_n, C'_n = spacecraft constants

τ = doppler sample interval, seconds

However, no values for the constants were ever determined (or if they were, they certainly have not survived¹) and so this formulation is of little inherent interest. Since the most important parameter for system noise is the doppler sample interval, it was felt that a reasonable starting point would be

an (empirical) investigation of doppler noise variation with sample interval, for spacecraft *not* in solar-conjunction phases.

A. System Noise as a Function of Doppler Sample Interval

Four spacecraft not currently in solar conjunction phases were available for doppler noise variation with sample interval tests:

Pioneer 10
Pioneer 11
Helios 1
Helios 2

For each spacecraft, four tests (on different passes) were conducted to obtain typical variations of noise with sample interval. In each test, essentially 150 doppler samples³ were used to obtain an "average" doppler noise value for the following doppler sample intervals:

1 second
2 seconds
5 seconds
10 seconds
20 seconds
60 seconds

The signatures obtained for the four spacecraft were quite different, but all showed a small to moderate increase in phase jitter with doppler sample interval:

$$\text{Rms phase jitter} \sim \tau^{0.1 - 0.2}$$

or

$$\text{Noise} \sim \frac{1}{\tau^{0.8 - 0.9}}$$

That the noise versus sample interval signatures were quite different is not surprising as many factors enter into the process, such as:

- (1) Spacecraft characteristics (spin, transponder, receiver/transmitter).
- (2) Frequency standard, combined with τ .
- (3) Doppler extractor, combined with signal level.

²This model was used in the DSN IBM 360 era (1970-1975) and remains in the MCCC Pseudo-Residual Program.

³Obtained by averaging 10 noise calculations, each noise calculation derived from 15 samples.

- (4) Doppler resolver quantization, combined with doppler level.

All available evidence appears to point to the first two as the major contributors to system noise (the "system" noise definition here broadened to include both ground and spacecraft systems, i.e., everything but "media" noise). There exists a persistent misconception that signal level plays an important part in modeling doppler noise — this having been empirically demonstrated by the author not to be true with actual Mariner 9 data (Ref. 7) in 1972. The unimportance of signal level (except in cases where there exists less than 10 dB of margin above threshold) can also be seen in a system noise model constructed by W. D. Chaney (Ref. 8) from tracking subsystem performance parameters, as follows (when $RTL > \tau$):

Rms phase jitter, cycles

$$= \left\{ [2 \sigma_R^2 + 2 \sigma_Q^2 + 2 \sigma_T^2] + \left[\frac{\Delta f}{f} (2.3 \times 10^9) \tau \right]^2 + \left[\frac{\Delta \phi}{\Delta T} \tau \right]^2 \right\}^{1/2}$$

where

σ_R = receiver phase jitter ≈ 0.019 cycle under strong signal

σ_Q = resolver quantization ≈ 0.01 cycle

σ_T = 1-pulse/second timing jitter ≈ 0.04 cycle

$\Delta f/f$ = rubidium frequency stability $\approx 1 \times 10^{-12}$ to 5×10^{-12}

$\Delta \phi/\Delta t$ = station phase stability $\approx 1.5 \times 10^{-4}$

Except at very low signal levels (less than 10 dB above threshold, other terms, particularly $\Delta f/f$ at the normal 60-second sample interval, obviously predominate over the signal level dependent term — σ_R . In a subsequent section, the "Chaney" formulation will be compared to the actual results obtained.

B. System Noise Versus Sample Interval Test Results

Initial examination of the data indicated that a general expression of the form:

$$\text{Rms phase jitter, deg} = \left\{ \left[D_0 \left(\frac{\tau}{60} \right) \right]^2 + \left(D_1 \tau^{D_2} \right)^2 \right\}^{1/2}$$

or

$$\text{Noise, Hz} = \left\{ (D'_0)^2 + \left[D'_1 \left(\frac{60}{\tau} \right)^{D'_2} \right]^2 \right\}^{1/2}$$

where

D_n, D'_n = empirically determined constants

would yield a satisfactory representation for the test data. Individual spacecraft test results are described below.

1. Pioneer 10. Figure 1 presents the sample interval test results for the Pioneer 10 spacecraft; a reasonable fit to these data was obtained as:

$$\text{Rms phase jitter} = 36 \{ \tau \}^{0.1}, \text{ deg}$$

or

$$\text{Noise} = 0.0025 \left\{ \frac{60}{\tau} \right\}^{0.9}, \text{ Hz}$$

2. Pioneer 11. Figure 2 presents the sample interval test results for the Pioneer 11 spacecraft; these results were similar to those obtained for Pioneer 10, but at an elevated level:

$$\text{Rms phase jitter} = 48 \{ \tau \}^{0.1}, \text{ deg}$$

or

$$\text{Noise} = 0.0033 \left\{ \frac{60}{\tau} \right\}^{0.9}, \text{ Hz}$$

3. Helios 1. Figure 3 presents sample interval test results for the Helios 1 spacecraft. These data were not as amenable to fit as were the Pioneer data, and the results at the larger sample intervals (20 seconds and particularly 60 seconds) are at least twice what routine experience dictates. This is

partially explained by the fact that DSS 44, which provided all of the sample interval tests for Helios 1, was subsequently found to be perhaps 30-50 percent noisier than the other DSSs. This can be easily seen by comparing the one Helios 2-DSS 44 test case (Fig. 4d) to the other three Helios 2 test cases (Figs. 4a, b, c). At any rate, a fair fit to the Helios 1 data, but biased lower because of the DSS 44 (Australia) above-average noise, and biased towards the expected 60-second performance, is:

$$\text{Rms phase jitter} = 24 \{\tau\}^{0.2}, \text{ deg}$$

or

$$\text{Noise} = 0.0025 \left\{ \frac{60}{\tau} \right\}^{0.8}, \text{ Hz}$$

4. Helios 2. Figure 4 presents sample interval data for the Helios 2 spacecraft. These data were notable for being so low, particularly at the smaller sample intervals. The lowest 1-second sample interval data (DSS 14, Goldstone, Fig. 4a) indicated an rms phase jitter of only 10 degrees!

It was found necessary to add a small linear term in τ to the phase jitter to bring the expression, when evaluated at $\tau = 60$ seconds, up to more commonly experienced results:

$$\text{Rms phase jitter} = \left\{ (12 \{\tau\}^{0.2})^2 + \left(30 \left\{ \frac{\tau}{60} \right\} \right)^2 \right\}^{1/2}, \text{ deg}$$

or

$$\text{Noise} = \left\{ \left(0.0013 \left\{ \frac{60}{\tau} \right\}^{0.8} \right)^2 + (0.0014)^2 \right\}^{1/2}, \text{ Hz}$$

The results for all four spacecraft are summarized in Table 1.

Based on the different spacecraft characteristics and the radically different RTLs, it seems reasonable to accept large differences between the Pioneer spacecraft and the Helios spacecraft. There is much less reason to think the smaller differences obtained between Pioneers 10 and 11 and, likewise, between Helios 1 and 2 are significant or that these differences could be confidently predicted into the future. It would seem to make more sense to average the Pioneer 10 and 11 results, and, similarly, the Helios 1 and 2 results. For

future doppler noise modeling, a "Pioneer" and "Helios" model will be adopted as follows:

$$\begin{aligned} \text{Pioneer} & \left\{ \begin{aligned} \text{rms phase jitter} &= 42 \{\tau\}^{0.1}, \text{ deg} \\ \text{Noise} &= 0.0029 \left\{ \frac{60}{\tau} \right\}^{0.9}, \text{ Hz} \end{aligned} \right. \\ \text{Helios} & \left\{ \begin{aligned} \text{rms phase jitter} &= \left[(18 \{\tau\}^{0.2})^2 + \left(30 \left\{ \frac{\tau}{60} \right\} \right)^2 \right]^{1/2}, \text{ deg} \\ \text{Noise} &= \left[\left(0.0019 \left\{ \frac{60}{\tau} \right\}^{0.8} \right)^2 + (0.0014)^2 \right]^{1/2}, \text{ Hz} \end{aligned} \right. \end{aligned}$$

Figure 5 presents these expressions as compared to the Chaney formulation for the following parameter values:

$$\sigma_R = 0.019 \text{ cycle}$$

$$\sigma_Q = 0.010 \text{ cycle}$$

$$\sigma_T = 0.040 \text{ cycle}$$

$$\Delta f/f = 1 \times 10^{-12}$$

$$\Delta \phi / \Delta T = 1.5 \times 10^{-4}$$

Additionally, included in Fig. 5 for comparison are results obtained by M. Brockman (Ref. 9) for the following conditions:

Frequency standard	= rubidium
Doppler extractor phase noise	= 22 degrees
Timing jitter on doppler sampling	= 5×10^{-9} second
Doppler resolver counter quantization	= 2×10^{-9} second

Considering that this is the first serious attempt to obtain an operational modeling of system noise as a function of sample interval, the correspondence between the Chaney formulation, the Brockman data, and the empirically derived formulations presented here is considered favorably.

III. Plasma-Induced Doppler Noise Dependence Upon Doppler Sample Interval

In July 1976, an initial study was conducted to ascertain the dependence of solar plasma-induced doppler noise upon doppler sample interval, using low Sun-Earth-probe (SEP) doppler noise data from the April-May 1976 solar conjunction of the Helios 2 spacecraft. At that time, a relationship was hypothesized as follows:

$$\frac{\text{Noise } (\tau_2)}{\text{Noise } (\tau_1)} = \left(\frac{\tau_1}{\tau_2} \right)^x$$

where

τ = doppler sample interval

Solving for the exponent (x) in 12 cases where different doppler sample intervals were available at (approximately) the same SEP, a mean value of x was determined as follows:

$$x = 0.285$$

with a standard deviation over the 12 cases of:

$$\sigma(x) = 0.120$$

The recent solar conjunction of the four Viking spacecraft afforded an opportunity to retest the (sample interval dependence) hypothesis, and it was considered reasonable to utilize this opportunity.

Thirty sets of different doppler sample intervals at approximately the same time (hence, SEP) were identified, with the following sample interval comparisons available:

1 second/10 seconds
1 second/60 seconds
2 seconds/10 seconds
10 seconds/60 seconds

The same hypothesis applied to the Helios 2 data was applied to the 30 Viking cases, and the results are seen in Table 2. These cases produced an average value for the exponent (x) of:

$$x = 0.294$$

and a standard deviation of:

$$\sigma(x) = 0.106$$

Although, the standard deviation of the exponent solutions is large (as was the case with the Helios 2 data), the average values produced by the Helios 2 data and the subsequent Viking data are extremely close. It should, of course, be cautioned that the results are partially dependent upon the type of processing done in the Network Operations Control Center (NOCC) Pseudo-Residual Program.⁴

For future modeling of doppler noise during solar conjunction periods, the following exponent value (x) will be adopted:

$$x = 0.3$$

so that plasma-induced doppler noise ("ISED") will be scaled by:

$$\left(\frac{60}{\tau} \right)^{0.3}$$

where

τ = doppler sample interval

IV. Plasma-Induced Doppler Noise Dependence Upon Downlink Frequency

A great deal of S- and X-band doppler (and, hence, doppler noise statistics) has been accumulated during the recent Viking solar conjunction phase. Using the inverse proportionality between plasma-induced phase error and frequency, it is easy to derive an expected ratio of X-band doppler noise to S-band doppler noise. It would then seem reasonable to see how close the actual Viking X-band/S-band doppler noise ratio is to the calculated expression.

A. Expected X-band/S-band Doppler Noise Ratio

One begins by defining the following frequencies and frequency ratios:

$$f_{sup} = \text{S-band uplink frequency (2113 MHz)}$$

⁴ The doppler noise computed in the NOCC Pseudo-Residual Program is a "running" standard deviation of the most recent 15 samples calculated about a linear curve to these samples (residuals).

f_{sdn} = S-band downlink frequency (2295 MHz)

f_{xdn} = X-band downlink frequency (8415 MHz)

$f_{sdn}/f_{sup} = 240/221$

$f_{xdn}/f_{sdn} = 11/3$

$\Delta\phi_{sdn}$ = S-band downlink phase error

$= K_1/f_{sdn}$

$\Delta\phi_{xdn}$ = X-band downlink phase error

$= K_1/f_{xdn}$

From Ref. 10, one has the phase error caused by fluctuating electron density:

$$\begin{aligned}\Delta\phi &= r_e \lambda n \Delta z \\ &= r_e \left(\frac{c}{f} \right) n \Delta z\end{aligned}$$

where

$\Delta\phi$ = phase error

r_e = classical electron radius

$= 2.8 \times 10^{-18}$ km

λ = wavelength

c = speed of light

f = frequency, Hz

n = electron density

Δz = region containing electron density

Now consider:

$$r_e c n \Delta z = K_1$$

so that

$$\begin{aligned}\Delta\phi_{sup} &= \text{S-band uplink phase error} \\ &= K_1/f_{sup}\end{aligned}$$

To calculate the ratio of X-band doppler noise to S-band doppler noise, the following assumptions are made:

- (1) If fluctuations in electron density are proportional to electron density, then rms phase jitter will be proportional to the phase error expression from Ref. 10.
- (2) "Total" phase jitter on the downlink can be obtained by root sum squaring (rss) the phase jitter induced on the uplink (multiplied to downlink level) with the phase jitter induced on the downlink.

Using the above (with the constant of proportionality between noise and phase error = K_2), one constructs an expression for S-band noise:

$$\begin{aligned}\text{Noise}_s &= K_2 \left[(\Delta\phi_{sup})^2 (240/221)^2 + (\Delta\phi_{sdn})^2 \right]^{1/2} \\ &= K_2 \left[(K_1/f_{sup})^2 (240/221)^2 + (K_1/f_{sdn})^2 \right]^{1/2} \\ &= K_1 K_2 \left[(1/f_{sup})^2 (240/221)^2 + (1/f_{sdn})^2 \right]^{1/2}\end{aligned}$$

and for X-band noise:

$$\begin{aligned}\text{Noise}_x &= K_2 \left[(\Delta\phi_{sup})^2 (240/221)^2 (11/3)^2 + (\Delta\phi_{xdn})^2 \right]^{1/2} \\ &= K_2 \left[(K_1/f_{sup})^2 (240/221)^2 (11/3)^2 + (K_1/f_{xdn})^2 \right]^{1/2} \\ &= K_1 K_2 \left[(1/f_{sup})^2 (240/221)^2 (11/3)^2 + (1/f_{xdn})^2 \right]^{1/2}\end{aligned}$$

The ratio is then obtained:

$$\frac{\text{Noise}_x}{\text{Noise}_s} = \frac{\left[(1/f_{sup})^2 (240/221)^2 (11/3)^2 + (1/f_{xdn})^2 \right]^{1/2}}{\left[(1/f_{sup})^2 (240/221)^2 + (1/f_{sdn})^2 \right]^{1/2}}$$

$$\begin{aligned}
&= \frac{[(240/221)^2 (11/3)^2 + (f_{sup}/f_{sdn})^2]^{1/2}}{[(240/221)^2 + (f_{sup}/f_{sdn})^2]^{1/2}} \\
&= \frac{[(240/221)^2 (11/3)^2 + (221/240)^2 (3/11)^2]^{1/2}}{[(240/221)^2 + (221/240)^2]^{1/2}} \\
&= \frac{[(240/221)^2 (11/3)^2 + (240/221)^{-2} (11/3)^{-2}]^{1/2}}{[(240/221)^2 + (240/221)^{-2}]^{1/2}}
\end{aligned}$$

Now the X-band noise computed by the Network Operations Control Center (NOCC) RTM is scaled by the downlink S/X ratio:

$$\text{Noise}'_x = \left\{ \frac{3}{11} \right\} \text{noise}_x$$

so that the ratio of X-band noise to S-band noise as computed by the RTM would be:

$$\begin{aligned}
\frac{\text{Noise}'_x}{\text{Noise}_s} &= \frac{3}{11} \frac{[(240/221)^2 (11/3)^2 + (240/221)^{-2} (11/3)^{-2}]^{1/2}}{[(240/221)^2 + (240/221)^{-2}]^{1/2}} \\
&= 0.764
\end{aligned}$$

B. Measured Ratio of X-Band to S-Band Doppler Noise

During the period from 1 July 1976 to 1 October 1976, frequent measurements of the X-band to S-band doppler noise ratio were recorded. The measurements were made for doppler data taken at the 64-meter stations, and, in all cases, were made for identical 15-minute time periods of 60-second sample interval data. The only constraint imposed was that the S-band noise be greater than 0.010 Hz, so as to minimize the non-plasma component of the doppler noise. A total of 405 measurements, equivalent to a total of 101 hours, were recorded during the 1 July-1 October period, and these measurements yielded a composite average of (with X-band "normalized" to S-band level):

$$\frac{\text{Noise}'_x}{\text{Noise}_s} = 0.704$$

The difference between the measured value (above) and the predicted value from Section II is about 8 percent:

$$\frac{\text{Measured ratio}}{\text{Predicted ratio}} \approx 0.92$$

For future doppler noise modeling, the following will be adopted (with X-band noise "normalized" to S-band level):

$$\frac{\text{Noise}'_x}{\text{Noise}_s} = 0.7$$

V. A Composite Two-Way Doppler Noise Model

Combining the results from the previous three sections with the ISEDB (Refs. 1 and 2) model, one has (the "ISEDC" model):

$$\begin{aligned}
\text{ISEDC, Hz} &= \left[\left(\left\{ A_0 \left[\frac{\beta}{(\sin \alpha)^{1.3}} \right] F(\alpha, \beta) \right. \right. \right. \\
&\quad \left. \left. + A_1 \left[\frac{1}{(\sin \alpha)^5} \right] \right\} 10^{-A_8 (|\phi_s|/90)} \right)^2 \\
&\quad \times (K(f_{dn}))^2 \left(\left\{ \frac{60}{\tau} \right\}^{0.3} \right)^2 \\
&\quad \left. + (D'_0)^2 + \left(D'_1 \left\{ \frac{60}{\tau} \right\}^{D'_2} \right)^2 \right]^{1/2}
\end{aligned}$$

where

f_{dn} = downlink frequency (S- or X-band)

$$K(f_{dn}) = \begin{cases} 1.0 & f_{dn} = \text{S-band} \\ 0.7 & f_{dn} = \text{X-band} \end{cases}$$

τ = doppler sample interval, seconds

$$D'_0 = \begin{cases} 0 & \text{Pioneer spacecraft} \\ 0.0014 & \text{Helios spacecraft} \end{cases}$$

$$D'_1 = \begin{cases} 0.0029 & \text{Pioneer spacecraft} \\ 0.0019 & \text{Helios spacecraft} \end{cases}$$

$$D'_2 = \begin{cases} 0.9 & \text{Pioneer spacecraft} \\ 0.8 & \text{Helios spacecraft} \end{cases}$$

$$\begin{aligned}
F(\alpha, \beta) &= 1 - 0.05 \left\{ \frac{(\beta - \pi/2 + \alpha)^3 - (\alpha - \pi/2)^3}{\beta} \right\} \\
&\quad - 0.00275 \left\{ \frac{(\beta - \pi/2 + \alpha)^5 - (\alpha - \pi/2)^5}{\beta} \right\}
\end{aligned}$$

α = Sun-Earth-probe angle (SEP), radians

β = Earth-Sun-probe angle (ESP), radians

and

ϕ_s = heliographic latitude, degrees

$$= \sin^{-1} [\cot \alpha (-\cos \delta_d \sin \alpha_{ra} \sin \epsilon + \sin \delta_d \cos \epsilon)]$$

α_{ra} = right ascension

δ_d = declination

ϵ = the obliquity of the ecliptic (23.445 deg)

with

$$A_0 = 9.65 \times 10^{-4}$$

$$A_1 = 5 \times 10^{-10}$$

$$A_8 = 9 \times 10^{-1}$$

VI. Summary

The dependence upon doppler sample interval of both the media and system components of doppler noise has been empirically deduced from actual data and appropriately modeled. Additionally, the ratio of media noise for X-band downlinks as compared to S-band downlinks has been solved for and is shown to be in reasonable agreement with observations. These functional relationships are combined with previous media noise modeling (ISEDDB) to obtain a comprehensive two-way doppler noise model – ISEDC. This model greatly enhances DSN capability to predict two-way doppler noise levels for a great variety of circumstances.

References

1. Berman, A. L., Wackley, J. A., and Rockwell, S. T., "The 1976 Helios and Pioneer Solar Conjunctions — Continuing Corroboration of the Link Between Doppler Noise and Integrated Signal Path Electron Density," in *The Deep Space Network Progress Report 42-36*, pp. 121-137, Jet Propulsion Laboratory, Pasadena, California, December 15, 1976.
2. Berman, A. L., Wackley, J. A., Rockwell, S. T., and Yee, J. G., "The Pioneer 11 1976 Solar Conjunction: A Unique Opportunity to Explore the Heliographic Latitudinal Variations of the Solar Corona," in *The Deep Space Network Progress Report 42-35*, pp. 136-147, Jet Propulsion Laboratory, Pasadena, California, October 15, 1976.
3. Berman, A. L., and Wackley, J. A., "Doppler Noise Considered as a Function of the Signal Path Integration of Electron Density," in *The Deep Space Network Progress Report 42-33*, pp. 159-193, Jet Propulsion Laboratory, Pasadena, California, June 15, 1976.
4. Berman, A. L., "Analysis of Solar Effects Upon Observed Doppler Data Noise During the Helios 1 Second Solar Conjunction," in *The Deep Space Network Progress Report 42-32*, pp. 262-276, Jet Propulsion Laboratory, Pasadena, California, April 15, 1976.
5. Berman, A. L., and Rockwell, S. T., "Correlation of Doppler Noise During Solar Conjunctions with Fluctuations in Solar Activity," in *The Deep Space Network Progress Report 42-30*, pp. 264-272, Jet Propulsion Laboratory, Pasadena, California, December 15, 1975.
6. Berman, A. L., and Rockwell, S. T., "Analysis and Prediction of Doppler Noise During Solar Conjunctions," in *The Deep Space Network Progress Report 42-30*, pp. 230-263, Jet Propulsion Laboratory, Pasadena, California, December 15, 1975.
7. Berman, A. L., "Mariner 9 Doppler Noise Study," in *The Deep Space Network Progress Report*, Technical Report 32-1526, Vol. XIII, pp. 227-235, Jet Propulsion Laboratory, Pasadena, California, February 15, 1973.
8. Private communication with W. D. Chaney.
9. Brockman, M. H., "Revision to TRK-20," *Deep Space Network/Flight Project Interface Design Handbook*, Document 810-5, Rev. D, to be published (JPL internal document).
10. Cronyn, W. M., "The Analysis of Radio Scattering and Space-Probe Observations of Small-Scale Structure in the Interplanetary Medium," *Astrophys. J.* Vol. 161, pp. 755-763, August 1, 1970.

Table 1. System noise versus sample interval test results

Parameter	Pioneer 10	Pioneer 11	Helios 1	Helios 2
RTLT, s	10,850	3600	350	150
Spacecraft spin	Yes	Yes	No ^a	No ^a
D_0 , deg	0	0	0	30
D'_0 , Hz	0	0	0	0.0014
D_1 , deg	36	48	24	12
D'_1 , Hz	0.0025	0.0033	0.0025	0.0013
D_2	0.1	0.1	0.2	0.2
D'_2	0.9	0.9	0.8	0.8

^aAt least insofar as any appreciable effect in the doppler is concerned.

Table 2. Viking solar conjunction doppler noise exponent solutions for different sample intervals

Day of year	Spacecraft	Sample intervals, seconds/seconds	α
309	VO1, VO2	10/60	0.392
310	VO1, VO2	10/60	0.196
310	VO1, VO2	10/60	0.249
311	VO1, VO2	10/60	0.305
312	VO1, VO2	10/60	0.159
313	VO1, VO2	10/60	0.249
314	VO1, VO2	10/60	0.177
314	VO1, VO2	10/60	0.126
315	VO1, VO1	10/60	0.221
319	VO1, VO2	10/60	0.098
320	VO1, VO2	10/60	0.258
320	VO1, VO1	10/60	0.299
321	VO2, VO2	2/10	0.333
321	VO2, VL2	2/10	0.526
323	VO2, VL2	2/10	0.478
324	VO1, VO2	10/60	0.225
325	VO1, VL2	2/10	0.332
326	VO2, VL2	2/10	0.285
326	VL2, VL2	2/10	0.226
333	VO1, VL1	1/10	0.329
333	VL1, VL1	1/10	0.264
334	VO1, VL1	1/60	0.391
334	VO1, VL1	1/10	0.310
334	VO1, VO1	10/60	0.500
335	VO1, VL1	1/10	0.339
337	VO1, VL1	1/10	0.400
338	VO1, VL1	1/10	0.408
339	VO2, VL1	1/10	0.328
340	VO2, VL1	1/10	0.187
341	VO2, VL1	1/10	0.245

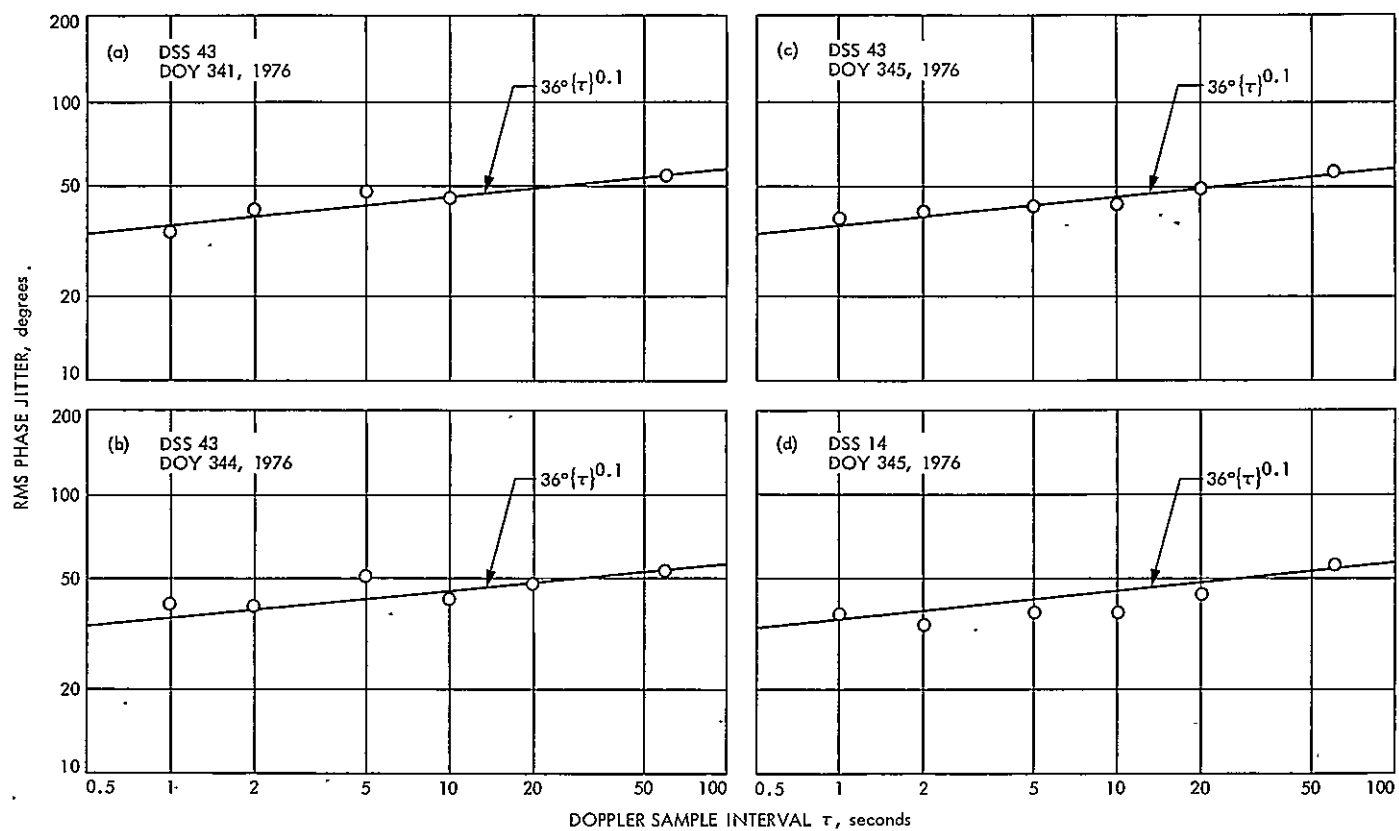


Fig. 1. Pioneer 10 rms phase jitter versus doppler sample interval

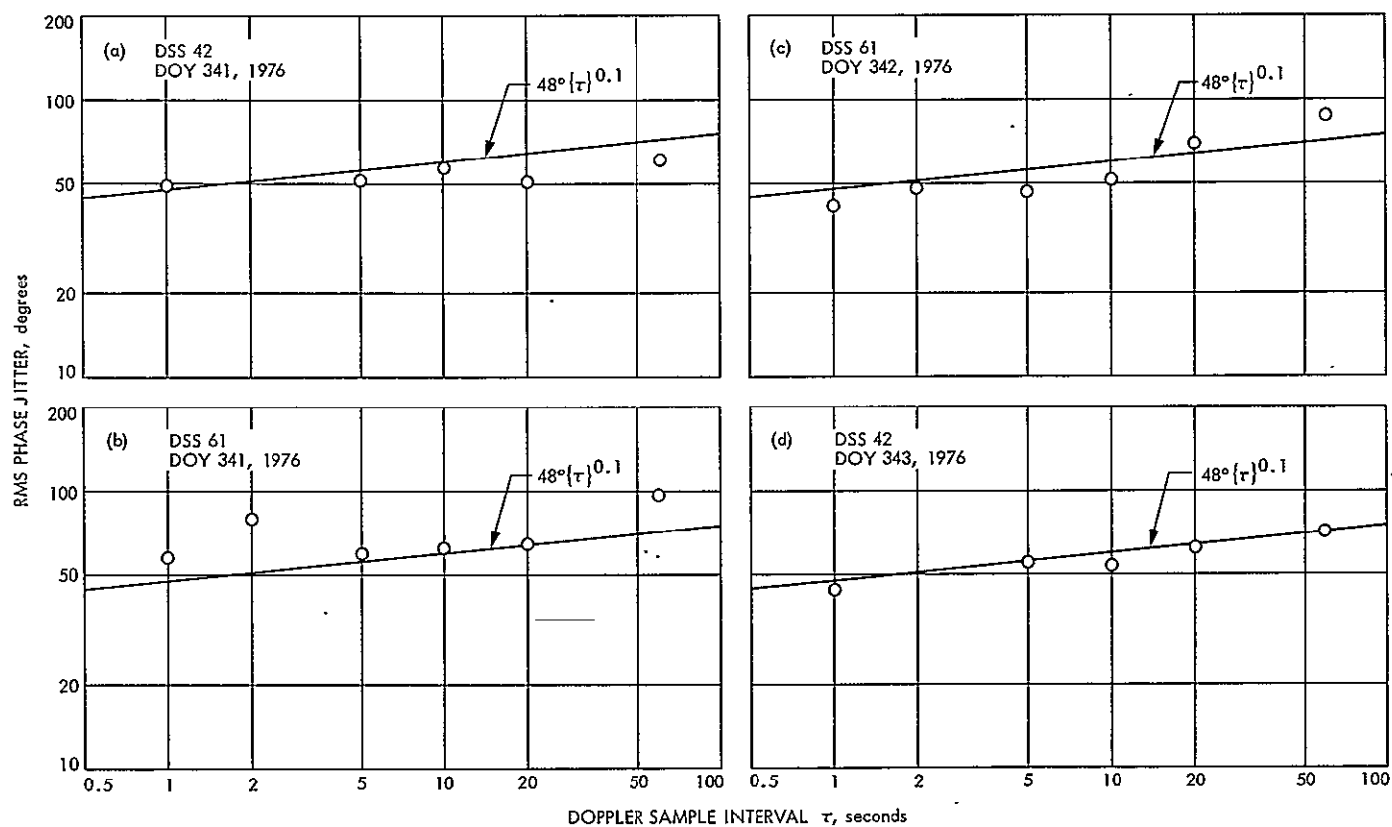


Fig. 2. Pioneer 11 rms phase jitter versus doppler sample interval

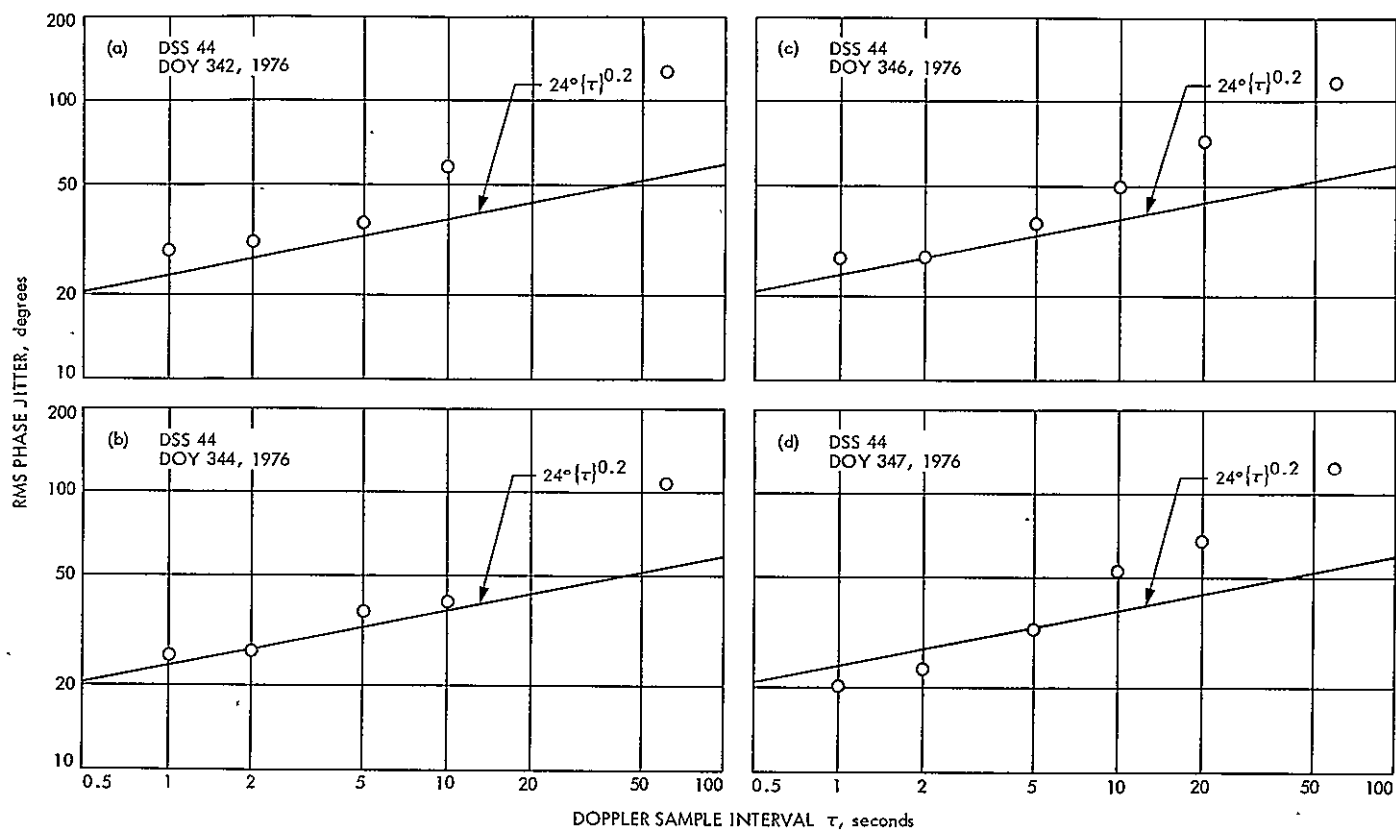


Fig. 3. Helios 1 rms phase jitter versus doppler sample interval

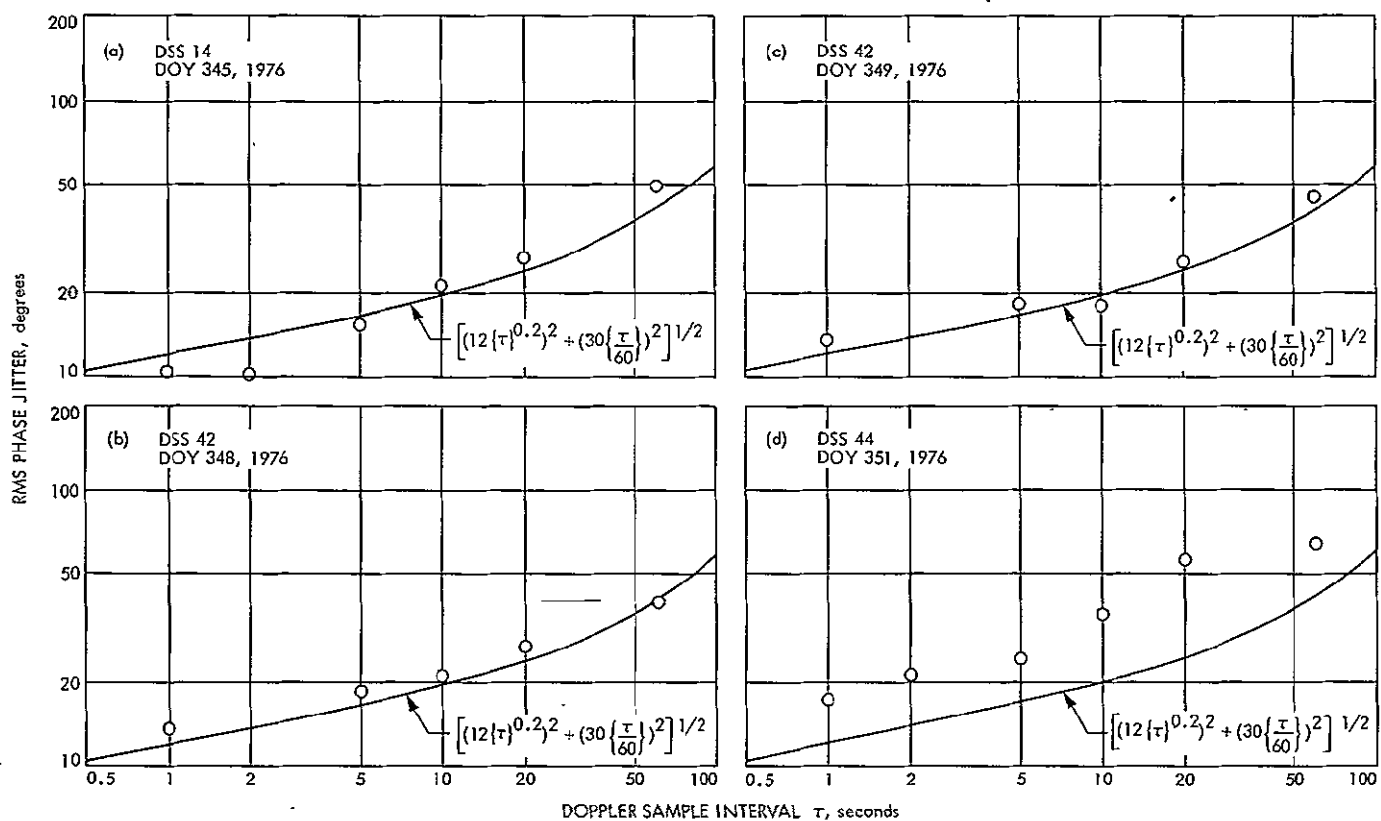


Fig. 4. Helios 2 rms phase jitter versus doppler sample interval

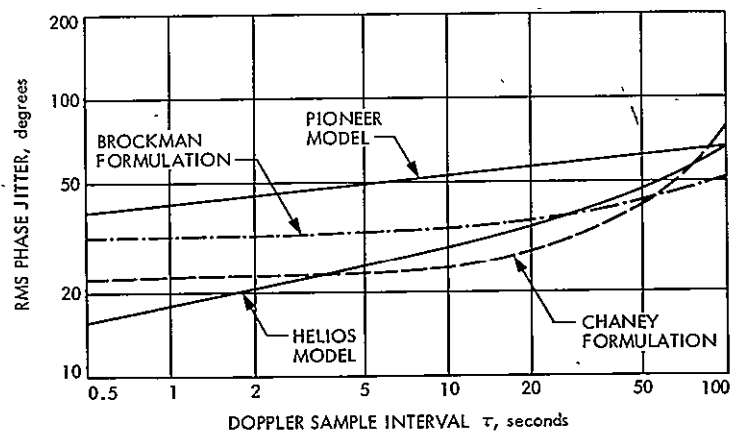


Fig. 5. Doppler system noise model comparisons

N77-19120

DSN System Performance Test Doppler Noise Models; Noncoherent Configuration

R. Bunce

DSN Network Operations Section

Recent DSN System Performance Test requirements (for pending missions) contain implied long-term measurements for which existing noncoherent test models are inadequate. The new models needed are those of the first two moments, mean and variance, of doppler noise under long-term conditions, and in noncoherent test mode. In this paper, the newer model for variance, the Allan technique, now adopted for testing, is analyzed in the subject mode. A model is generated (including considerable contribution from the station secondary frequency standard), and rationalized with existing data.

A mean-frequency model is subsequently proposed, based on data available, but this model is not considered rigorous. It is an introductory idea, to be evaluated and incorporated if proved valid. It uses a fractional-calculus integral to obtain a quasi-stable result, as observed, with integrable spectrum poles.

The variance model is definitely sound; the Allan technique mates theory and measure. The mean-frequency model is an estimate; this problem is yet to be rigorously resolved. The unaltered defining expressions are nonconvergent, and the observed mean is quite erratic.

I. Introduction

DSN site doppler noise measurements, in noncoherent mode, do not fit existing models. New models for variance and mean-frequency are outlined in this paper.

Initially, the doppler counter and data processing are explained, and their expression as a frequency transfer function for Allan variance developed. Next, spectral densities are discussed, and the transfer function above combined

with these to yield an Allan variance model. The model parameters are iterated with (DSS 11) data to define the variable model parameters, and a specific result for the site is plotted.

The mean-frequency function is then investigated (nonconvergent-integral), and a fractional filter proposed. Based on this filter, and an unknown parameter, an expression for the mean frequency is presented.

II. Doppler Counter Operation and Phase Data Reduction: Mean and Variance

The doppler counter input is a replica of the receiver carrier, phase-differenced with the exciter carrier (appropriately frequency translated), with mixing such that this input centers on a nominal 1.0 or 5.0 MHz bias frequency. All system phase variation, deterministic or random, appears as a composite time variation of phase, transformable to a phase-frequency spectrum, on the bias carrier. Phase variation (degrees, cycles, or radians) is referenced to the nominal phase of the bias frequency.

The counter ignores the amplitude of the input waveform. It simply registers, or counts, positive-going zero-crossings (cycles) of the input, and, upon receipt of a release data time pulse, resolves the (final) count to 10 nanoseconds, or 0.01 cycle at 1.0 MHz (3.6 deg), then releases data.

The time between release data pulses is the preset measurement period, T . The counter thus *integrates* the phase-frequency *continually*, releasing the integral to date at each N^{th} time-series increment NT . It does not automatically reset; the count is cumulative. The output count is thus a very large number, containing all cycles counted since last (arbitrary) manual reset. The format is a series of decimal digits:

$$\begin{array}{ccc} \text{XXXXXX} & \text{XXXXXXXXXX} & \text{XXX} = \Phi_N \text{ (readout)} \\ \text{time} & \text{accumulated} & \text{resolver count} \\ & \text{cycle count} & [1 \times 10^{-9} \text{ s of bias} \\ & & \text{cycle, resolution}] \end{array}$$

expressed as waveform functions (bias integral linear).

$$A(t) = \text{input waveform} = a \sin \left[\Phi_0 + Bt + \int_0^t \dot{\varphi}(t) dt \right]$$

$$\Phi_N = \Phi_0 + BNT + \int_0^{NT} \dot{\varphi}(t) dt \text{ (resolver incorporated)}$$

The desired data consists of the difference between successive values of the trailing integral. This is the deviation from nominal; the integral of the phase frequency across a measurement period. This data time series is

$$\begin{aligned} \varphi_N(NT) &= \Phi_N - \Phi_{N-1} - BT \text{ (by data reduction)} \\ &= \int_{(N-1)T}^{NT} \dot{\varphi}(t) dt \end{aligned} \quad (1)$$

The set $\{\varphi_N\}$ is processed to yield mean and variance of the data over a block of M measures [block period $\tau = MT$]:

$$\begin{aligned} \hat{\varphi} &= \frac{1}{M} \sum_{N=1}^M (\varphi_N) \\ \hat{\sigma}^2(\varphi) &= \frac{1}{M-1} \left[\sum_{N=1}^M (\varphi_N)^2 - M(\hat{\varphi})^2 \right] \end{aligned} \quad (2)$$

Also, for nonstationary mean

$$\hat{F}\phi = (\hat{\varphi})/\tau, \text{ Hz,} = (\Phi_M - \Phi_1 - MBT)/\tau$$

where $F\phi$ is the system phase-frequency offset.

III. Allan Variance Data Processing

The Allan variance technique, newly adopted for DSN testing, is a variation of Eq. (2) where the mean, τ , is set to only $2T'$, and collective variance of sequential data pairs is averaged. This technique leads to expression of non-stationary data expectation by stationary spectral models; the variance measure is, in general, stabilized as a rational function of T . Variance becomes:

$$\begin{aligned} \hat{\sigma}_{AV}^2(\varphi) &= \frac{1}{M} \sum_{N=1}^M \left[\frac{(\varphi_N^2 + \varphi_{N-1}^2)}{2} - \left(\frac{\varphi_0 + \varphi_{N-1}}{2} \right)^2 \right] \\ &= \frac{1}{M} \sum_{N=1}^M (\varphi_N - \varphi_{N-1})^2 \end{aligned} \quad (3)$$

Eq. (3), therefore, is the quantity to be predicted by the spectral model; further variance discussion will be limited to this technique alone.

IV. Allan Variance General Model and Filter Functions

Expected value of measures obtained from Eq. (3) can best be modeled as some combination of noise spectral densities of

various orders (order in this paper is the order, or exponent, of the (predominant) denominator term of the density), as filtered by the counter-data-reduction process. To start, assume the variance contribution of an arbitrary noise source, as filtered:

$$E(\sigma_N^2) = K_N \int_{a_N}^{b_N} |H_N(j\omega)|^2 \cdot |F(j\omega)|^2 d\omega \quad (4)$$

where

N = N th noise source index

K_N = noise constant

$H_N(j\omega)$ = spectral density function

$F(j\omega)$ = counter/data process frequency transfer function (Allan variance)

a_N, b_N = arbitrary integral frequency limits, or/cutoffs.

The filter function is invariant with noise spectrum, depending only on sample period T . We derive it from its Laplace time transform for a single Allan measurement:

$$F(S) = \underbrace{\left[\frac{1 - e^{-ST}}{S} \right]}_{\text{sample}} - \frac{1}{2} \underbrace{\left[\frac{1 - e^{-2ST}}{S} \right]}_{\text{mean}} \quad (5)$$

This simply states that each measurement of the waveform is differenced with its value T earlier, with mean over $2T$ subtracted; a parallel to elements of Eq (3) Eq. (5), by manipulation, leads to the desired transfer function.

$$\begin{aligned} |F(j\omega)|^2 &= \frac{1}{4} [1 + \cos(2\omega T) - 2 \cos(\omega T)]^2 \\ &\quad + \frac{1}{4} [\sin(2\omega T) - 2 \sin(\omega T)]^2 \\ &= \left\{ [\cos^2(\omega T)] + [\sin^2(\omega T)] \right\} [1 - \cos(\omega T)]^2 \\ &= [1 - \cos(\omega T)]^2 \text{ (Allan variance only)} \end{aligned} \quad (6)$$

Expression (6) is remarkable in that its leading term is of fourth power, assuring convergence of integrals with spectral densities up to and including that order. Equation (6) thus enters Eq. (4) as the defined transfer characteristic, leaving the spectral densities and constants to be determined.

V. Noise Spectral Densities and Sources

When doppler noise is measured under strong-signal coherent conditions, variance is small, stationary, and consists only of system residual sources, lumped as ϕ_0^2 . The standard deviation of this residual is only a few degrees (3 deg typical), and is assumed present in all test configurations. It is background noise, undoubtedly the rms combination of a number of minor sources. It is carried here as a single parameter, to be determined during model-data fit iteration. It is flat noise, order zero.

When the test configuration is altered to the noncoherent strong signal mode, very large nonstationary elements appear in the data. The predominant element is a strong quasi-stable mean. This mean, divided by the sampling period, represents a nearly stationary phase-frequency ($F\phi$, Hz), or slope that often holds within ± 5 percent for several hours, then suddenly changes state by ratios as much as 50:1. The mean behavior is analyzed later in this discussion. The Allan variance technique largely avoids these mean effects, as they influence variance; the mean is short-term.

The presence of the long-term mean does, however, indicate a dominant third-order spectrum, often called $1/F$ noise (referred to integrator inputs). However, during short measurement periods, the variance is approximately linear, indicating second-order source or sources. By reference to specifications, it was determined that the prime latter-source was the *secondary standard*; it literally swamped the variance for T of ten seconds or less, while giving third-order indications at longer periods.

To complete the set, assume some second-order contribution for system sources other than the standard. Before forming the model using these spectra, an analysis of spectral continuity of frequency standards in general is pertinent. The orders for this and the system are shown in Table 1.

VI. Frequency Standard Noise Models

The phase-noise contribution of frequency standards in the system is well understood to be large during short measure-

ment periods, settling finally into a third-order spectral mode during longer periods.

Published frequency variance data indicate some combination of second- and third-order phase-power spectra. The question is whether both spectra are continuous and overlapping, with saturated integrals, or whether the composite spectral density crosses over from third order to second order form at a particular defined frequency; the second order integral subsequently continuous to saturation. When the latter is assumed, it is often replaced by a break-point time approximation. The frequency variance is considered log-linear with time before the break-point, and subsequently constant. The break-point measurement time varies from 30 seconds to 300 seconds with common standards of various quality.

The three models are outlined in Table 2, and results for the present DSN primary standard are shown in Fig. 1.

Model 2 (see Table 2) was obviously chosen, for it rides below the maximums, but is otherwise very close to the published break-point data. It appears that frequency standard noise is best modeled as sequential, rather than continuous, power spectral density orders.

During non-coherent test mode, results of Fig. 1 cannot be applied directly, for the site secondary standard is in use. The standard exhibits frequency variance that is much degraded over that of the primary standard. Also, definitive specifications are not available.

However, Model 2 was still assumed to apply, but with different cross-over frequency (F_c) and amplitude constant. These were given bounded ranges by degrading the primary standard data by one-half to one order of magnitude. Within these ranges, the parameters were iterated with the other system model estimates and data, as described later in the discussion.

VII. Final Allan Variance Model and Parameters

Since Model 2 of Table 2 was chosen for the standard, the same form (spectral cross-over) was finally chosen for the rest of the system. The choice was hardly trivial; the other models did not fit the data. The two models differed only in the selection of the amplitude constants and crossover frequencies. The final total model is (the spectral model of Eq. (3)).

$$E \{ \sigma_{AV}^0 \}^2 = (\varphi_0)^2 \quad (\text{residual})$$

$$\left. \begin{aligned} &+ K_0 T^2 \int_0^{\omega_0 T} \frac{[1 - \cos(x)]^2}{X^3} dx \\ &+ \frac{K_0 T}{\omega_0} \int_{\omega_0 T}^{\infty} \frac{[1 - \cos(x)]^2}{X^2} dx \end{aligned} \right\} \text{system sources}$$

$$\left. \begin{aligned} &+ K_s T^2 \int_0^{\omega_c T} \frac{[1 - \cos x]^2}{X^3} dx \\ &+ \frac{K_s T}{\omega_c} \int_{\omega_c T}^{\infty} \frac{[1 - \cos x]^2}{X^2} dx \end{aligned} \right\} \text{secondary standard} \quad (7)$$

K_0, K_s = noise amplitude constants, $(\text{deg/sec})^2 \cdot (\text{rad})^2$

ω_0, ω_c = crossover frequencies, (rad/sec)

T = measurement time, sec

The four main constants ($K_0, \omega_0, K_s, \omega_c$) and φ_0 interact, and no solution would be possible unless their ranges could be bounded. Extrapolation of known frequency standard data to apparent secondary standard degradation gave such bounds to K_s and ω_c . It was obvious from data behavior that ω_0 was much greater than ω_c ; system $1/F$ noise predominated over any possible standard contribution at long measurement intervals.

Four prime data points were used for iteration (to minimum rms error, normalized, model vs data), but several lower-confidence points were used as checks (all within $\pm 10\%$). The prime data points were (from DSS 11) as listed in Table 3.

Iteration was a manually aided machine variation of parameters technique, using Eq. (7) where, for each combination increment the sigma error of each point, and normalized rms error of all points, was calculated.¹ The points are those for a single site (DSS 11); other parameters would apply elsewhere.

The iteration data were as listed on Table 4.

Final fit of Eq. (7) to data, using Table 4 values, is shown in Fig. 2. The figure displays the long-term stationary parameter

¹For use with Eq. (7), series solutions of the integrals were programmed

σ/T , rather than σ directly. To obtain σ in degrees, the ordinate must be multiplied by T .

A program is planned to incorporate Eq. (7) and the iteration process into a station performance test algorithm. Finally, a discussion of $F\phi$ behavior and its implications follow.

VIII. Noncoherent Doppler Mean and Mean Frequency

The doppler phase noise mean value is simply the difference between the last and first total phase measure over a (long) block period, τ . The mean frequency, $F\phi$, is this measure divided by τ , normally expressed in Hz. The counter/data process filter transfer function for this quantity contains a sine-squared term:

$$\begin{aligned} F_M(s) &= 1 - e^{-s\tau} \\ |F_M(j\omega)|^2 &= [1 - \cos(\omega\tau)]^2 + [\sin(\omega\tau)]^2 \quad (8) \\ &= 4 \sin^2\left(\frac{\omega\tau}{2}\right) \end{aligned}$$

Concentrating on $F\phi$ (since the block mean is not used for Allan variance), the expressions consist of substituting Eq. (8) in Eq. (7) and dividing by τ .

This total model becomes (less φ , which is mean-zero), and expressed in Hz^2 :

$$\begin{aligned} E\left(\frac{MN}{\tau}\right)^2 &= E(F_0)^2 \\ &= \frac{K_0}{(360)^2} \int_0^{(\omega_0\tau/2)} \frac{\sin^2(x)}{X^3} dx \\ &\quad + \frac{K_0}{\omega_0\tau(360)^2} \int_{(\omega_0\tau/2)}^{\infty} \frac{\sin^2(x)}{X^2} dx \\ &\quad + \frac{K_s}{(360)^2} \int_0^{(\omega_c\tau/2)} \frac{\sin^2(x)}{X^3} dx \\ &\quad + \frac{K_s}{\omega_c\tau(360)^2} \int_{(\omega_c\tau/2)}^{\infty} \frac{\sin^2(x)}{X^2} dx \end{aligned} \quad (9)$$

Now, when

$$1/\tau \ll \omega_0, \omega_c \quad [\tau > 100 \text{ sec}]$$

The x^2 (order 2) integrals become insignificant. Also, since $\omega_c \ll \omega_0$, in any definitive solution of Eq. (9), the initial integral will predominate. We can thus say, with reasonable certainty that — $F\phi$ is a third-order system effect, essentially independent of all dynamic frequency standard spectral noise.

This does *not* mean that the standards are free of contribution; $F\phi$ is a dc frequency offset; a phase accumulation. It simply means that dynamic (short-term-time-variant) frequency-standard contribution is ruled out; $F\phi$ and its variations are very-long-term processes, largely unspecified. In a mission sense, $F\phi$ is the station doppler (velocity) error, a contribution, during tracking, to the overall spacecraft velocity error.

Admitting to both third-order system effects, by model, and unmodeled standard frequency offsets (a third-order contribution), we restate Eq. (9), in Hz^2 , as:

$$E(F\phi)_N^2 \Big|_{\tau} = C_N \int_0^{(\omega_F\tau)} \frac{\sin^2(x)}{X^3} dx \quad (10)$$

where

N = index of N^{th} value of $F\phi$

C_N = prevailing offset magnitude constant during measure N , $(\text{Hz})^2 \cdot (\text{rad})^2$

ω_F = to coin a term, "the $F\phi$ noise bandwidth," or average frequency beyond which mean and $F\phi$ contributions are insignificant. If you placed a low-pass filter at ω_F , $F\phi$ would not be significantly affected.

Expression (10) has a magnificent drawback; it does not converge at the origin. It simply says " $F\phi$ is infinite" $[-\log(0)]$, a straight vertical phase slope, forever. This does not synchronize with reality.

The problem of this model non-convergence vs real measures has been investigated in many ways. The major conclusion has been that Eq. (10) does *not* represent any real spectrum when ω is very very small, and measures show that statistical generalizations no longer apply.

One approach, in particular, is to insert a sharp high-pass filter within Eq. (10). It attenuates the ambiguous region and converges the integral. Such a filter, generalized, has been most lately expressed in detail by Greenhall (Ref. 1) in connection

with VCO spectral density estimates, where linear trends have been subtracted.

Assuming some-such general high-pass filter (steep enough to have no significant effect on the variance measure), we restate Eq. (10) as

$$\left. \begin{aligned} E(F\phi)_N^2 \Big|_{\tau} &= C_N \int_0^{\omega_{F\tau}} \frac{\sin^2(x)}{X^3} \cdot G(x) dx \\ G(x) &= \text{a high-pass filter, plus added} \\ &\quad \text{form to express observed} \\ &\quad \text{data.} \\ \text{for no effect on variance } G(x) &= 1 \left\{ \begin{array}{l} x > \Delta x \\ \Delta x \ll 1 \end{array} \right\} \end{aligned} \right\} \quad (11)$$

The applicable form of $G(x)$ was approached here by a survey of DSN site $F\phi$ behavior, as gathered from noncoherent doppler test data.

$F\phi$ behaves in a peculiar manner (one look at Eq. (11) would suggest this). It maintains a fixed value for hours, then suddenly jumps to a new value, entirely different. The time integral, or phase waveform, is a series of constant slopes with sharp break points to new linear values. Such a break is plotted in Fig. 3, detected during a four-hour test at DSS 11.

Data are too scarce to estimate accurately any periodic sequence to this behavior. However, $F\phi$ appears to be absolutely statistically bounded; its various states seem to fall within probabilistic regions, with (at least close to) a mean of zero: The DSS 11 data showed a standard deviation of about 0.07 Hz. (6 samples; mean = 0.02 Hz; 4 month scattered data samples).

Since a given $F\phi$ value persists for such a long period, it appears quasi-stable, and any filter leading to its model must contain, upon integration, a *quasi-stable constant* component, applicable over (long) discrete time intervals

The only known integrands that yield direct constants are those of fractional form. We thus assume that

Assumption 1: " $G(x)$, near the origin, results in an integral of fractional form, yielding a constant quasi-stable integration order."

This suggests that some system function fractionally integrates the low-frequency end of the spectrum. This source, if it exists, is indeterminate.

Accepting $F\phi$ as a mean-zero convergent random variable, its time waveform has, inherently, a finite Fourier transform, but resolveable over only over very long time periods (months). If mean-zero, the time-transform would, by assumption, show *no dc component*. Thus:

Assumption 2: " $G(x)$ must attenuate the pole at the origin (contain a high-pass filter) to represent the data. Data indicate an integrable pole at zero."

The third assumption, a virtual corollary to the first, is that the spectrum must contain a pole at all times, other than (or in place of) that attenuated at zero. The fractional integral of assumption 1 requires a definitive pole. Let the pole symbol be ω_p . The pole ω_p *need not be constant*. It is sufficient that its time period be that of the differential $F\phi$ break points. Thus, if a Fourier transform were taken over this interval, the ω_p component would far surpass all others in amplitude; that is, it would be the "pole of the measure." This is certainly sufficient for a daily tracking period in site operational use. The assumption is therefore:

Assumption 3: " $G(x)$ must contain a quasi-stable finite pole, defining $F\phi$ (daily) transient excursions as (daily) pole-frequency period."

Noting the above, the form chosen for $G(x)$, meeting all three assumptions, was unusually simple:²

$$G(x) = \left(\frac{x}{|(\omega_p \tau) \cdot x|} \right)^{\Delta} \quad (12)$$

$\Delta = \text{order of fractional integration}$

Inserting this in Eq. (11), and separating integrals at the pole:

$$\begin{aligned} E(F\phi)_N^2 \Big|_{\tau} &= C_N \int_0^{\omega_{pN\tau}} \left[\frac{\sin^2(x)}{x^2} \right] \cdot \frac{x^{\Delta-1}}{(\omega_{pN\tau} - x)^{\Delta}} dx \\ &+ C_N \int_{\omega_{pN\tau}}^{\omega_{F\tau}} \left[\frac{\sin^2(x)}{x^2} \right] \cdot \frac{x^{\Delta-1}}{(x - \omega_{pN\tau})^{\Delta}} dx \end{aligned} \quad (13)$$

²The form is not rigorously established; measured data and source characteristics at these extremes are too scarce. The form is simply one (of possibly many) that meets the assumptions, as based on available data.

To obtain an upper bound (disposing of considerable numerical complication), let.

$$\frac{\sin^2(x)}{x^2} = 1$$

This gives (τ cancels out) the bound (with parameter interchange):

$$\begin{aligned} E \{(F\phi)^2\}_N &< C_N \Gamma(\Delta) \int_0^{\omega_{P_N}} \frac{X^\Delta}{\Gamma(\Delta) [\omega_{P_N} - X]^{1-\Delta}} dX \\ &+ C_N \int_{\omega_{P_N}}^{\omega_F} \frac{X^{\Delta-1}}{(X - \omega_{P_N})^\Delta} dX \end{aligned} \quad (14)$$

The first integral is of the fractional calculus form,³ leading to a constant, as transiently observed. The second leads to a log ratio and trailing series, the latter insignificant if Δ is small. The slightest Δ converges the integral (solution of Eq. (10)):

$$\begin{aligned} \frac{E \{(F\phi)^2\}_N}{C_N} &< \left\{ \frac{\Gamma(1+\Delta) \Gamma(1-\Delta)}{\Delta} + \log \left[\frac{\omega_F}{\omega_{P_N}} \right] \right. \\ &+ \underbrace{\Delta \sum_{K=1}^{\infty} \frac{\Gamma(K+\Delta) \left[1 - \left(\frac{\omega_F}{\omega_{P_N}} \right)^K \right]}{\Gamma(1+\Delta) (K)! - K}}_{\text{normally insignificant, } \Delta \ll 1} \left. \right\} \end{aligned} \quad (15)$$

Expression (15)⁴ does not admit to small values of $F\phi$, occasionally observed (Fig. 3, early data), if Δ small, as required. It is but a maximum rms amplitude constant, some other snap-action parameter is determining it is quasi-period level. The parameter seems, at this point, to have three

common states: small, large +, and large -. The resulting $F\phi$ model, with this unknown parameter, is therefore:

$$E \{F\phi\}_N \approx \left\{ \sqrt{C_N} \sqrt{\frac{\Gamma(1+\Delta_N) + \Gamma(1-\Delta_N)}{\Delta_N}} + \log \left[\frac{\omega_F}{\omega_{P_N}} \right] \right\} \times \{A_N\}$$

N = index of period ($F\phi$ transition count)

C_N = $F\phi$ variance (site noise constant), during N .

Δ_N = spectrum fractional integration parameter ($\Delta_N \ll 1$, possibly site-constant) for DSN 11 data, $\Delta \approx 0.057$.

ω_F = noise bandwidth of mean power

ω_{P_N} = apparent pole frequency during N .

A_N = unknown step parameter with three apparent states: (0, +1, -1) $\pm 5\%$ (16)

To conclude, the $F\phi$ function is hardly rigorously determined. However Eq. (16) does provide a lead-in to its understanding, and represents a convergent solution to Eq. (10). For a more definitive model, extensive data would be required.

IX. Summary and Conclusions

- (1) The Allan variance technique leads to predictable expected doppler noise values. The values depend upon DSN site-dependent parameters, and these numbers must be determined, for each location, in noncoherent mode. An appropriate algorithm is in process.
- (2) The present DSN site secondary-frequency-standards severely contaminate – even mask – the true system noise, particularly during short measurement periods. The desired system measure is severely degraded by this source.
- (3) The doppler mean-offset-frequency is quasi-stable, but erratic on a long-term scale. Available data are insufficient for a thorough analysis, and all models are non-convergent unless an arbitrary high-pass filter is

³The expression is a specific expression of the “Riemann-Liouville” fractional calculus integral (about 1850)

⁴Note that the Δ function is independent of ω_{P_N} first-term amplitude is not affected by pole location

added. This parameter is a maverick, expressing the finite reality of an infinite theoretical prediction. The fractional-integration model herein is but one of many possible descriptions.

- (4) The mean-offset frequency above has a large mission significance. It is the velocity error of the spacecraft, as contributed by the DSN sites. It would be expedient to locate and stabilize its sources.

Reference

1. Greenhall, C.A., "Models for Flicker Noise in DSN Oscillators," in *The Deep Space Network*, Technical Report 32-1526, Vol. XIII, pp. 183-193, Feb. 15, 1973.

Table 1. Doppler spectral elements

Order	$ H(j\omega) ^2$	Probable source
0	1	System residual φ_0
2	$1/\omega^2$	Secondary standard
3	$1/\omega^3$	and system

Table 2. Frequency standard models

Ordinate/symbol	Model	Expression/definition
$\sigma^2 \left(\frac{\Delta\varphi}{T} \right)$ $\approx \alpha^2 \left(\frac{\Delta F}{F} \right)$ Frequency standard variance	1	$K_0 \int_0^\infty \frac{F_c(X)}{X^3} dX + \frac{K_1}{T} \int_0^\infty \frac{F_c(X)}{X^2} dX$ $= K'_0 + \frac{K'_1}{T}$
	2	$K_0 \int_0^{\omega_c T} \frac{F_c(X)}{X^3} dX + \frac{K_0}{\omega_c T} \int_{\omega_c T}^\infty \frac{F_c(X)}{X^2} dX$
	3	$\left. \begin{array}{l} \frac{K'_1}{T} \text{ if } T < T_c \\ K'_0 \text{ if } T > T_c \end{array} \right\} \text{Break point } (T_c) \text{ approximation}$
$F'_c(X)$	1, 2, 3	Sampling power function, Allan variance $[1 - \cos(X)]^2$
K_0, K_1	1, 2	Third- and second-order noise constants, dimensioned to yield $[\text{deg/sec}]^2$
K'_0, K'_1	1, 3	K_0 and K_1 with integral limit values included
ω_c	2	Cross-over frequency = $1/T_c$

Table 3. Prime variance data

Point	T , sec	$\sigma_{(\text{Allan})}^0$
1	1	15.56
2	10	49.34
3	60	219
4	120	504

Table 4. Parameter iteration using DSS II data

Parameter	Initial range	Initial value	Final value
φ_0	$0 < \varphi_0 < 10$	5	2.0
K_0	$10 < K_0 < 25$	20	13.52
ω_0	$0.05 < \omega_0 < 0.5$	0.05	0.1486
K_s	$5 < K_s < 20$	20	11.87
ω_c	$0.01 < \omega_c < 0.05$	0.01	0.0294
	rms error	0.2850	0.0116

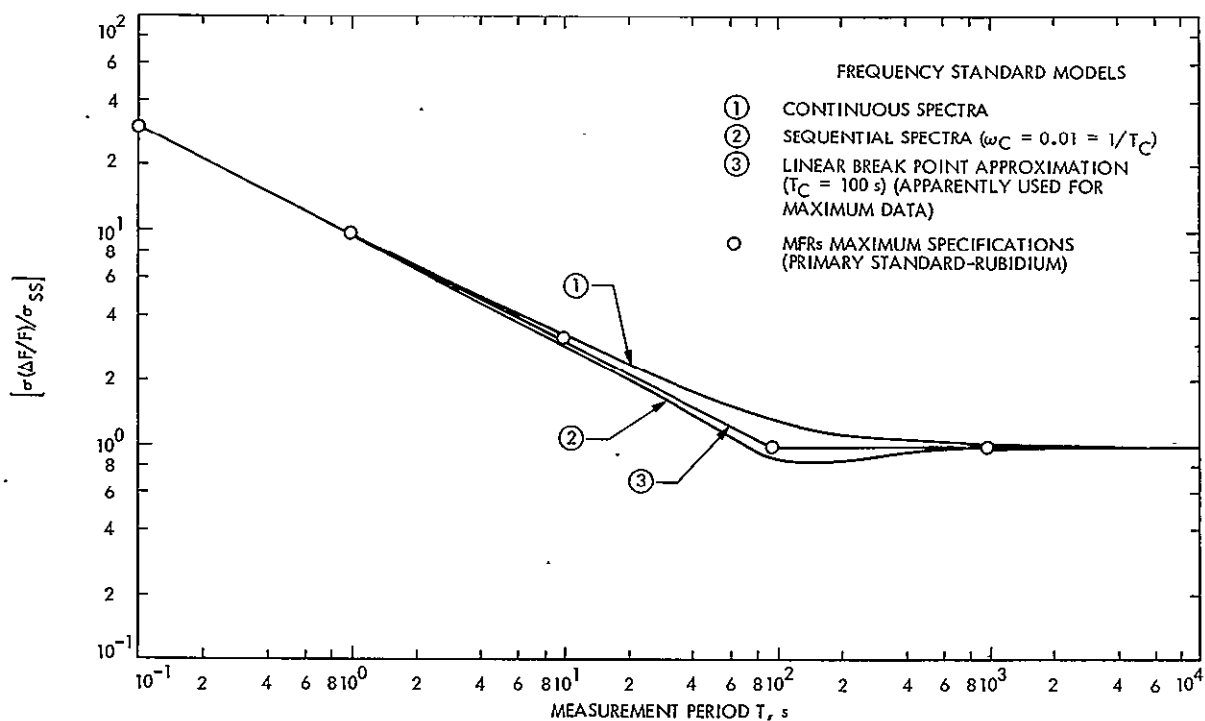


Fig. 1. Comparison of frequency standard noise models

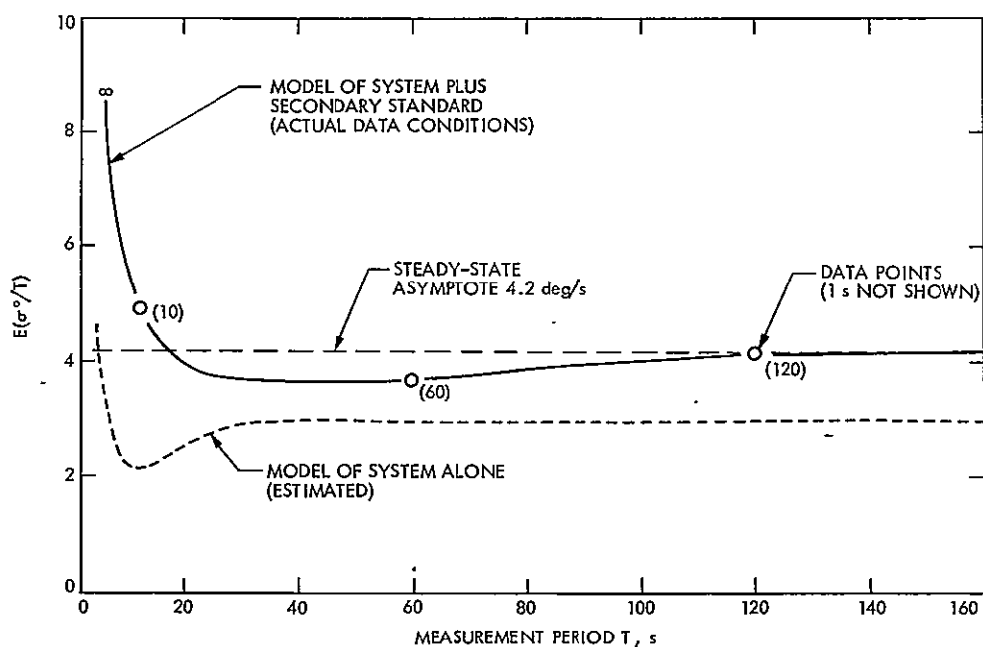


Fig. 2. Allan variance model, DSS 11 data, non-coherent mode

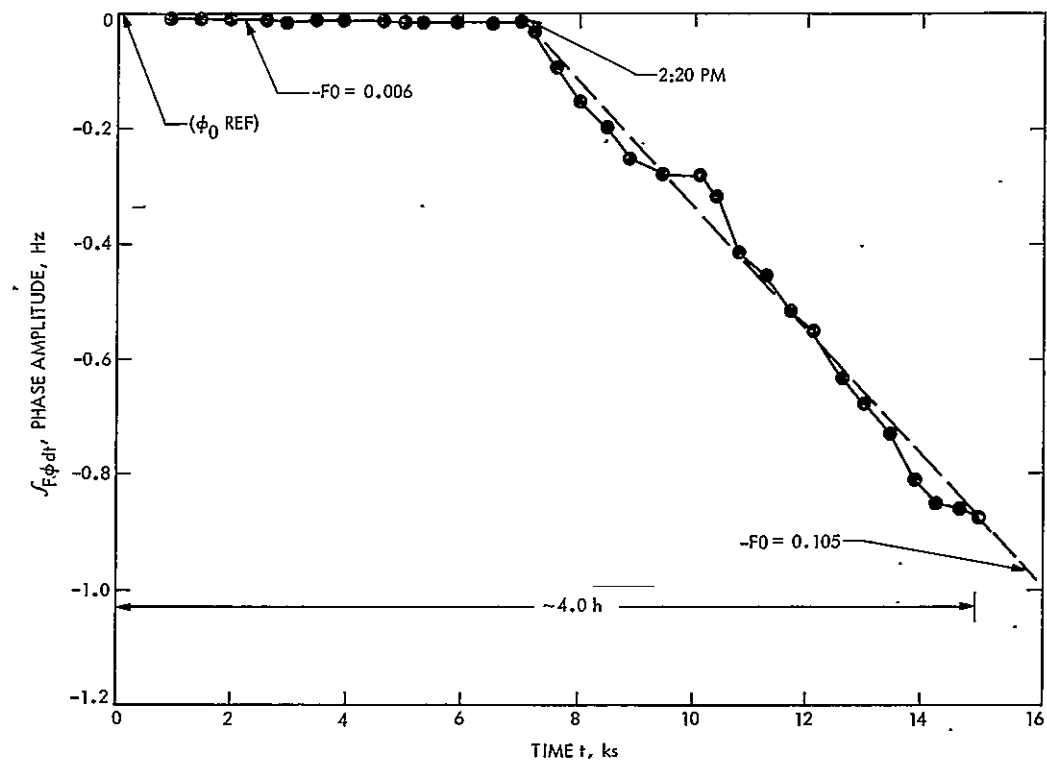


Fig. 3. Phase waveform of DSS 11 $F\phi$ break point, Day 17

Bibliography

- Anderson, J. D., Null, G. W., and Thornton, C. T., *The Evaluation of Certain Astronomical Constants from the Radio Tracking of Mariner II*, Technical Report 32-476, Jet Propulsion Laboratory, Pasadena, Calif., reprinted from *Progr. Astronaut. Aeronaut.*, Vol. 14, 1964.
- Anderson, J. D., *Determination of the Masses of the Moon and Venus and the Astronomical Unit from Radio Tracking Data of the Mariner II Spacecraft*, Technical Report 32-816, Jet Propulsion Laboratory, Pasadena, Calif., July 1, 1967.
- Anderson, J. D., et al., "The Radius of Venus as Determined by Planetary Radar and Mariner V Radio Tracking Data," *J. Atmos. Sci.*, pp. 1171-1174, Sept. 25, 1968.
- Anderson, J. D., and Hilt, D. E., "Improvement of Astronomical Constants and Ephemerides from Pioneer Radio Tracking Data," *AIAA J.*, Vol. 7, No. 6, pp. 1048-1054, June 1969.
- Anderson, J. D., "Determination of Astrodynamic Constants and a Test of the General Relativistic Time Delay With S-Band Range and Doppler Data From Mariners 6 and 7," *Space Research*, Vol. XI, pp. 105-112, Akademie-Verlag, Berlin, 1971.
- Barnum, P. W., et al., *Tracking and Data System Support for the Mariner Mars 1971 Mission: Orbit Insertion Through End of Primary Mission*, Technical Memorandum 33-523, Vol. III, Jet Propulsion Laboratory, Pasadena, Calif., May 15, 1973.
- Barnum, P. W., and Renzetti, N. A., *Tracking and Data System Support for the Mariner Mars 1971 Mission: Extended Mission Operations*, Technical Memorandum 33-523, Vol. IV, Jet Propulsion Laboratory, Pasadena, Calif., Dec. 15, 1973.
- Barton, W. R., and Miller, R. B., *Tracking and Data System Support for the Pioneer Project: Pioneer 11—Prelaunch Planning Through Second Trajectory Correction: to May 1, 1973*, Technical Memorandum 33-584, Vol. II, Jet Propulsion Laboratory, Pasadena, Calif., Mar. 15, 1975.
- Bartos, K. P., et al., *Implementation of the 64-Meter-Diameter Antennas at the Deep Space Stations in Australia and Spain*, Technical Memorandum 33-692, Jet Propulsion Laboratory, Pasadena, Calif., Jan. 15, 1975.
- Bathker, D. A., *Radio-Frequency Performance of an 85-ft Ground Antenna: X-Band*, Technical Report 32-1300, Jet Propulsion Laboratory, Pasadena, Calif., July 1, 1968.
- Bathker, D. A., *Radio Frequency Performance of a 210-ft Ground Antenna: X-Band*, Technical Report 32-1417, Jet Propulsion Laboratory, Pasadena, Calif., Dec. 15, 1969.
- Bathker, D. A., *Predicted and Measured Power Density Description of a Large Ground Microwave System*, Technical Memorandum 33-433, Jet Propulsion Laboratory, Pasadena, Calif., Apr. 15, 1971.
- Bathker, D. A., Brown, D. W., and Petty, S. M., *Single- and Dual-Carrier Microwave Noise Abatement in the Deep Space Network*, Technical Memorandum 33-733, Jet Propulsion Laboratory, Pasadena, Calif., Aug. 1, 1975.

- Baumert, L., et al., *Coding Theory and Its Applications to Communications Systems*, Technical Report 32-67, Jet Propulsion Laboratory, Pasadena, Calif., Mar. 31, 1961.
- Baumgartner, W. S., *High-Power CW Radar Transmitter*, Technical Report 32-656, Jet Propulsion Laboratory, Pasadena, Calif., Sept. 1, 1964.
- Berman, A. L., *Tracking System Data Analysis Report, Ranger VII Final Report*, Technical Report 32-719, Jet Propulsion Laboratory, Pasadena, Calif., June 1, 1965.
- Berman, A. L., and Rockwell, S. T., *New Optical and Radio Frequency Angular Tropospheric Refraction Models for Deep Space Applications*, Technical Report 32-1601, Jet Propulsion Laboratory, Pasadena, Calif., Nov. 1, 1975.
- Biber, K. W., and Whittlesey, A. C., *Description and Analysis of 890-MHz Noise-Measuring Equipment*, Technical Report 32-898, Jet Propulsion Laboratory, Pasadena, Calif., Mar. 31, 1966.
- Born, G. H., et al., "The Determination of the Satellite Orbit of Mariner 9," *Celest. Mech.*, Vol. 9, No. 3, pp. 395-414, May 1974.
- Brockman, M. H., et al., *Extraterrestrial Radio Tracking and Communication*, External Publication 808, Jet Propulsion Laboratory, Pasadena, Calif., Nov. 12, 1959. Also available in *Proc. IRE*, Vol. 48, 1960.
- Brockman, M. H., and Posner, E. C., *Power Requirements for Deep-Space Telecommunication Links*, Technical Report 32-1395, Jet Propulsion Laboratory, Pasadena, Calif., reprinted from *IEEE Spectrum*, Vol. 6, No. 3, pp. 95-99, Mar. 1969.
- Bunce, R. C., *Unified S-Band Receiver-Exciter Subsystem*, Technical Report 32-809, Jet Propulsion Laboratory, Pasadena, Calif., Sept. 15, 1968.
- Butman, S., "A General Formulation of Linear Feedback Communication Systems with Solutions," *IEEE Trans. Inform. Theor.*, Vol. IT-15, No. 3, pp. 392-400, May 1969.
- Butman, S., "Rate-Distortion Over Band-Limited Feedback Channels," *IEEE Trans. Inform. Theor.*, Vol. IT-17, No. 1, pp. 110-112, Jan. 1971.
- Butman, S., and Timor, U., "Interplex—An Efficient Multichannel PSK/PM Telemetry System," *IEEE Trans. Commun.*, Vol. COM-20, No. 3, pp. 415-419, June 1972.
- Cain, D. L., and Hamilton, T. W., *Determination of Tracking Station Locations by Doppler and Range Measurements to an Earth Satellite*, Technical Report 32-534, Jet Propulsion Laboratory, Pasadena, Calif., Feb. 1, 1964.
- Carey, C. N., and Sjogren, W. L., *Gravitational Inconsistency in the Lunar Theory: Confirmation by Radio Tracking*, Technical Report 32-1290, Pt. II, Jet Propulsion Laboratory, Pasadena, Calif., reprinted from *Science*, Vol. 160, No. 3830, pp. 875-876, May 24, 1968.
- Carpenter, R. L., *Study of Venus by CW Radar—1964 Results*, Technical Report 32-963, Jet Propulsion Laboratory, Pasadena, Calif., reprinted from *Astron. J.*, Vol. 71, No. 2, pp. 142-152, Mar. 1966.
- Carr, R. E., *The Jet Propulsion Laboratory Method of Tracking Lunar Probes*, External Publication 793, Jet Propulsion Laboratory, Pasadena, Calif., June 4, 1959.

- Chadwick, H. D., and Springett, J. C., "The Design of a Low Data Rate MSFK Communication System," *IEEE Trans. Commun. Technol.*, Vol. COM-18, No. 6, pp. 740-750, Dec. 1970.
- Chaney, W. D., *Final Mariner II Tracking System Data Analysis Report*, Technical Report 32-727, Jet Propulsion Laboratory, Pasadena, Calif., Sept. 1, 1965.
- Charles, F. J., and Lindsey, W. C., *Some Analytical and Experimental Phase-Locked Loop Results for Low Signal-to-Noise Ratios*, Technical Report 32-1027, Jet Propulsion Laboratory, Pasadena, Calif., reprinted from *Proc. IEEE*, Vol. 54, No. 9, pp. 1152-1166, Sept. 1966.
- Clark, B. G., et al., "High Resolution Observations of Compact Radio Sources at 13 cm," *Astrophys. J.*, Vol. 161, pp. 803-809, Sept. 1970.
- Clauss, R. C., et al., *Total System Noise Temperature: 15°K*, Technical Report 32-691, Jet Propulsion Laboratory, Pasadena, Calif., Nov. 1964.
- Clauss, R. C., *A 2388-Mc Two-Cavity Maser for Planetary Radar*, Technical Report 32-583, Jet Propulsion Laboratory, Pasadena, Calif., reprinted from *Microwave J.*, Vol. 8, pp. 74-77, May 1965.
- Clauss, R. C., *A Traveling Wave Maser for Deep Space Communication at 2295 and 2388 MHz*, Technical Report 32-1072, Jet Propulsion Laboratory, Pasadena, Calif., Feb. 15, 1967.
- Cohen, M. H., et al., "Compact Radio Source in the Nucleus of M87," *Astrophys. J.*, Vol. 158, No. 2, Pt. 2, pp. L83-L85, Nov. 1969.
- Coyner, J. V., Jr., *Radial Rib Antenna Surface Deviation Analysis Program*, Technical Memorandum 33-518, Jet Propulsion Laboratory, Pasadena, Calif., Dec. 15, 1971.
- Curkendall, D. W., and McReynolds, S. R., "A Simplified Approach for Determining the Information Content of Radio Tracking Data," *J. Spacecraft Rockets*, Vol. 6, No. 5, pp. 520-525, May 1969.
- Curkendall, D. W., and Stephenson, R. R., "Earthbased Tracking and Orbit Determination—Backbone of the Planetary Navigation System," *Astronaut. Aeronaut.*, Vol. 7, No. 5, pp. 30-36, May 1970.
- Curkendall, D. W., "Planetary Navigation: The New Challenges," *Astronaut. Aeronaut.*, Vol. 7, No. 5, pp. 26-29, May 1970.
- "The Deep Space Network—An Instrument for Radio Navigation for the Mariner Mission to Mars—1969," *Proceedings of the Second International Conference of STM and AERA*, Reidel Publishing Company, Holland, May 1969.
- Description of the Deep Space Network Operational Capabilities as of January 1, 1966*, Technical Memorandum 33-255, Jet Propulsion Laboratory, Pasadena, Calif., July 1, 1966.
- Description of World Network for Radio Tracking of Space Vehicles*, Publication 135, Jet Propulsion Laboratory, Pasadena, Calif., July 1, 1958.
- Didday, R. L., and Lindsey, W. C., *Subcarrier Tracking Methods and Communication System Design*, Technical Report 32-1317, Jet Propulsion Laboratory, Pasadena, Calif., reprinted from *IEEE Trans. Commun. Technol.*, Vol. COM-16, No. 4, pp. 541-550, Aug. 1968.

- Downs, G. S., and Reichley, P. E., "Observations of Interstellar Scintillations of Pulsar Signals at 2388 MHz," *Astrophys. J.*, Vol. 163, No. 1, Pt. 2, pp. L11-L16, Jan. 1971.
- Downs, G. S., et al., "Mars Radar Observation, A Preliminary Report," *Science*, Vol. 174, No. 4016, pp. 1324-1327, Dec. 24, 1971.
- Downs, G. S., et al., "Martian Topography and Surface Properties as Seen by Radar: The 1971 Opposition," *Icarus*, Vol. 18, No. 1, pp. 8-21, Jan. 1973.
- Downs, G. S., Reichley, P. E., and Morris, G. A., "Pulsar Detections at Frequencies of 8.4 and 15.1 GHz," *Astrophys. J.*, Vol. 181, No. 3, Part 2, pp. L143-L146, May 1, 1973.
- Easterling, M., *A Long-Range Precision Ranging System*, Technical Report 32-80, Jet Propulsion Laboratory, Pasadena, Calif., July 10, 1961.
- Easterling, M., *Methods for Obtaining Velocity and Range Information from CW Radars*, Technical Report 32-657, Jet Propulsion Laboratory, Pasadena, Calif., Sept. 1, 1964.
- Easterling, M., and Goldstein, R., *The Effect of the Interplanetary Medium on S-Band Telecommunications*, Technical Report 32-825, Jet Propulsion Laboratory, Pasadena, Calif., Sept. 1, 1965.
- Edelson, R. E. (ed.), *Telecommunications Systems Design Techniques Handbook*, Technical Memorandum 33-571, Jet Propulsion Laboratory, Pasadena, Calif., July 15, 1972.
- Efron, L., and Solloway, C. B., *Proceedings of the Conference on Scientific Applications of Radio and Radar Tracking in the Space Program*, Technical Report 32-1475, Jet Propulsion Laboratory, Pasadena, Calif., July 1, 1970.
- Eimer, M., and Stevens, R., *Tracking and Data Handling for the Pioneer III and Pioneer IV Firings*, External Publication 701, Jet Propulsion Laboratory, Pasadena, Calif., Aug. 14, 1959.
- Esposito, P. B., and Wong, S. K., "Geocentric Gravitational Constant Determined from Mariner 9 Radio Tracking Data," paper presented at the International Symposium on Earth Gravity Models (American Geophysical Union, NASA), St. Louis, Aug. 1972.
- Fearey, J. P., and Renzetti, N. A., "Navigation Results on the Mariner Mars Mission to Mars 1969," International Navigation Conference, Hamburg, Oct. 1969.
- Fjeldbo, G., Kliore, A. J., and Seidel, B. L., "Bistatic Radar Measurements of the Surface of Mars with Mariner 1969," *Icarus*, Vol. 16, No. 3, pp. 502-508, June 1972.
- Fjeldbo, G., and Eshleman, V. R., "Radio Occultation Measurements and Interpretations," in *The Atmospheres of Venus and Mars*, p. 225, Gordon and Breach, Science Publishers, Inc., New York, N.Y., 1968.
- Fjeldbo, G., "Radio Occultation Experiments Planned for Pioneer and Mariner Missions to the Outer Planets," *Planet. Space Sci.*, Vol. 21, No. 9, pp. 1533-1547, Sept. 1973.
- Flanagan, F. M., et al., *Deep Space Network Support of the Manned Space Flight Network for Apollo. 1962-1968*, Technical Memorandum 33-452, Vol. I, Jet Propulsion Laboratory, Pasadena, Calif., July 1970.

- Flanagan, F. M., et al., *Deep Space Network Support of the Manned Space Flight Network for Apollo: 1969-1970*, Technical Memorandum 33-452, Vol. II, Jet Propulsion Laboratory, Pasadena, Calif., May 1, 1971.
- Fredricksen, H., *Error Correction for Deep Space Network Teletype Circuits*, Technical Report 32-1275, Jet Propulsion Laboratory, Pasadena, Calif., June 1, 1968.
- Gary, B., Olsen, E. T., and Rosenkranz, P. W., "Radio Observations of Cygnus X-3 and the Surrounding Region," *Nature Phys. Sci.*, Vol. 239, No. 95, pp. 128-130, Oct. 23, 1972.
- Gates, C. R., and Johnson, M. S., *A Study of On-Site Computing and Data Processing for a World Tracking Network*, Publication 154, Jet Propulsion Laboratory, Pasadena, Calif., Feb. 9, 1959.
- Georgevic, R. M., *Mathematical Model of the Solar Radiation Force and Torques Acting on the Components of a Spacecraft*, Technical Memorandum 33-494, Jet Propulsion Laboratory, Pasadena, Calif., Oct. 1, 1971.
- Goldstein, R., Stevens, R., and Victor, W. K., *Radar Exploration of Venus: Goldstone Observatory Report for October-December 1962*, Technical Report 32-396, Jet Propulsion Laboratory, Pasadena, Calif., Mar. 1, 1965.
- Goldstein, R. M., *The Analysis of Uncooperative Radar Targets*, Technical Report 32-658, Jet Propulsion Laboratory, Pasadena, Calif., Sept. 1, 1964.
- Goldstein, R. M., et al., *The Superior Conjunction of Mariner IV*, Technical Report 32-1092, Jet Propulsion Laboratory, Pasadena, Calif., Apr. 1, 1967.
- Goldstein, R. M., "Radar Time-of-Flight Measurements to Venus," *Astron. J.*, Vol. 73, No. 9, Aug. 1968.
- Goldstein, R. M., et al., "Preliminary Radar Results of Mars," *Radio Sci.*, Vol. 5, No. 2, pp. 475-478, Feb. 1970.
- Goldstein, R. M., and Rumsey, H., "A Radar Snapshot of Venus," *Science*, Vol. 169, Sept. 1970.
- Goldstein, R. M., "Radar Observations of Mercury," *Astron. J.*, Vol. 76, No. 10, pp. 1152-1154, Dec. 1971.
- Goldstein, R. M., Holdridge, D. B., and Lieske, J. H., "Minor Planets and Related Objects: XII. Radar Observations of (1685) Toro," *Astron. J.*, Vol. 78, No. 6, pp. 508-509, Aug. 1973.
- Golomb, S. W., "New Problems of Space Communications: Part I. Beware of the Tigers," *Astronautics*, Vol. 7, No. 6, p. 19, June 1962.
- Golomb, S. W., "New Problems in Space Communications: Part 3," *Astronautics*, Vol. 7, No. 8, p. 26, Aug. 1962.
- Golomb, S. W., "Ferretting Signals Out of Noise," *Int. Sci. Technol.*, No. 22, pp. 72-82 and 120, Oct. 1963.
- Gordon, H. J., et al., *The Mariner 6 and 7 Flight Paths and Their Determination From Tracking Data*, Technical Memorandum 33-469, Jet Propulsion Laboratory, Pasadena, Calif., Dec. 1, 1970.
- Gottlieb, P., et al., "Lunar Gravity over Large Craters from Apollo 12 Tracking Data," *Science*, Vol. 168, No. 3930, pp. 477-479, Apr. 1970.

- Gray, R. M., and Tausworthe, R. C., "Frequency-Counted Measurements, and Phase Locking to Noise Oscillators," *IEEE Trans. Commun. Technol.*, Vol. COM-19, No. 1, pp. 21-30, Feb. 1971.
- Gubbay, J., et al., "Variations of Small Quasar Components at 2,300 MHz," *Nature*, Vol. 224, No. 5224, pp. 1094-1095, Dec. 1969.
- Gulkis, S., and Gary, B., "Circular Polarization and Total-Flux Measurements of Jupiter at 13.1 cm Wavelength," *Astron. J.*, Vol. 76, No. 1, pp. 12-16, Feb. 1971.
- Gulkis, S., et al., "Observations of Jupiter at 13-cm Wavelength During 1969 and 1971," *Icarus*, Vol. 18, No. 2, pp. 181-191, Feb. 1973.
- Hachenberg, O., et al., "The 100-meter Radio Telescope at Effelsberg," *Proc. IEEE*, Vol. 61, No. 9, pp. 1288-1295, Sept. 1973.
- Hall, J. R., and Easterling, M., "The Technology of Ground Stations in the Deep Space Network from 1958 to 1968," *IEEE Conf. Rec.*, Vol. 4, pp. 576-585, 1968.
- Hall, J. R., et al., "The General Problem of Data Return from Deep Space," *Space Sci. Rev.*, Vol. 8, pp. 595-664, 1968.
- Hall, J. R., *Tracking and Data System Support for Lunar Orbiter*, Technical Memorandum 33-450, Jet Propulsion Laboratory, Pasadena, Calif., Apr. 1970.
- Hamilton, T. W., et al., *The Ranger IV Flight Path and Its Determination From Tracking Data*, Technical Report 32-345, Jet Propulsion Laboratory, Pasadena, Calif., Sept. 15, 1962.
- Hartop, R. W., *Power Loss Between Arbitrarily Polarized Antennas*, Technical Report 32-457, Jet Propulsion Laboratory, Pasadena, Calif., Sept. 1, 1964.
- Havens, W. F., et al., *Scan Pointing Calibration for the Mariner Mars 1971 Spacecraft*, Technical Memorandum 33-556, Jet Propulsion Laboratory, Pasadena, Calif., Aug. 1, 1972.
- Heftman, K., and Renzetti, N. A., "Data Return Capabilities of the Deep Space Network in the 1970's," AIAA Paper 67-648, *Proceedings of the AIAA Space Program Issues of the 70's Meeting*, Aug. 1967.
- Higa, W. H., *Low-Level Microwave Mixing in Ruby*, Technical Report 32-1016, Jet Propulsion Laboratory, Pasadena, Calif., reprinted from *Proc. IEEE*, Vol. 54, No. 10, p. 1453, Oct. 1966.
- Higa, W. H., "Time Synchronization via Lunar Radar," *Proc. IEEE*, Vol. 60, No. 5, pp. 552-557, May 1972.
- Higa, W. H., *The Superconducting Cavity-Stabilized Maser Oscillator*, Technical Memorandum 33-805, Jet Propulsion Laboratory, Pasadena Calif., Dec. 15, 1976.
- Holmes, J. K., "On a Solution to the Second-Order Phase-Locked Loop," *IEEE Trans. Commun. Technol.*, Vol. COM-18, No. 2, pp. 119-126, Apr. 1970.
- Holmes, J. K., "First Slip Times Versus Static Phase Error Offset for the First and Passive Second-Order Phase-Locked Loop," *IEEE Trans. Commun. Technol.*, Vol. COM-19, No. 2, pp. 234-235, Apr. 1971.
- Holmes, J. K., and Tegnalia, C. R., *Digital Command System Second-Order Subcarrier Tracking Performance*, Technical Report 32-1540, Jet Propulsion Laboratory, Pasadena, Calif., Oct. 1, 1971.

- Holmes, J. K., "Performance of a First Order Transition Sampling Digital Phase-Locked Loop Using Random-Walk Models," *IEEE Trans. Commun.*, Vol. COM-20, No. 2, pp. 119-131, Apr. 1972.
- Hurd, W. J., and Anderson, T. O., *Digital Transition Tracking Symbol Synchronizer for Low SNR Coded Systems*, Technical Report 32-1488, Jet Propulsion Laboratory, Pasadena, Calif., reprinted from *IEEE Trans. Commun. Technol.*, Vol. COM-18, No. 2, pp. 141-147, Apr. 1970.
- Hurd, W. J., "An Analysis and Demonstration of Clock Synchronization by VLBI," *IEEE Trans. Instr. Meas.*, Vol. IM-23, No. 1, pp. 80-89, March 1974.
- Jaffe, R., and Rechtin, E., *Design and Performance of Phase-Lock Loops Capable of Near-Optimum Performance over a Wide Range of Input Signal and Noise Levels*, Progress Report 20-243, Jet Propulsion Laboratory, Pasadena, Calif., Dec. 1, 1954; also available in *IRE Trans. Inform. Theory*, No. 1, pp. 66-67, Mar. 1955.
- Jordan, J. F., "Orbit Determination for Powered Flight Space Vehicles on Deep Space Missions," *J. Spacecraft Rockets*, Vol. 6, No. 5, pp. 545-550, May 1969.
- Jordan, J. F., Melbourne, W. G., and Anderson, J. D., "Testing Relativistic Gravity Theories Using Radio Tracking Data From Planetary Orbiting Spacecraft," *Space Research XIII*, pp. 83-92, Akademie-Verlag, Berlin, 1973.
- Kellerman, K. I., et al., "High Resolution Observations of Compact Radio Sources at 13 Centimeters," *Astrophys. J.*, Vol. 161, No. 3, pp. 803-809, Sept. 1970.
- Kelly, A. J., *Microwave Probe for Plasma Flumes*, Technical Report 32-625, Jet Propulsion Laboratory, Pasadena, Calif., Feb. 1965.
- Kliore, A., Cain, D. L., and Hamilton, T. W., *Determination of Some Physical Properties of the Atmosphere of Mars from Changes in the Doppler Signal of a Spacecraft on an Earth-Occultation Trajectory*, Technical Report 32-674, Jet Propulsion Laboratory, Pasadena, Calif., Oct. 15, 1964.
- Kliore, A., and Tito, D. A., *Radio Occultation Investigations of the Atmosphere of Mars*, Technical Report 32-1157, Jet Propulsion Laboratory, Pasadena, Calif., reprinted from *J. Spacecraft Rockets*, Vol. 4, No. 5, pp. 578-582, May 1967.
- Kliore, A., "Radio Occultation Measurements of the Atmospheres of Mars and Venus," in *The Atmospheres of Venus and Mars*, edited by J. C. Brandt and M. B. McElrow, p. 205, Gordon and Breach Science Publishers, Inc., New York, N.Y., 1968.
- Kliore, A. J., et al., "Summary of Mariner 6 and 7 Radio Occultation Results on the Atmosphere of Mars," *Space Research*, Vol. XI, pp. 165-175, Akademie-Verlag, Berlin, 1971.
- Kliore, A. J., et al., "Mariner 9 S-Band Martian Occultation Experiment: Initial Results on the Atmosphere and Topography of Mars," *Science*, Vol. 175, No. 4019, pp. 313-317, Jan. 1972.
- Kliore, A. J., et al., "The Atmosphere of Mars From Mariner 9 Radio Occultation Measurements," *Icarus*, Vol. 17, No. 2, pp. 484-516, Oct. 1972.
- Kliore, A. J., et al., "S Band Radio Occultation Measurements of the Atmosphere and Topography of Mars with Mariner 9: Extended Mission Coverage of Polar and Intermediate Latitudes," *J. Geophys. Res.*, Vol. 78, No. 20, pp. 4331-4351, July 10, 1973.

- Labrum, R. G., et al., *The Surveyor V, VI, and VII Flight Paths and Their Determination from Tracking Data*, Technical Report 32-1302, Jet Propulsion Laboratory, Pasadena, Calif., Dec. 1, 1968.
- Laeser, R. P., et al., *Tracking and Data System Support for the Mariner Mars 1971 Mission: Prelaunch Phase Through First Trajectory Correction Maneuver*, Technical Memorandum 33-523, Vol. I, Jet Propulsion Laboratory, Pasadena, Calif., Mar. 15, 1972.
- Layland, J. W., "On Optimal Signals for Phase-Locked Loops," *IEEE Trans. Commun. Technol.*, Vol. COM-17, No. 5, pp. 526-531, Oct. 1969.
- Layland, J. W., and Lushbaugh, W. A., "A Flexible High-Speed Sequential Decoder for Deep Space Channels," *IEEE Trans. Commun. Technol.*, Vol. COM-19 No. 5, pp. 813-820, Oct. 1971.
- Layland, J. W., "Buffer Management for Sequential Decoding," *IEEE Trans. Commun.*, Vol. COM-22, No. 10, pp. 1685-1690, Oct. 1974.
- Leavitt, R. K., *The Least-Squares Process of MEDIA for Computing DRVID Calibration Polynomials*, Technical Memorandum 33-542, Jet Propulsion Laboratory, Pasadena, Calif., May 15, 1972.
- Lesh, J. R., *Signal-to-Noise Ratios in Coherent Soft Limiters*, Technical Report 32-1589, Jet Propulsion Laboratory, Pasadena, Calif., Sept. 15, 1973.
- Lesh, J. R., "Signal-to-Noise Ratios in Coherent Soft Limiters," *IEEE Trans. Commun.*, Vol. COM-22, No. 6, pp. 803-811, June 1974.
- Levitt, B. K., "Optimum Frame Synchronization for Biorthogonally Coded Data," *IEEE Trans. Commun.*, Vol. COM-22, No. 8, pp. 1130-1134, Aug. 1974.
- Levy, G. S., Otschi, T. Y., and Seidel, B. L., *Ground Instrumentation for Mariner IV Occultation Experiment*, Technical Report 32-984, Jet Propulsion Laboratory, Pasadena, Calif., Sept. 15, 1966.
- Levy, G. S., et al., *Lunar Range Radiation Patterns of a 210-Foot Antenna at S-Band*, Technical Report 32-1079, Jet Propulsion Laboratory, Pasadena, Calif., reprinted from *IEEE Trans. Antennas Propagation*, Vol. AP-15, No. 2, pp. 311-313, Mar. 1967.
- Levy, G. S., et al., *The Ultra Cone: An Ultra-Low-Noise Space Communication Ground Radio-Frequency System*, Technical Report 32-1340, Jet Propulsion Laboratory, Pasadena, Calif., reprinted from *IEEE Trans. Microwave Theor. Tech.*, Vol. MTT-16, No. 9, pp. 596-602, Sept. 1968.
- Levy, G. S., et al., "Pioneer 6: Measurement of Transient Faraday Rotation Phenomena Observed During Solar Occultation," *Science*, Vol. 166, No. 3905, pp. 596-598, Oct. 1969.
- Lieske, J. H., and Null, G. W., "Icarus and the Determination of Astronomical Constants," *Astron. J.*, Vol. 74, No. 2, Mar. 1969.
- Lieske, J. H., et al., "Simultaneous Solution for the Masses of the Principal Planets from Analysis of Optical Radar and Radio Tracking Data," *Celest. Mech.*, Vol. 4, No. 2, pp. 233-245, Oct. 1971.
- Lindsey, W. C., *Optimum and Suboptimum Frequency Demodulation*, Technical Report 32-637, Jet Propulsion Laboratory, Pasadena, Calif., June 15, 1964.
- Lindsey, W. C., *Improvements to be Realized Through the Use of Block-Coded Communication Systems*, Technical Report 32-947, Jet Propulsion Laboratory,

- Pasadena, Calif., reprinted from *IEEE Trans. Aerosp. Electron. Syst.*, Vol. AES-2, No. 3, pp. 364-366, May 1966.
- Lindsey, W. C., *Phase-Shift-Keyed Signal Detection with Noisy Reference Signals*, Technical Report 32-968, Jet Propulsion Laboratory, Pasadena, Calif., reprinted from *IEEE Trans. Aerosp. Electron. Syst.*, Vol. AES-2, No. 4, pp. 393-401, July 1966.
- Lindsey, W. C., *A Theory for the Design of One-Way and Two-Way Phase-Coherent Communication Systems: Phase-Coherent Tracking Systems*, Technical Report 32-986, Jet Propulsion Laboratory, Pasadena, Calif., July 15, 1969.
- Lindsey, W. C., *Optimal Design of One-Way and Two-Way Coherent Communication Links*, Technical Report 32-988, Jet Propulsion Laboratory, Pasadena, Calif., reprinted from *IEEE Trans. Commun. Technol.*, Vol. COM-14, No. 4, pp. 418-431, Aug. 1966.
- Lindsey, W. C., and Charles, F. J., *A Model Distribution for the Phase Error in Second-Order Phase-Locked Loops*, Technical Report 32-1017, Jet Propulsion Laboratory, Pasadena, Calif., reprinted from *IEEE Trans. Commun. Technol.*, Vol. COM-14, No. 10, pp. 662-664, Oct. 1966.
- Lindsey, W. C., *Performance of Phase-Coherent Receivers Preceded by Bandpass Limiters*, Technical Report 32-1162, Jet Propulsion Laboratory, Pasadena, Calif., Sept. 15, 1967.
- Lindsey, W. C., "Block Coding for Space Communications," *IEEE Trans. Commun. Technol.*, Vol. COM-17, No. 2, pp. 217-225, Apr. 1969.
- Lindsey, W. C., *Block-Coded Communications*, Technical Report 32-1380, Jet Propulsion Laboratory, Pasadena, Calif., Aug. 15, 1969.
- Lindsey, W. C., *Nonlinear Analysis of Generalized Tracking Systems*, Technical Report 32-1453, Jet Propulsion Laboratory, Pasadena, Calif., reprinted from *Proc. IEEE*, Vol. 57, No. 10, pp. 1705-1722, Oct. 1969.
- Lindsey, W. C., and Simon, M. K., "The Effect of Loop Stress on the Performance of Phase-Coherent Communication Systems", *IEEE Trans. Commun. Technol.*, Vol. COM-18, No. 5, pp. 569-588, Oct. 1970.
- Lindsey, W. C., and Simon, M. K., "Carrier Synchronization and Detection of Polyphase Signals," *IEEE Trans. Commun.*, Vol. COM-20, No. 3, pp. 441-454, June 1972.
- Lindsey, W. C., and Simon, M. K., "L-Orthogonal Signal Transmission and Detection," *IEEE Trans. Commun.*, Vol. COM-20, No. 5, pp. 953-960, Oct. 1972.
- Lindsey, W. C., and Simon, M. K., "On the Detection of Differentially Encoded Polyphase Signals," *IEEE Trans. Commun.*, Vol. COM-20, No. 6, pp. 1121-1128, Dec. 1972.
- Lindsey, W. C., *Synchronization Systems in Communication and Control*, Prentice-Hall, Inc., Englewood Cliffs, N. J., 1972.
- Lindsey, W. C., and Tausworthe, R. C., *A Bibliography of the Theory and Application of the Phase-Lock Principle*, Technical Report 32-1581, Jet Propulsion Laboratory, Pasadena, Calif., Apr. 1, 1973.

- Lindsey, W. C., and Simon, M. K., *Telecommunication Systems Engineering*, Prentice-Hall, Inc., Englewood Cliffs, N. J., 1973.
- Lorell, J., Anderson, J. D., and Sjogren, W. L., *Characteristics and Format of the Tracking Data to Be Obtained by the NASA Deep Space Instrumentation Facility for Lunar Orbiter*, Technical Memorandum 33-230, Jet Propulsion Laboratory, Pasadena, Calif., June 15, 1965.
- Lorell, J., Sjogren, W. L., and Boggs, D., *Compressed Tracking Data Used for First Iteration in Selenodesy Experiment, Lunar Orbiters I and II*, Technical Memorandum 33-343, Jet Propulsion Laboratory, Pasadena, Calif., May 1, 1967.
- Lorell, J., and Sjogren, W. L., *Lunar Orbiter Data Analysis*, Technical Report 32-1220, Jet Propulsion Laboratory, Pasadena, Calif., Nov. 15, 1967.
- Lorell, J., *Lunar Orbiter Gravity Analysis*, Technical Report 32-1387, Jet Propulsion Laboratory, Pasadena, Calif., June 15, 1969.
- Lorell, J., et al., "Icarus: Celestial Mechanics Experiment for Mariner," *Int. J. Sol. Sys.*, Vol. 12, Jan. 1970.
- Lorell, J., and Laing, P. A., *Compilation of Lunar Orbiter Tracking Data Used for Long-Term Selenodesy*, Technical Memorandum 33-419, Jet Propulsion Laboratory, Pasadena, Calif., Feb. 1, 1970.
- Lorell, J., "Estimation of Gravity Field Harmonics in the Presence of Spin-Axis Direction Error Using Radio Tracking Data," *J. Astronaut. Sci.*, Vol. XX, No. 1, pp. 44-54, Aug. 1972.
- Ludwig, A. C., et al., *Gain Calibration of a Horn Antenna Using Pattern Integration*, Technical Report 32-1572, Jet Propulsion Laboratory, Pasadena, Calif., Oct. 1, 1972.
- Madrid, G. A., et al., *Tracking System Analytic Calibration Activities for the Mariner Mars 1971 Mission*, Technical Report 32-1587, Jet Propulsion Laboratory, Pasadena, Calif., Mar. 1, 1974.
- Martin, D. P., *A Combined Radar-Radiometer With Variable Polarization*, Technical Memorandum 33-570, Jet Propulsion Laboratory, Pasadena, Calif., Oct. 15, 1972.
- Mathison, R. P., *Tracking Techniques for Interplanetary Spacecraft*, Technical Report 32-284, Jet Propulsion Laboratory, Pasadena, Calif., Aug. 1, 1962.
- McEliece, R. J., *Optimal Communications Nets*, Technical Report 32-697, Jet Propulsion Laboratory, Pasadena, Calif., Apr. 15, 1965.
- McNeal, C. E., *Ranger V Tracking Systems Data Analysis Final Report*, Technical Report 32-702, Jet Propulsion Laboratory, Pasadena, Calif., Apr. 15, 1965.
- Melbourne, W. G., et al., *Constants and Related Information for Astrodynamical Calculations*, Technical Report 32-1306, Jet Propulsion Laboratory, Pasadena, Calif., July 15, 1968.
- Melbourne, W. G., "Planetary Ephemerides," *Astronaut. Aeronaut.*, Vol. 7, No. 5, pp. 38-43, May 1970.
- Melbourne, W. G., "Navigation between the Planets," *Sci. Amer.*, Vol. 234, No. 6, pp. 58-74, June 1976.

- Merrick, W. D., et al., *Deep Space Communications*, Technical Release 34-10, Jet Propulsion Laboratory, Pasadena, Calif., Jan. 29, 1960; also available in *IRE Trans. Mil. Electron.*, Vol. MIL-4, No. 2-3, pp. 158-163, April-June 1960.
- Miller, L., et al., *The Atlas-Centaur VI Flight Path and Its Determination from Tracking Data*, Technical Report 32-911, Jet Propulsion Laboratory, Pasadena, Calif., Apr. 15, 1966.
- Miller, R. B., *Tracking and Data System Support for the Pioneer Project: Pioneers 6-9. Extended Missions: July 1, 1972-July 1, 1973*, Technical Memorandum 33-426, Vol. XII, Jet Propulsion Laboratory, Pasadena, Calif., March 1, 1974.
- Miller, R. B., *Tracking and Data System Support for the Pioneer Project: Pioneer 10-From April 1, 1972, Through the Jupiter Encounter Period, January 1974*, Technical Memorandum 33-584, Vol. III, Jet Propulsion Laboratory, Pasadena, Calif., June 15, 1975.
- Miller, R. B., et al., *Tracking and Data System Support for the Pioneer Project: Pioneer 10-From January 1974 to January 1975; Pioneer 11-From May 1, 1973 Through Jupiter Encounter Period, January 1975*, Technical Memorandum 33-584, Vol. IV, Jet Propulsion Laboratory, Pasadena, Calif., Dec. 1, 1975.
- Moyer, T. D., *Mathematical Formulation of the Double-Precision Orbit Determination Program (DPODP)*, Technical Report 32-1527, Jet Propulsion Laboratory, Pasadena, Calif., May 17, 1971.
- Muhleman, D. O., *Relationship Between the System of Astronomical Constants and the Radar Determinations of the Astronomical Unit*, Technical Report 32-477, Jet Propulsion Laboratory, Pasadena, Calif., Jan. 15, 1964.
- Muhleman, D. O., Goldstein, R., and Carpenter, R., *A Review of Radar Astronomy-Parts I, II*, Technical Report 32-824, Jet Propulsion Laboratory, Pasadena, Calif., Jan. 30, 1966, reprinted from *IEEE Spectrum*, Oct. and Nov. 1965.
- Muhleman, D. O., et al., *JPL Radar Range and Doppler Observations of Venus, 1961-1966*, Technical Report 32-1123, Jet Propulsion Laboratory, Pasadena, Calif., July 1, 1968.
- Muhleman, D. O., et al., "Radio Propagation Measurements of the Solar Corona and Gravitational Field: Applications to Mariner 6 and 7," in *Proceedings of the Conference on Experimental Tests of Gravitational Theories*, California Institute of Technology, Pasadena, Calif., Nov. 1970.
- Mulhall, B. D., et al., *Tracking System Analytic Calibration Activities for the Mariner Mars 1969 Mission*, Technical Report 32-1499, Jet Propulsion Laboratory, Pasadena, Calif., Nov. 15, 1970.
- Mulholland, J. D., and Sjogren, W. L., *Lunar Orbiter Ranging Data*, Technical Report 32-1087, Jet Propulsion Laboratory, Pasadena, Calif., reprinted from *Science*, Vol. 155, No. 3758, pp. 74-76, Jan. 6, 1967.
- Mulholland, J. D., *Proceedings of the Symposium on Observation, Analysis and Space Research Applications of the Lunar Motion*, Technical Report 32-1386, Jet Propulsion Laboratory, Pasadena, Calif., Apr. 1969.
- Muller, P. M., and Sjogren, W. L., *Consistency of Lunar Orbiter Residuals With Trajectory and Local Gravity Effects*, Technical Report 32-1307, Jet Propulsion Laboratory, Pasadena, Calif., Sept. 1, 1968.

- Muller, P. M., and Sjogren, W. L., *Mascons: Lunar Mass Concentrations*, Technical Report 32-1339, Jet Propulsion Laboratory, Pasadena, Calif., reprinted from *Science*, Vol. 161, No. 3842, pp. 680-684, Aug. 16, 1968.
- Muller, P. M., Sjogren, W. L., and Wollenhaupt, W. R., "Lunar Gravity: Apollo 15 Doppler Radio Tracking," *The Moon*, Vol. 10, No. 2, pp. 195-205, June 1974.
- The NASA/JPL 64-Meter-Diameter Antenna at Goldstone, California: Project Report*, Technical Memorandum 33-671, Jet Propulsion Laboratory, Pasadena, Calif., July 15, 1974.
- Newburn, R. L., Jr., et al., *Earth-Based Research on the Outer Planets During the Period 1970-1985*, Technical Report 32-1456, Jet Propulsion Laboratory, Pasadena, Calif., Mar. 15, 1970.
- Null, G. W., et al., *Mariner IV Flight Path and Its Determination From Tracking Data*, Technical Report 32-1108, Jet Propulsion Laboratory, Pasadena, Calif., Aug. 1, 1967.
- O'Neil, W. J., et al., *The Surveyor III and Surveyor IV Flight Paths and Their Determination From Tracking Data*, Technical Report 32-1292, Jet Propulsion Laboratory, Pasadena, Calif., Aug. 15, 1968.
- O'Neil, W. J., et al., *Mariner 9 Navigation*, Technical Report 32-1586, Jet Propulsion Laboratory, Pasadena, Calif., Nov. 13, 1973.
- Otoshi, T. Y., *The Effect of Mismatched Components on Microwave Noise-Temperature Calibrations*, Technical Report 32-1345, Jet Propulsion Laboratory, Pasadena, Calif., reprinted from *IEEE Trans. Microwave Theor. Tech.*, Vol. MTT-16, No. 9, pp. 675-686, Sept. 1968.
- Otoshi, T. Y., Stelzried, C. T., and Yates, B. C., "Comparisons of Waveguide Losses Calibrated by the DC Potentiometer, AC Ratio Transformer, and Reflectometer Techniques," *IEEE Trans. Microwave Theor. Tech.*, Vol. MTT-18, No. 7, pp. 406-409, July 1970.
- Otoshi, T. Y., and Stelzried, C. T., "A Precision Compact Rotary Vane Attenuator," *IEEE Trans. Micro. Theor. Technique*, Vol. MTT-19, No. 11, pp. 843-854, Nov. 1971.
- Otoshi, T. Y., "Precision Reflectivity Loss Measurements of Perforated-Plate Mesh Materials by a Waveguide Technique," *IEEE Trans. Instr. Meas.*, Vol. IM-21, No. 4, pp. 451-457, Nov. 1972.
- Pease, G. E., et al., *The Mariner V Flight Path and Its Determination From Tracking Data*, Technical Report 32-1363, Jet Propulsion Laboratory, Pasadena, Calif., July 1, 1969.
- Posner, E. C., *Properties of Error-Correcting Codes at Low Signal-to-Noise Ratios*, Technical Report 32-602, Jet Propulsion Laboratory, Pasadena, Calif., June 15, 1964.
- Potter, P. D., *The Design of a Very High Power, Very Low Noise Cassegrain Feed System for a Planetary Radar*, Technical Report 32-653, Jet Propulsion Laboratory, Pasadena, Calif., Aug. 24, 1964.
- Potter, P. D., Merrick, W. D., and Ludwig, A. C., *Large Antenna Apertures and Arrays for Deep Space Communications*, Technical Report 32-848, Jet Propulsion Laboratory, Pasadena, Calif., Nov. 1, 1965.

- Potter, P. D., *A Computer Program for Machine Design of Cassegrain Feed Systems*, Technical Report 32-1202, Jet Propulsion Laboratory, Pasadena, Calif., Dec. 15, 1967.
- Potter, P. D., et al., *A Study of Weather-Dependent Data Links for Deep Space Applications*, Technical Report 32-1392, Jet Propulsion Laboratory, Pasadena, Calif., Oct. 15, 1969.
- Preston, R. A., "Dual-Spacecraft Radio Metric Tracking," *The Deep Space Network: May and June 1974*, DSN Progress Report, pp. 51-65. Jet Propulsion Laboratory, Pasadena, Calif., Aug. 15, 1974.
- Rechtin, E., "Communication Techniques for Space Exploration," *IRE Trans. Space Electron. Telem.*, Vol. SET-5, No. 3, pp. 95-98, Sept. 1959.
- Rechtin, E., Stevens, R., and Victor, W. K., *Data Transmission and Communications*, Technical Release 34-55, Jet Propulsion Laboratory, Pasadena, Calif., Apr. 30, 1960.
- Rechtin, E., *Space Communications*, Technical Release 34-68, Jet Propulsion Laboratory, Pasadena, Calif., May 1, 1960.
- Rechtin, E., et al., *JPL Range and Doppler System*, Technical Memorandum 33-13, Jet Propulsion Laboratory, Pasadena, Calif., Sept. 22, 1961.
- Rechtin, E., Rule, B., and Stevens, R., *Large Ground Antennas*, Technical Report 32-213, Jet Propulsion Laboratory, Pasadena, Calif., Mar. 20, 1962.
- Rechtin, E., *Lunar Communications*, Technical Memorandum 33-133, Jet Propulsion Laboratory, Pasadena, Calif., June 28, 1963.
- Rechtin, E., "Surprises on Venus," *Int. Sci. Technol.*, No. 20, pp. 13-14, Aug. 1963.
- Rechtin, E., "Long Range Planning for the Deep Space Network," *Astronaut. Aeronaut.*, Vol. 6, No. 1, pp. 28-35, Jan. 1968.
- Reid, M. S., et al., "Low-Noise Microwave Receiving Systems in a Worldwide Network of Large Antennas," *Proc. IEEE*, Vol. 61, No. 9, pp. 1330-1335, Sept. 1973.
- Renzetti, N. A., et al., "Radio Tracking Techniques and Performance of the U.S. Deep Space Instrumentation Facility," *Space Research II, Proceedings of the Second International Space Science Symposium*, Florence, Italy, April 1961, North Holland Publishing Company, Amsterdam.
- Renzetti, N. A., and Ostermier, B. J., *Communications with Lunar Probes*, Technical Report 32-148, Jet Propulsion Laboratory, Pasadena, Calif., Aug. 23, 1961.
- Renzetti, N. A., "DSIF in the Ranger Project," *Astronautics*, Vol. 6, No. 1, pp. 34-37, 70, Sept. 1961.
- Renzetti, N. A., *Tracking and Data Acquisition for Ranger Missions I-V*, Technical Memorandum 33-174, Jet Propulsion Laboratory, Pasadena, Calif., July 1, 1964.
- Renzetti, N. A., *Tracking and Data Acquisition for Ranger Missions VI-IX*, Technical Memorandum 33-275, Jet Propulsion Laboratory, Pasadena, Calif., Sept. 15, 1966.

- Renzetti, N. A., *Tracking and Data Acquisition Support for the Mariner Venus 1962 Mission*, Technical Memorandum 33-212, Jet Propulsion Laboratory, Pasadena, Calif., July 1, 1965.
- Renzetti, N. A., *Tracking and Data Acquisition Report, Mariner Mars 1964 Mission: Near-Earth Trajectory Phase*, Technical Memorandum 33-239, Vol. I, Jet Propulsion Laboratory, Pasadena, Calif., Jan. 1, 1965.
- Renzetti, N. A., *Tracking and Data Acquisition Report, Mariner Mars 1964 Mission: Cruise to Post-Encounter Phase*, Technical Memorandum 33-239, Vol. II, Jet Propulsion Laboratory, Pasadena, Calif., Oct. 1, 1967.
- Renzetti, N. A., *Deep Space Network Support, Atlas/Centaur Missions 1-9*, Technical Memorandum 33-347, Jet Propulsion Laboratory, Pasadena, Calif., Sept. 15, 1967.
- Renzetti, N. A., "Tracking and Data Acquisition System for Mariner Missions," *Proceedings of the Seventh International Symposium on Space Technology and Science*, Tokyo, 1967.
- Renzetti, N. A., *Tracking and Data Acquisition Report, Mariner Mars 1964 Mission: Extended Mission*, Technical Memorandum 33-239, Vol. III, Jet Propulsion Laboratory, Pasadena, Calif., Dec. 1, 1968.
- Renzetti, N. A., and Fearey, J. P., "The Deep Space Network: An Instrument for the Radio Navigation for the Mariner Mission to Mars 1969," IInd International Conference on Space Engineering, Venice, Italy, D. Reidel Publishing Co., Dordrecht, Holland, May 1969.
- Renzetti, N. A., *Tracking and Data System Support for Surveyor: Missions I and II*, Technical Memorandum 33-301, Vol. I, Jet Propulsion Laboratory, Pasadena, Calif., July 15, 1969.
- Renzetti, N. A., *Tracking and Data System Support for Surveyor: Missions III and IV*, Technical Memorandum 33-301, Vol. II, Jet Propulsion Laboratory, Pasadena, Calif., Sept. 1, 1969.
- Renzetti, N. A., *Tracking and Data System Support for Surveyor: Mission V*, Technical Memorandum 33-301, Vol. III, Jet Propulsion Laboratory, Pasadena, Calif., Dec. 1, 1969.
- Renzetti, N. A., *Tracking and Data System Support for Surveyor: Mission VI*, Technical Memorandum 33-301, Vol. IV, Jet Propulsion Laboratory, Pasadena, Calif., Dec. 1, 1969.
- Renzetti, N. A., *Tracking and Data System Support for Surveyor: Mission VII*, Technical Memorandum 33-301, Vol. V, Jet Propulsion Laboratory, Pasadena, Calif., Dec. 1, 1969.
- Renzetti, N. A., *Tracking and Data System Support for the Mariner Venus 67 Mission: Planning Phase Through Midcourse Maneuver*, Technical Memorandum 33-385, Vol. I, Jet Propulsion Laboratory, Pasadena, Calif., Sept. 1, 1969.
- Renzetti, N. A., *Tracking and Data System Support for the Mariner Venus 67 Mission. Midcourse Maneuver Through End of Mission*, Technical Memorandum 33-385, Vol. II, Jet Propulsion Laboratory, Pasadena, Calif., Sept. 1, 1969.
- Renzetti, N. A., *Tracking and Data System Support for the Pioneer Project: Pioneer VI. Prelaunch to End of Nominal Mission*, Technical Memorandum 33-426, Vol. I, Jet Propulsion Laboratory, Pasadena, Calif., Feb. 1, 1970.

- Renzetti, N. A., *Tracking and Data System Support for the Pioneer Project: Pioneer VII. Prelaunch to End of Nominal Mission*, Technical Memorandum 33-426, Vol. II, Jet Propulsion Laboratory, Pasadena, Calif., Apr. 15, 1970.
- Renzetti, N. A., *Tracking and Data System Support for the Pioneer Project: Pioneer VIII. Prelaunch Through May 1968*, Technical Memorandum 33-426, Vol. III, Jet Propulsion Laboratory, Pasadena, Calif., July 15, 1970.
- Renzetti, N. A., *Tracking and Data System Support for the Pioneer Project: Pioneer IX. Prelaunch Through June 1969*, Technical Memorandum 33-426, Vol. IV, Jet Propulsion Laboratory, Pasadena, Calif., Nov. 15, 1970.
- Renzetti, N. A., *Tracking and Data System Support for the Pioneer Project: Pioneer VI. Extended Mission: July 1, 1966-July 1, 1969*, Technical Memorandum 33-426, Vol. V, Jet Propulsion Laboratory, Pasadena, Calif., Feb. 1, 1971.
- Renzetti, N. A., *Tracking and Data System Support for the Pioneer Project: Pioneer VII. Extended Mission: February 24, 1967-July 1, 1968*, Technical Memorandum 33-426, Vol. VI, Jet Propulsion Laboratory, Pasadena, Calif., Apr. 15, 1971.
- Renzetti, N. A., *Tracking and Data System Support for the Pioneer Project: Pioneer VII. Extended Mission: July 1, 1968-July 1, 1969*, Technical Memorandum 33-426, Vol. VII, Jet Propulsion Laboratory, Pasadena, Calif., Apr. 15, 1971.
- Renzetti, N. A., *Tracking and Data System Support for the Pioneer Project: Pioneer VIII. Extended Mission: June 1, 1968-July 1, 1969*, Technical Memorandum 33-426, Vol. VIII, Jet Propulsion Laboratory, Pasadena, Calif., May 1, 1971.
- Renzetti, N. A., *Tracking and Data System Support for the Pioneer Project: Pioneers VI-IX. Extended Missions: July 1, 1969-July 1, 1970*, Technical Memorandum 33-426, Vol. IX, Jet Propulsion Laboratory, Pasadena, Calif., Aug. 15, 1971.
- Renzetti, N. A., and Siegmeth, A. J., *Tracking and Data System Support for the Pioneer Project: Pioneers 6-9. Extended Missions: July 1, 1971-July 1, 1972*, Technical Memorandum 33-426, Vol. XI, Jet Propulsion Laboratory, Pasadena, Calif., May 1, 1973.
- Renzetti, N. A., et al., *Tracking and Data System Support for the Mariner Mars 1969 Mission: Planning Phase Through Midcourse Maneuver*, Technical Memorandum 33-474, Vol. I, Jet Propulsion Laboratory, Pasadena, Calif., May 15, 1971.
- Renzetti, N. A., et al., *Tracking and Data System Support for the Mariner Mars 1969 Mission: Midcourse Maneuver Through End of Nominal Mission*, Technical Memorandum 33-474, Vol. II, Jet Propulsion Laboratory, Pasadena, Calif., Sept. 1, 1971.
- Renzetti, N. A., Linnes, K. W., and Taylor, T. M., *Tracking and Data System Support for the Mariner Mars 1969 Mission: Extended Operations Mission*, Technical Memorandum 33-474, Vol. III, Jet Propulsion Laboratory, Pasadena, Calif., Sept. 15, 1971.
- Renzetti, N. A., *A History of the Deep Space Network: From Inception to January 1, 1969*, Technical Report 32-1533, Vol. I, Jet Propulsion Laboratory, Pasadena, Calif., Sept. 1, 1971.

- Renzetti, N. A., "Radio Communications at Planetary Distances," paper presented at the International Convention on Radio Communication, Rome and Bologna, Italy, Mar. 1974.
- Richter, H. L., Rechlin, E., and Walter, W. K., *National Ground-Based Surveillance Complex (U)*, Publication 146, Jet Propulsion Laboratory, Pasadena, Calif., Feb. 16, 1959 (Confidential).
- Rocci, S. A., "The 210-ft Parabolic Fully Steerable Tracking Antennas for a Deep Space Instrumentation Facility," in *Deep Space and Missile Tracking Antennas*, pp. 50-70, ASME, New York, 1966.
- Rusch, W. V. T., *Phase Error and Associated Cross-Polarization Effects in Cassegrainian-Fed Microwave Antennas*, Technical Report 32-610, Jet Propulsion Laboratory, Pasadena, Calif., May 30, 1965.
- Rusch, W. V. T., and Stelzried, C. T., *Observations of the Lunar Eclipse of December 19, 1964, at a Wavelength of 3.3 MM*, Technical Report 32-1097, Jet Propulsion Laboratory, Pasadena, Calif., reprinted from *Astrophys. J.*, Vol. 148, No. 1, pp. 255-259, Apr. 1967.
- Rusch, W. V. T., *Applications of Two-Dimensional Integral-Equation Theory to Reflector-Antenna Analysis*, Technical Memorandum 33-478, Jet Propulsion Laboratory, Pasadena, Calif., May 1, 1971.
- Rusch, W. V. T., "Double Aperture Blocking by Two Wavelength-Sized Feed-Support Struts," *Electron. Lett.*, Vol. 10, No. 15, pp. 296-297, July 25, 1974.
- Sanger, D. K., *Digital Demodulation with Data Subcarrier Tracking*, Technical Report 32-1314, Jet Propulsion Laboratory, Pasadena, Calif., Aug. 1, 1968.
- Siegmeth, A. J., Purdue, R. E., and Ryan, R. E., *Tracking and Data System Support for the Pioneer Project: Pioneers 6-9. Extended Missions: July 1, 1970-July 1, 1971*, Technical Memorandum 33-426, Vol. X, Jet Propulsion Laboratory, Pasadena, Calif., Aug. 15, 1972.
- Siegmeth, A. J., et al., *Tracking and Data System Support for the Pioneer Project: Pioneer 10—Prelaunch Planning Through Second Trajectory Correction December 4, 1969 to April 1, 1972*, Technical Memorandum 33-584, Vol. I, Jet Propulsion Laboratory, Pasadena, Calif., Apr. 1, 1973.
- Simon, M. K., "Nonlinear Analysis of an Absolute Value Type of an Early-Late Gate Bit Synchronizer," *IEEE Trans. Commun. Technol.*, Vol. COM-18, No. 5, pp. 589-596, Oct. 1970.
- Simon, M. K., "Optimization of the Performance of a Digital-Data-Transition Tracking Loop," *IEEE Trans. Commun. Technol.*, Vol. COM-18, No. 5, pp. 686-689, Oct. 1970.
- Simon, M. K., and Lindsey, W. C., "Data-Aided Carrier Tracking Loops," *IEEE Trans. Commun. Technol.*, Vol. COM-19, No. 2, pp. 157-168, Apr. 1971.
- Simon, M. K., "On the Selection of an Optimum Design Point for Phase-Coherent Receivers Employing Bandpass Limiters," *IEEE Trans. Commun.*, Vol. COM-20, No. 2, pp. 210-214, Apr. 1972.
- Simon, M. K., "On the Selection of a Sampling Filter Bandwidth for a Digital Data Detector," *IEEE Trans. Commun.*, Vol. COM-20, No. 3, pp. 438-441, June 1972.

- Simon, M. K., and Springett, J. C., "The Performance of a Noncoherent FSK Receiver Preceded by a Bandpass Limiter," *IEEE Trans. Commun.*, Vol. COM-20, No. 6, pp. 1128-1136, Dec. 1972.
- Simon, M. K., and Springett, J. C., *The Theory, Design, and Operation of the Suppressed Carrier Data-Aided Tracking Receiver*, Technical Report 32-1583, Jet Propulsion Laboratory, Pasadena, Calif., June 15, 1973.
- Simon, M. K., and Smith, J. G., "Hexagonal Multiple Phase-and-Amplitude-Shift-Keyed Signal Sets," *IEEE Trans. Commun.*, Vol. COM-21, No. 10, pp. 1108-1115, Oct. 1973.
- Simon, M. K., and Smith, J. G., "Carrier Synchronization and Detection of QASK Signal Sets," *IEEE Trans. Commun.*, Vol. COM-22, No. 2, pp. 98-106, Feb. 1974.
- Simon, M. K., *Data-Derived Symbol Synchronization of MASK and QASK Signals*, Technical Memorandum 33-720, Jet Propulsion Laboratory, Pasadena, Calif., Dec. 15, 1974.
- Sjogren, W. L., et al., *The Ranger V Flight Path and Its Determination From Tracking Data*, Technical Report 32-562, Jet Propulsion Laboratory, Pasadena, Calif., Dec. 6, 1963.
- Sjogren, W. L., et al., *The Ranger VI Flight Path and Its Determination From Tracking Data*, Technical Report 32-605, Jet Propulsion Laboratory, Pasadena, Calif., Dec. 15, 1964.
- Sjogren, W. L., *The Ranger III Flight Path and Its Determination From Tracking Data*, Technical Report 32-563, Jet Propulsion Laboratory, Pasadena, Calif., Sept. 15, 1965.
- Sjogren, W. L., et al., *Physical Constants as Determined From Radio Tracking of the Ranger Lunar Probes*, Technical Report 32-1057, Jet Propulsion Laboratory, Pasadena, Calif., Dec. 30, 1966.
- Sjogren, W. L., *Proceedings of the JPL Seminar on Uncertainties in the Lunar Ephemeris*, Technical Report 32-1247, Jet Propulsion Laboratory, Pasadena, Calif., May 1, 1968.
- Sjogren, W. L., "Lunar Gravity Estimate: Independent Confirmation," *J. Geophys. Res.*, Vol. 76, No. 29, Oct. 10, 1971.
- Sjogren, W. L., et al., "Lunar Gravity via Apollo 14 Doppler Radio Tracking," *Science*, Vol. 175, No. 4018, pp. 165-168, Jan. 14, 1972.
- Slobin, S. D., "Beam Switching Cassegrain Feed System and Its Applications to Microwave and Millimeterwave Radioastronomical Observations," *Rev. Sci. Instr.*, Vol. 41, No. 3, pp. 439-443, Mar. 1970.
- Spier, G. W., *Design and Implementation of Models for the Double Precision Trajectory Program (DPTRAJ)*, Technical Memorandum 33-451, Jet Propulsion Laboratory, Pasadena, Calif., Apr. 15, 1971.
- Springett, J. C., *Telemetry and Command Techniques for Planetary Spacecraft*, Technical Report 32-495, Jet Propulsion Laboratory, Pasadena, Calif., Jan. 15, 1965.
- Springett, J. C., and Simon, M. K., "An Analysis of the Phase Coherent-Incoherent Output of the Bandpass Limiter," *IEEE Trans. Commun. Technol.*, Vol. COM-19, No. 1, pp. 42-49, Feb. 1971.

- Stelzried, C. T., *Post-Amplifier Noise Temperature Contribution in a Low-Noise Receiving System*, Technical Report 32-446, Jet Propulsion Laboratory, Pasadena, Calif., Jan. 1964.
- Stelzried, C. T., Reid, M. S., and Petty, S. M., *A Precision DC-Potentiometer Microwave Insertion-Loss Test Set*, Technical Report 32-887, Jet Propulsion Laboratory, Pasadena, Calif., Mar. 15, 1966.
- Stelzried, C. T., Reid, M. S., and Nixon, D., *Precision Power Measurements of Spacecraft CW Signal With Microwave Noise Standards*, Technical Report 32-1066, Jet Propulsion Laboratory, Pasadena, Calif., Feb. 15, 1968.
- Stelzried, C. T., and Reid, M. S., *Precision Power Measurements of Spacecraft CW Signal Level With Microwave Noise Standards*, Technical Report 32-1070, Jet Propulsion Laboratory, Pasadena, Calif., reprinted from *IEEE Trans. Instrum. Measurement*, Vol. IM-15, No. 4, pp. 318-324, Dec. 1966.
- Stelzried, C. T., and Rusch, W. V. T., *Improved Determination of Atmospheric Opacity From Radio Astronomy Measurements*, Technical Report 32-1115, Jet Propulsion Laboratory, Pasadena, Calif., reprinted from *J. Geophys. Res.*, Vol. 72, No. 9, pp. 2445-2447, May 1, 1967.
- Stelzried, C. T., and Otoshi, T. Y., "Radiometric Evaluation of Antenna-Feed Component Losses," *IEEE Trans. Instrum. Measurement*, Vol. IM-18, No. 3, pp. 172-183, Sept. 1969.
- Stelzried, C. T., "Precision Microwave Waveguide Loss Calibrations," *IEEE Trans. Instrum. Measurement*, Vol. IM-19, No. 1, pp. 23-25, Feb. 1970.
- Stelzried, C. T., *A Faraday Rotation Measurement of a 13-cm Signal in the Solar Corona*, Technical Report 32-1401, Jet Propulsion Laboratory, Pasadena, Calif., July 15, 1970.
- Stelzried, C. T., et al., "The Quasi-Stationary Coronal Magnetic Field and Electron Density as Determined From a Faraday Rotation Experiment," *Sol. Phys.*, Vol. 14, No. 2, pp. 440-456, Oct. 1970.
- Stelzried, C. T., "Operating Noise-Temperature Calibrations of Low-Noise Receiving Systems," *Microwave J.*, Vol. 14, No. 6, pp. 41-46, 48, June 1971.
- Stelzried, C. T., et al., "Transformation of Received Signal Polarization Angle to the Plane of the Ecliptic," *J. Space. Rock.*, Vol. 9, No. 2, pp. 69-70, Feb. 1972.
- Stevens, R., and Victor, W. K., *The Goldstone Station Communications and Tracking System for Project Echo*, Technical Report 32-59, Jet Propulsion Laboratory, Pasadena, Calif., Dec. 1, 1960.
- System Capabilities and Development Schedule of the Deep Space Instrumentation Facility 1963-1967*, Technical Memorandum 33-83, Jet Propulsion Laboratory, Pasadena, Calif., Mar. 2, 1962.
- Tardani, P. A., *Madrid Site Selection Report*, Technical Memorandum 33-149, Jet Propulsion Laboratory, Pasadena, Calif., July 17, 1963.
- Tausworthe, R. C., *A Precision Planetary Range-Tracking Radar*, Technical Report 32-779, Jet Propulsion Laboratory, Pasadena, Calif., reprinted from *IEEE Trans. Space Electron. Telem.*, Vol. SET-11, No. 2, pp. 78-85, June 1965.
- Tausworthe, R. C., *Theory and Practical Design of Phase-Locked Receivers*, Technical Report 32-819, Vol. I, Jet Propulsion Laboratory, Pasadena, Calif., Feb. 15, 1966.

- Tausworthe, R., *Cycle Slipping in Phase-Locked Loops*, Technical Report 32-1127, Jet Propulsion Laboratory, Pasadena, Calif., reprinted from *IEEE Trans. Commun. Technol.*, Vol. COM-15, No. 3, pp. 417-421, June 1967.
- Tausworthe, R. C., Easterling, M. F., and Spear, A. J., *A High-Rate Telemetry System for the Mariner Mars 1969 Mission*, Technical Report 32-1354, Jet Propulsion Laboratory, Pasadena, Calif., Apr. 1, 1969.
- Tausworthe, R. C., *DSS Subsystem Implementation by Time-Shared Computer*, Technical Memorandum 33-420, Jet Propulsion Laboratory, Pasadena, Calif., Oct. 1, 1969.
- Tausworthe, R. C., "Convergence of Oscillator Spectral Estimators for Counted-Frequency Measurements," *IEEE Trans. Commun.*, Vol. COM-20, No. 2, pp. 213-217, Apr. 1972.
- Tausworthe, R. C., "Simplified Formula for Mean-Slip Time of Phase-Locked Loops With Steady-State Phase Error," *IEEE Trans. Commun.*, Vol. COM-20, No. 3, pp. 331-337, June 1972.
- Tausworthe, R. C., and Crow, R. B., "Improvements in Deep-Space Tracking by Use of Third-Order Loops," *Proceedings of the 1972 International Telemetry Conference, Los Angeles, California, October 10-12, 1972*, pp. 577-583.
- Telecommunications Systems Design Techniques Handbook*, Technical Memorandum 33-571, edited by R. E. Edelson, Jet Propulsion Laboratory, Pasadena, Calif., July 15, 1972.
- Textor, G. P., Kelly, L. B., and Kelly, M., *Tracking and Data System Support for the Mariner Mars 1971 Mission: First Trajectory Correction Maneuver Through Orbit Insertion*, Technical Memorandum 33-523, Vol. II, Jet Propulsion Laboratory, Pasadena, Calif., June 15, 1972.
- Thornton, J. H., Jr., *The Surveyor I and Surveyor II Flight Paths and Their Determination From Tracking Data*, Technical Report 32-1285, Jet Propulsion Laboratory, Pasadena, Calif., Aug. 1, 1968.
- Timor, U., "Equivalence of Time-Multiplexed and Frequency-Multiplexed Signals in Digital Communications," *IEEE Trans. Commun.*, Vol. COM-20, No. 3, pp. 435-438, June 1972.
- Titsworth, R. C., and Welch, L. R., *Power Spectra of Signals Modulated by Random and Pseudorandom Sequences*, Technical Report 32-140, Jet Propulsion Laboratory, Pasadena, Calif., Oct. 10, 1961.
- Titsworth, R. C., *The Algebra of Periodic Sequences*, Technical Report 32-381, Jet Propulsion Laboratory, Pasadena, Calif., Jan. 7, 1963.
- Titsworth, R. C., *Correlation Properties of Cyclic Sequences*, Technical Report 32-388, Jet Propulsion Laboratory, Pasadena, Calif., July 1, 1963.
- Titsworth, R. C., *Optimal Ranging Codes*, Technical Report 32-411, Jet Propulsion Laboratory, Pasadena, Calif., Apr. 15, 1963.
- Titsworth, R. C., *Equivalence Classes of Periodic Sequences*, Technical Report 32-568, Jet Propulsion Laboratory, Pasadena, Calif., June 15, 1964, reprinted from *Ill. J. Math.*, Vol. 8, No. 2, June 1964.
- Titsworth, R. C., *The Role of Pseudorandom Codes in Communications*, Technical Memorandum 33-185, Jet Propulsion Laboratory, Pasadena, Calif., Aug. 3, 1964.

- "Tracking and Data Acquisition System for Mariner Missions," *Proceedings of the Seventh International Symposium on Space Technology and Science*, Tokyo, May 1967.
- Vegos, C. J., et al., *The Ranger IX Flight Path and Its Determination From Tracking Data*, Technical Report 32-767, Jet Propulsion Laboratory, Pasadena, Calif., Nov. 1, 1968.
- Victor, W. K., *Precision Frequency Control—A Communications Requirement of the Space Age*, External Publication 627, Jet Propulsion Laboratory, May 13, 1959.
- Victor, W. K., and Stevens, R., "The Role of the Jet Propulsion Laboratory in Project Echo," *IRE Trans.*, Vol. SET-7, pp. 20-29, Mar. 1961.
- Victor, W. K., Stevens, R., and Golomb, S. W., *Radar Exploration of Venus: Goldstone Observatory Report for March-May 1961*, Technical Report 32-132, Jet Propulsion Laboratory, Pasadena, Calif., Aug. 1, 1961.
- Victor, W. K., Titsworth, R. C., and Rechlin, E., *Telecommunication Aspects of a Manned Mars Mission*, Technical Report 32-501, Jet Propulsion Laboratory, Pasadena, Calif., Aug. 20, 1963.
- Viterbi, A. J., *Acquisition Range and Tracking Behavior of Phase-Locked Loops*, External Publication 673, Jet Propulsion Laboratory, Pasadena, Calif., July 14, 1959.
- Viterbi, A. J., *On Coded Phase-Coherent Communications*, Technical Report 32-25, Jet Propulsion Laboratory, Pasadena, Calif., Aug. 15, 1960.
- Viterbi, A. J., *Classification and Evaluation of Coherent Synchronous Sampled-Data Telemetry Systems*, Technical Report 32-123, Jet Propulsion Laboratory, Pasadena, Calif., June 15, 1961.
- Viterbi, A. J., *Phase-Locked Loop Dynamics in the Presence of Noise by Fokker-Planck Techniques*, Technical Report 32-427, Jet Propulsion Laboratory, Pasadena, Calif., Mar. 29, 1963; also reprinted in *IEEE Proc.*, Vol. 51, No. 12, pp. 1737-1753, Dec. 1963.
- Viterbi, A. J., *Orthogonal Tree Codes for Communication in the Presence of White Gaussian Noise*, Technical Report 32-1120, Jet Propulsion Laboratory, Pasadena, Calif., reprinted from *IEEE Trans. Commun. Technol.*, Vol. COM-15, No. 2, pp. 238-242, Apr. 1967.
- Weber, W. J., Ackerknecht, W. E., and Kollar, F. J., *Viking X-Band Telemetry Experiment Final Report*, Technical Memorandum 33-794, Jet Propulsion Laboratory, Pasadena, California, Sept. 1, 1976.
- Winn, F. B., "Selenographic Location of Surveyor VI," in *Surveyor VI Mission Report: Part II. Science Results*, Technical Report 32-1262, Jet Propulsion Laboratory, Pasadena, Calif., Jan. 10, 1968.
- Winn, F. B., "Post Landing Tracking Data Analysis," in *Surveyor VII Mission Report: Part II. Science Results*, Technical Report 32-1264, Jet Propulsion Laboratory, Pasadena, Calif., Mar. 15, 1968.
- Winn, F. B., "Surveyor Post-Touchdown Analysis of Tracking Data," in *Surveyor Project Final Report: Part II. Science Results*, Technical Report 32-1265, Jet Propulsion Laboratory, Pasadena, Calif., June 15, 1968.

- Winn, F. B., *Surveyor Posttouchdown Analyses of Tracking Data*, NASA SP-184, National Aeronautics and Space Administration, Washington, D.C., p. 369.
- Wollenhaupt, W. R., *Tracking System Data Analysis Report, Ranger 4 Final Report*, Technical Report 32-523, Jet Propulsion Laboratory, Pasadena, Calif., Mar. 1, 1964.
- Wollenhaupt, W. R., et al., *The Ranger VII Flight Path and Its Determination From Tracking Data*, Technical Report 32-694, Jet Propulsion Laboratory, Pasadena, Calif., Dec. 15, 1964.
- Wong, S. K., and Reinbold, S. J., "Earth-Moon Mass Ratio From Mariner 9 Radio Tracking Data," *Nature*, Vol. 241, No. 5385, pp. 111-112, Jan. 12, 1973.
- Woo, R., and Ishimaru, A., "Remote Sensing of the Turbulence Characteristics of a Planetary Atmosphere by Radio Occultation of a Space Probe," *Radio Sci.*, Vol. 8, No. 2, pp. 103-108, Feb. 1973.
- Woo, R., et al., *Effects of Turbulence in the Atmosphere of Venus on Pioneer Venus Radio-Phase I*, Technical Memorandum 33-644, Jet Propulsion Laboratory, Pasadena, Calif., June 30, 1973.
- Yuen, J. H., "A Double-Loop Tracking System," *IEEE Trans. Commun.*, Vol. COM-20, No. 6, pp. 1142-1150, Dec. 1972.
- Yuen, J. H., *A Practical Statistical Model for Telecommunications Performance Uncertainty*, Technical Memorandum 33-732, Jet Propulsion Laboratory, Pasadena, Calif., June 15, 1975.

